Identification and Characterization of Faults Using Deep Learning

Master Thesis

Wiktor Bönke

Structural Geology and Tectonics

60 credits

Department of Geosciences

Faculty of Mathematics and Natural Sciences

(June 2022)

Supervisors: Anita Torabi, Behzad Alaei and Alvar Braathen

Identification and Characterization of Faults Using Deep Learning

This work is published digitally through DUO – “Digitale Utgivelser ved UiO”.

http://www.duo.uio.no/

Print: Reprosentralen, Universitetet i Oslo

Abstract

The identification and characterization of faults is an important process that provides necessary knowledge from the subsurface in geological and geophysical research. 3D seismic surveys are commonly utilized for the task of exploring the structural framework of the subsurface, as they enable the view of entire large structures in 3D. In seismic interpretation manual interpretation of faults is a tedious and complicated process, additionally the results are prone to human error. Another approach for interpreting faults on seismic data is to use attributes. Attributes that highlight discontinuity on seismic data have been used to detect faults. Although, these methods are not capable to evolve independently, thus constantly rely on the interpreters knowledge. Recently, Machine Learning (ML) techniques in general and Convolutional Neural Networks (CNN) as part of Deep Neural Networks (DNN) have been used to detect and image faults on seismic data with the aim of making the process more automated. CNN networks learn and evolve from manually annotated or labeled fault interpretations.

In this study I have applied supervised CNN to image faults through binary segmentation, where faults are detected pixel-wise as ones and other background as zeros. The task was solved on 3D seismic surveys collected from three separate locations along the Norwegian Continental Shelf and the Efficient UNET and Light UNET CNN architectures were utilized to perform the task. Additionally, techniques such as data augmentation (geometric transformations) and hyperparameter adjustments were applied to improve the learning process and performance of the deep learning algorithms.

The application of data augmentation to the training and testing data, generally led to improvement in the performance of CNN on fault predictions. Although the magnitude of improvement was varying with respect to the different surveys. The initial CNN fault prediction improvement mainly relied on the quality, and size of faults present in the 3D seismic volume. Further, improvement was achieved by the adjustment of certain hyperparameters affecting the training and testing process of the CNN. Regardless, little to no improvement was noticed particularly on one seismic volume containing high levels of noise.

The characterization of fault geometries and the width of fault damage zone utilizing the best performing CNN was successfully conducted. Additionally, fault frequency plots and cumulative fault frequency plots were created to estimate the extent of the fault damage zone with focus on one fault. Although, the precision of the characterization is limited in detail due to seismic resolution and the interval spacing of fault frequency plots.

Acknowledgement

This Master thesis is written as a collaboration between Earth Science Analytics AS (ESA) and the Department of Geosciences at the University of Oslo.

First, I would like to thank my principal supervisor, Anita Torabi (University of Oslo), for giving me the chance to conduct a study on such a new, exciting and innovative topic. Thank you for sharing your ideas, knowledge and giving me helpful feedback during this process.

I would also like to thank my co-supervisors Behzad Alaei (Earth Science Analytics AS) and Alvar Braathen (University of Oslo). Specially, I want to thank Behzad and the team at Earth Science Analytics AS for providing me with the EarthNet software, which establishes the foundation of my work. Thank you for guiding me through the workflow of the software, shearing your wide knowledge of machine learning, providing me with technical support and providing me with the 3D seismic surveys utilized in this thesis.

Further, I would like to thank my fellow students at the Department of Geoscience at the University of Oslo for providing such a good working environment, motivation and support.

Last, but not least, I want to thank my parents for always believing in me and supporting me.

- Wiktor Bönke, Oslo, Norway, June 2022.

Table of Contents

1 Introduction

1.1 Study Background

The understanding of subsurface features such as faults, has for a long time been important in several geological disciplines. Faults are common geological features present in numerous geological settings within the brittle portion of Earth's crust, and exist as many different types. Most types of faults can be located in most of the tectonic regimes on earth, ranging from compressional tectonic regimes (e.g. accretionary orogens and collisional orogens) commonly related to the thrusting and folding, thus stacking of different lithological sequences. Moving through strike-slip regimes, all the way to extensional settings where rifting commonly results in rifted margins.

Rifted continental margins such as the Norwegian rifted continental margin encompass several graben structures, half-graben structures, structural highs and platforms, bounded by large faults and fault complexes (Faleide et al., 2015). Graben and platform structures are further generally divided into fault blocks, which are again internally faulted. A majority of the fault structures in rifted settings involve normal faults, but generally all margins host components of compression and strike-slip, or a mixture (transtension or transpression) such as in the rifted margin between the western Barents Sea and Svalbard (Faleide et al., 2008), resulting in reverse or strike-slip faults.

Fault geometries have by utilizing several different methods like field studies, analog sandbox experiments and seismic surveys been extensively studied. Various studies of faults are conducted as they play significant roles when it comes to fluid flow and fluid-rock interactions. As individual faults grow and form different structures due to the interaction of various rock lithologies, stress, strain and other factors, they can connect and form large complexes with complicated geometries (McClay et al., 2004; Groshong, 2006; Fredman et al., 2007). Such complexes can provide excellent pathways for fluids or create barriers (Bense et al., 2013) by the juxtaposition of impermeable lithologies and by the formation of gouge or clay smear in the so-called fault core, thus faults commonly provide great oil and gas reservoirs (Gabrielsen et al., 1990). The intense deformation within fault cores generally encompass slip surfaces, fault rock assemblages, diagenetic structures and lenses of undeformed rock (Wibberley et al., 2008; Bastesen et al., 2009; Braathen et al., 2009). Fluid flow is generally enhanced by the surrounding damage zone, which has gone through less intense deformation (Torabi et al., 2020).

It is therefore desirable to characterize fault geometries. Often studied geometric fault attributes include fault displacement, fault height and length, and the thickness of the damage zone and the fault core (Torabi and Berg, 2011).

Seismic imaging has for decades been used to image and characterize faults, commonly used with accompanying well data in areas such as the Norwegian continental shelf (Faleide et al., 2015) where extensive search for hydrocarbon reservoirs is still ongoing. The detection and characterization of faults in seismic images is a challenging task, as manual tracing of faults conducted by interpreters is a highly time-consuming task (Bahorich and Farmer, 1995; Aqrawi and Boe, 2011). The task commonly also is affected by human bias and the experience of the interpreter. The development of several seismic tools has assisted interpreters such as coherence feature extraction (Bahorich and Farmer, 1995), automatic discontinuity tracking (Admasu et al., 2006) and automatic fault extraction (Dorn et al., 2005). Such methods often come with limitations, involving difficulties of adapting to different seismic surveys and not being able to learn or evolve based on the interpreters knowledge (Xiong et al., 2018).

Machine learning methods, especially deep learning, are in contrast to more traditional tools well suited for learning from human input (Fulkerson, 1995; LeCun et al., 2015; Schmidhuber, 2015). These methods are well known for analyzing big-data automatically. For tasks such as image recognition and classification, CNN (LeCun and Bengio, 1998; Krizhevsky et al., 2012) have proven to be successful. Despite the great success of CNN, performance can always be improved, thus in recent years a technique known as data augmentation was introduced to CNN in order to boost their performance. Data Augmentation is applied for several different tasks, thereunder object detection (Redmon et al., 2016) and semantic segmentation (Long et al., 2014). One commonly applied CNN is the UNET (Ronneberger et al., 2015). Data augmentation in form of simple geometric transformations were in this study applied to Efficient UNET and Light UNET which are variations of the UNET architecture. In this approach I train the Efficient and Light UNET on data augmented slices from three different 3D seismic surveys located along the Norwegian continental shelf in order to boost their fault imaging performance. In addition, certain parameters are changed to change the architecture of the UNET, aiming to achieve further performance increase.

1.2 Study Areas

In this study, three 3D seismic volumes from three different seismic surveys are utilized:

1. Volume LN17001_Full_Stack from LN17001 3D survey.
2. Volume ST14200Z15_OBN_Full_Stack from ST14200_OBN 3D survey.
3. Volume SG9202_Full_Stack from SG9202 3D survey.

The seismic volumes have separate locations, distributed in the Norwegian North Sea and the Barents Sea (figure 1-1). In the following I will present the location for each 3D seismic survey area, individually.

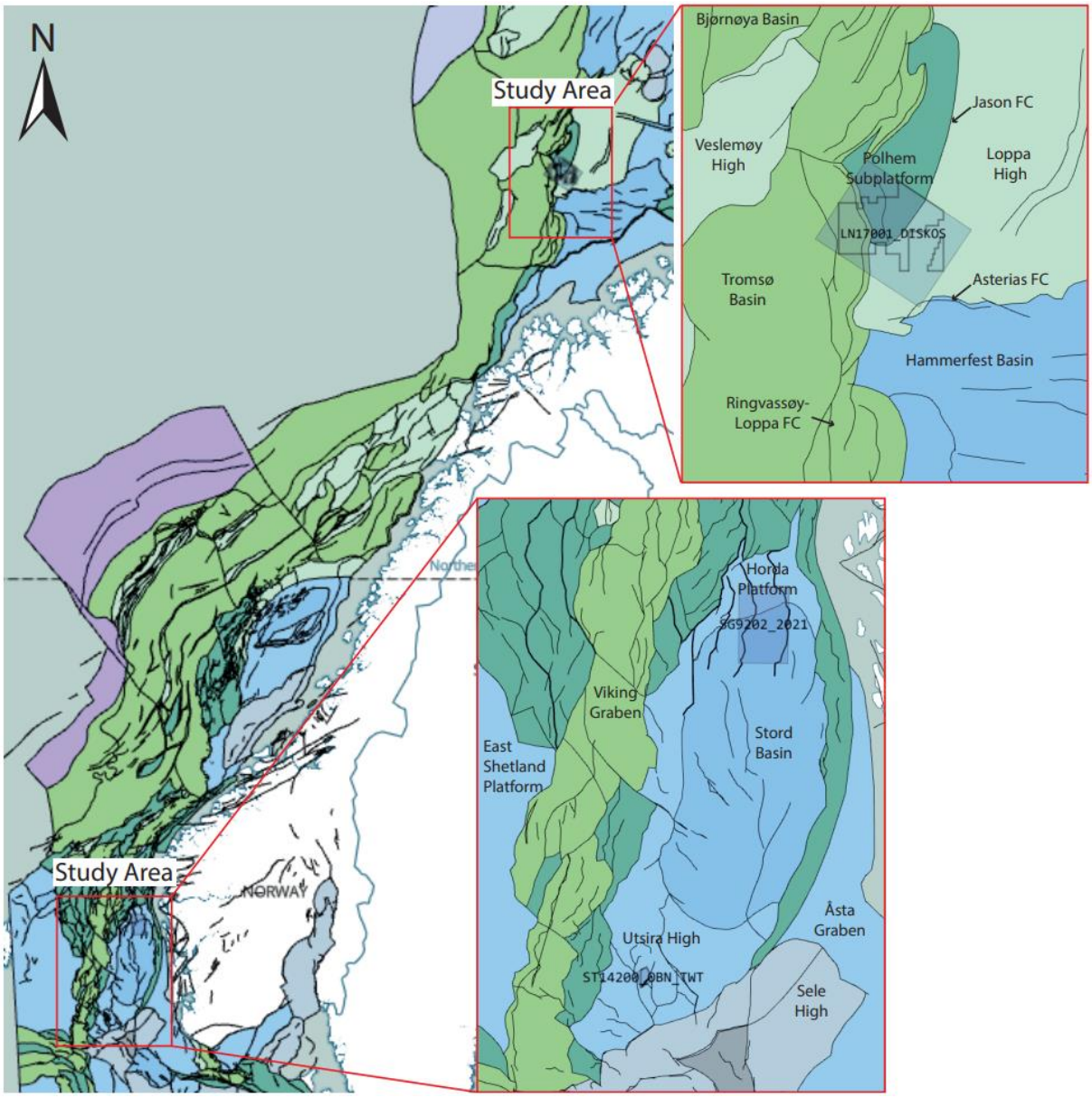

Figure 1-1: Map over the location of the study areas.

1.2.1 LN17001 3D Survey, Loppa High, Southwestern Barents Sea

LN17001 3D seismic survey in this study is acquired on the Loppa High in the southwestern Barents Sea. Seismic data from this area was collected in September 2018, utilizing TopSeis technology and covers the Loppa High blocks of PL609, PL492, PL533 and PL902 exploration licenses. These blocks are in this study represented by the full stack seismic volume of LN17001. The survey was shot by CGG in operation for Lundin Norway AS and it includes part of the southwestern Loppa High transitioning trough the Jason Fault Complex (Jason FC) in to the Polhem Subplatform. LN17001 is a pre-stack time migrated seismic survey with the following geometry: 3685 inlines (IL) with 8,33 m IL spacing, 6561 crosslines (XL) with 6,25 m XL spacing and a 2ms sample interval. The location of the survey is shown in the figure 1-1.

1.2.2 ST14200Z15_OBN_Full_Stack 3D Survey, Johan Sverdrup Field, Norwegian North Sea

The full stack seismic volume of 3D seismic survey ST14200Z15_OBN covers Johan Sverdrup block 16/2 and data was collected in February 2016 by SGS in operation for Statoil. ST1400Z15_OBN is a merged full angle seismic survey in two-way-travel time (TWT) with the following geometry: 728 IL with 12,50 m IL spacing, 694 XL with 12,50 m XL spacing and a 4ms sample interval. The Johan Sverdrup field is located in the Utsira High in the Norwegian North Sea and the studied seismic volume covers the southern part of the Utsira High. The Utsira High is located about 190 km west of Stavanger, Norway, bounding to the Stord Basin to the west and the southern Viking Graben to the east (Riber et al., 2015). The exact location of the survey is shown in figure 1-1.

1.2.3 SG9202 3D Survey, Horda Platform, Northern North Sea

The SG9202 3D survey used in this thesis is located in the Horda platform (The northern part of the volume), and the Stord Basin in the south. The survey is acquired in 1992 and covers the middle portion of the Northern Horda Platform and northern-most part of the Stord Basin, including middle sections of the major Vette Fault in the east and Tusse Fault in the west. The SG9202 survey has the following geometry: 2215 IL with 12,50 m IL spacing, 3451 XL with 12,50 m XL spacing and a 2ms sample interval. The location of volume SG9202_Full_Stack is shown in figure 1-1.

1.3 Study Objectives

The aim of this study is to image faults using CNN and study the role of data augmentation on the fault enhancement and subsequently characterizing some of the faults in one of the survey areas by extracting fault statistics along certain scanlines spatially and in depth. The following steps were followed in order to achieve the main objectives. The steps are organized as bullet points under the main objectives:

1. Using Fault detection and imaging using Deep Learning
    - Creating training labels
    - Creating baseline CNN
    - Applying data augmentation to the CNN
    - Adjusting training and testing hyperparameters
    - Exploring the effect of training and testing CNN only on seismic inlines or crosslines
    - Comparing the performance of different CNN architectures: Efficient UNET and Light UNET
2. Fault characterization using 3D fault volumes
    - Creating 3D fault models
    - Creating scanlines and fault frequency plots
    - Focusing on one fault for more detailed characterization

1.4 State of the Art on Fault Identification and Characterization

Many studies have been conducted on fault geometries like length, width, displacement, height, fault core and damage zone (Walsh and Watterson, 1988; Shipton et al., 2006; Wibberley et al., 2008; Bastesen et al., 2013; Childs et al., 2009). In outcrop, faults can be observed in great detail. The numerous features in the complicated fault core can in a good outcrop be closely examined, this includes features such as different slip surfaces, fault rock assemblages (gouge, clay smear, breccia, cataclasites), factures and veins, cementation and mineralization. In outcrop, the surrounding damage zone and its numerous amounts of minor faults and fractures or veins can also be closely evaluated.

On the other hand, it is often challenging to view the entire extent of a fault and its surrounding damage zone in the field, as its full extent is not visible. Thus, statistical distributions of fault attributes mentioned above are used to determine the relationship between them and estimate their dimensions in the subsurface. Research on the distribution and spacing of deformation bands and fractures surrounding faults have been used to estimate the width of damage zones (Barnett et al., 1987; Walsh and Watterson, 1988; Nicol et al., 1996; Torabi and Berg, 2011). Additionally, fault attribute relationships have been utilized to predict the evolution of faults such as the relationship between displacement and damage zone width (e.g. Scholz et al., 1993; Shipton et al., 2006; Torabi and Berg, 2011) or the relationship between displacement and fault length (e.g. Cowie and Scholz, 1992; Dawers et al., 1993; Kim and Sanderson, 2005; Kolyukhin and Torabi, 2012). Anyways, it is important to keep in mind that these statistics are limited (Choi et al., 2016).

When considering the use of seismic images, it is easier to capture the full extent of faults in terms of their height, displacement and length. At least to the extent seismic resolution allows it. In 3D seismic images faults are generally recognized by causing discontinuities in lateral reflections. Accordingly, several methods utilizing the calculation of attributes measuring the reflection continuity in seismic have been used to detect faults. Such attributes are for instance different types of coherence (Marfurt et al., 1999; Li and Lu, 2014; Wu, 2017). However, these methods are sensitive to noise and stratigraphic features, and thus insufficient to detecting faults when used alone (Hale, 2013).

Complimentary to the seismic attribute methods such as coherence, Gersztenkorn and Marfurt (1999) introduced vertically elongated windows to enhance faults, based on the observation that faults are typically more vertical than seismic reflectors. Other complimentary methods applied to coherence or semblance are smoothing in directions normal to seismic reflectors (Bakker, 2002; Hale, 2009; Wu, 2017), involving assumptions that faults always are perpendicular to seismic reflectors, which is somewhat inaccurate. By

modifying this approach slightly researchers (Hale, 2013; Wu and Hale, 2016) smoothened the numerator and denominator along fault strike and dip. This approach is known as the fault likelihood, calculating the fault-oriented semblance. Pedersen et al. (2002; 2003) introduced “artificial ants” involving the smoothing of fault attributes of all existing fault strike and dip combinations to better enhance fault features. This method was further evolved by Wu and Fomel (2018), more efficiently utilizing the maximum fault attributes to find optimal surfaces and using these to generate fault images of fault probability, strike and dip.

CNN methods have recently been introduced to the detection of faults as a pixel-wise fault classification, where individual pixels are identified as fault or non-fault (Huang et al., 2017; Di et al., 2018; Guo et al., 2018; Wu et al., 2018, 2019; Zhao and Mukhopadhyay, 2018). Such CNN methods come with high computational costs, thus more efficient methods have been proposed. Several powerful CNN architectures have been established which achieve great image segmentation results (e.g. Girshick et al., 2014; Ronneberger et al., 2015; Xie and Tu, 2015; Badrinarayanan et al., 2017; He et al., 2017; Ren et al., 2017).

Wu et al. (2019) created a simplified efficient end-to-end CNN based on the UNET from Ronneberger et al. (2015) for conducting 3D binary fault segmentation. In the approach of Wu et al. (2019) synthetic 3D seismic data is created automatically to train the CNN by using a parameterized workflow designed to generate fold and fault structures, wavelet peaks and noise. Choosing random sets of parameters, numerous sets of seismic images can be generated. In addition, Wu et al. (2019) apply data augmentation (vertical and horizontal flip) during training to increase diversity in the dataset. Other approaches to identifying faults in seismic using synthetic seismic data (Wu et al., 2020) or a combining both real and synthetic seismic (Aseev et al., 2019) have been introduced with great success, even when applied to completely different real seismic surveys (Wu et al., 2019). CNN based methods generally exceed the performance of more traditional methods, for instance Xiong et al. (2018) stated that fault probabilities derived from CNN better highlight seismic discontinuities than seismic coherence.

1.5 Thesis Outline

This thesis consists of the following 6 chapters listed below:

- **Chapter 1- Introduction:** A brief introduction to the topic of using ML for the task of identifying and characterizing fault in seismic, introducing the study areas, presenting the study objectives and providing an overview over the state of the art on fault identification and characterization.
- **Chapter 2- Geological Setting:** Providing context to the geological evolution of the study areas and their present-day geology.
- **Chapter 3- Methods:** Introducing concepts and different ML networks with focus on supervised learning, CNN and data augmentation, in addition to giving insight to the workflow used in this thesis.
- **Chapter 4- Results:** Imaging of faults in 3D seismic data volumes using Efficient UNET and Light UNET when applying different data augmentation techniques and hyper parameter values. Thereafter, using a CNN for fault characterization.
- **Chapter 5- Discussion:** Discussing the main findings.
- **Chapter 6- Conclusions:** Summarizing the most important observations of this study.

2 Geological Setting: Evolution of the Barents Sea and the North Sea

The three seismic surveys used in this thesis are located in the Norwegian North Sea and Southwestern Barents Sea. The Norwegian continental margin is characterized by two distinguishable segments; 1) a dominantly rifted volcanic margin located 62-70°N offshore mid-Norway and 2) the dominantly sheared margin stretching along the western Barents Sea and Svalbard, 70-82°N (figure 2-1). The Norwegian continental shelf is considered part of the margin, including the Norwegian continental slope, leading into the deep NE Atlantic Ocean (Faleide et al., 2008).

The shallower North Sea and Barents Sea were before the opening of the Atlantic Ocean in early Cenozoic time, part of a larger epicontinental ocean, situated between Fennoscandia, Svalbard and Greenland. Since the Devonian (i.e. after the Caledonian collapse), the margin of Norway, Greenland (Brekke, 2000; Skogseid et al., 2000; Hamann et al., 2005; Tsikalas et al., 2005) and the Barents Sea (Faleide et al., 1993; Gudlaugsson et al., 1998) underwent extension comprising several events until the early Cenozoic breakup. These margins are included in the North Atlantic Volcanic Province (NAVP) (Saunders et al., 1997), thus imprints of extrusive and intrusive magmatism form the breakup can be found at different crustal levels of the rifted margins.

The interplay of geological structures and compositions of stratigraphy within the Norwegian continental shelf, stretching from the Norwegian continental margin to onshore Norway, is a result of pre-breakup basin evolution, breakup-related tectonism and magmatism, and post-breakup margin evolution. In this chapter the geological evolution of the Barents Sea and the North Sea is presented. In addition, more detailed descriptions of the Loppa High (southwestern Barents Sea), the Johan Sverdrup field (Norwegian North Sea) and the Horda Platform (northern North Sea) will be given.

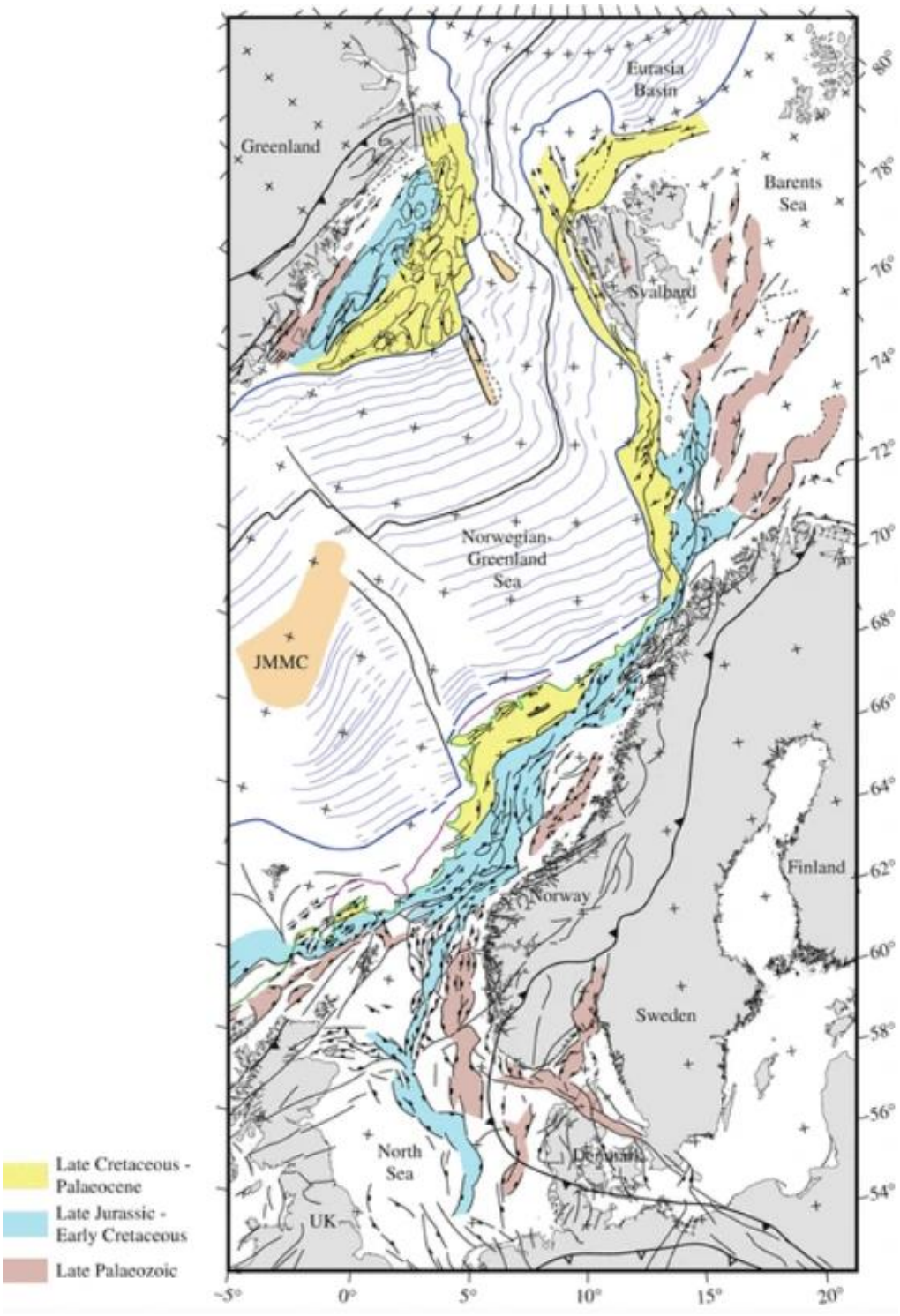

Figure 2-1: Regional structural map of the NE Atlantic region including the most important rift phases and areas that are affected by the evolution of the Norwegian Rifted Margin. From Faleide et al. (2015) (modified/updated from Faleide et al. (2008)). JMMC = Jan Mayen microcontinent.

2.1 Geological Evolution of the Barents Sea

The Barents Sea at present day is an epicontinental sea situated in the northwestern corner of the Eurasian tectonic plate. The continental shelf below it has undergone several extensional events since the Caledonian orogen collapsed (e.g. Faleide et al., 1984), forming multiple basins, highs and fault complexes (Gabrielsen et al., 1990). After the Caledonian collapse multiple rifting events occurred. In Late Paleozoic, rift basins between Norway and Greenland were created in the western Barents Sea along the NE-SW trend of the Caledonites. Thereafter, prior to the opening of the Atlantic Ocean, in Late Jurassic to Early Cretaceous, rift events along the northeastern Atlantic-Arctic margin formed deep Cretaceous basins in the southwestern Barents Sea (Faleide et al., 2008). Doré (1991) has suggested that the major Late Paleozoic to early Mesozoic rift events occurred in mid-Carboniferous, Carboniferous to Permian and Permian to Early Triassic times. Although, due to younger tectonic overprint and deep sedimentary burial, these events are poorly resolved. An Upper Carboniferous to Lower Permian carbonate platform overlayed large portions of the present-day Arctic continental blocks. Below it, commonly carboniferous rift structures are found in the western Barents Sea (Gudlaugsson et al., 1998). In Late Paleozoic rift basins along the southwestern Barents Sea margin, thick evaporites were deposited.

During a late Middle Jurassic to earliest Cretaceous rift episode of the NE Atlantic-Arctic margin a change in the extensional stress field to NW-SE was noticed. The event is related to the northward movement of the Atlantic rifting (Faleide et al., 1993), and led in the southwestern Barents Sea to the formation of the Harstad, Tromsø, Bjørnøya, and Sørvestsnaget basins. Further, differential subsidence and segmentation divided the basins into sub-basins and highs (Faleide et al., 2008). In mid Cretaceous another mild extensional episode was noticed in the southwestern Barents Sea, well constrained to Aptian time (Faleide et al., 1993). During the Cretaceous, regional uplift occurred in the north, which resulted in sediment progradation southward in the Barents Sea (Faleide et al., 2008).

In the Late Cretaceous to Paleocene, just prior to the NE Atlantic breakup the De Geer Zone was accommodating strike-slip movement during the extension between Norway and Greenland, forming pull-apart basins in the southwestern Barents Sea (e.g., Faleide et al., 1993; Breivik et al., 1998; Ryseth et al., 2003), thus a deep marine Paleocene succession was deposited in the Sørvestsnaget Basin and Vestbakken Volcanic Province (Ryseth et al., 2003).

Approximately, 55-54 Ma final lithospheric breakup at the Norwegian margin occurred, with a duration of 3 to 6 million years. Due to the sheared margin setting of the western Barents Sea-Svalbard margin, its evolution became quite complex. The southwestern Barents Sea

margin developed during the opening of the Norwegian-Greenland Sea in Eocene time, along the Senja Fracture Zone. It first developed by continent-continent shear, further developing into continent-ocean shear, which eventually turned passive in the earliest Oligocene. Within the Sørvestsnaget Basin conditions remained deep marine throughout the Eocene, characterized during the Middle Eocene by the deposition of sandy sub-marine fans (Ryseth et al., 2003). Thick Eocene sediments were also deposited in the Vestbakken Volcanic Province, after magmatic activity and down-faulting related to the breakup (Faleide et al., 2008). During Eocene, the Bjørnøya-Spitsbergen margin segment underwent oblique continent-continent shear and some continent-ocean shear, with both transtensional and transpressional components (Grogan et al., 1999; Bergh and Grogan, 2003).

In earliest Oligocene, the tectonic plate movement was reorientated, and Greenland moved in a more westerly direction relative to Eurasia (Faleide et al., 2008). Rifting related to this event, reactivated mostly NE-SW oriented fault blocks in the Vestbakken Volcanic Province, occurring in Early Oligocene. Additionally, in the Eocene to Oligocene transition, pronounced marine shallowing happened in the Sørvestsnaget Basin (Ryseth et al., 2003).

After the margin breakup, the complex, mainly sheared western Barents Sea-Svalbard margin became passive over time, with different segments of the margin reaching this state at various times (Faleide et al., 2008). In the Late Miocene, at the western Barents Sea margin, uplift happened which was increasingly significant towards the eastern part of the Vestbakken Volcanic Province and possibly linked to pre-glacial tectonic uplift of the Barents shelf (Jebsen and Faleide, 1998).

A clear unconformity is found within the entire continental shelf, which marks the change to glacial sediment depositions with oldest ages dated approximately 2,6 Ma (Pliocene), during the glaciation of the Northern Hemisphere. For instance, in the Barents Sea the unconformity on the slope becomes a downlap surface for large prograding, sandy and silty mud wedges formed with sediments from the mainland around the NE Atlantic and continental shelfs. Within the Pliocene sediments, scattered deposits of ice-rafted debris exist, marking events of regional cooling and the formation of glaciers. As a consequence of ice streams eroding the shelf, large deposits of Plio-Pleistocene sediments formed in deep throughs (Faleide et al., 1996; Laberg and Vorren, 1996; Dahlgren et al., 2005; Nygård et al., 2005; Rise et al., 2005). During the Pliocene and Pleistocene, the glacial erosion of the Barents Shelf and major deposition of glacial deposits in submarine fans combined with uplift, led to reginal tilt of the Norwegian margin (Dimakis et al., 1998). A stratigraphic chart summarizing major stratigraphic sequences including locations in and around the Barents Sea, thereunder the Tromsø Basin, can be found in figure 2-2. Glacial sediments make up about 50 percent of

the total post-opening sediments along the western Barents Sea margin. That large amount of Pliocene and Pleistocene sediments in the submarine fans was a factor leading to instability and numerous submarine slides over a longer period of time (Bryn et al., 2005; Evans et al., 2005; Solheim et al., 2005; Hjelstuen et al., 2007).

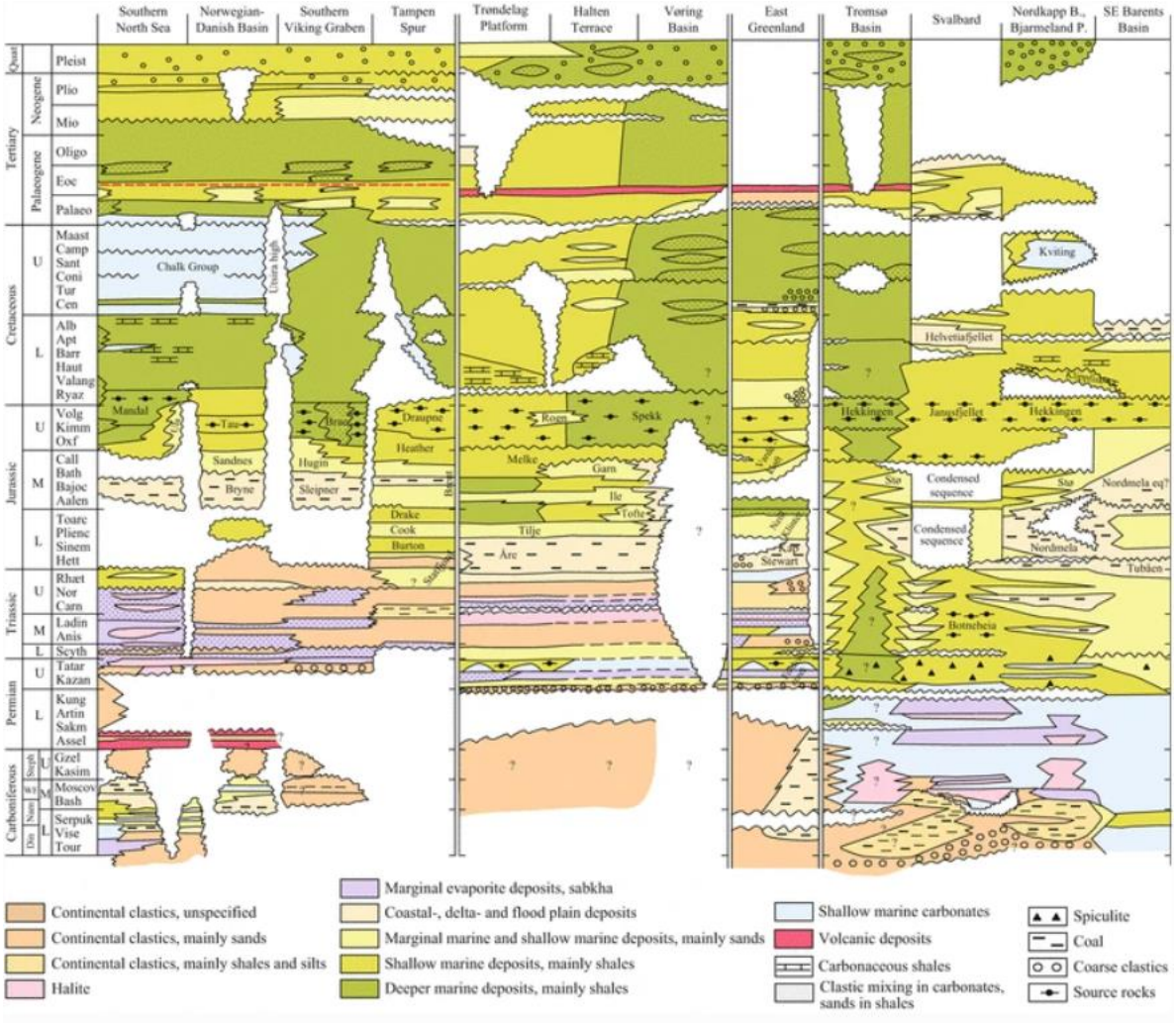

Figure 2-2: Stratigraphic chart providing a overview over the general stratigraphic sequences in the North Sea and Barents Sea formed after Devonian time (Faleide et al., 2015; modified from Brekke et al., 2001).

2.1.1 Geological Evolution of the North Sea, Focusing on the Northern North Sea

The present-day North Sea is an intracontinental basin located on the Baltican continental crust (Faleide et al., 2015). The ocean is bounded by the NE Atlantic in the north, the Shetland Islands and Great Britain in the northwest and west, respectively, Central Europe in the south and Scandinavia in the east (figure 2-3).

The North Sea, in similarity to the Barents Sea, was affected by the evolution of the Norwegian Continental Margin. In contrast to the Barents Sea, the North Sea was rather affected by the dominantly rifted volcanic margin located 62-70°N offshore mid-Norway than the dominantly sheared margin stretching along the western Barents Sea and Svalbard, 70-82°N as introduced in figure 2-1. The formation and collapse of the Caledonian orogeny amongst other events, also had a large influence on the structural evolution of the North Sea basin (Faleide et al., 2015). According to Faleide et al. (2015) in addition to the two previously mentioned marginal provinces, the North Sea is considered as its own Norwegian continental shelf province. The North Sea has a long history of multiple events that hosted stretching/thinning and subsidence of the crust. Essentially, these were rift phases that occurred in late Carboniferous, Permian to Early Triassic and Late Jurassic times. The rift phases were always followed by thermal cooling and regional subsidence of the basins (Faleide et al., 2015).

Major elements of the Northern North Sea province include the Viking Graben which towards the north becomes the Sogn Graben. West of these grabens are the East Shetland Basin and the Tampen Spur, and to the east of the grabens the Horda Platform is located (figure 2-3). A cross-section of these Jurassic to Cretaceous structural features is shown in figure 2-4. Crustal thinning occurred in the late Middle to Late Jurassic, followed by subsidence and sedimentation in the Cretaceous. However, below the Jurassic to Cretaceous structures earlier rift basins are found, presumably of Permian to Early Triassic age. The axis of this rift system is located below the Horda Platform and the eastern and western boundaries are the Øygarden Fault zone and the Eastern Shetland Platform, respectively. Generally, this area consists of half-grabens formed by rotation of fault blocks during lithospheric extension and crustal thinning (figure 2-4). Most likely during late Devonian time, the area was also affected by post-Caledonian extension (Faleide et al., 2015).

Further south, along the graben structures of the Viking Graben, we transition into the Norwegian Central North Sea Province where the northwestern part of the Central Graben is located. The Central Graben is of Jurassic-Cretaceous age and its strata was affected by halokinesis in the Triassic, forming large salt-structures in the graben in pre-Jurassic times. Although, some areas hosted salt movement until the Tertiary. The formation of large, rotated fault blocks during Jurassic rifting led to area dependent major erosion. Further complexity was added to the area as tectonic inversion occurred in the Cretaceous. In addition to the Central Graben, the Norwegian-Danish Basin also contains numerous salt structures, but the basin was not involved in any significant rifting events (Faleide et al., 2015).

The Caledonian basement rocks which underlie most of the North Sea sedimentary basin, including zones of weakness originated from the Caledonian Orogeny have influenced its shape, together with the thickness of the continental crust. The Hercynian (Variscan) mountain range, oriented E-W, occurring in Germany, northern France and southwestern England marks the southern boundary of the North Sea Basin. This mountain range was formed in Carboniferous to Permian time. Contraction and uplift caused large amounts of sediments to be deposited to the north, initiating basin formation in the North Sea (Faleide et al., 2015). figure 2-2 includes a stratigraphic summary of a few areas scattered around the North Sea Basin.

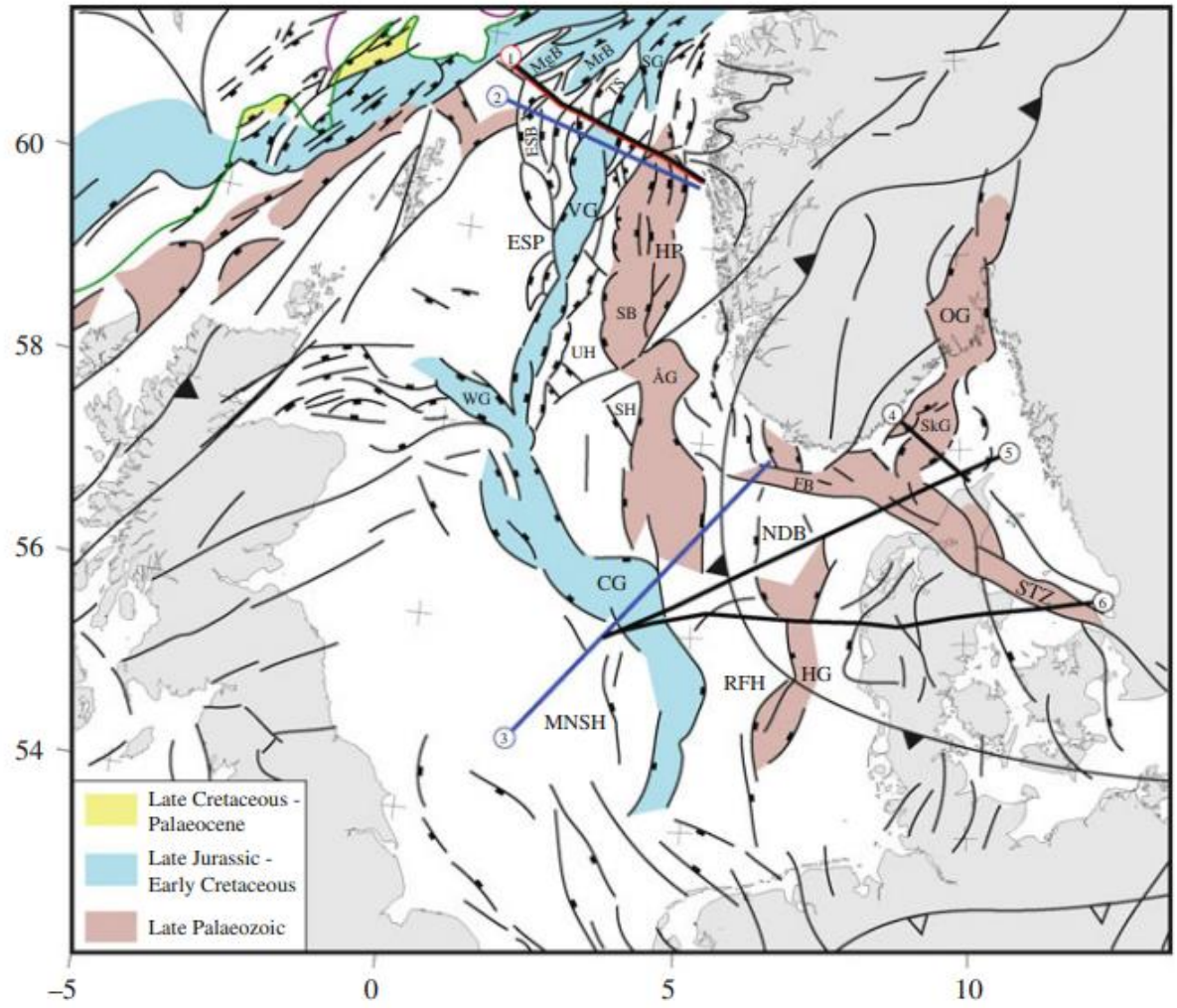

Figure 2-3: Major structural features in the North Sea (close-up from figure 2-1 – from Faleide et al., 2015 (modified/updated from Faleide et al., 2008)). The cross-section marked with a red line (1) is shown in Figure 2-4. CG = Central Graben, ESB = East Shetland Basin, ESP = East Shetland Platform, HG = Horn Graben, HP = Horda Platform, MgB = Magnus Basin, MNSH = Mid North Sea High, MrB = Marulk Basin, NDB = Norwegian-Danish Basin, OG = Oslo Graben, RFH = Ringkøbing-Fyn High, SB = Stord Basin, SG = Sogn Graben, SH = Sele High, SkG = Skagerrak Graben, STZ = SorgenfreiTornquist Zone, TS = Tampen Spur, UH = Utsira High, VG = Viking Graben, WG = Witchground Graben, ÅG = Åsta Graben.

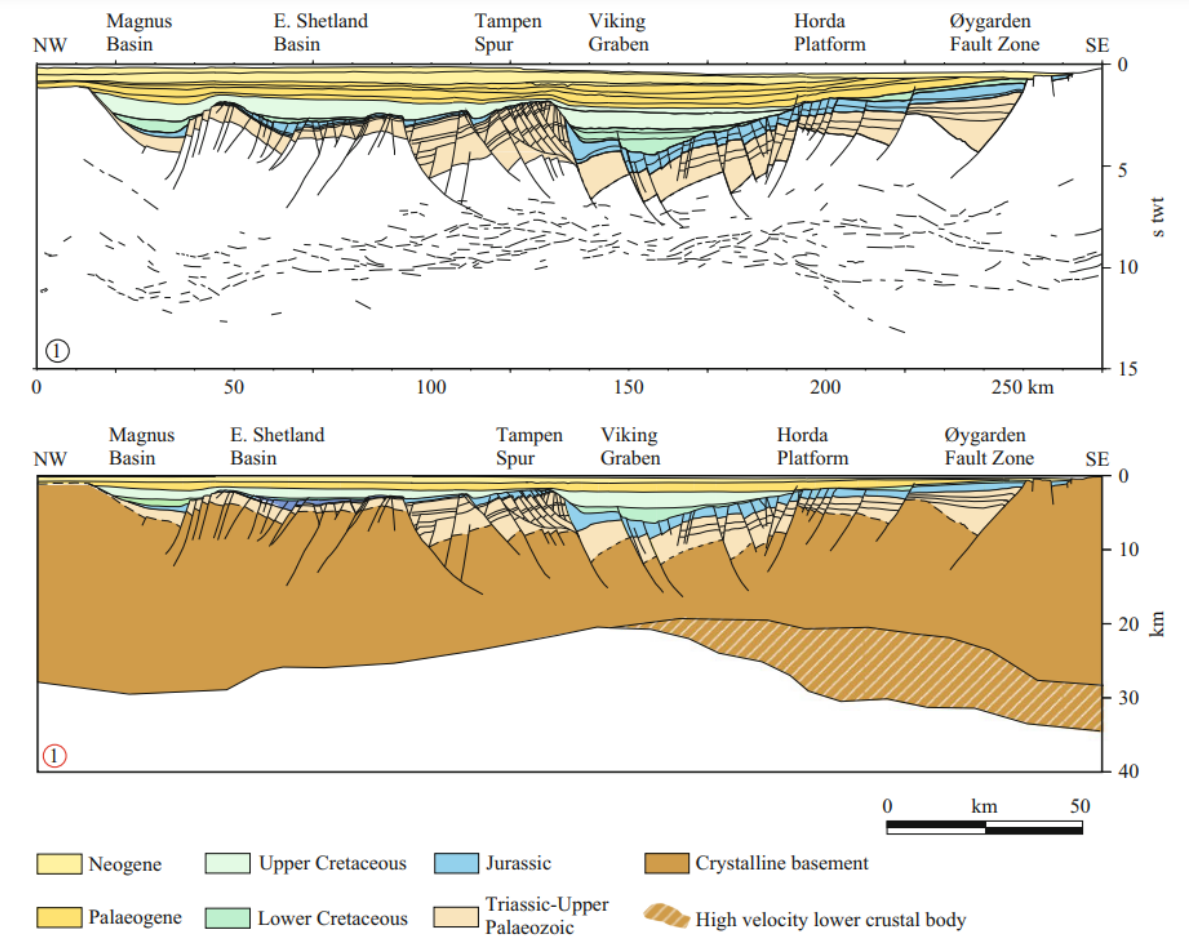

Figure 2-4: Interpreted regional cross-section from regional deep seismic lines across the northern North Sea. From Faleide et al. 2015 (modified from Christiansson et al., 2000).

2.2 Geological Evolution and Stratigraphy Specific to the Survey Locations

2.2.1 Loppa High, Southwestern Barents Sea

Geological Evolution of the Loppa High and Polhem Subplatform

In the southwestern Barents Sea, Rifting discontinued after the opening of the North Atlantic and Arctic Oceans. During the late stages of rifting the southwestern Barents Sea was characterized by a simple rift system in the south, transitioning to a dextral transform system in the northwest, connecting the North Atlantic rift to the Arctic rift system (Faleide et al., 2008). In total, the southern Barents Sea has a history of extension ranging over at least 300 million years. Multiple researchers have found evidence of tectonic inversion occurring as late Paleozoic to Cenozoic events, amongst the researchers are Gabrielsen et al. (1990) who also discovered an important example around the Loppa High. The prominent example occurred during early Cretaceous, where the uplift of a late Triassic to mid-Jurassic

depocenter caused the high to form an island. Simultaneously, transpression along the Bjørnøyrenna Fault Complex (Bjørnøyrenna FC) (Gabrielsen et al., 1997) and wrench-related tectonic inversion in the area occurred (Rønnevik et al., 1982). Areas that are involved in the tectonic inversion which occurred during early Cretaceous include the Loppa High, the Polhem Subplatform, the Hammerfest Basin, the Bjørnøya Basin and the Tromsø Basin (figure 2-5).

The Loppa High is in the west separated from the Polhem Subplatform, by the Jason FC. The Polhem Subplatform, which was part of the Loppa High for a majority of its existence, has its southwestern and northwestern boundaries by the Ringvassøy-Loppa Fault Complex and Bjørnøyrenna FC, respectively. The northeastern portion of the Bjørnøyrenna FC also acts as the border between the Loppa High and the Bjørnøya Basin. Towards the south, the Loppa High is separated from the Hammerfest basin by the southward dipping Asterias Fault Complex (Asterias FC). In the east, the Loppa High connects to the Bjarmeland Platform (figure 2-5).

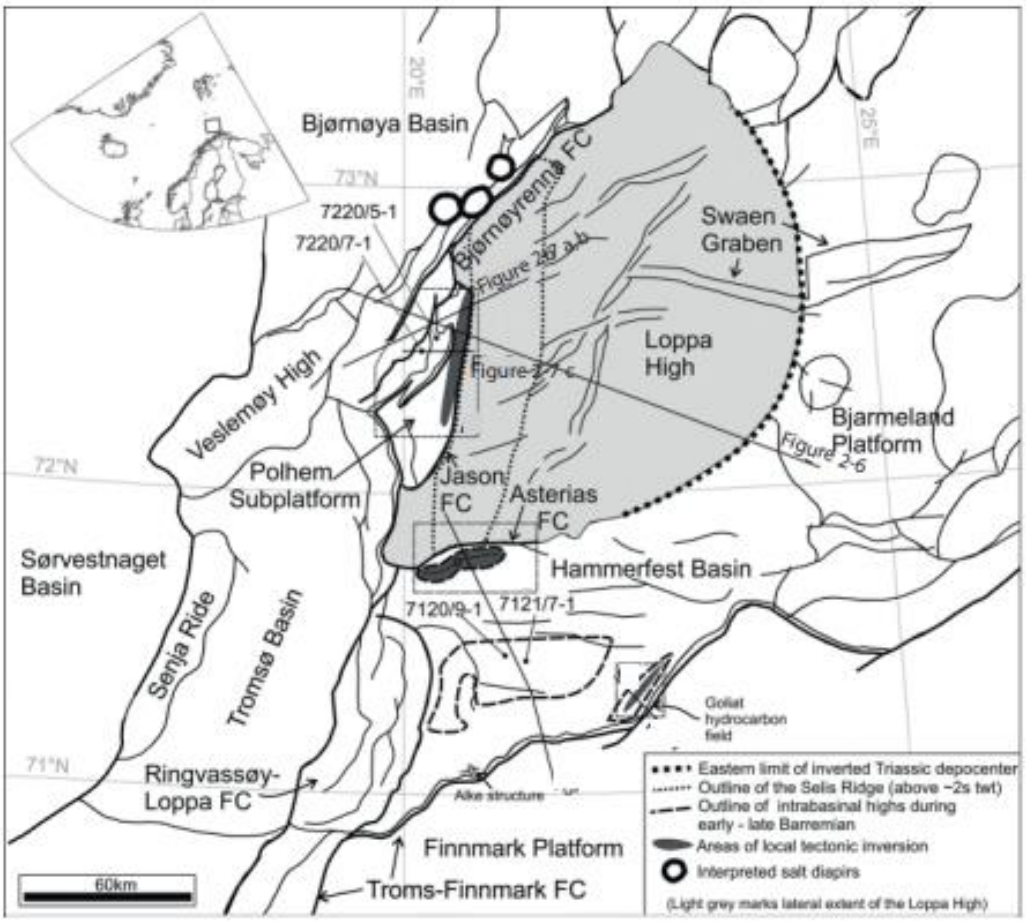

Figure 2-5: Map over the main structural elements of the Loppa High (Marked in grey) and the main surrounding structural features. The location of seismic lines in Figures 2-6 and 2-7 are also marked on the map. Modified from Indrevær et al. (2016).

The Loppa High underwent multiple subsidence and uplift events. The Selis Ridge, an eastward tilted high, now buried along the western side within the Loppa High is known as the “paleo-Loppa High”. “Paleo-Loppa High” indicates that it existed as a structural high or platform, prior to the present-day Loppa High. The Selis Ridge formed as the footwall of the westward dipping Ringvassøy-Loppa and Bjørnøyrenna FC which was uplifted in the late Carboniferous, early Permian, late Permian and early to middle Triassic (Riis et al. 1986; Wood et al. 1989; Gudlaugsson et al. 1998; Glørstad-Clark et al. 2010; Glørstad-Clark 2011). Part of the Selis Ridge was down faulted in the early to middle Triassic, forming the Polhem Subplatform (Gabrielsen et al., 1990). The N-S-striking Selis Ridge became an elongated structural high functioning as a barrier for sediments (Gudlaugsson et al., 1998). Thereafter, the Selis Ridge was subsided and by the Late Triassic a large sediment depocenter was formed on top of the ridge. During the late Jurassic or earliest Cretaceous a larger platform encompassing the Selis Ridge and Polhem Subplatform was uplifted causing the late Triassic to mid-Jurassic depocenter to create a subaerially exposed Loppa High (Wood et al., 1989). Estimations made by Clark et al. (2014) suggest that the platform was uplifted 300 m. Composite tectonism in the southwestern Barents Sea with pronounced increase in subsidence of the Tromsø and Bjørnøya basins in the early Cretaceous caused by regional wrench tectonics, is by several authors with different arguments and observations (Ziegler, 1978; Rønnevik et al., 1982; Gabrielsen, 1984; Berglund et al., 1986; Riis et al., 1986; Sund et al., 1986; Gabrielsen and Færseth, 1988; Gabrielsen et al., 1993; Gabrielsen et al., 2011) suggested to have caused uplift of the Loppa High. Gradual erosion and subsidence of the Loppa High during the early Cretaceous, brought it down to similar levels as the Barents Sea shelf by the late Cretaceous (Glørstad-Clark, 2011). Some of the structures within or bounding the Loppa High described in this paragraph and the paragraphs bellow, such as the Selis ridge, Jason FC and Polhem subplatform are to be found in volume LN17001 of this study. The structures are visible in the scanlines presented in section 4.2 of this thesis.

Present-day Geology and Stratigraphy of the Loppa High

The interior of the Loppa High contains an asymmetric deposition of sub-Carboniferous rocks which shallow towards the west and become the structurally elevated Selis Ridge. The eastern flank of the Selis Ridge is onlapped by Carboniferous and Permian sedimentary rocks (comprising Carbonates). The sub-Carboniferous, Carboniferous and Permian units are covered by upper Triassic to mid-Jurassic sedimentary units which were uplifted in the late Triassic or earliest Cretaceous to form the Loppa High. Jurassic rocks are mainly characterized as sandstones (Faleide et al., 2015). Those units are thickening towards the

eastern part of the Loppa High, away from the Selis Ridge and thinning when entering the Bjarmeland Platform. Generally, there is an absence of younger sediments (Jurassic and younger) on top of the Loppa High, due to erosion. Locally, lower Cretaceous and Jurassic sediments are preserved by NNE-SSW-and NE-SW-oriented grabens bounded by faults converging with depth and terminating in Permian evaporites (figure 2-6).

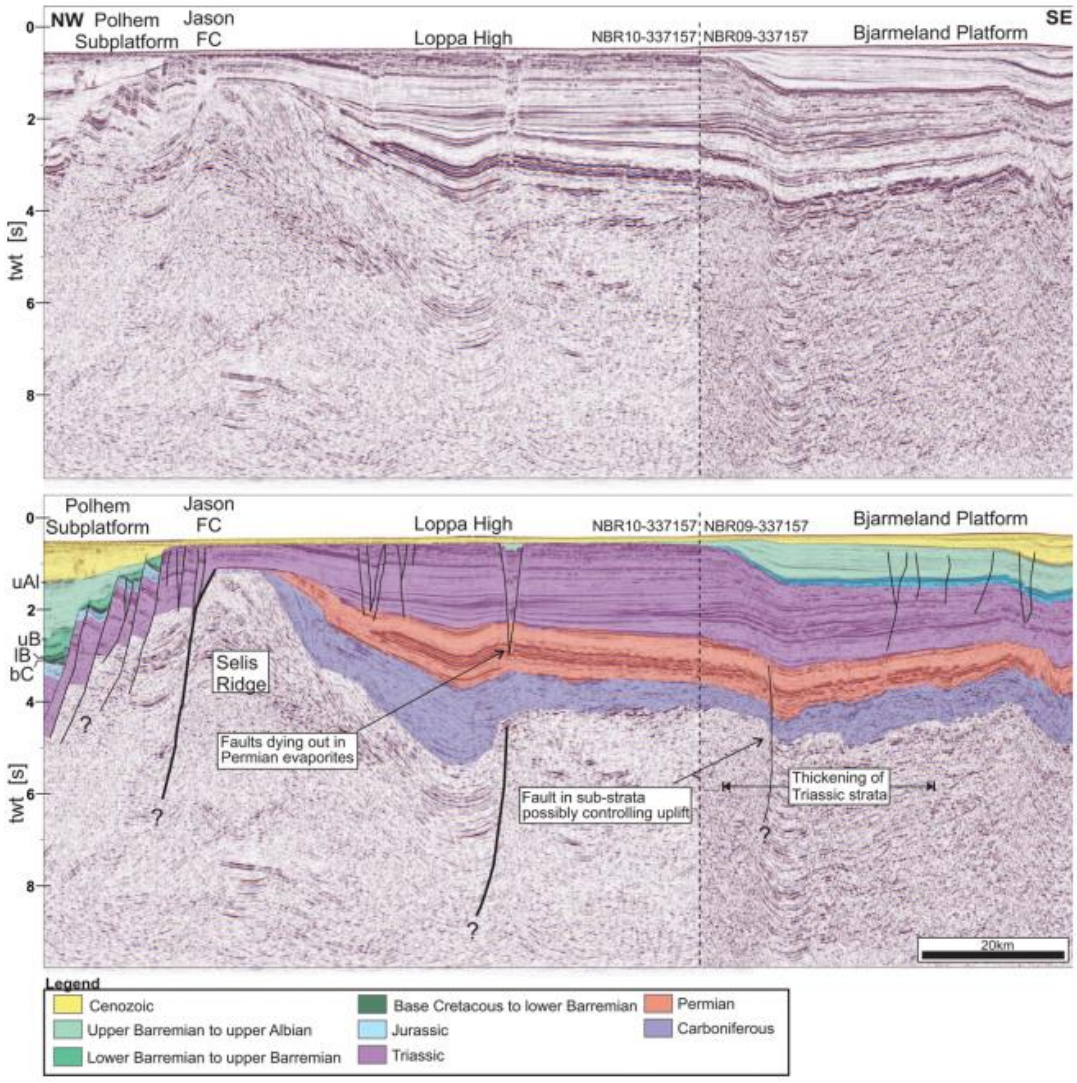

Figure 2-6: Uninterpreted and interpreted seismic image encompassing the Bjarmeland Platform in the SE and the Loppa High, Selis Ridge, Jason FC and Polhem Subplatform moving NW. The location of the seismic line is indicated in figure 2-5. From Indrevær et al. 2016.

Present-day Geology and Stratigraphy of the Polhem Subplatform

The Polhem Subplatform consists of multiple N-S-striking fault blocks that are rotated and bordered by several west-dipping large normal faults (figure 2-7). Those large normal faults are most easily determined at the base Cretaceous. In the hanging walls of the faults sedimentary wedges are formed, indicating synsedimentary faulting which began in the late Jurassic. In addition, accelerated subsidence by the early Barremian and onwards is suggested. Located closely to the Jason FC are densely spaced fault block (figure 2-7 b). Within the fault blocks are at least four anticlines forming a left-stepping en-echelon pattern. The blocks are forming a positive flower structure when viewed in a WSW-ENE-oriented cross-section, which is forming a N-S- orientated, elongated and elevated structure, traceable for about 40 km along the northern part of the Jason FC, on the hanging wall side. Further west on the Polhem Subplatform, fault blocks are also generally internally folded and locally contain growth wedges of Ryazanian to late Barremian age showing signs of localized inversion indicated by the reverse activation of faults at graben boundaries and/or internal folding (figure 2-7 c). Both, the fault blocks in the immediate hanging wall of the Jason FC and the fault blocks located further west are characterized by erosional surfaces at the crests, which should be of similar age. The erosional surfaces truncate the contractional structures found in the fault blocks, thus the erosional event occurred simultaneously as the compressional event or afterwards. Within the growth wedges the upper Barremian sequence onlaps the lower Barremian sequence. The lower Barremian sequence shows more folding, whilst the upper Barremian sequence only is affected by later minor folding. Further, these units are overlain by upper Barremian to middle Albian sediments. Combining these observations, the inversion of the Polhem Subplatform can be constrained to have occurred between the early Barremian and middle Albian time (Indrevær et al., 2016).

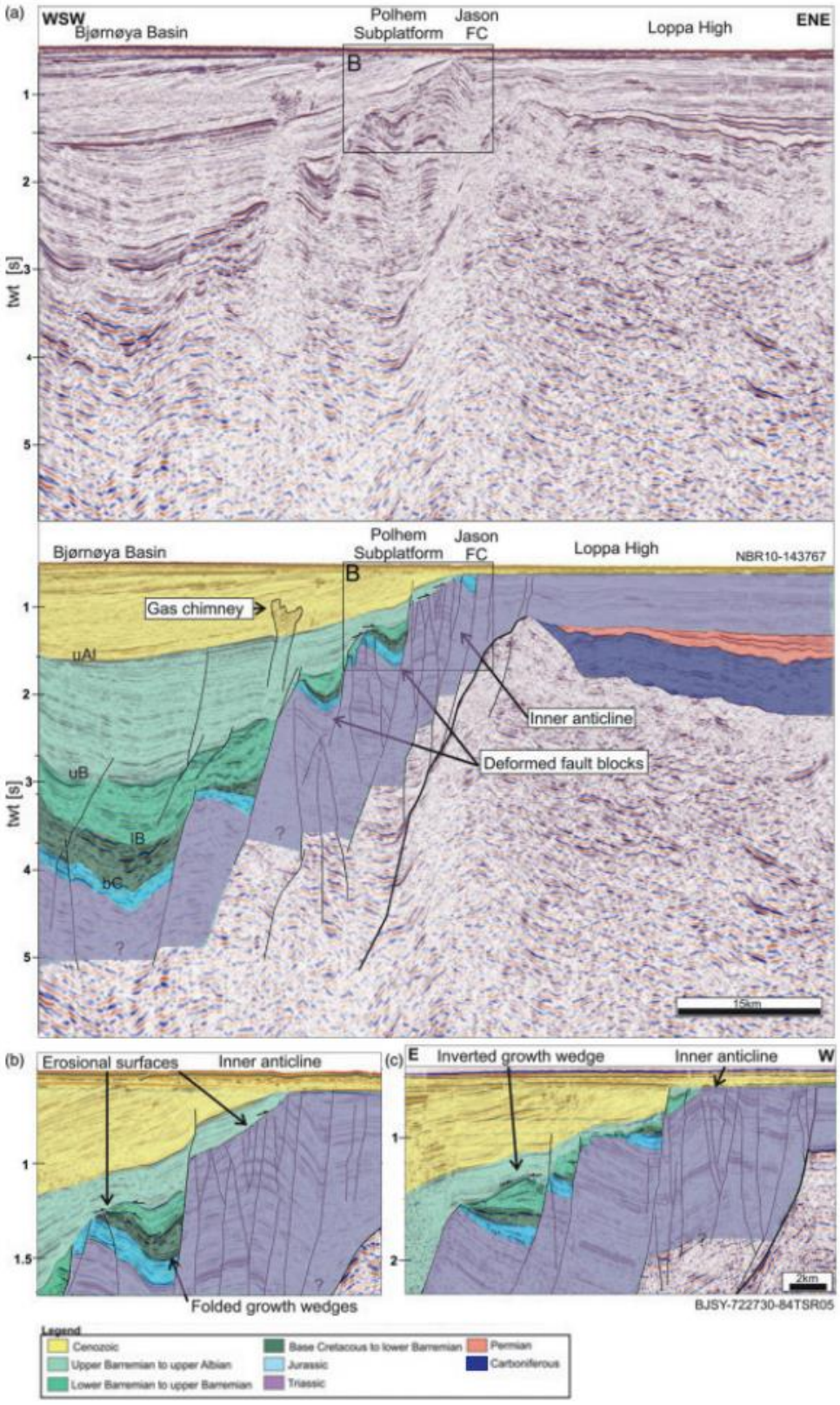

Figure 2-7: (a) Uninterpreted and interpreted seismic line capturing a cross-section of the Loppa High ENE and moving across the Jason FC, Polhem Subplatform and Bjørnøya Basin (b) More detailed section from (a). (c) Details from the same area. Locations of the seismic lines are marked in figure 2-5. Modified from Indrevær et al. 2016.

2.2.2 Utsira High (Johan Sverdrup), Northern North Sea

The Johan Sverdrup field which is part of this study is located in the Utsira High. The Utsira High is one of several intrabasinal structural highs located in the Norwegian North Sea, bounded by grabens. To the west, the Utsira High is bounded by the southern Viking Graben, and to the north and east by the Stord Basin. Just south of the Utsira High, the Ling Depression is located (figure 2-8).

In the Silurian to Early Devonian times uplift, exhumation and erosion of the Caledonian mountain chain happened fast (Coward et al., 2003; Fossen et al., 2008; Gabrielsen et al., 2010). During the Devonian the North Sea was located in a hot, arid and continental setting, moving from 20°S to 15°S (Downie, 1998), depositing sandstone (Old Red Sandstone) in half graben basins (Marshall and Hewett, 2003). The sandstones are found in basins in western Norway and on the British Isles, but have not been detected as a continuous layer across the North Sea (Seranne and Seguret, 1987; Downie, 1998).

In Early Carboniferous, the North Sea was located close to the equator, which led to warm and more moist conditions (Glennie and Underhill, 1998). Transgression occurred in the Early Carboniferous and covered the Devonian landscape changing deposition from mostly continental to marine (Glennie and Underhill, 1998; Bruce and Stemmerik, 2003). Clastic sedimentation sourced from the north increased during the Middle Carboniferous, as kaolinite is found to be the dominant clay mineral on the British Isles (Weaver, 1989; Brekke et al., 2001). This was followed by folding and trusting due to the Variscan Orogeny. The North Sea was affected by uplift and erosion combined with sedimentation sourced from the south (Besly, 1998; Lundmark et al., 2013). Carboniferous sediments are thought to be preserved on the Utsira High in pre-Permian half grabens (Brekke et al., 2001).

During the Permian, climate in the North Sea changed to more dry and arid conditions as the region continued to drift northwards to approximately 20°N (Glennie and Underhill, 1998). A climate barrier was formed as a combined result of the closing of the Caledonian and Variscan oceans and formation of mountain belts (Coward et al., 2003). As the Variscan Orogen collapsed in Early Permian the area south of the Norwegian sector developed extensional fracture systems and widespread volcanism (Glennie and Underhill, 1998). Thermal relaxation of the lithosphere, as a post-extensional reaction, formed the Permian basins in the North Sea (Ziegler, 1992).

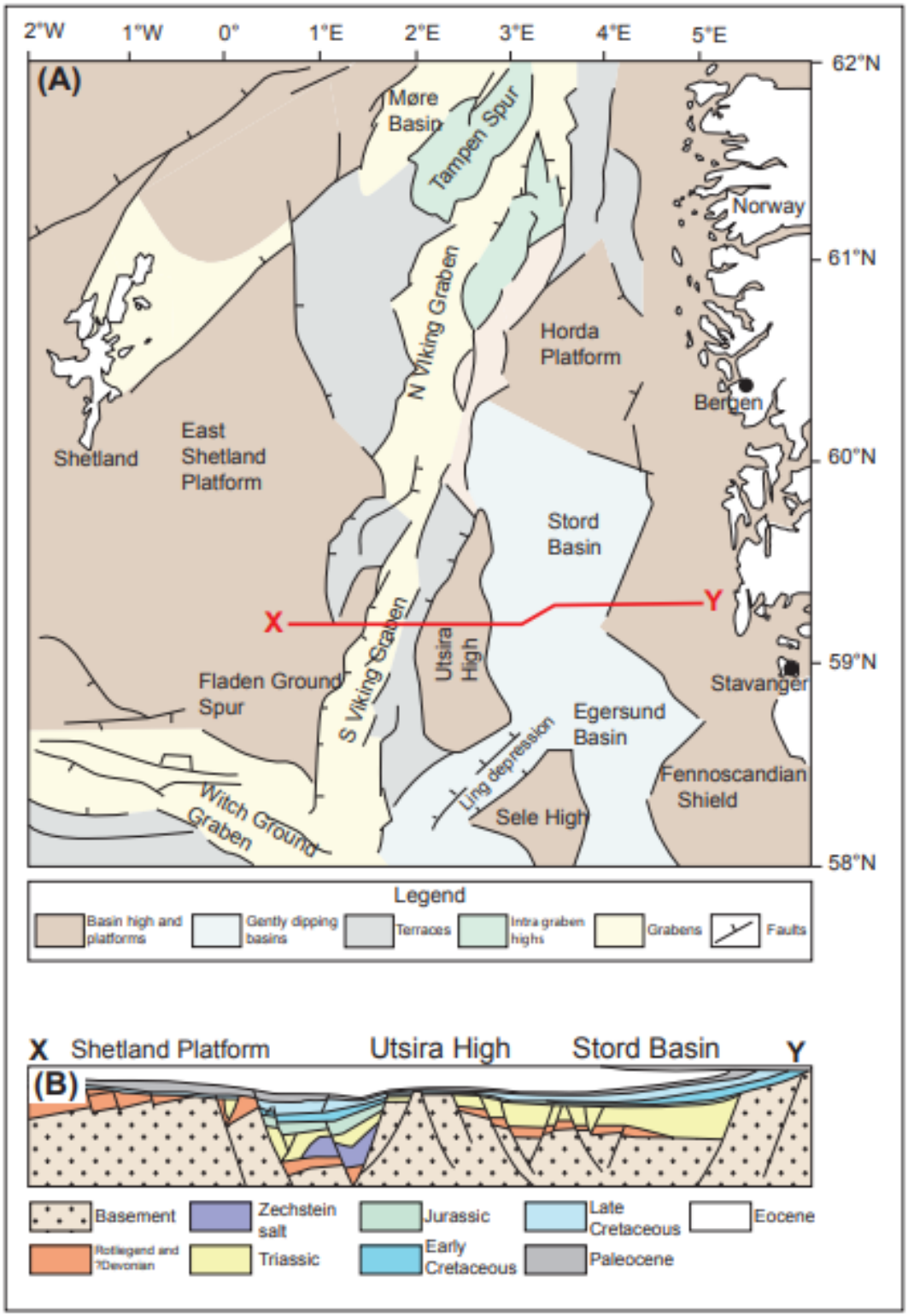

Figure 2-8: (A) Regional map of the North Sea area, taken from Riber et al. 2015 (modified from Gregersen et al., 1997) with cross-section marked X–Y. (B) Cross-section (X–Y) of the Shetland Platform, South Viking Graben, Utsira High and Stord Basin (modified from Ziegler, 1992).

A phase of rifting occurred during Permian and Triassic times, although its onset is under debate, it most likely lasted until the Middle Triassic (Glennie, 1995; Odinsen et al., 2000). The Permo-Triassic rifting caused lithospheric stretching resulting in the absence of pre-Permian sediments on the structural highs due to tilting and deep erosion. This also exposed basement rocks and formed half grabens (Færseth et al., 1995; Nøttvedt et al., 1995; Gabrielsen et al., 2010). In grabens within the Utsira High Permian sediments are found, probably related to the Permian transgression of the Zechstein Sea, probably through the Viking graben where 2-3 km of Zechstein Group sediments (shales, carbonates and evaporites) were deposited (Ziegler, 1992; Taylor, 1998). Such Permian sediments are absent elsewhere on the Utsira High, proposing exposure during deposition or erosion in the Late Triassic (Laursen et al., 1995; Bergslien, 2002; Coward et al., 2003; Sørlie et al., 2014).

During the Early Triassic rifting, the northern North Sea was characterized by N-S trending graben geometry (Ziegler, 1992; Lervik, 2006). Simultaneously, regression of the Zechstein Sea changed deposition from carbonates and fine-grained marine sediments to continental red bed sediments (Fisher and Mudge, 1998). It is suggested that the Utsira High was exposed subaerially at the time (Steel and Ryseth, 1990; Lervik, 2006).

The warm and arid climate lasted from the Permian to Late Triassic and Permo-Triassic denudation surfaces onshore (Fennoscandian Shield), were a result of peneplanation that progressed during that time (Lidmar-Bergström, 1993; Fisher and Mudge, 1998). Thick layers of sediment filled the basins formed previously from thermal subsidence, and onlapped structural highs (Fisher and Mudge, 1998). A shift in climate characterized by more humidity during the Late Triassic was a result of the North Sea region drifting further North, to approximately 40°N (Lidmar-Bergström, 1982; Preto et al., 2010) and the break-up of Pangea allowing humid air to reach the area (Nøttvedt et al., 2008). The denudated surfaces of the Fennoscandian Shield underwent deep weathering (Lidmar-Bergström, 1993), probably stretching into the North Sea. At the same time the Tethys Sea formed further south providing the southern North Sea with marine incursions due to episodic transgression. The southern Utsira High was affected by fluvial channel deposits, known as the Eiriksson Formation in the Statfjord Group, which are found in the grabens of the High (Sørlie et al., 2014). Late Triassic to earliest Jurassic extension of the Boreal Sea resulted in deposition of marine facies in the northern North Sea (Clemmensen et al., 1980).

In Early Jurassic (Pliensbachian-Sinemurian) time the Shetland Platform and the Fennoscandian Shield marked the outer boundaries of a channel connecting the northern Boreal Sea and the southern Tethys Sea (Hamar et al., 1980; Ziegler, 1992; Charnock et al., 2001; Husmo et al., 2002). From that time depositions of marine shales and sandstones

(Dunlin Group) are preserved in the Viking Graben, Horda Platform and the northern part of the Utsira High. The deposits resulted from transgression from the north (Vollset and Dorè, 1984). The established gateway between the Boreal and Tethys Sea was blocked as a consequence of thermal doming of the central North Sea combined with global regression. As a consequence of the blockage, Early Jurassic and older sediments were eroded (Vail et al., 1977; Ziegler, 1992), marked by the mid-Cimmerian or intra-Aalenian unconformity in the region, between Lower Jurassic and Middle and Upper Jurassic deposits (Davies et al., 1999).

From Late Bajocian time, influence of sedimentation from the North Sea Dome on the Viking Graben was reduced due to synrift development, transgression from north and reconnection of the Boreal and Tethys seas (Bathonian to Callovian times) (Ziegler, 1992; Husmo et al., 2002; Coward et al., 2003). The main Jurassic rifting phase followed (Callovian to early Kimmeridgian) establishing the main structural setting for the Viking Graben (Coward et al., 2003). The Utsira High is in latest Jurassic times believed to have experienced subaerial exposure, indicated by coarse-grained Callovian to Volgian clastics found in grabens within the high (Sørlie et al., 2014). Drowning of the source area resulted in a transition from Draupne sandstone to marine Draupne shale depositions (Sørlie et al., 2014).

Rifting terminated in Early Cretaceous in the southern Viking Graben linked to fast subsidence and burial (Ziegler, 1992; Nøttvedt et al., 2008). On the Utsira High the end of subaerial exposure is marked by Early Cretaceous shallow-marine sediments. The Utsira High has since subsided to its present depth (Riber et al., 2015). Basement and sedimentary logs derived from well drilled on the Utsira High are presented in figure 2-9.

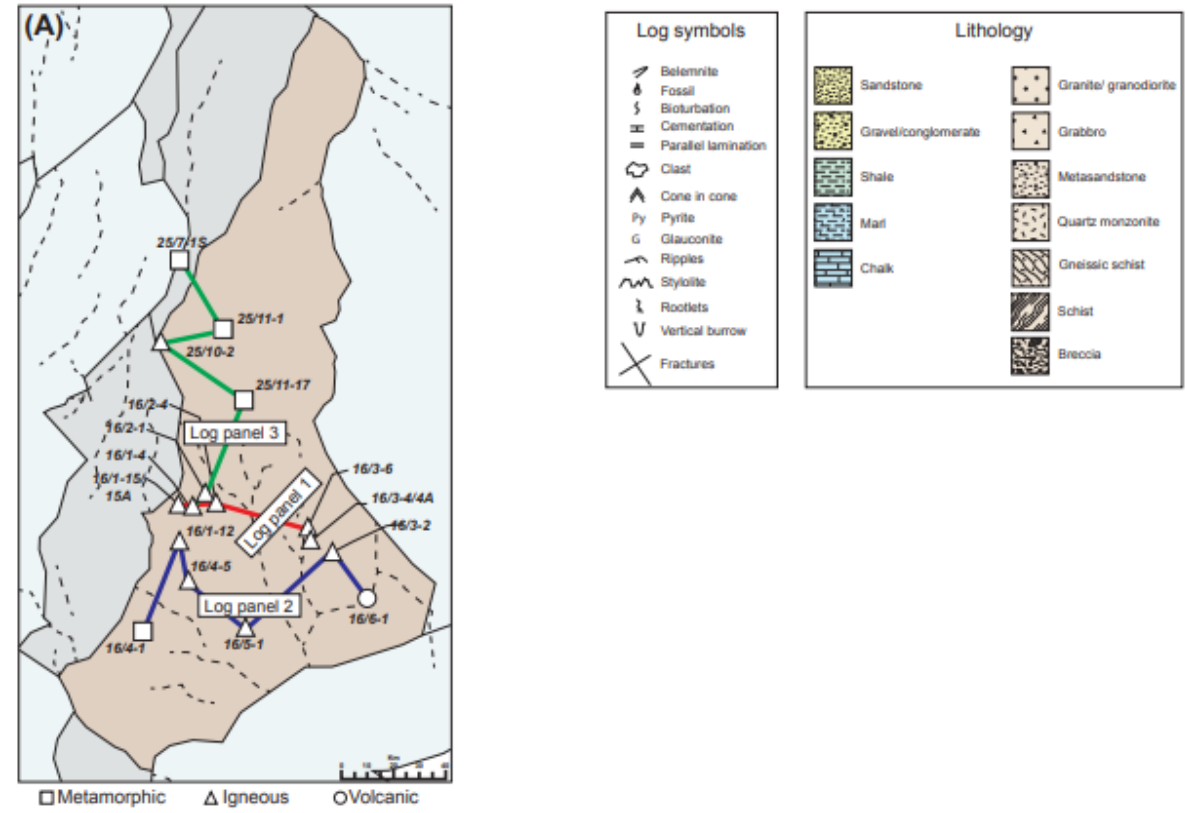
(A)
25/7-1S
25/11-1
25/10-2
25/11-17
16/2-4
16/2-1
16/1-4
16/1-15
15A
Log panel 3
Log panel 1
16/3-6
16/3-4/4A
16/3-2
16/1-12
16/4-5
Log panel 2
16/6-1
16/4-1
16/5-1
Metamorphic
Igneous
Volcanic
Log symbols
Belemnite
Fossil
Bioturbation
Cementation
Parallel lamination
Clast
Cone in cone
Py Pyrite
G Glauconite
Ripples
Stylolite
Rootlets
Vertical burrow
Fractures
Lithology
Sandstone
Gravel/conglomerate
Shale
Marl
Chalk
Granite/ granodiorite
Grabbro
Metasandstone
Quartz monzonite
Gneissic schist
Schist
Breccia

(B)

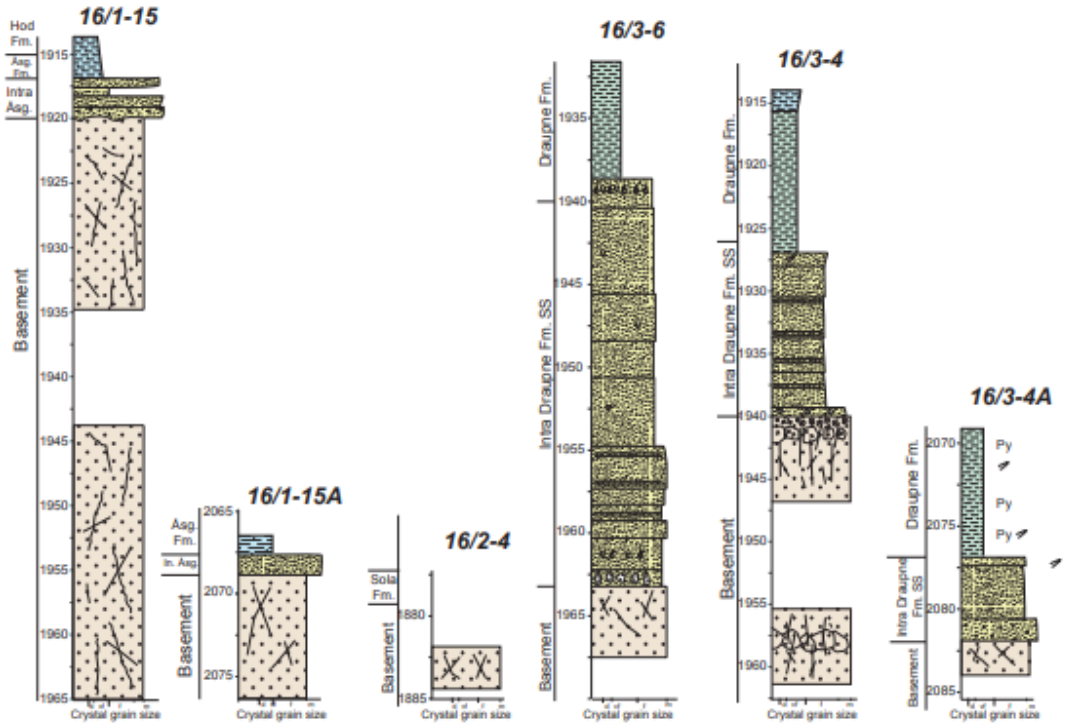
16/1-15
Hod Fm.
Asg. Fm.
Intra Asg.
Basement
Crystal grain size
16/1-15A
Asg. Fm.
In. Asg.
Basement
16/2-4
Sola Fm.
Basement
16/3-6
Draupne Fm.
Intra Draupne Fm. SS
Basement
16/3-4
Draupne Fm.
Intra Draupne Fm. SS
Basement
16/3-4A
Draupne Fm.
Intra Draupne Fm. SS
Basement
Py

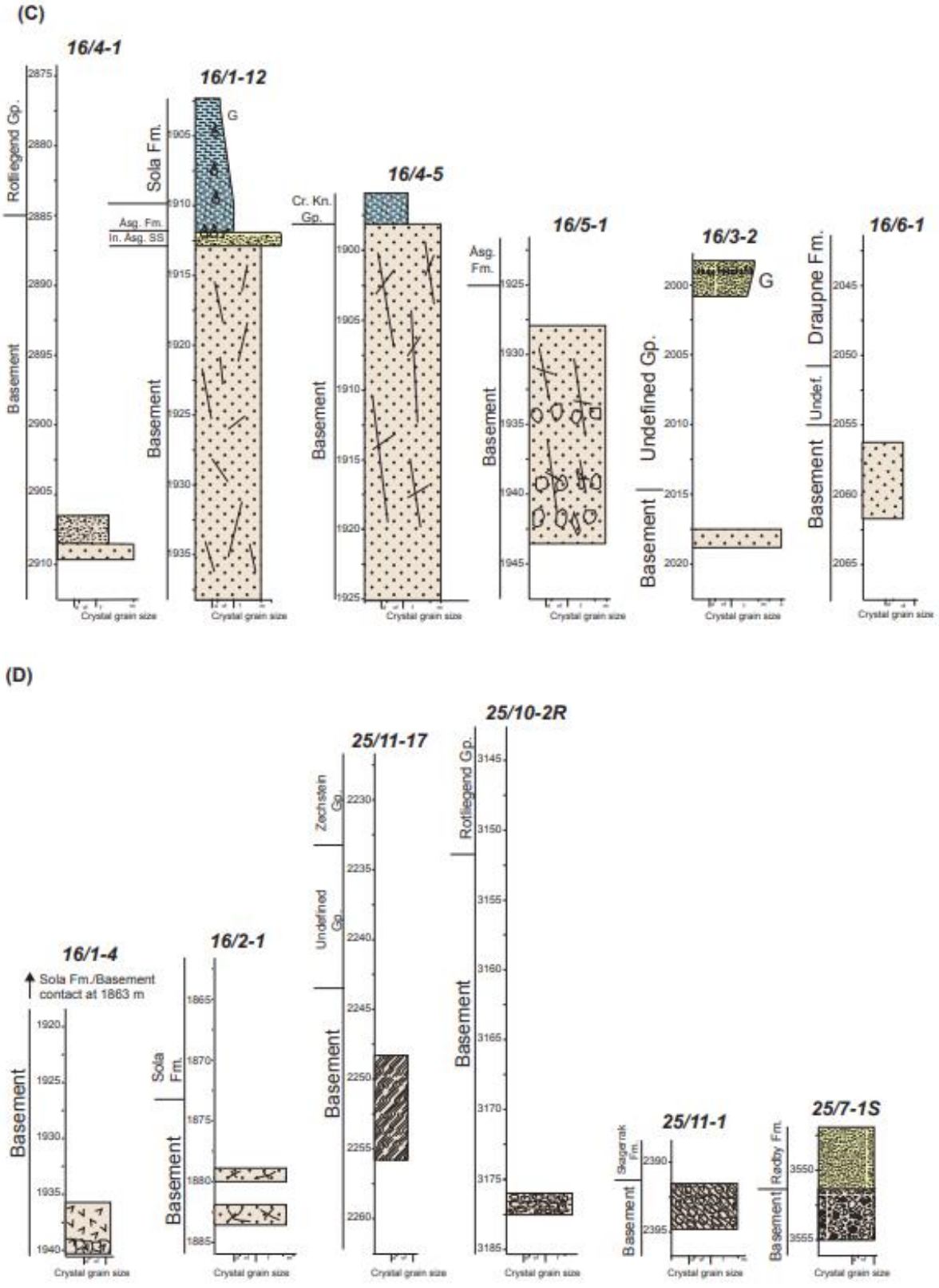

Figure 2-9: Sedimentary well logs from the Utsira High presenting basement rocks and sedimentary sequences. (A) Map showing the well locations and the distribution of igneous, volcanic and metamorphic rocks. (B) Log panel 1 including wells: 16/1–15, 16/1–15A, 16/2–4, 16/3–6, 16/3–4 and 16/3–4A. (C) Log panel 2 including wells: 16/4–1, 16/1–12, 16/4–5, 16/5–1, 16/3–2 and 16/6–1. (D) Log panel 3 including wells: 16/1–4, 16/2–1, 25/11–17, 25/10–2R, 25/11–1 and 25/7– 1S. (from Riber et al., 2015).

2.2.3 Horda Platform, Northern North Sea

The Horda Platform is located by the coast of western Norway, characterized as a N-S trending structural high (Whipp et al., 2014). As observed in figure 2-8, this study area is located close to the Utsira High. Moving south from the Horda Platform we transition into the Stord Basin. At the western margin of the Stord Basin, the Utsira High is located. The Utsira High is located towards the southwest with respect to the Horda Platform. To the East, the Horda Platform is bounded by the Øygarden Fault Complex (Øygarden FC), the Nordfjord-Sogn detachment towards the north, the Viking Graben towards northwest and the Hardangerfjord Shear Zone towards the south (Phillips et al., 2019).

Geologically and climatically, the Horda Platform experienced similar changes as the Utsira High throughout its existence, thus sedimentary depositions are somewhat similar. But of course, the structural and depositional history of the two structural highs is not identical. Bellow, the main tectonic and stratigraphic evolution of the Horda Platform is summarized with respect to the evolution of the North Sea.

Devonian sediments from the continental depositional setting (Marshall and Hewett, 2003) are believed to exist in Triassic half grabens under the Horda Platform (Faleide et al., 2015). The Stord Basin and northern Horda Platform acted as large depocenters during the Late Permian to Early Triassic rifting. In the northern Horda Platform, the Tusse, Vette and Øygarden faults formed half grabens comprising syn-rift wedges (Phillips et al., 2019). During that time the Hegre Group sandstones and mudstones were deposited and are considered the lowest synrift strata (Steel and Ryseth, 1990; Lervik, 2006).

After the rifting phase, during Early to Middle Jurassic the northern Horda Platform was affected by thermal subsidence (Roberts et al., 1993; Steel, 1993; Roberts et al., 1995). As a result, deposited sediments were of fluvial deltaic and shallow marine origin, known as the Statfjord, Dunlin and Brent groups (figure 2-10) (Helland-Hansen et al., 1992; Steel, 1993; Færseth and Ravnås, 1998). During the period most faults were inactive, although wedges of sediments west on the Horda Platform indicate rifting during Bajocian to latest Oxfordian times (Rattey and Hayward, 1993; Steel, 1993; Ravnås and Bondevik, 1997; Færseth and Ravnås, 1998; Ravnås et al., 2000).

During Late Jurassic rifting in the northern North Sea, the faults in the Horda Platform were mostly inactive, as no sedimentary thickening in the Hanging walls of the Tusse, Vette and Øygarden faults is observed in sediments of that age (Phillips et al., 2019). Exceptions regarding N-S and NW-SE striking faults are suggested by Whipp et al. (2014), showing extension which rotated fault blocks within the high eastwards during Late Kimmeridgian to Late Berrisian time. During this period marine deposition of sediments continued. The three

lowest formations (Krossfjord, Fensfjord and Sognefjord formations) of the Viking Group (middle Jurassic to Lower Cretaceous) were deposited (figure 2-10) during fault-driven subsidence. The formations consist of stacked, regressive, shallow marine, clastic sequences (Dreyer et al., 2005; Bell et al., 2014). The upper Viking Group; the Draupne Formation (figure 2-10) consisting of deep marine mudstones were deposited in Late Kimmeridgian to Late Beriasian after flooding occurred (Bell et al., 2014).

A Cretaceous unconformity truncates the Viking Group. The unconformity is associated with the termination of rifting (Kyrkjebø et al., 2004). In the Cenozoic uplift of clastic sources and subsidence led to mud-dominated sedimentation, burying the Viking Group and carbonate Cromer Knoll and Shetland groups (figure 2-10) (Deng et al., 2017).

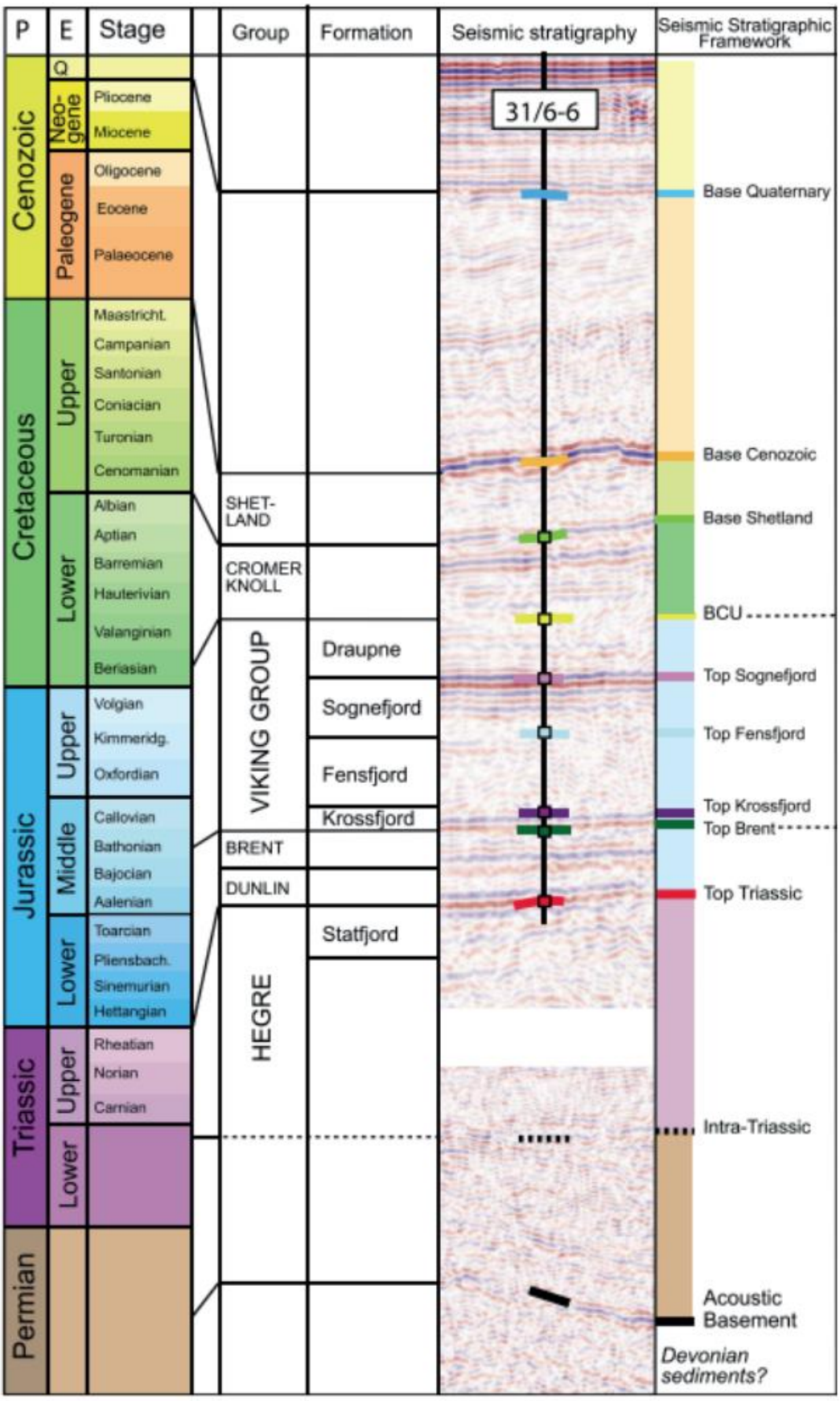

Figure 2-10: Northern North Sea stratigraphic column also relevant for the Horda Platform (modified from Whipp et al. (2014)). P=Period, E=Epoch. The main stratigraphic groups and formations are added and tied to a typical seismic section. Horizons are marked with their respective age, derived from well 31/6-6. (Modified from Bell et al. 2014).

3 Method: ML and Methods for Identifying and Characterizing Faults

3.1 Introduction to ML and Historic Background

ML is a subcategory of artificial intelligence (AI) and is highly connected to applied statistics, which is about creating computational models that use inference and pattern recognition rather than a large set of rules (Dramsch, 2020).

A ML algorithm is in general written as

$$y = f(x)$$

where x is the input, y is the output and f is the function used by the algorithm to determine the correct output (y) based on the input (x). f is learned during training to eventually, make independent predictions.

ML algorithms can be divided into several types based on specific criteria, and algorithms can consist of different model architectures. Generally, ML has found numerous applications across a broad range of industries and domains. Just to give a brief overview, ML is used in algorithmic trading (Sezer and Ozbayoglu, 2018), online fraud detection (Bhattacharyya et al., 2011), natural language processing (NLP) (Boiy and Moens, 2009; Luo et al., 2019), health (Shickel et al., 2017), surveillance (Liu et al., 2016) and speech recognition (Lei et al., 2014). It should also be mentioned that ML has led to important progress in sciences such as biology (Ching et al., 2018), chemistry (Schütt et al., 2017), medicine (Shen et al., 2017), pharmacology (Kadurin et al., 2017) and geosciences (Wu et el., 2019).

The term ML was first introduced by Arthur Samuel in 1959 (Samuel, 1959). ML is regarded as a subdivision of AI, which for the first time was introduced only a few years prior, in 1950 by Alan Mathison Turing (Turing, 1950). The Perceptron, proposed by Rosenblatt in 1958, was the first artificial neural network (Rosenblatt, 1958).

In the beginning, ML led to great optimism, and machines in the 1950s and 1960s learned simple tasks such as playing simple games and route mapping. Already in the 60s rather simple methods like k-means (Preston and Henderson, 1964), Markov models (Krumbein and Dacey, 1969) and decision trees (Newendorp, 1976) were applied to complete tasks in geoscience.

The 1970s was a decade with few developments in ML and AI in general, marking the “first AI winter”. The absence of progress led to a loss in interest, which was restored in the 1980s. The year 1982 marks the first significant achievement, when the first bidirectional network

was implemented by Hopfield. Building on bidirectional networks, backpropagation was introduced to neural networks in 1986 (Zhao and Mendel, 1988). Backpropagation enabled adjusting the networks by running data backwards through them, these were so-called “expert systems”. This enabled the use of multiple layers, but interest in ML, despite this progress was limited. The “second AI winter” occurred during that same time (late 1980s) due to the collapse of a large hardware industry, caused by desktop hardware from non-specialist vendors outperforming the expensive machines built specifically for the “expert systems”. The interest in ML increased in 1997, when the world champion in chess was beat by the IBM computer Deep Blue.

During the 2000s, significant changes and new developments, which continuously are happening to this day, significantly increased both the use and usability of ML. Contributing to the increased use and improved usability is a change in tooling. The majority of tools and software used to run ML projects had prior to this been proprietary, like Matlab with the Neural Network Toolbox and Wolfram Mathmatica, or independent university projects, like the Stuttgart Neural Network Simulator (SNNS). Generally, tools and software were hard to access and difficult to operate due to very limited complimentary documents. The change in tooling gave easier access to tools and software through free open-source software (FOSS), in addition new accompanying documents were more frequently published (Dramsch, 2020). Another important factor contributing to the increased use of machines learning, were more powerful computers, allowing more complex models to process larger sets of data in a shorter amount of time. Powerful computers allow to run complex deep learning architectures more efficiently. In 2012 Alex Net won the ImageNet competition (Krizhevsky et al., 2012). Since then, the field of deep learning has evolved, introducing several different model architectures and techniques, constantly improving the performance on various tasks.

3.2 Learning-Structures for ML Algorithms

In order to understand ML algorithms learning structures it must be understood how the term “learning” is defined in ML to begin with. A definition is provided by Mitchell (1997) “A computer program is said to learn from experience E with respect to some class of tasks T and performance measure P, if its performance at tasks in T, as measured by P, improves with experience E.” What also needs to be clear is that there are numerous different experiences E, Tasks T and performance measures P (Goodfellow et al., 2016). Thus, a large variety of ML algorithms exist, which to some degree can be categorized. For chapter 3.2, the focus is on tasks T and experience E.

3.2.1 Supervised Learning vs. Unsupervised Learning

Broadly, learning structures can be divided into supervised and unsupervised learning based on what they are allowed to experience when learning. Although there is no clear margin between those two types, as there is no clear definition distinguishing the experiences (Goodfellow et al., 2016). The following sections provide some elements of distinction.

3.2.1.1 Supervised Learning

Algorithms that learn in a supervised fashion, experience a dataset containing features, but the solutions are given in form of labels or targets (Goodfellow et al., 2016). Supervised learning algorithms are trained on prelabeled data so that the algorithm can learn certain features and details necessary to succeed in any identification task it is designed for. In the case of an image recognition task the algorithm will be fed with images. During training the label would inform the algorithm what the image contains. The algorithm then would analyze the contents of the image and recognize features and details that would help the algorithm to identify that same contents independently at a later stage. Supervised learning requires enough size of training data.

3.2.1.1.1 CLASSIFICATION VS. REGRESSION

Usually, ML tasks such as classification and regression are referred to supervised learning (Goodfellow et al., 2016). Classification places the output in defined classes. Classification is applied to discrete data which is normally found in tasks such as image recognition or lithofacies classification, where different objects (humans, cars, cats etc.) can be identified in form of numerical codes and are categorized in different categories (Goodfellow et al., 2016). Regression is similar to classification, but it is used in cases where data consists of continuous numerical values, resulting in a different output format. It is also possible to convert continuous data into discrete data in order to use classification. In this case the numerical values are divided into intervals or bins. An example is converting porosity values from 0 to 0.30 into 6 bins of 0.05 range for each bin.

3.2.1.2 Unsupervised Learning

In cases where training data is not so easy to obtain or variables in the input data are unknown, unsupervised algorithms are suitable. These algorithms experience datasets with several features and learn important structural properties of a dataset. Meaning that they do not need training labels, but rather find hidden patterns and group similar data in similar outputs (Goodfellow et al., 2016).

3.2.2 Supervised Learning Structure

3.2.2.1 Train/Test Split

The aim in ML is to create an algorithm that performs well on new, unseen data based on its experience from the training data. The ability to perform well on new inputs is known as generalization. Good generalizability is achieved from performing a train/test split of the training dataset. When dividing the data into training and testing data, essentially a minor part of the total training data is hidden from the network and is used to later test the algorithm on unseen data. A well performing ML algorithm should ideally be able to achieve 1) a small training error and 2) a small gap between training and test error. The training and test (or generalization) errors are the algorithms respective, performance measures on the training and test data (Goodfellow et al., 2016).

With that in mind, train/test split can be used to determine whenever a model is underfitting or overfitting. Underfitting corresponds to situations where the algorithm cannot achieve a sufficiently low error value on the training dataset and overfitting is related to the gap between training error and test error being too large. One factor controlling the models likelihood of underfitting or overfitting is the capacity, which is the ability a model has to fit a large variety of functions. If the capacity is too low, the model might struggle to fit the training data (underfitting) and on the other hand, too high capacity may lead to memorization of properties that give a disadvantage on the test data (Overfitting) (Goodfellow et al., 2016). An example of underfitting and overfitting due to capacity is shown in figure 3-1, where hypothesis space is used as a way to control the capacity. In the example, a linear, quadratic and degree-9 predictor are compared in the attempt to fit a problem where the underlying function is quadratic. The linear function is underfitting as it is not able to capture the curvature of the underlying problem. On the other hand, the degree-9 function is overfitting the test dataset as it is represents the wrong structure of the test dataset. It is capable of representing the correct function, but this is difficult to achieve as it is capable of finding an infinite number of other functions that fit all the data points in the test dataset. In this example, the quadratic function has the perfect capacity and is neither underfitting nor overfitting as it is able to perfectly fit the test data points while representing the correct structure of the underlying problem (Goodfellow et al., 2016).

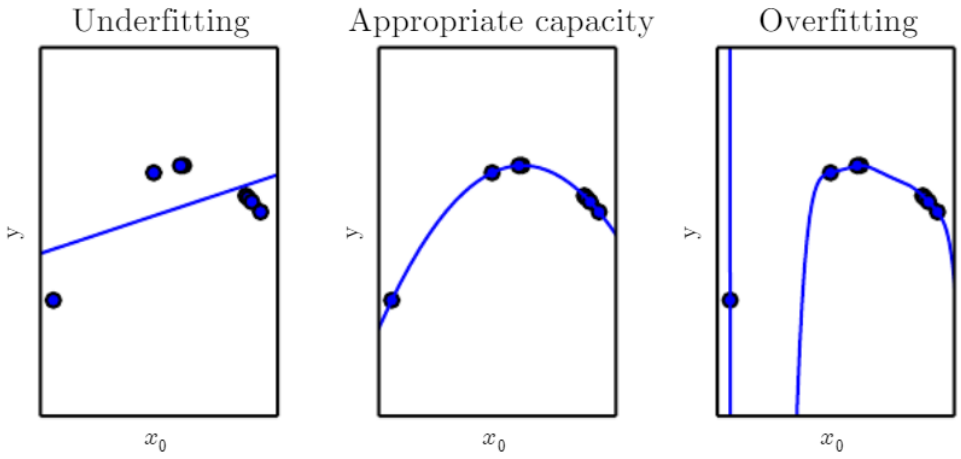

Figure 3-1: The 10 blue data points represent data from an previously unseen (test) data. The model on the left using a linear function is underfitting as it is not able to capture the curvature of the test dataset due to missing capacity. In the center the model using a quadratic function is able to fit the test dataset quite well, reflecting an appropriate capacity. On the right, the model using polynomial of degree 9 is overfitting the test dataset as it does not represent the correct structure of the test dataset, although it passes though all the data points exactly (Goodfellow et al., 2016).

3.2.2.2 Hyperparameter Tuning

Hyperparameters are found in most ML algorithms and are defined as settings that can adjust the algorithm's behavior, but the learning algorithm itself does not adapt the values of hyperparameters (Goodfellow et al., 2016). Looking at the earlier example from figure 3-1, the degree of the polynomial is the single hyperparameter and acts as a capacity hyperparameter. In general, hyperparameters are chosen to be hyperparameters whenever they are too complicated to learn or, more commonly, it is not appropriate for the model to learn them on the training dataset. Capacity is a good example of a hyperparameter that is not appropriate to learn from the training dataset as it is easier for the model to fit a function to the data points when capacity is high, which in return results in overfitting (figure 3-1).

3.2.2.3 Validation Sets and Cross-Validation

To solve the problems associated with the learning of hyperparameters, a validation dataset needs to be used. The validation set needs to be separate from the test set, and usually the training set is split, where some portion of the training data (for example 20 percent) is used for validation. This creates two disjoint subsets. The validation set then can be used to estimate the generalization error and the hyperparameters can be tuned thereafter (Goodfellow et al., 2016).

Cross-Validation is used in cases where only small datasets are available. This is more accurate than dividing the set into fixed training and test sets. When using fixed sets, the test set becomes very small, resulting in high statistical uncertainty in the estimated test error. Making it difficult to determine whether one algorithm performs a given task better compared

to another algorithm. Cross-Validation solves this problem by completing several training and testing runs, always using different, nonoverlapping, randomly chosen subsets of the initial dataset. The average test error from the repeated training and testing then may be computed (Goodfellow et al., 2016).

3.3 ML Algorithms

Generally, we distinguish between shallow and deep ML. Shallow ML encompasses rather simple methods or algorithms with simple architectures or structures. Such methods include models like, random forests, gradient boost, support-vector machines, and simple neural networks like Multi Linear Perceptron (MLP). When increasing the complexity of tasks and patterns in the data become more complicated, the algorithms that are supposed to solve them need to be structurally more advanced. This usually involves adding more layers and components to a model. The model is then referred to as a deep ML model, including several variants of deep neural networks (DNN) e.g. feed-forward neural networks, CNN, recurrent neural networks (RNN) and generative adversarial networks (GAN) (Dramsch, 2020).

3.3.1 Traditional Algorithms

3.3.1.1 Random Forests

Random forests is a method based on decision trees, which ask a series of yes or no questions in order to make a decision. These models can become very complex, which makes them powerful predictive models (Breiman, 2001). Random forests also are well suited for approximating regression problems and time series, being able to perform tasks within seismological applications like localization (Dodge and Harris, 2016), event classification in volcanic tremors (Maggi et al. 2017) and slow slip analysis (Hulbert et al. 2018). The fact that random forests treat each data sample independently, unlike neural networks, makes them of limited use when applied to ASI (Guillen et al. 2015).

3.3.1.2 Support-Vector Machines (SVM)

SVM can be applied for all the different types of ML problems, such as classification, regression and clustering. In the case of a two-class problem, the algorithm aims to determine hyperplanes that separates the different classes of input. However, there can be two different types of scenarios: 1) the data has no overlap, 2) the data has overlap. In cases where the data has no overlap, the classes are linearly separable in terms of a hard margin. In most cases there is overlap in the data. The SVM is dealing with a more complex optimalization problem, trying to find the best-fit hyperplane. This ability increases the success of such algorithms (Dramsch, 2020). Due to the strong mathematical foundation of

SVM they can be applied to microseismic event classification (Zhao and Gross, 2017), seismic well ties (Chaki et al., 2018) and landslide susceptibility (Marjanovic et al., 2011).

3.3.2 Neural Networks

Neural networks function in a similar way as the human brain. Inspired by the human brain, neural networks use neurons in order to learn and memorize. Different model architectures can change the level of complexity and make them more suitable for variations of tasks. The simplest neural network architectures comprise an input layer, one hidden layer and an output layer, evolving to DNN with multiple hidden layers. However, in general each layer in a neural network consists of neurons. In the input and output layer the number of neurons depends on the amount of input and output variables, respectively. In the hidden layer the number of neurons is determined otherwise. Neural networks also use activation functions, loss functions, weights and biases to be able to learn and perform well on identification tasks. The strength of neural networks lays within the ability to learn patterns in any given training data, as long as there is enough data available. This is performed by forming complex nonlinear rules in high-dimensional spaces, rather than defining any specific rules. Therefore, neural networks are suited to complete several tasks, such as image recognition, audio recognition or identifying object based different input parameters (e.g. weight, height, volume etc.). Bellow, different types of neural networks such as Feed-Forward Networks, CNN, RNN, and GAN are explained.

3.3.2.1 (Deep) Feed-Forward Networks

The simplest neural network which is the feed-forward network consists of an input and output layer with only one hidden layer between, it also has a feed-forward architecture (Schmidhuber, 2015). The term “deep” indicates the presence of multiple hidden layers (figure 3-2), reflecting the depth (complexity) of the network. Feed-forward networks compared to networks such as RNN (section 3.3.2.3), do not possess the ability of receiving feedback from their own outputs. Referring to the general function $y = f(x)$, “feed-forward” indicates that information evaluated from x flows through the function f, defined by intermediate calculations, and results in the final output y. The term “network” is referred to the composition of different functions, which typically is the case. Functions are arranged in chains. As an example, a chain comprising three functions $f^{(1)}$, $f^{(2)}$, $f^{(3)}$ may be written as $f(x) = f^{(3)}(f^{(2)}(f^{(1)}(x)))$. A function corresponds to a layer in the network, so increasing the number of functions increases the networks depth, increasing the complexity. The final layer within the feed-forward networks is the output layer. (Goodfellow et al., 2016). Increased network complexity, adds a larger number of parameters, emphasizing the need of large training datasets. The name “hidden layers” is derived from the training process. During the

training of neural networks, the aim is to approximate a function which is as similar to the actual function $(f(x))$ as possible. Training data provides approximate and noisy examples x of $f(x)$, at different points during training. x is connected to a label $y \approx f(x)$. The training data defines that the output layer needs to generate a value close y at point x, but the training data does not define the behavior of the other layers, therefore the name “hidden layers”. In the hidden layers, the algorithm must decide what should happen in order to achieve the desired output. Hidden layers are vector valued, and their dimensionality define the “width” of the neural network (Goodfellow et al., 2016).

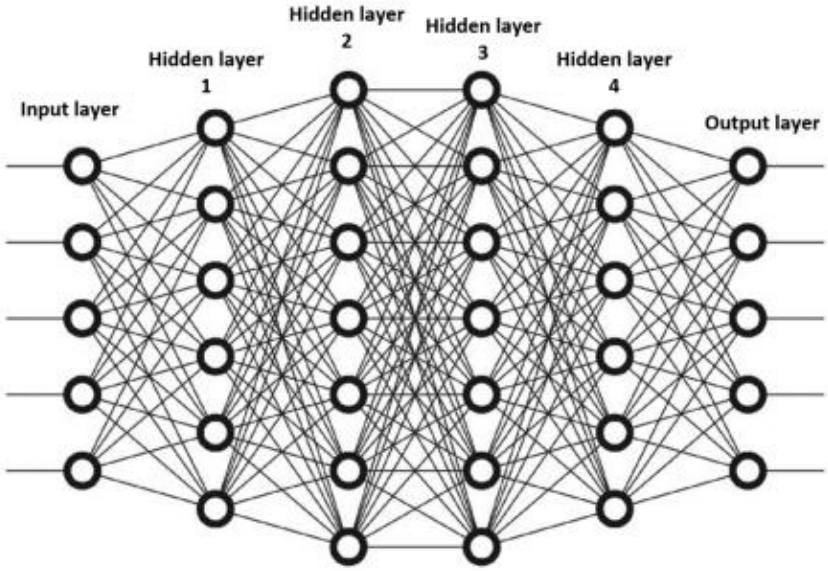

Figure 3-2: A deep feed-forward neural network, in this case comprising four hidden layers (Ahmed (2020), modified from Jamil (2020)).

3.3.2.2 Convolutional Neural Networks (CNN)

A CNN is a specialized type of DNN. The architecture of this network uses convolution layers and pooling layers instead of the conventional layers seen in figure 3-2. The layers allow the CNN to learn hierarchical feature representations form information-rich data like images and videos. An example of a CNN architecture is illustrated in figure 3-3. The convolution layers contain filters, which for example are of size 5 x 5 or 3 x 3 pixels, that are able to detect features and patterns like edges, shapes, textures or even whole objects, in images. The size of the filters tells us the size of the block of pixels the filter processes simultaneously in an image. The specific example in figure 3-3 is learning to identify objects associated with roads, such as cars, trucks, vans, bicycles etc. The pooling layers reduce the dimensions of the input data by removing features that are insignificant to the convolutional layers. This procedure increases the processing speed. Finally, the reduced input is flattened and fed to a fully connected layer (Saha, 2018).

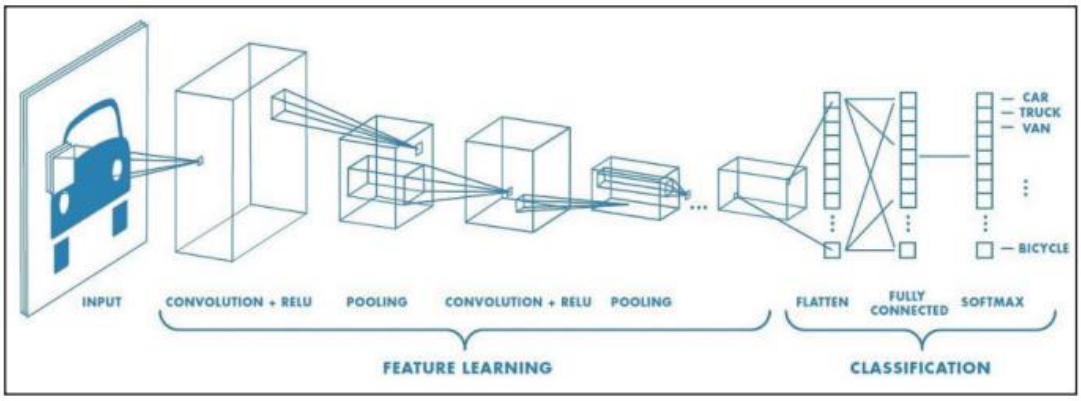

Figure 3-3: A typical architecture of a convolutional neural network (CNN) (Saha, 2018).

3.3.2.3 Recurrent Neural Networks (RNN)

RNN are bi-directional (figure 3-4), allowing them to have an internal memory state. In comparison to feed-forward neural networks, RNN are able to loop data between the hidden layers. This enables previously used inputs to be taken into account together with new inputs. In practice, each neuron produces an output based on inputs from previous neurons combined with current inputs (IBM Cloud Education, 2020). The internal memory state makes these networks well suited for handwriting detection and speech recognition. Different types of RNN exist, like Long Short-Term Memory Networks and Hopfield Networks.

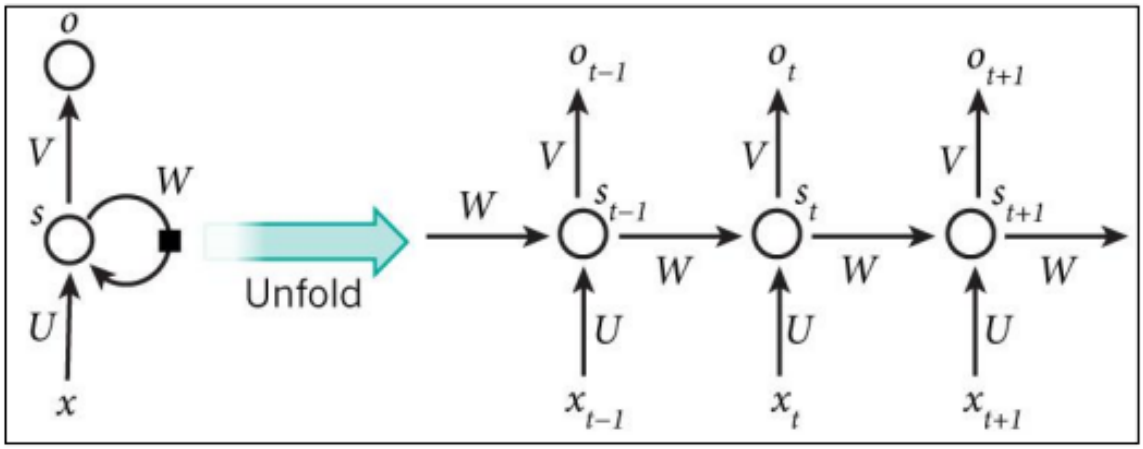

Figure 3-4: A typical architecture of a recurrent neural network (RNN) (Matlab one, 2022).

3.3.2.4 Generative Adversarial Networks (GAN)

GAN in contrast to other neural networks have two algorithms: a generator and a discriminator (figure 3-5). The generators task is to learn the description of the data in order to generate fake data. The generators goal is to produce realistic, fake data and trick the discriminator which has the task of distinguishing between real and fake data. This procedure makes the algorithms work together to understand variations in a dataset (Goodfellow et al., 2014). In geoscience GAN have been used to generate unconditional simulations of pore-

and reservoir-scale models of the petrophysical properties of oil and gas reservoirs (Mosser et al., 2018).

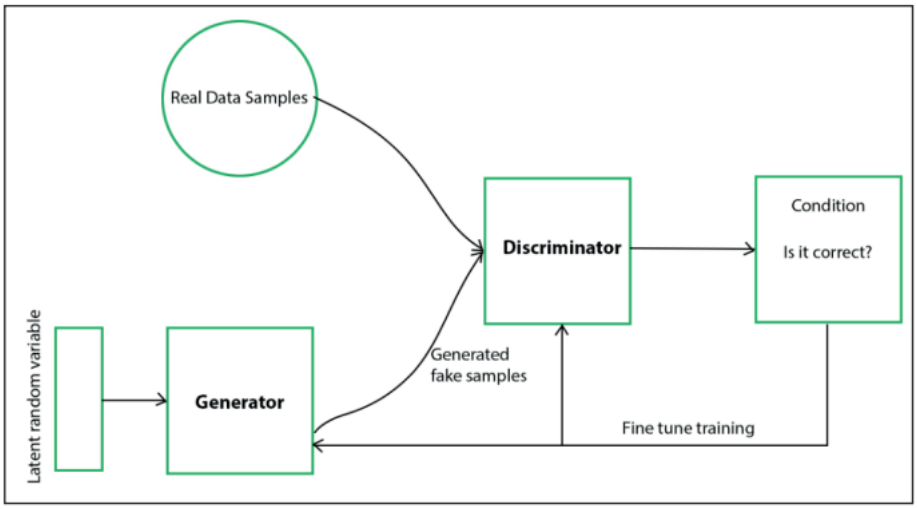

Figure 3-5: A typical architecture of a generative adversarial network (GAN) (Roy, 2019).

3.3.3 Neural Network Components

3.3.3.1 Metrics

Metrics are a measure of performance for ML models. There are several different metrics which can present unique measures of performance. The metrics covered in this section are accuracy, mean Intersection Over Union (IOU) and F1 score. In relation to metrics, terms like true positives (TP), true negatives (TN), false positives (FP) and false negatives (FN) are often used. The terms “positives” and “negatives” are in classification problems referred to as the ground truth label and background, respectively, and “true” and “false” refers to if the prediction is correct or not. In the following section about loss functions it will become clear that some metrics and loss functions are closely related.

Accuracy:

Accuracy is a ratio which determines what portion of the total predictions made by a ML model actually are correct. Hence, accuracy can be written as:

$$Accuracy = \frac{TP + TN}{TP + TN + FP + FN}$$

Accuracy is useful in ML problems where the number of positives and negatives are well balanced but can be extremely misleading in cases where the number of negatives is significantly larger than the number of positives. That is due to the fact that the negatives, which are far less challenging to classify correctly, overshadow cases where a low portion of positives are classified correctly. Accuracy can therefore be really high even if a model is overfitting the data (Agarwal, 2019).

Mean IOU:

Intersection-Over-Union (IOU) or mean IOU, for multi-class classification, is commonly used in semantic segmentation (Matcha, 2021). Keras' definition of IOU is written as:

$$IOU = \frac{TP}{TP + FP + FN}$$

(TensorFlow, 2021).

The IOU metric essentially is a ratio telling what portion of the models predicted labels overlap with the ground truth labels (figure 3-6). In other words, IOU is a measure of similarity comparing the ground truth labels to the models predicted labels. The ratio ranges from 0 to 1, which is no overlap and full overlap, respectively (Matcha, 2021).

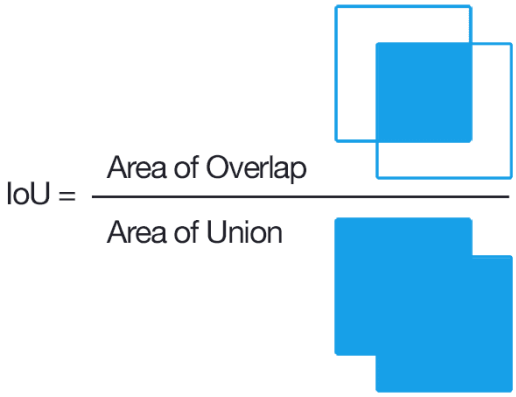

Figure 3-6: Visualization of the IOU (Rosebrock, 2016).

F1 Score:

The F1 Score or F1 macro consists of two metrics; precision and recall. Precision can be written as

$$Precision = \frac{TP}{TP + FP}$$

and recall can be written as

$$Recall = \frac{TP}{TP + FN}$$

The F1 score is defined as the harmonic mean of the two metrics and is written as

$$F1\ Score = 2\frac{Precision \cdot Recall}{Precision + Recall}$$

telling the certainty of a model on predicting a true positive (Precision) combined with the proportion of true positive actually identified by the model. Again, this metric is also a ratio ranging from 0 to 1 where 1 is the best possible score (Agarwal, 2019).

3.3.3.2 Activation Functions

In CNN we distinguish between activation functions used within each independent convolutional layer and activation functions used in the output layer. Within the convolutional layers functions like ReLU (Rectified Linear Unit) are used and contribute to the non-linear activation of neurons. On the other hand, output activation functions are applied to output vectors from CNN (s) before loss is calculated. The purpose is to normalize the output within a certain range and popular choices are the sigmoid or softmax activation functions. In this thesis we utilize ReLU within the layers and the softmax activation function for outputs.

ReLU

The ReLU is one of the functions that commonly are used in convolutional layers of a CNN. These functions implement non-linear relationship to the activation of neurons, which is necessary for solving complex tasks. Without activation functions like ReLU the output calculated by neurons in one layer would just be the linear response to the calculated output from neurons in the previous layer. ReLU also normalizes neuron outputs in such a way that all negative values become 0 and positive values remain the same (figure 3-7).

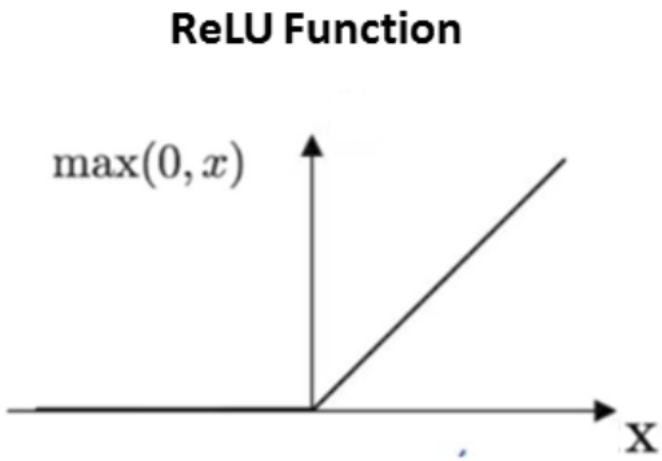

Figure 3-7: ReLU (Rectified Linear Unit) function (Datacamp, 2019).

Sigmoid

A sigmoid activation functions normalizes a vector between 0 and 1. It is applied independently to each element of the output vector score s s_i. A sigmoid shaped graph is visualized in figure 3-8. And the sigmoid function is written as:

$$f(S_i) = \frac{1}{1 + e^{-S_i}}$$

(Gómez, 2018).

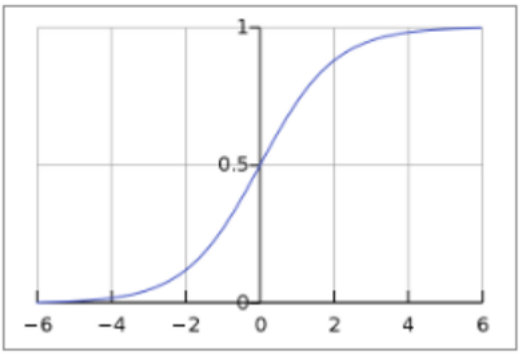

Figure 3-8: Sigmoid function (Gómez, 2018).

Softmax

A softmax activation function is a function that gives the output vector a value between 0 and 1, and the resulting elements add up to 1. The function is applied to the output scores s. As elements represent classes, they can be interpreted as class probabilities. The function can unlike the sigmoid function not be applied independently to each vector score s_i, since it depends on all vector scores s. For a given class the vector score s_i can be written as:

$$f(s)_i = \frac{e^{s_i}}{\sum_j^C e^{s_j}}$$

Where s_j are the scores inferred by the net for each class in C. The Softmax activation for a class s_i depends on all the score in s (Gómez, 2018). An example of how a softmax function may look is provided in figure 3-9.

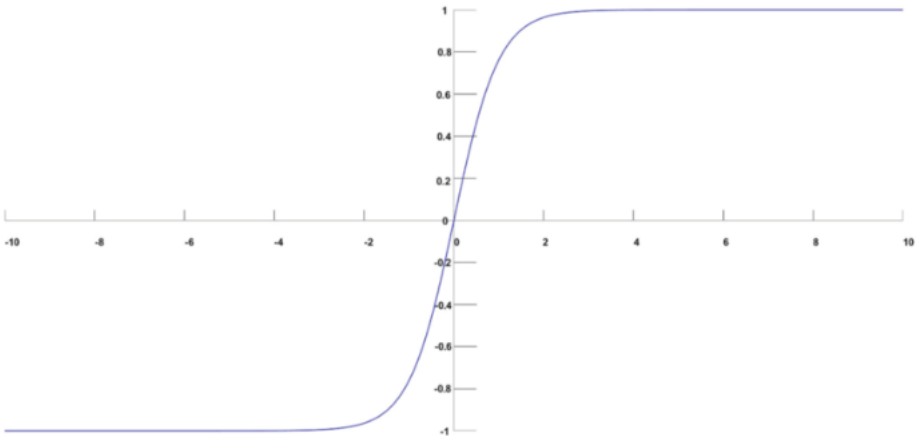

Figure 3-9: Example of a softmax function (Shen et al., 2019).

3.3.3.3 Loss Functions

Loss functions are used to calculate how wrong the prediction of a model is (difference between prediction and ground truth), which further is used to propagate it back to the network layers and adjust the weights to achieve minimal loss. Loss functions are different from metric. Metrics are quantities that are used to judge the performance of a given model. Loss functions tell our models how they can improve on the training data. Popular choices of loss functions for semantic segmentation are different variations of Cross Entropy loss and Jaccard loss. In our approach we use Categorical Cross-Entropy loss and Jaccard loss as loss functions for our CNN.

Cross-Entropy Loss

Other names for Cross-Entropy loss are Logistic loss and Multinominal Logistic loss. The function of Cross-Entropy Loss is written as:

$$CE = -\sum_{i}^{C} t_i \log(s_i)$$

where t_i are the ground truth labels and s_i are the CNN scores for each class $_i$ in C. Cross-Entropy Loss, contains under-categories. The ones introduced here are Binary Cross-Entropy Loss and Categorical Cross-Entropy Loss. The difference in these two Cross-Entropy losses lays in type of classification problem they are used for and whether the Cross-Entropy Loss is combined with a sigmoid or softmax activation (Gómez, 2018). Cross-entropy losses are either used for multi-class classification or multi-label classification problems (figure 3-10).

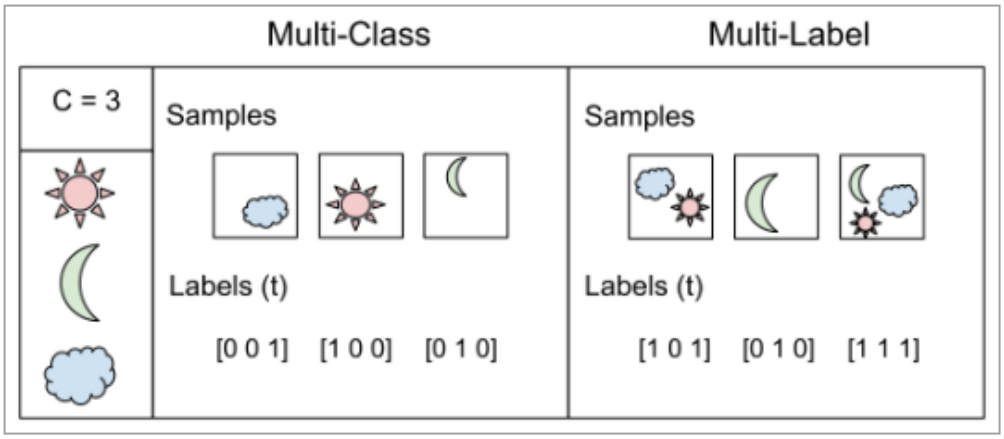

Figure 3-10: Visualization of the differences between multi-class classification and multi-label classification (Gómez, 2018).

Binary Cross-Entropy Loss

Binary Cross-Entropy Loss also known as Sigmoid Cross-Entropy loss is a variation of Cross-Entropy loss and is used for multi-label classification, where there can be more labels in one image which can belong to several classes (figure 3-10). The model needs to predict to which class each label belongs. The Binary Cross-Entropy loss is a combination of a Sigmoid activation and a Cross-Entropy loss and visualized with these formulas (Gómez, 2018):

$$f(S_i) = \frac{1}{1+e^{-S_i}} \qquad CE = -t_1 \log\big(f(s_1)\big) - (1-t_1)\log\,(1-f(s_1))$$

Categorical Cross-Entropy Loss

Categorical Cross-Entropy Loss also known as Softmax loss is a variation of the of the Cross-Entropy Loss is for Multi-class classification (figure 3-10 (or in cases of one class label)) where each image contains one label and the model should predict to what class the label belongs. The Cross-Entropy loss function for multi-class classification looks like this:

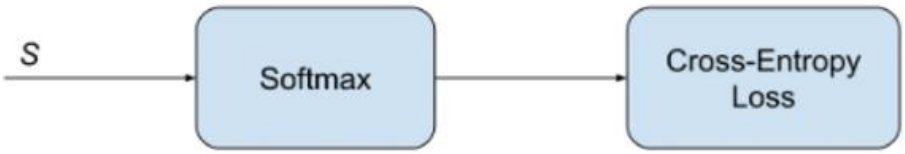

$$f(s)_i = \frac{e^{s_i}}{\sum_j^C e^{s_j}} \qquad CE = -\sum_i^C t_i \log\,(s_i)$$

But as this classification problem is One-hot problem, only the identified positive class C_p label = 1, and the rest = 0. The only component of the target vector t that is not 0 is $t_i = t_p$. So the function can be written as a negative logarithm of the softmax class probability of a single label/class (Gómez,2018):

$$CE = -\log\left(\frac{e^{s_p}}{\sum_j^C e^{s_j}}\right)$$

where s_p is the positive class CNN score.

Jaccard Loss

Jaccard Loss is a loss function well suited for semantic segmentation (Duque-Arias et al., 2021) based on the Jaccard distance (Deza and Deza, 2009), which is written as

$$J_d = 1 - \frac{|A \cap B|}{|A \cup B|}$$

where $\frac{|A \cap B|}{|A \cup B|}$ is the Jaccard index introduced by Jaccard (1901). The Jaccard index measures the similarity between finite sample sets A and B as the IoU. The Jaccard index will therefore be zero when the samples have no similarities and 1 if they are identical. The Jaccard distance is preferably used over the Jaccard index for minimization purposes (Duque-Arias et al., 2021).

The implementation of the Jaccard distance as a loss function is presented as different functions where the purpose is, during segmentation, to evaluate each pixel i by measuring the distance between the ground truth label $y_i \in \{0, 1\}$ and the models output label $\hat{y}_i$. For simplicity the i is removed from y_i and $\hat{y}_i$. Straightforward, the Jaccard distances replaces the IoU the following way (Rahman and Wang, 2016; Martire et al., 2017):

$$J_1(y, \hat{y}) = \frac{(y \cdot \hat{y}) + \varepsilon}{(y + \hat{y} - y \cdot \hat{y}) + \varepsilon}$$

where ε is preventing zero division.

3.3.3.4 Optimizers

Optimizers are algorithms used to find the optimal weight when adjusting the weights in a model during training, in order to achieve the lowest loss. Several different optimizers exist, which can be suiting for different ML problems. Optimizers constantly adjust the weights as training progresses and the optimizers are exposed to more model output vectors. A simple optimizer such as Gradient decent, will adjust the weight for every new model output vector. Constantly differing outputs will cause oscillation, making the optimizer less efficient. Momentum is often used to reduce the oscillation by taking previous outputs into account, adjusting the loss on a more average output rather than individual outputs. Momentum will cause acceleration towards the minimal loss, making the optimizer more efficient (Dozat, 2016). Momentum can be implemented in two different approaches. One being the classical momentum (which is described above) and another being Nesterov's momentum. The differences between these two momentums also marks the difference between the following optimizers: Adam and Nadam.

Adam (Adaptive momentum estimation, (Kingma and Ba, 2014)) combines classical momentum with RMSprop (Tieleman and Hinton, 2012). RMSprop is an alternative to AdaGrad (Adaptive subgradient descent, (Duchi et al., 2011)), allowing a model to learn indefinitely.

Nadam (Nesterov-accelerated adaptive moment estimation, (Dozat, 2016)) adds NAG (Nesterov's accelerated gradient, (Nesterov, 1983)) or Nesterov's momentum to Adam. NAG is generally better than classical momentum (Sutskever et al., 2013). Dozat (2016) concluded that Nadam in the majority of cases is better suited than Adam in combination with RMSprop. The Nadam optimizer is utilized whilst training models in this study.

3.4 Model Optimization Techniques

Model optimization techniques have become significantly important with the increased use of CNN in recent years. The objective of these techniques is to improve one of the great struggles of CNN models which is generalizability. Generalizability refers to the difference of performance a model has on training data and testing data. In cases where a model has good performance on the training data, but bad performance on the testing data, we would refer to poor generalizability, also referred to as overfitting. Generalizability can further be linked to the “experience” a model gathers during training, which has an impact on its future performance on unseen data. In other words, a model will have good generalizability when it is able to identify a large variety of the same objects or images. This is most commonly achieved in two different approaches; 1) by addressing the problem at its origin (training data) with the use of data augmentation or 2) applying modifications to the architecture of the network.

3.4.1 Data Augmentation

Data augmentation, as implied by its name, is generally used to increase the size of a training dataset. Data augmentation has several different purposes and techniques, all adding up to improving the generalizability of a model. CNN are deep learning models with often complex architectures where already the simplest model architectures can contain a few million parameters. For instance, the Efficient UNET used in this study contains 3 056 166 trainable parameters and 16 880 non-trainable parameters, and the Light UNET contains 4 370 594 trainable parameters and 5 136 non-trainable parameters. The large number of parameters ideally requires an equally large amount of training samples. With that in mind, data augmentation can be used for the simple purpose of increasing the training data for better performance, but the augmentation of data often brings several other benefits. The benefits include improving the diversity of the training data, increasing the number of relevant training data and balancing out minority and majority classes. Data augmentation techniques can be divided into simple and more advanced techniques. The simple techniques are also known as original data augmentation and apply changes to the existing data. Like the methods presented in this thesis in the sections below. More advanced techniques are developed rather recently, with the implementation of GAN and other deep learning algorithms that have the ability to create completely new synthetical data from the original data. Original data augmentation encompasses the use of kernel filters, color space transformations, geometric transformations, random erasing and mixing images. Examples of advanced augmentation techniques are neural style transfer and the use of conditional GANs.

Data augmentation is one of the techniques which in recent years massively have boosted the performance of ML models, in the field of CNN especially. Early examples go back to LeNet-5 (LeCun et al., 1998), where CNN were applied to handwritten digit classification for the first time. One of the more familiar CNN, AlexNet (Krizhevsky et al., 2012), which revolutionized image classification on the ImageNet dataset, used simple data augmentation techniques such as random cropping, horizontal flip and changing the intensity of RGB channels. Data augmentation improved the error rate of the model by over 1%, as claimed by the authors.

The introduction of GAN (Goodfellow et al., 2014) enabled the implementation of more advanced data augmentation techniques like Neural Style Transfer (Gatys et al., 2015) and Neural Architecture Search (NAS) (Zoph and Le, 2017). Meta learning which are concepts from NAS have become popular applications to data augmentation with works like Neural Augmentation (Perez and Wang, 2017), Smart Augmentation (Lemley et al., 2017) and Auto Augment (Cubuk et al., 2018). The use of GAN-based data augmentation in medical imaging has been documented in numerous papers, which demonstrate the positive effect of data augmentation on image classification. In 2018, Frid-Adar et al. used GAN-based data augmentation for liver lesion classification, which resulted in a classification performance increase from 78,6% sensitivity and 88,4% specificity using the original augmentation to 85,7% sensitivity and 92,4% specificity.

For the most part, data augmentation is focused on improving image recognition models, but it can be utilized in other computer vision tasks like object detection (Redmon et al., 2016) or semantic segmentation (Long et al., 2014) with algorithms like UNET (Ronneberger et al., 2015). This idea is further explored in this study, by applying data augmentation to the semantic segmentation task of predicting faults in seismic images.

3.4.1.1 Data Augmentation in EarthNet

The EarthNet software by Earth Science Analytics provides easy application of data augmentation for image segmentation or seismic interpretation on 3D seismic volumes. Data augmentations included in the software are methods encompassing three types of geometric transformations like horizontal flip, grid distortion 1D and elastic transformation 1D. The following sections go into detail on each individual augmentation type and how they were applied to the seismic in this study.

3.4.1.1.1 HORIZONTAL FLIP

As the name implies, horizontal flip rotates the original seismic image (figure 3-11 a) 180 degrees around its vertical axis, resulting in a horizontally flipped image (figure 3-11 b). This data augmentation technique essentially duplicates every image in the data set it is applied

to, doubling the amount of data. In addition to increasing the training data for the CNN in this study, it also ads variety to the data set. Most noticeably in figure 3-11 is that the majority of faults have the same orientation, horizontal flip in this case ads variety to the orientations of faults.

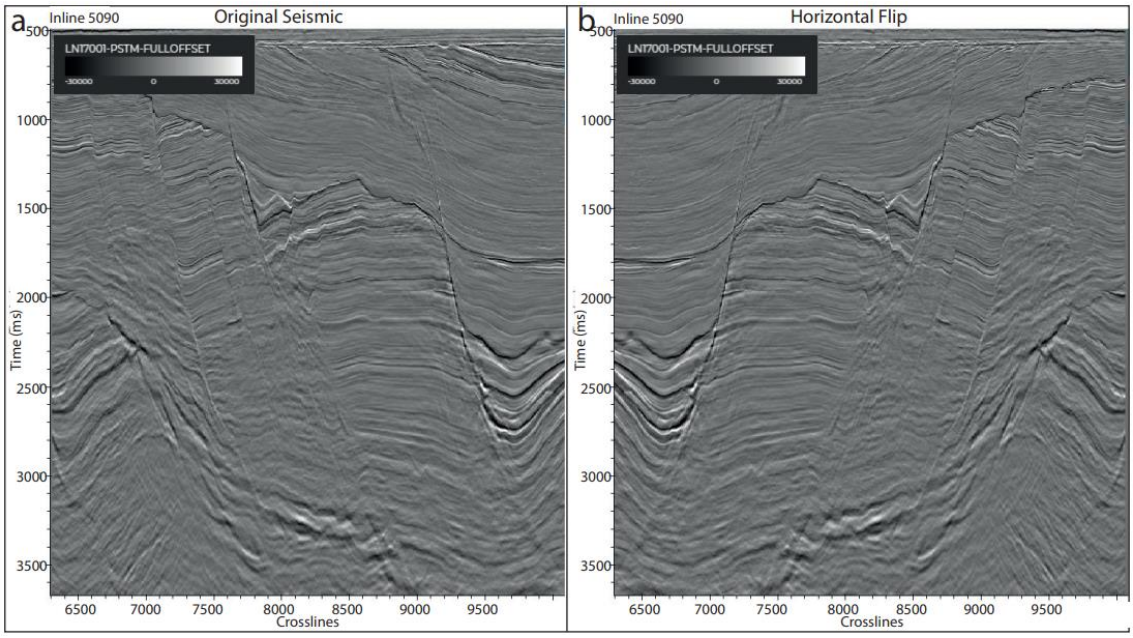

Figure 3-11: A section out of Inline 5090, survey LN17001_Full_Stack and volume LN17001 3D survey.(a) Displays the original seismic which is compared to the same section when horizontal flip is applied (b).

3.4.1.1.2 GRID DISTORTION 1D

Grid distortion 1D creates new seismic images by applying a slightly more complex geometric transformation than horizontal flip. As illustrated in figure 3-12, it distorts the seismic images resulting in sections of varying size that are offset with respect to each other. Obvious changes in the distorted image (figure 3-12 b) are offset features like faults and bedding in addition gaps without any seismic are left within the image as a direct consequence of the distortion. It is worth mentioning that the steps observed in the example shown in figure 3-12 b is not happening when using data augmentation in practice in EarthNet. The patch sizes are large enough to avoid such offsets which have no geological meaning. This type of artifacts have to be avoided in any data augmentation approach for automatic interpretation using CNN. Grid distortion 1D in contrast to horizontal flip has several adjustable parameters allowing to determine the amount of distortion. For seismic interpretation it is desirable to apply mild, but noticeable changes while avoiding to make the image unrecognizable. The major parameters for controlling the grid distortion are “number of steps” and distortion limit, controlling the degree of distortion. Parameters used for data augmentation, can be found in table 3-1.

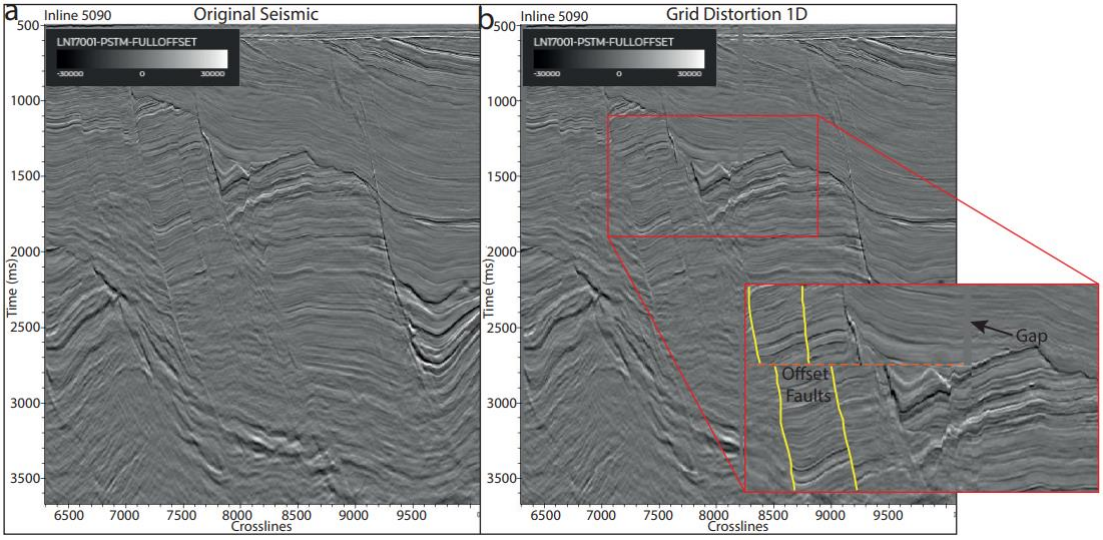

Figure 3-12: A section out of Inline 5090, survey LN17001_Full_Stack and volume LN17001 3D survey. (a) Displays the original seismic which is compared to the same section when grid distortion 1D is applied (b). Offset faults are marked in yellow.

3.4.1.1.3 ELASTIC TRANSFORMATION 1D

Elastic transformation 1D in similarity to grid distortion 1D, is an adjustable geometric transformation. This type of data augmentation distorts the grid of the seismic image, and in addition it has a component of elastic transformation. As marked in figure 3-13, we observe areas within the seismic image where the elastic transformation is especially pronounced. Marked in yellow ellipses we see that originally rather straight lines (figure 3-13 a), have become more curved (figure 3-13 b). The elastic transformation paired with the distortion element, results in new seismic images where the curvature, position and angle of both seismic bedding reflectors and faults are changed. Parameters determining the elastic transformation 1D are alpha, sigma and alpha affine, where each parameter controls individual aspects of the elastic transformation. The exact parameters used, can be found in table 3-1.

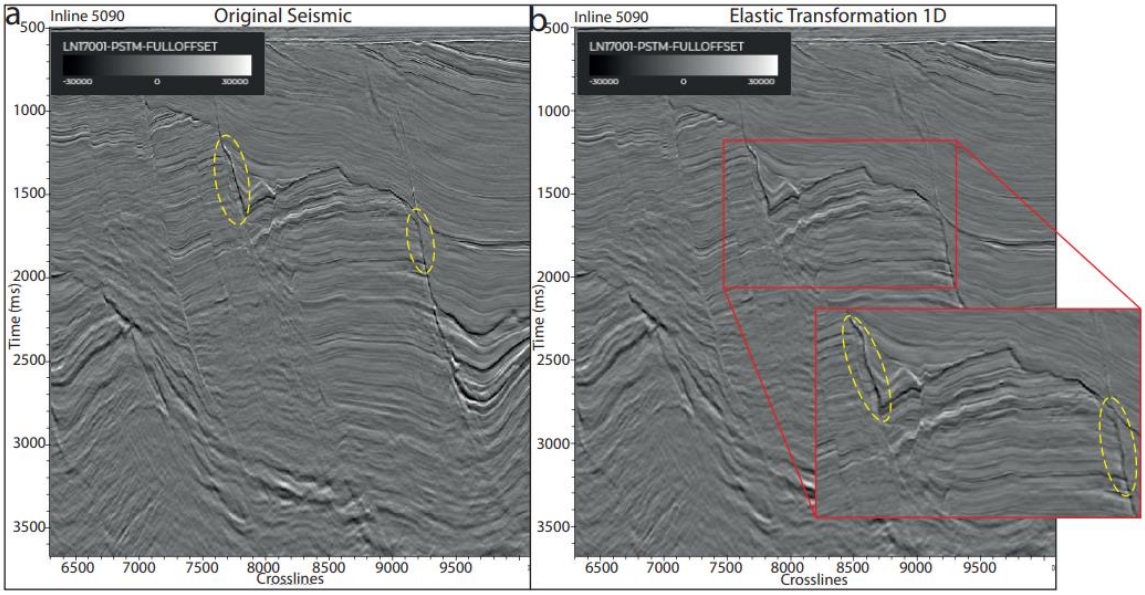

Figure 3-13: A section out of Inline 5090, survey LN17001_Full_Stack and volume LN17001 3D survey.(a) Displays the original seismic which is compared to the same section when elastic transformation 1D is applied (b). Clearly transformed areas are marked with yellow ellipses.

3.5 ML in Geoscience

Geoscience is part of the early history of machine learning. Initially, k-means, Markov models and decision trees have been used already since the early 60s. K-means was used in the field of sedimentology (Preston and Henderson, 1964). Markov chains had several purposes early on, within the fields of sedimentology (Schwarzacher, 1972), well log analysis (Agterberg, 1966), hydrology (Matalas, 1967) and volcanology (Wickman, 1968). Decision tree-based methods were applied in economic geology and prospectivity mapping (Newendorp, 1976; Reddy and Bonham-Carter, 1991).

During the late 80s, new tools for automatic differentiation and backpropagation for error-correcting were introduced, which made neural networks usable in geophysics. As a result, a RNN (Hopfield network) was used by Zhao and Mendel (1988) to conduct seismic deconvolution. A few years later, Dowla et al. (1990) used feed-forward neural networks to distinguish between natural earthquakes and underground nuclear explosions, reaching accuracies of 97%. In addition, Huang et al. (1990) published work on picking seismic horizons with a type of unsupervised neural network called self-organizing maps.

The shift from knowledge-driven to a data-driven approach in machine learning during the 90s, marks the establishment of SVM (Cortes and Vapnik, 1995), Random Forests (Ho, 1995) and Long Short-Term Memories (Hochreiter and Schmidhuber, 1997). SVM initially were used for land usage classification in remote sensing (Hermes et al., 1999) and later on to approximate the Zoeppritz equations for AVO inversion (Kuzma, 2003). The

implementation of the two other methods was rather poor, at least in geoscience during this decade.

An important factor for the development of ML algorithms in geoscience was the implementation of free open-source software (FOSS), machine learning libraries and languages. The ones with the largest significance, are the WEKA (Witten and Frank, 2005) and LibSVM (Chang and Lin, 2011) free open-source softwares and the PyTorch (Paszke et al., 2017), Theano and Scikit-learn (Theano Development Team, 2016; Pedregosa et al. 2011) libraries. The WEKA software mainly supports SVM efficiently. SVM including other shallow machine learning algorithms like random forests and shallow neural networks are supported by Scikit-learn, whilst DNN are well supported by Theano.

In recent years shallow machine learning algorithms have found several applications due to scikit-learn. Random forests and gradient boosting were applied to several seismological (Dodge and Harris, 2016; Maggi et al., 2017; Hulbert et al., 2018) and geochemical applications (Valera et al., 2017; Rouet-Leduc et al., 2017, 2018; Cao and Roy, 2017). Gradient boosted trees were also in the 2016 SEG ML challenge as winning models (Hall and Hall, 2017).

3.5.1 ML for Seismic Interpretation

The task of seismic interpretation in geology can be difficult and time consuming. Machine learning algorithms can be used as a way for geologists to easier understand relationships in large geological datasets. Since seismic data consists of images, neural networks are well suited for this kind of interpretation task and both supervised and unsupervised learning can be used. However, due to the heterogeneity of earth, supervised neural networks can get very unprecise if the unseen data is very different to the training data (Smith, 2010). Hence, unsupervised neural networks are preferred.

Although unsupervised neural networks are preferred, supervised neural networks can still be used for seismic interpretation. In case of pattern recognition, approximation and classification, a multi-layered perceptron is used (Roden and Santogrossi, 2017). Another method involves the use of probabilistic neural networks. This method uses vectors to show how close the input is to the training data and calculates the probability, ranging from 1 to 0, where 1 is the maximum probability (Mohri et al., 2012).

Unsupervised algorithms on the other hand, do not require labeled training data. They can figure out patterns in the data and use conventional analytical methods to display missing geological features. Unsupervised algorithms can be used to determine fluid properties,

lithological changes, well analysis and the optimal seismic attributes to interpret the seismic (Smith, 2010).

A possible workflow when interpreting seismic data using an unsupervised neural network is illustrated in figure 3-14. This kind of workflow is known as a multi-attribute ML interpretation, which involves the use of a principal component analysis (PCA) and self-organizing maps (SOM) (Roden, 2017). In such a workflow, first the interpretation task needs to be defined (e.g. interpretation of facies, stratigraphy, bed thickness, direct hydrocarbon indicators (DHIs), etc.) It is important to choose the most significant attributes needed to perform the task. Those are determined by the PCA (Roden and Santogrossi, 2017).

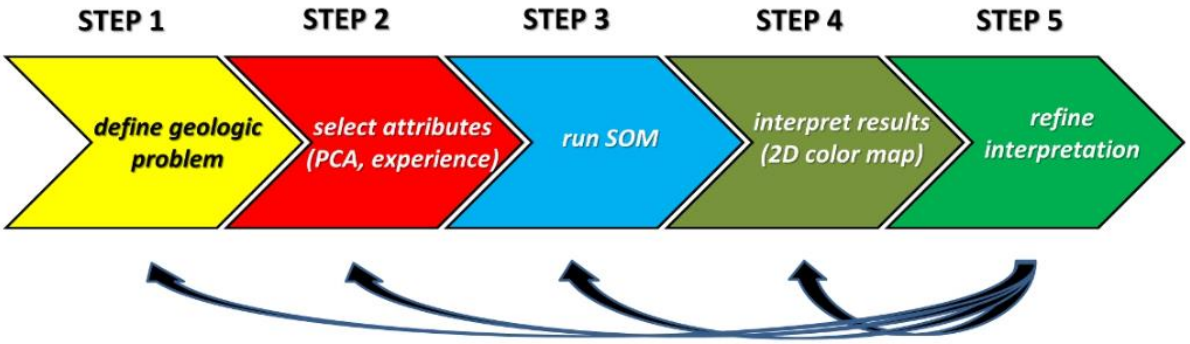

Figure 3-14: Typical unsupervised multi-attribute ML interpretation workflow (Roden, 2017).

Thereafter, SOM are used to organize multiple seismic attributes into volumes of classification and probability (Kohonen, 1982). As a part of DNN, SOM analyze clusters and patterns in a nonlinear way. Basically, a SOM takes a various amount of seismic datasets and organizes the data in a 2D colormap (Roden, 2017), as shown in figure 3-15.

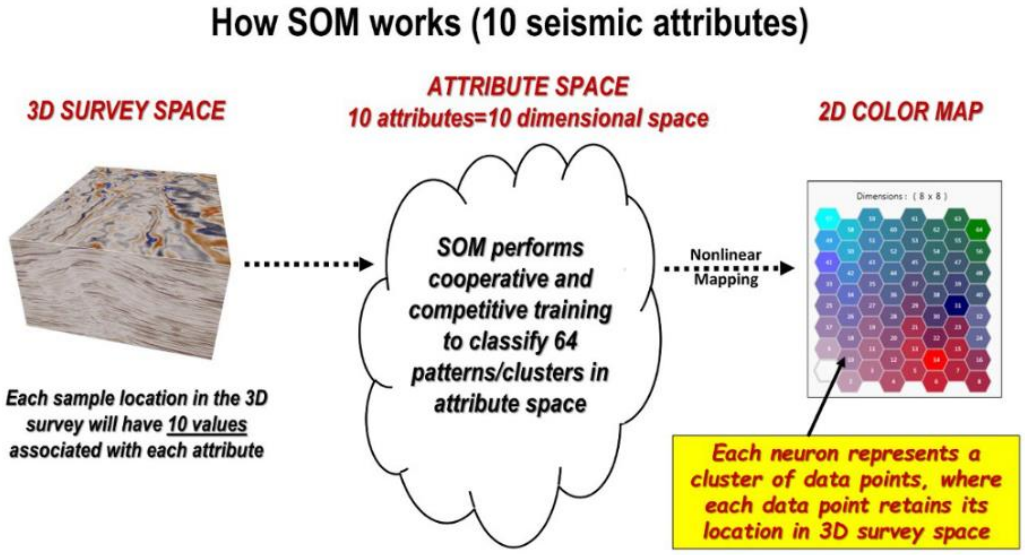

Figure 3-15: SOM processing of 3D seismic survey (Roden, 2017).

3.5.1.1 ML for Fault Interpretation

In geological context, fault interpretation using seismic images plays a significant role. It is important for hydrocarbon reservoir characterization (Knipe et al., 1998), well planning (Ellevset et al., 1998; Rivenæs et al., 2005), building structure models (Caumon et al., 2009) and tectonic analysis (Kusznir and Karner, 2007; Baudon and Cartwright, 2008). As, we move on from original deterministic methods developed to make fault interpretation more automated, we apply methods involving the use of CNN. Some approaches similar to our approach are mentioned bellow.

Xiong et al. (2018) introduced a CNN to interpret faults from 3D seismic data-cubes. They used real seismic data to train the network in a supervised fashion. The network interprets the seismic in form of an image classification task. During training, labels were applied to the data, denoted as fault (1) or non-fault (0). When, later on, applied to a different sets of data the CNN managed to perform better than the conventional seismic coherence method. The CNN was showing about the same fault probability as the seismic coherence, but the seismic discontinuities were better highlighted (figure 3-16).

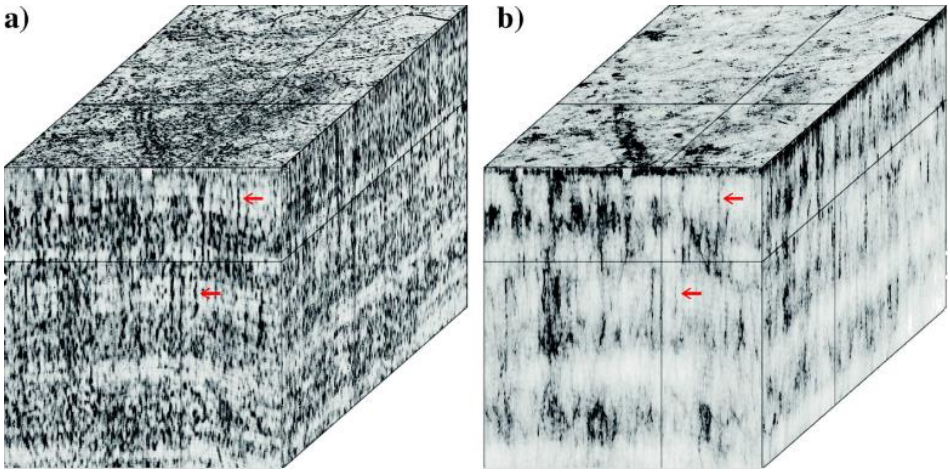

Figure 3-16: a) Fault probability interpreted by the CNN with b) the corresponding coherence cube as reference (Xiong et al. 2018).

Similarly, Wu et al. (2019) introduced the use of a supervised fully convolutional neural network to perform image-to-image fault segmentation. Even though the network only was trained on synthetic data, it managed to very precisely detect faults in real seismic data. This method was found to predict faults more accurately than the conventional methods mentioned earlier. The architecture of the CNN is a simplified UNET (figure 3-17). The UNET consist of a contraction path to the left and an expansion path to the right. The contraction path consists of several steps, with two 3 x 3 x 3 convolutional layers. Thereafter comes a ReLU activation followed by a 2 x 2 x 2 max poling for down-sampling. As the data is down-sampled, the number of features is doubled. In the expansion path, the steps consist of a 2 x

2 x 2 up-sampling, a pairing of features from the contraction path and 3 x 3 x 3 convolutional layers with ReLU activation functions. A simplified version encompasses reduction of convolutional layers and features at each layer to save memory and computational capacity.

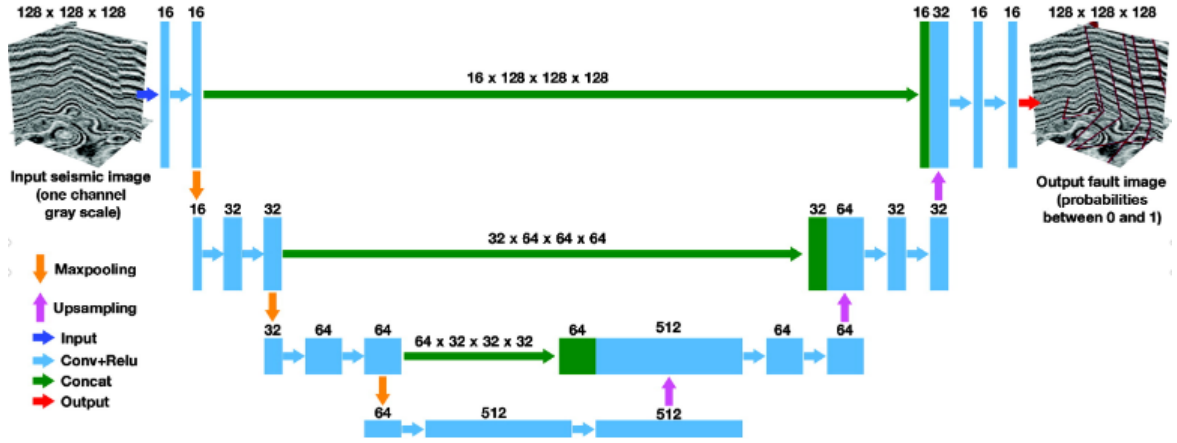

Figure 3-17: The UNET structure of a simplified end-to-end convolutional neural network (CNN) for 3D fault detection (Wu et al., 2019).

3.6 Applied Workflow

In this study the CNN architectures Efficient UNET and Light UNET are utilized. They are modified versions of the original UNET architecture (figure 3-17) developed by Ronneberger et al. (2015). The UNET, Efficient UNET and Light UNET architectures are described in the sections bellow.

3.6.1 UNET Architecture

The first UNET architecture, created by Ronneberger et al. (2015) for semantic segmentation, was inspired the “fully convolutional network” (Long et al., 2014). The nearly symmetrical u-shaped encoder/decoder architecture (figure 3-18) is the result of a increased number of feature channels, further enabling the network to propagate context information to layers with higher resolution. Another difference to the network of Long et al. (2014) is that the UNET does not have fully connected layers, in addition only the valid portion of each convolution is used, i.e. the segmentation map only contains pixels, where the full context is provided in the input image.

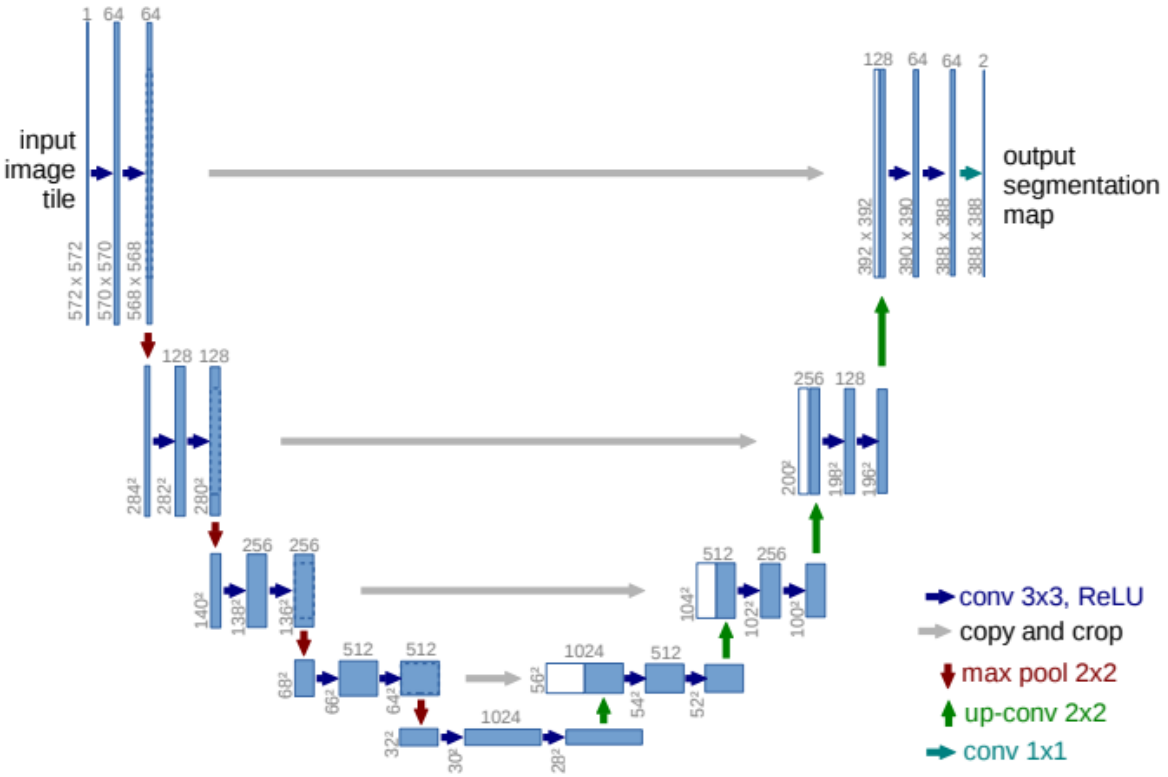

Figure 3-18: UNET architecture with 32 x 32 pixels at the lowest resolution. Multi-channel feature maps are represented by the blue boxes with the number of channels and the x-y-size denoted at the top and bottom left of the boxes, respectively. The white portion of the boxes are copied feature maps and the arrows denote the different operation performed (Ronneberger et al., 2015).

The architecture proposed by Ronneberger et al. (2015) is illustrated in figure 3-18. It consists of a encoder (contracting) and decoder (expansive) path. The encoder still represents the typical architecture of a convolutional network: repeatedly, two 3 x 3 convolutions (unpadded convolutions) are applied, each followed by ReLU and a 2 x 2 max pooling (stride 2 for downsampling, where the number of feature channels is doubled). In the encoder upsampling of the feature map, halves the number of feature channels as it is followed up by a 2 x 2 convolution (“up-convolution”), additionally it is followed by a concatenation with the correspondingly cropped feature map from the encoder and two 3 x 3 convolutions, each followed by a ReLU. In every convolution, pixels are lost at the borders thus cropping is necessary. The final layer applies a 1 x 1 convolution so each of the 64-component feature vectors are mapped to the amount of classes. Overall, the network comprises 23 convolutional layers.

Efficient UNET

The Efficient UNET architecture builds on the u-shaped encoder and decoder UNET architecture by Ronneberger et al. (2015) in figure 3-18, and additionally employs the

technique of automatic compound scaling. Tan and Le (2019) introduced the uniform (determined by ratio) compound scaling of convolutional network depth (number of layers), width (number of feature channels) and resolution (resolution of input; number of pixels) in order to most efficiently adapt and solve any given problem. In figure 3-19 the compound scaling introduced by Tan and Le (2019) is compared to a baseline network layout, and the adjustment of width, depth and resolution individually. In the EarthNet software it is possible to change the network sizes by choosing different presets from the efficient encoder parameter (setting a1 is used in this thesis).

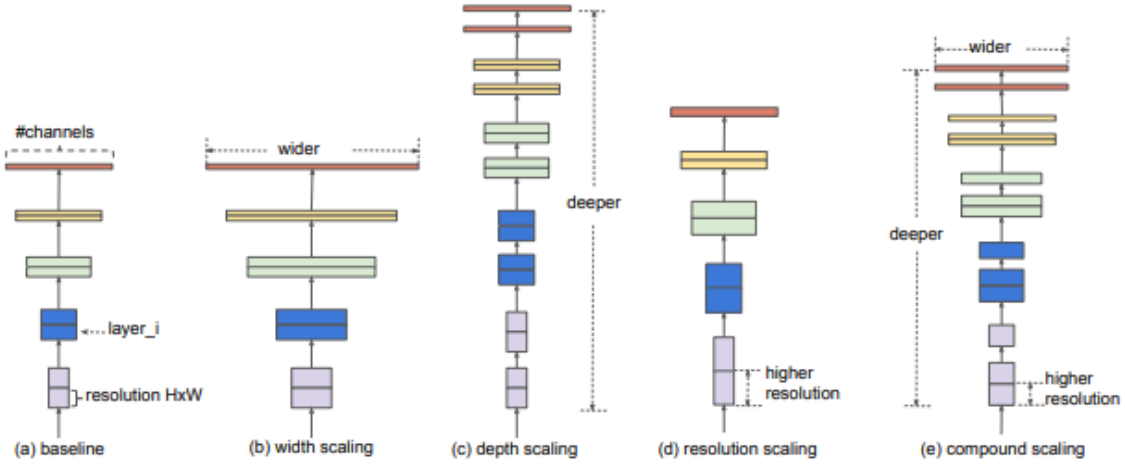

Figure 3-19: Model scaling. (a) example of baseline network; (b)-(d) conventional scaling where only adjusting one dimension at the time (width, depth or resolution); (e) compound scaling proposed by Tan and Le (2019) which uniformly scales the tree dimensions given a fixed ratio (Tan and Le, 2019).

Light UNET

The Light UNET architecture is similar to the UNET architecture proposed by Ronneberger et al. (2015) in figure 3-18, but additionally the Light UNET is fully adjustable. This provides the possibility to adjust the number of initial feature channels, by what number the feature channels should be multiplied for each convolution, number of layers in the encoder and decoder, whether a depth channel should be added, and which activation function to use. In this thesis the Light UNET architecture comprises 24 initial feature channels, x2 feature channel multiplier, 4 convolutional layers in the encoder and 4 convolutional layers in the decoder, no depth channel and ReLU activation function.

3.6.2 Software

I have used the fault automatic interpretation module of EarthNet. The software is developed by Earth Science Analytics (earthanalytics.ai). EarthNet is a cloud-native web-based software which enables to easily apply ML on seismic data. The software has multiple functions where large amounts of data containing information about the subsurface can be

combined with human interpretations and artificial intelligence. EarthNet allows interpreters to access, and quality control, both well data and 3D seismic data volumes and crate training labels in order to customize and train their own ML models for seismic interpretation and 1D/3D reservoir characterization.

3.6.2.1 Model assisted Labeling

The labeling of geological features for seismic interpretation and faults in case of this study is an essential part of training a ML algorithm for the task of fault prediction in seismic. In the approach of using supervised learning on Efficient UNET and Light UNET the training dataset is created by human interpreted labels. The process of labeling faults involved a pretrained Light UNET model in combination with manual human quality control and labeling. The pretrained Light UNET provided by earth science analytics was trained on tens of 3D seismic surveys from the Norwegian Continental Shelf and open data from other localities such as Australia and New Zealand. This pretrained model was used to carry out the so-called model assisted labeling by predicting faults on selected 2D slices. Thereafter, validation of the interpretations was necessary and changes were made if needed. Model assisted labeling reduces the time needed for the time consuming task of fault labeling. Training labels were created on both inlines and crosslines within all three 3D seismic volumes that are part of this study. A certain interval spacing between the training labels with respect to the size of the 3D seismic volume was used to achieve an even distribution and to create labels representing the seismic variety throughout the volumes. For the smaller seismic volume ST14200Z15-OBN in survey ST14200_OBN with in total 728 inlines and 694 crosslines, an inline and crossline spacing of 50 was chosen, resulting in 12 labeled inlines and 12 labeled crosslines. For the larger 3D seismic volumes SG9202_Full_Stack in survey SG9202 and LN17001_Full_Stack in survey LN17001 the total number of labeled inlines and crosslines was larger. Volume SG9202_Full_Stack with a total of 2215 inlines and 3451 crosslines a total of 21 inlines and 21 crosslines were labeled with a spacing of 110 and 170, respectively. Volume LN17001_Full_Stack with a total of 3685 inlines and 6561 crosslines a total of 22 inlines and 20 crosslines were labeled with a spacing of 180 and 240, respectively.

3.6.2.2 Training

The Efficient and Light UNET were trained independently on labels from all three 3D seismic data volumes, meaning that one model only was trained on labels from the same seismic volume, never on labels from two different volumes. Models were also trained with and without data augmentation applied. Data augmentation was applied in form of horizontal flip, grid distortion 1D and elastic transformation 1D. The different types of data augmentation were applied separately. An important step to determining the effect of data augmentation is finding the optimal augmentation parameters. The parameters for grid distortion 1D and

elastic transformation 1D were determined, by experimenting with different settings and using geological understanding to evaluate the effect of transformation on the seismic data volumes directly. The resulting parameters for the different data augmentations are summarized in table 3-1.

Table 3-1: All parameters related to the data augmentation utilized in this study.

Data Augmentation	Horizontal Flip	Grid Distortion 1D	Elastic Transformation 1D
Probability of Crop a Non-empty Mask	0,3	0,3	0,3
Probability of Random Crop Mask	0,3	0,3	0,3
Transform x	_	True	True
Probability	_	0,5	0,5
Number of Steps	_	15	_
Distortion Limit	_	0,3	_
Alpha	_	_	50
Sigma	_	_	10
Alpha Affine	_	_	1

The first step for data augmentation is to select a patch including labeled faults (a non-empty mask) and then select randomly some patches that may or may not include labels. I have applied equal probability (table 3-1) which means that equal patches of non-empty masks and random masks will be selected for data augmentation. 50% of the selected patches for augmentation will be used for the horizontal flip option. Then 50% of the selected patches for data augmentation (not another 50% compared to horizontal flip) will be used for grid distortion 1D and also 50% of the selected patches for the data augmentation will be used for elastic transformation 1D. These probabilities for horizontal flip, grid distortion 1D and elastic transformation 1D are independent of each other. This means that there could be patches that will be used for all of these three approaches.

Models were both trained on inlines and crosslines, but also inlines and crosslines separately. Both, Efficient UNET and Light UNET model architectures were trained using different hyperparameters. For this, the learning structure of the models was changed by implementing different values to hyperparameters, such as the training epochs and extra training epochs, training patch size and dropout. Notice that the amount of extra training epochs changes depending on the amount of training epochs. Extra training epochs always add an additional 50% of training epochs to the initial training epochs. When speaking of training epochs in the results, it should be understood that the extra training epochs are not considered within the numbers. Table 4-1 and 4-2 give an overview over the most important CNN fault prediction models including essential parameters.

3.6.2.3 CNN Evaluation and Testing

After training all fault prediction models they were evaluated and tested, and this was done both statistically and by blind testing the models on the 3D seismic volumes directly. Whenever a model has completed the training process in EarthNet a model review becomes available, containing a confusion matrix and confusion matrix validation, basically corresponding to the train and test subset of the labeled slices. The matrixes show the percentage of correctly identified faults and background, and wrongly identified faults and background, related to the terms true positives (TP), true negatives (TN), false positives (FP) and false negatives (FN) introduced in section 3.3.3.1. In the model review, training and validation metrics can also be evaluated, both final values and how those changed throughout training. Table 4-2 and 4-3 provide metrics, training and test scores for the most important models of this study.

In addition to the evaluation of the model statistics, it is important to actually test the models capability of identifying faults in the 3D seismic data and evaluating the quality of predictions on slices which the model has not seen. For this purpose, blind tests of the models were performed both on accompanying 3D seismic volumes inlines and crosslines. The process of blind testing the CNN encompasses choosing inlines or crosslines that are located right in the middle of labeled inlines or crosslines. This is done to test the model's true performance with as little influence from the labels as possible.

The different approaches of evaluation were performed in order to determine what model architecture, data augmentation technique and combination of hyperparameters resulted in the best performing models for predicting faults in the three different 3D seismic volumes. For volume LN17001_Full_Stack, this was also done in order to determine which model should be utilized for fault damage zone characterization. The performance of the various fault prediction model is compared both statistically and practically in chapter 4.

3.6.2.4 Fault Characterization

The fault predictions that were used for the fault characterization in chapter 4.2 were created by applying the best performing CNN to 3D seismic volume LN17001_Full_Stack. For this volume the best performing CNN was a Light UNET with model ID: 4852 (see figure 4-14 c or table 4-2 and 4-3). The application of the Light UNET on the 3D seismic volume involves creating a 3D fault volume, which covers CNN fault predictions across the entire 3D seismic volume. Additionally, an average between the inline and crossline fault predictions is created which further provides the fault probability estimation (for an example, see e.g. figure 4-17).

The scanlines were oriented in the inline orientation of 3D seismic volume LN17001_Full_Stack and the spacing between the scanlines is 1,5 km, corresponding to 180

inline spacing (8.33m). In total 7 scanlines (Inline 5000, 5180, 5360, 5540, 5720, 5900 and 6080) approximately varying between 23-28 km of length were placed crossing fault F3 (see figure 4-16 for reference). Additionally, 6 scanlines were placed at depths of 800, 1300, 1800, 2300, 2800 and 3300ms TWT (two-way-travel time) at each of the 7 inline scanline locations.

4 Results: ML Models for Fault Identification and Fault Characterization

The objective of the result section is divided into three parts; 1) determining the optimal configuration of ML models suited for the task of characterizing faults in 3D seismic data volumes, 2) utilizing the best performing model for the characterization of faults, with focus on one specific fault and the surrounding damage zone and finally 3) fault characterization using fault geometric data derived from fault probability volumes which were derived in step 2.

The results presented in the results-section are extracted from research completed by utilizing Efficient UNET and Light UNET networks on the full stack volumes of 3D seismic surveys ST14200_OBN, LN17001 and SG9202. Additionally, the characterization of faults was executed on the LN17001 3D survey by generating and analyzing 3D fault volumes.

4.1 ML Models for Fault Identification

The objective of this section is to figure out the best combination of ML model architectures, by using data augmentation and tuning hyperparameters. In this approach two different CNN model architectures were utilized; the Efficient UNET and the Light UNET. Initially, CNN with the Efficient UNET architecture were applied to the seismic. Further, we explored the effect of models trained and tested on both inlines and crosslines, compared to models trained and tested on inlines and crosslines separately. At last, the performance of Efficient UNET and Light UNET was compared.

4.1.1 The Effect of Applying Data Augmentation to 3D Seismic Data Volumes

This part of the study evaluates the effect application of simple data augmentation in terms of geometric transformation has on the performance of CNN, focusing on Efficient UNET and Light UNET networks. To begin with, we explore the effect of geometric transformations, known as horizontal flip, grid distortion 1D and elastic transformation 1D. The results from seismic volume ST14200Z15_OBN_Full_Stack show the effect of data augmentation on fault prediction (figure 4-1 c-e) compared to the performance of a baseline Efficient UNET, where no data augmentation is applied and hyperparameters are kept default (figure 4 b). From analyzing these images, it is noticeable that a large portion of the faults were missed. The baseline model has a few continuous fault predictions, but mostly large portions of most faults are missed, and predictions are highly discontinuous. It is clear that all data

augmentation techniques applied in this study contribute to a significant CNN performance increase (figure 4-1 c-e). Generally, all three techniques of data augmentation have identified the majority of faults with maintaining the continuity of faults. This is the case even for the larger faults, which often are more challenging capture. However, the Efficient UNET with grid distortion 1D applied had slightly more continuous fault predictions paired with slightly better fault detection than the two other data augmentations.

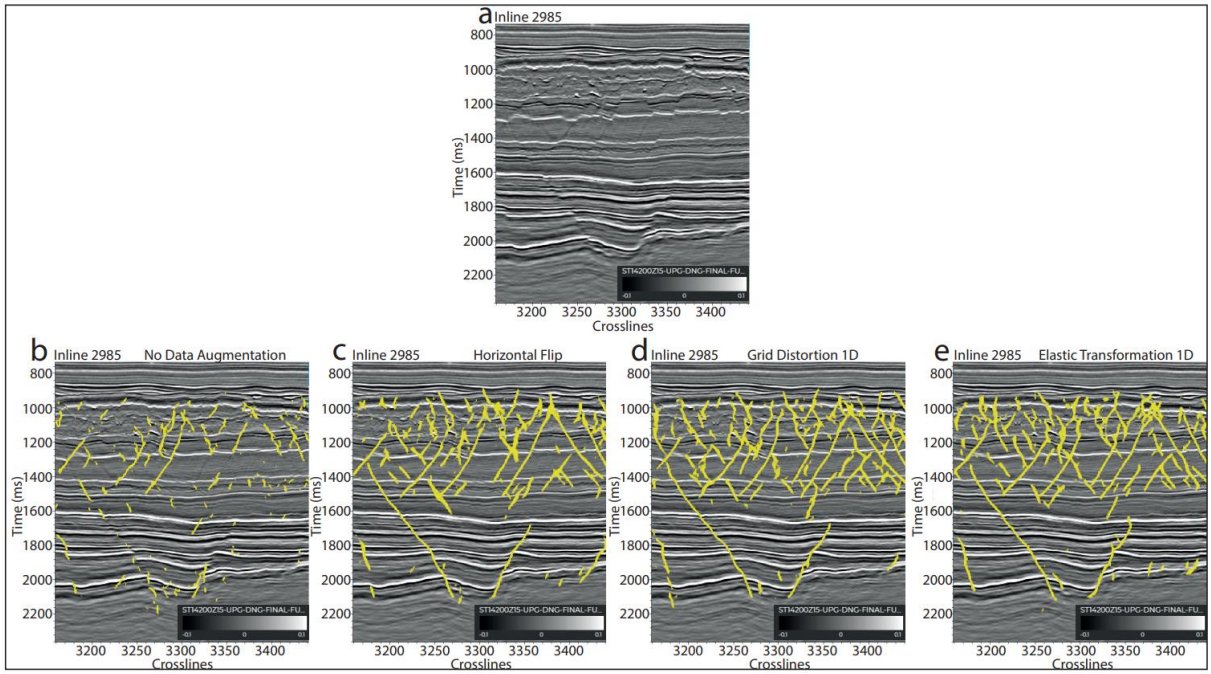

Figure 4-1: Images of Inline 2985 from volume ST14200Z15_OBN_Full_Stack in survey ST14200_OBN comparing the performance of Efficient UNET trained and tested on the different types of data augmentation. a) Inline 2985 without fault predictions, b) faults predicted by Efficient UNET (model ID: 4749) trained and tested on both inlines and crosslines without data augmentation c) faults predicted by Efficient UNET (model ID: 4757) trained and tested on both inlines and crosslines with Horizontal Flip, d) faults predicted by Efficient UNET (model ID: 4751) trained and tested on both inlines and crosslines with Grid Distortion, e) faults predicted by Efficient UNET (model ID: 4758) trained and tested on both inlines and crosslines with Elastic Transformation.

The same comparison made in figure 4-1 is made in figure 4-2, only for volume LN17001_Full_Stack. The two figures also reflect similar results, where the Efficient UNET with data augmentation applied (figure 4-2 c-e) outperform the baseline Efficient UNET (figure 4-2 b). Although, the CNN performance increase between the baseline Efficient UNET and the Efficient UNET applying data augmentation is less significant on volume LN17001_Full_Stack compared to volume ST14200Z15_Full_Stack.

While taking a closer look at the major fault in figure 4-2, it is noticeable that the Efficient UNET trained on augmented data (figure 4-2 c-e) generally have a more pronounced and continuous interpretation compared to the baseline model (figure 4-2 b). Comparing the baseline model to the model where horizontal flip is applied (figure 4-2 c), the baseline model has detected a larger portion of the major fault, but the horizontal flip model still has a more

continuous prediction. That also applies to the smaller faults surrounding the major fault. The models that apply grid distortion 1D (figure 4-2 d) and elastic transformation 1D (figure 4-2 e) have identified a similar portion of the major fault compared to the baseline model, but again, the augmented models have better prediction continuity, which also applies for the surrounding faults. The predictions of grid distortion 1D and elastic transform 1D are almost identical.

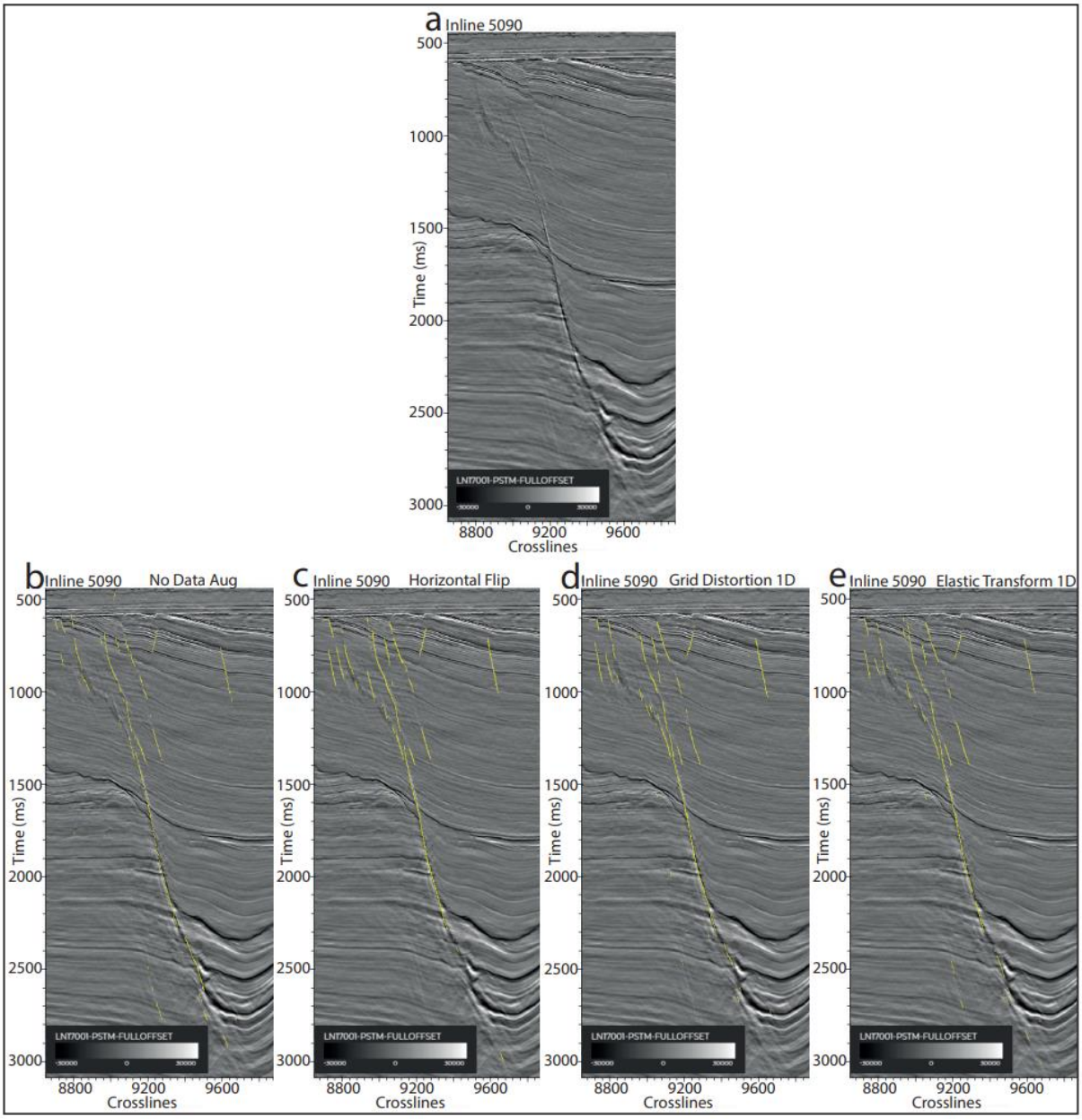

Figure 4-2: Images of Inline 5090 from volume LN17001_Full_Stack in survey LN17001 3D survey comparing the performance of Efficient UNET trained and tested on the different types of data augmentation. a) Inline 5090 without fault predictions, b) faults predicted by Efficient UNET (model ID: 4750) trained and tested on both inlines and crosslines without data augmentation c) faults predicted by Efficient UNET (model ID: 4772) trained and tested on both inlines and crosslines with Horizontal Flip, d) faults predicted by Efficient UNET (model ID:4755) trained and tested on both inlines and crosslines with Grid Distortion 1D, e) faults predicted by Efficient UNET (model ID: 4773) trained and tested on both inlines and crosslines with Elastic Transformation 1D.

When comparing Efficient UNET without data augmentation and Efficient UNET with data augmentation for 3D seismic volume SG9202_Full_Stack (figure 4-3), similar to 3D seismic volume LN17001_Full_Stack only minor details change. The none-augmented Efficient UNET (figure 4-3 b) images a moderate portion of the faults. The model has detected some fault segments with good continuity, and others with rather poor continuity. Generally, the CNN with data augmentation applied (figure 4-3 c-e) do not necessarily detect a larger portion of faults, but some of the predictions are just slightly more continuous and some faults are just better covered. Actually, one exception may be the predictions in figure 4-3 e (elastic transformation 1D) where a majority of the seismic in all aspects is somewhat worse interpreted than by the other models. When comparing the horizontal flip interpretation (figure 4-3 c) to the grid distortion 1D interpretation (figure 4-3 d) it is only possible to tell slight differences.

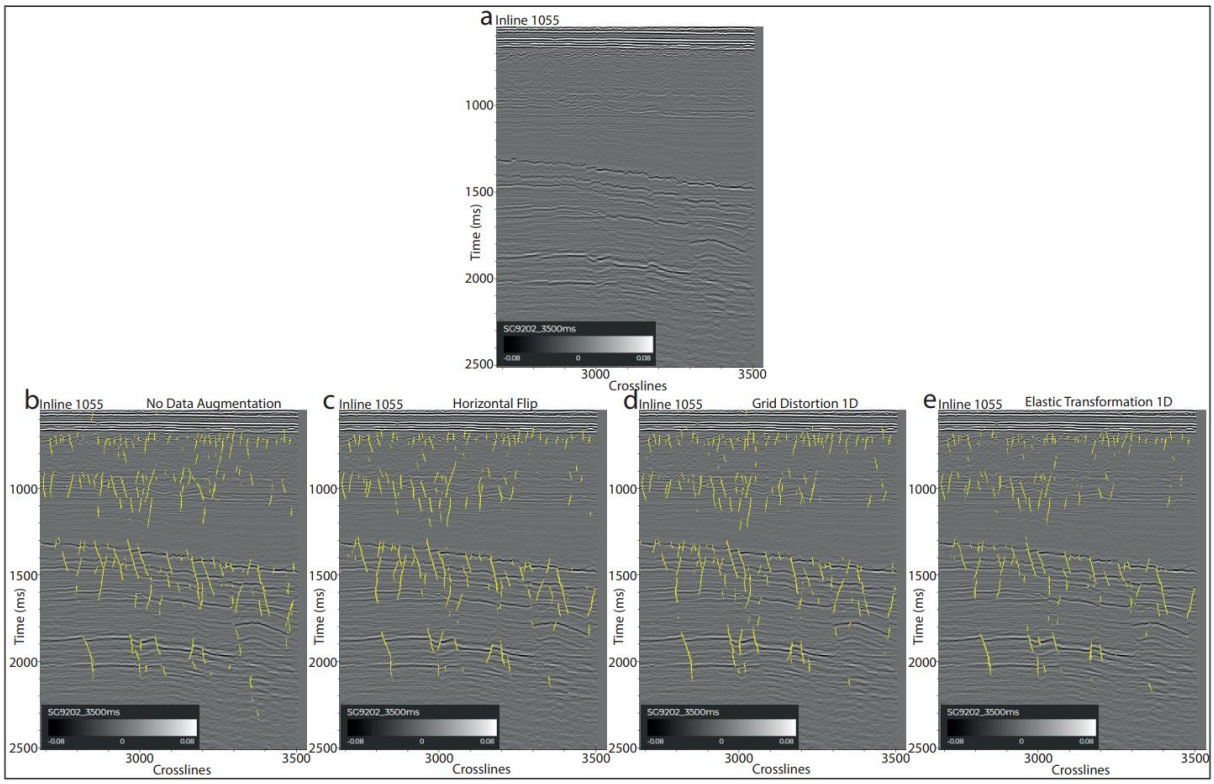

Figure 4-3: Images of Inline 1055 from volume SG9202_Full_Stack in survey SG9202 comparing the performance of Efficient UNET trained and tested on the different types of data augmentation. a) Inline 1055 without fault predictions, b) faults predicted by Efficient UNET (model ID: 4986) trained and tested on both inlines and crosslines without data augmentation c) faults predicted by Efficient UNET (model ID: 4987) trained and tested on both inlines and crosslines with Horizontal Flip, d) faults predicted by Efficient UNET (model ID:4988) trained and tested on both inlines and crosslines with Grid Distortion 1D, e) faults predicted by Efficient UNET (model ID: 4991) trained and tested on both inlines and crosslines with Elastic Transformation 1D.

When blind tests were run to test the Efficient UNET on the seismic volumes, the networks trained and tested on augmented data generally had an improved ability to identify faults over the networks trained and tested on non-augmented data. The improvement was most significant on 3D seismic volume ST14200Z15_Full_Stack. From the comparison so far, the

conclusion is that data augmentation (with some exceptions) leads to better performing Efficient UNET.

4.1.2 The Effect of Patch Size

For Efficient UNET, the default patch size in EarthNet is set to 192 x 192 pixels, which is the patch size used to explore the effect of data augmentation in section 4.1.1. Now the effect of a larger patch size (320 x 320 pixels) on the Efficient UNET performance will be determined. Grid distortion 1D was chosen to be applied to the CNN for further comparisons.

The results from seismic volume ST14200Z15_OBN_Full_Stack (figure 4-4, c) are evaluated in relation to figure 4-4 b where the original patch size (192 x 192 pixels) is used for training and testing. At first glance, in the fault predictions where the larger patch size is utilized for training and testing, overall less faults were detected. In addition, there is less connectivity between faults and less continuity in each individual fault. There are a few exceptions where the larger patch size has contributed to a better detection of some faults.

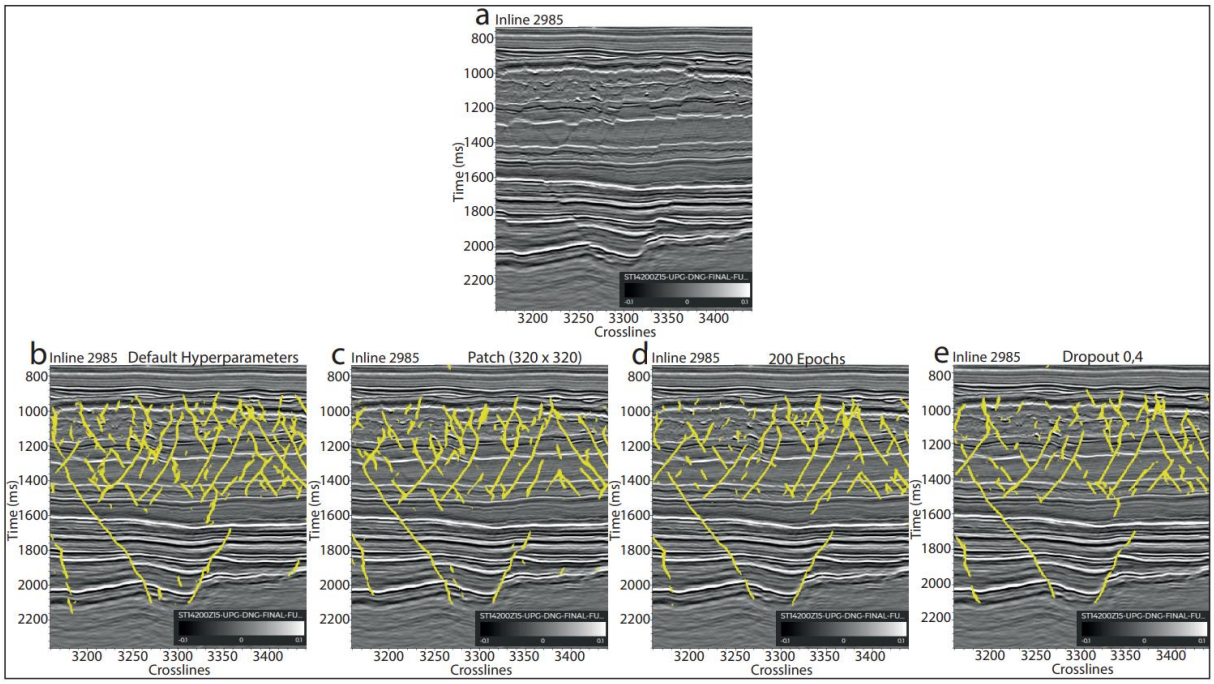

Figure 4-4: Images of Inline 2985 from volume ST14200Z15_OBN_Full_Stack in survey ST14200_OBN comparing the performance of Efficient UNET with grid distortion 1D and different hyperparameters for training and testing. a) Inline 2985 without fault predictions, b) faults predicted by Efficient UNET (model ID: 4751) trained and tested on both inlines and crosslines with grid distortion 1D and default hyperparameters (patch size 192 x 192, 50 training epochs and 0.3 dropout), c) faults predicted by Efficient UNET (model ID: 4754) trained and tested on both inlines and crosslines with grid distortion 1D, patch size 320 x 320, 50 training epochs and 0.3 dropout, d) faults predicted by Efficient UNET (model ID: 4842) trained and tested on both inlines and crosslines with grid distortion 1D, patch size 192 x 192, 200 training epochs and 0.3 dropout, e) faults predicted by Efficient UNET (model ID: 4843) trained and tested on both inlines and crosslines with grid distortion 1D, patch size 192 x 192, 50 training epochs and 0.4 dropout.

When comparing the results from seismic volume ST14200Z15_OBN_Full_Stack to the results form seismic volume LN17001_Full_Stack, the effect of a larger patch size is rather positive. In figure 4-5 c a larger portion of the of the major fault is detected, although the continuity of the fault prediction at depth is not great, it still performs better than the baseline model, with the smaller patch size in figure 4-5 b. In addition, the smaller surrounding faults are more continuous and overall better detected with the larger patch size.

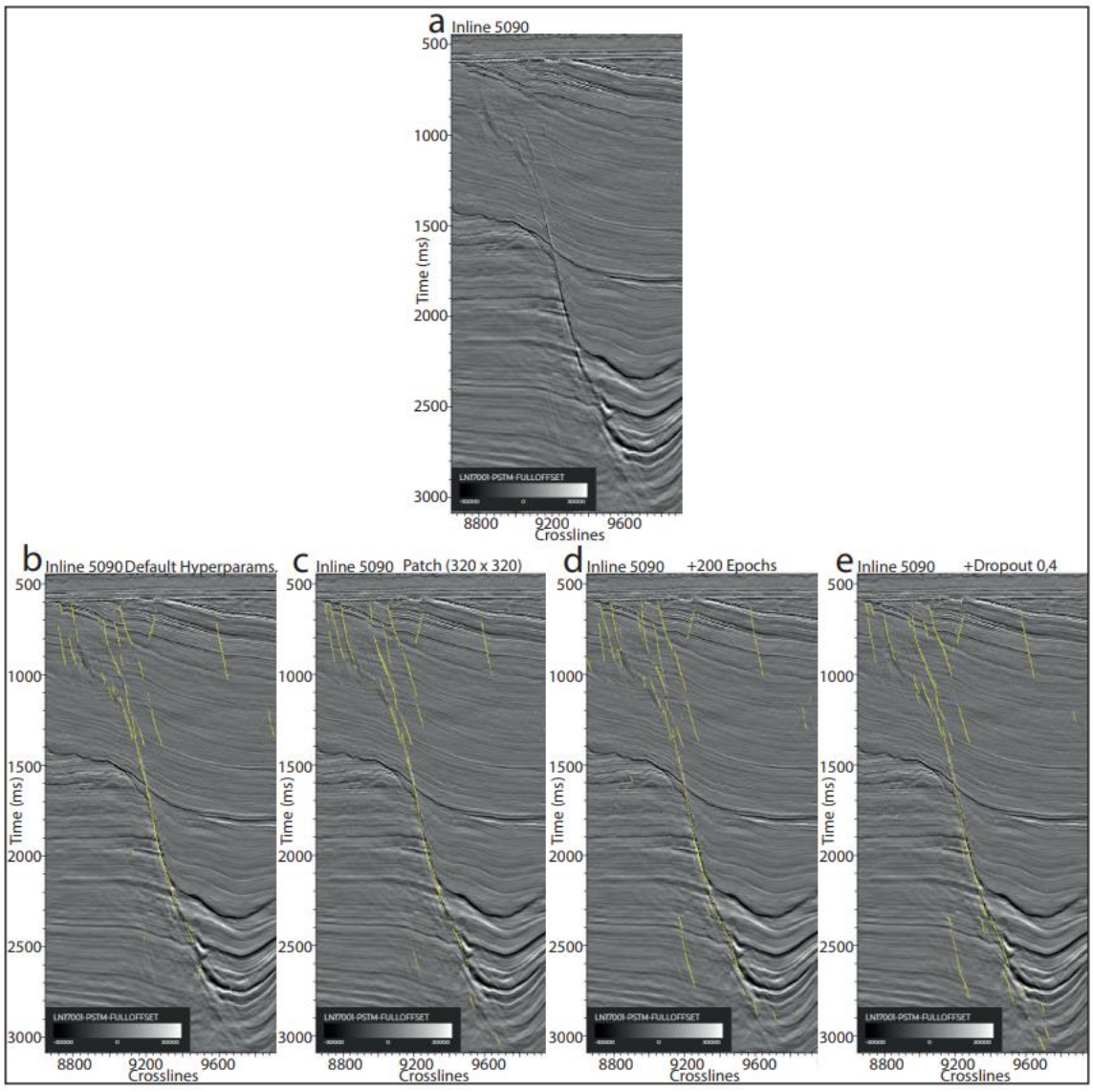

Figure 4-5: Images of Inline 5090 from volume LN17001_Full_Stack in survey LN17001 3D survey comparing the performance of Efficient UNET with grid distortion 1D and different hyperparameters for training and testing. a) Inline 5090 without fault predictions, b) faults predicted by Efficient UNET (model ID: 4755) trained and tested on both inlines and crosslines with grid distortion 1D and default hyperparameters (patch size 192 x 192, 50 training epochs and 0.3 dropout), c) faults predicted by Efficient UNET (model ID: 4756) trained and tested on both inlines and crosslines with grid distortion 1D, patch size 320 x 320, 50 training epochs and 0.3 dropout, d) faults predicted by Efficient UNET (model ID: 4839) trained and tested on both inlines and crosslines with grid distortion 1D, patch size 320 x 320, 200 training epochs and 0.3 dropout, e) faults predicted by Efficient UNET (model ID: 4840) trained and tested on both inlines and crosslines with grid distortion 1D, patch size 320 x 320, 200 training epochs and 0.4 dropout.

In section 4.1.1 when evaluation the performance of the Efficient UNET trained and tested on data augmented seismic for volume SG9202_Full_Stack, there were no clear advantages between horizontal flip and grid distortion 1D. Still, grid distortion 1D is applied in the following sections, as it is applied to the CNN used on the other 3D seismic volumes. The effect of increased patch size during training and testing on the Efficient UNET fault prediction performance is shown in figure 4-6 c. Compared to the Efficient UNET with default hyperparameters (figure 4-6 b) the larger patch size gives better fault interpretations when it comes to detecting faults and making continuous interpretations, although the improvement is not large.

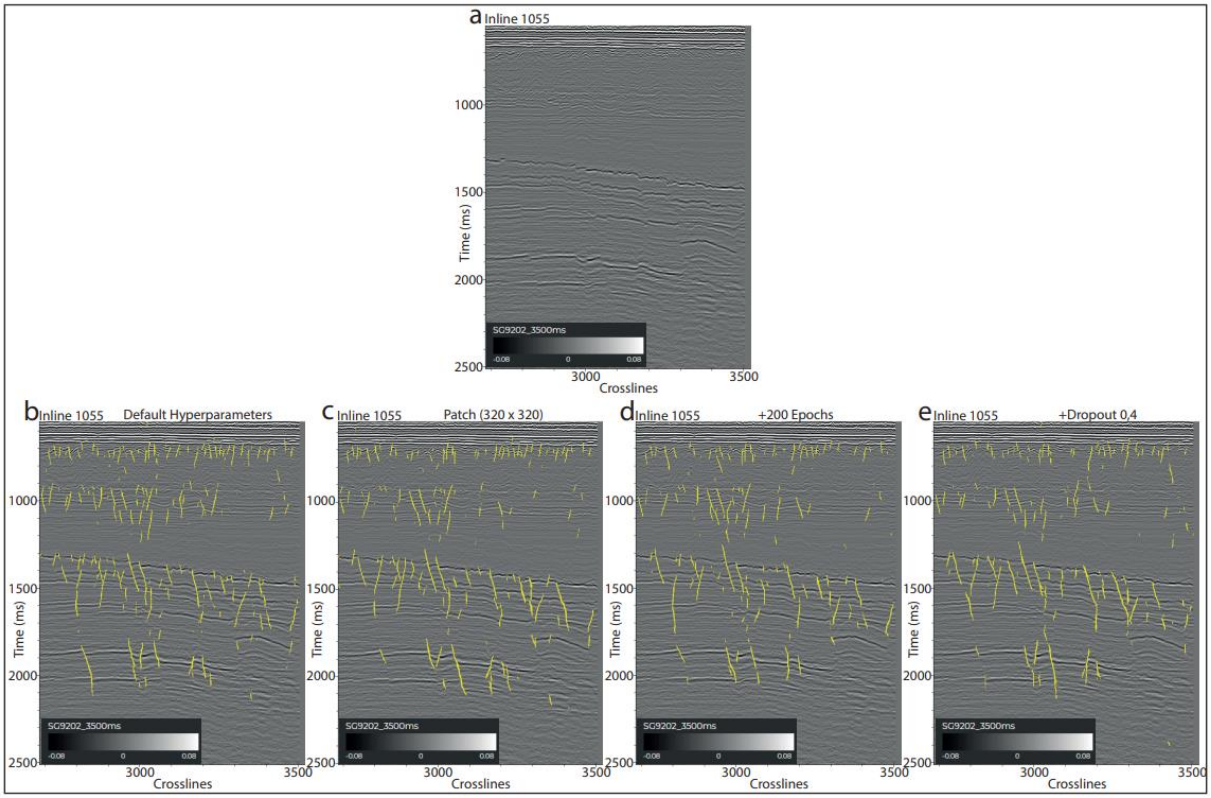

Figure 4-6: Images of Inline 1055 from volume SG9202_Full_Stack in survey SG9202 comparing the performance of Efficient UNET with grid distortion 1D and different hyperparameters for training and testing. a) Inline 1055 without fault predictions, b) faults predicted by Efficient UNET (model ID: 4988) trained and tested on both inlines and crosslines with grid distortion 1D and default hyperparameters (patch size 192 x 192, 50 training epochs and 0.3 dropout), c) faults predicted by Efficient UNET (model ID: 4992) trained and tested on both inlines and crosslines with grid distortion 1D, patch size 320 x 320, 50 training epochs and 0.3 dropout, d) faults predicted by Efficient UNET (model ID: 5115) trained and tested on both inlines and crosslines with grid distortion 1D, patch size 320 x 320, 200 training epochs and 0.3 dropout, e) faults predicted by Efficient UNET (model ID: 5118) trained and tested on both inlines and crosslines with grid distortion 1D, patch size 320 x 320, 200 training epochs and 04 dropout.

4.1.3 Effect of Epochs During Training and Testing

In search for further improvement of the Efficient UNET fault predictions, the effect of increasing the number of training epochs was investigated. In EarthNet the default number of epochs is set to 75, including 50 training epochs and 25 extra epochs. The duration of

training and testing was increased to 200 training epochs and 100 extra epochs, meaning 300 epochs in total.

The result of increasing the training epochs for Efficient UNET in seismic volume ST14200Z15_OBN_Full_Stack is illustrated in figure 4-4 d. Because the larger patch size (320 x 320 pixels) did not improve the Efficient UNET fault prediction, the original patch size was again used in combination with the larger number of epochs. From evaluating the fault prediction in figure 4-4 d it is observed that increasing the duration of training did not have the desired effect. The fault prediction in figure 4-4 d, is worse than the fault predictions in both figure 4-4 b (baseline Efficient UNET) and figure 4-4 c (320 x 320 pixels patch size). Again, what makes the prediction worse is poor detection of faults overall combined with worse continuity of individual faults and worse connectivity between fault predictions.

On the seismic volume LN17001_Full_Stack, the increase of training epochs had a positive effect compared to result of seismic volume ST14200Z15-OBN. The increased number of epochs was applied to the training of the Efficient UNET in addition to the larger patch size, as the larger patch size already had a positive effect on model performance. From figure 4-5 d a further increase in fault prediction performance from figure 4-5 c is observed. On the major fault of this particular section the detection and continuity in the deeper part of the seismic image was increased in figure 4-5 d, compared to figure 4-5 c. In the shallower part of the seismic the prediction in figure 4-5 c has some slightly more continuous prediction than figure 4-5 d, but the degree of detection is similar. Figure 4-5 d shows more detection of faults and a more continuous prediction for fault segments than figure 4-5 c on the smaller surrounding faults.

The application of the larger patch size also had a positive effect on the fault predicting performance on the Efficient UNET trained and tested on 3D seismic volume SG9202_Full_Stack, thus the increased number of epochs was applied in addition to the increased patch size (figure 4-6 d). When comparing figure 4-6 c to figure 4-6 d, there is one reoccurring observation which is similar to the comparison of figure 4-3 c and figure 4-3 d: there are some slight changes in the fault predictions with regards to continuity and detection, but overall it is difficult to determine a performance increase.

4.1.4 Effect of Dropout

The last hyperparameter of which the effect was explored is dropout. The objective was to determine whether the default dropout (0.3) or a slightly higher dropout (0.4) would give the better fault prediction.

Previously none of the hyperparameter adjustments had any positive effect on fault predictions of Efficient UNET on seismic volume ST14200Z15-OBN. Therefor the effect of a higher dropout value was explored while keeping the other hyperparameter values default. From observing figure 4-4 e (dropout 0.4) and comparing it to figure 4-4 b (default parameters) we see that dropout 0.4 in similarity to the other adjusted hyperparameters had a negative effect on the fault predictions.

For seismic volume LN17001_Full_Stack the higher dropout value was added to the Efficient UNET together with a patch size of 320 x 320 pixels and 200 training epochs, which already had shown a positive effect. The fault prediction of the Efficient UNET with a dropout of 0.4 is shown in figure 4-5 e. At first, the fault predictions in figure 4-5 d and figure 4-5 e look quite similar, but with some minor differences. In figure 4-5 e, the prediction of the main fault is similar to figure 4-5 d at larger depths, but with some differences at shallower parts. In figure 4-5 e a somewhat better continuity is observed. Both Efficient UNET have areas in the section where they perform better than the other, which in total is close to equalizing the UNET, but with the prediction of the model in figure 4-5 d being marginally more satisfactory.

The effect dropout 0.4 has on 3D seismic volume SG9202_Full_Stack in addition to 320 x 320 pixels patch size and 200 epochs is illustrated in figure 4-6 e. Faults from 1300ms TWT and downwards are similarly predicted when comparing figure 4-6 d to figure 4-6 e. The difference in the predictions prominently lies in the seismic above 1300ms TWT, where the Efficient UNET in figure 4-6 d both has better detection and continuity in its predictions than the Efficient UNET in figure 4-6 e.

In summary the adjustment of the hyperparameters presented in section 4.1.2 to 4.1.4 gave mixed results. In 3D seismic volume ST14200Z15_Full_Stack default hyperparameters remain superior. In contrast the adjustment of all hyperparameters (except dropout) increased the Efficient UNET performance on fault prediction on 3D seismic full stack LN17001. The conclusion for volume SG9202_Full_Stack is similar to LN17001_Full_Stack, only that the improvement is far less noticeable.

4.1.5 Effect of Training and Testing CNN on Inlines and Crosslines Individually

In the previous sections of this study all Efficient UNET were trained and tested on both inlines and crosslines in their respective seismic volumes. In addition, we attempted to train and test Efficient UNET individually on inlines or crosslines. The results of the fault predictions were compared to results from Efficient UNET that were trained and tested on both inlines and crosslines, but otherwise are identical (augmentation and hyperparameters).

The results were compared on both seismic inlines and crosslines in the respective surveys. In order to make the description of the results easier to follow, I refer to inline trained and tested, crossline trained and tested, and inline and crossline trained and tested as IL, XL, and IL/XL, respectively.

Based on the conclusion from section 4.1.4, the Efficient UNET from figure 4-4 b) is used as a base for further comparison. Comparing the performance of IL (figure 4-7 c) and XL (figure 4-7 d) Efficient UNET to a IL/XL Efficient UNET (figure 4-7 b) on inlines in seismic volume ST14200Z15-OBN_Full_Stack. It is noticeable that the IL/XL Efficient UNET is performing slightly better than the IL Efficient UNET, in terms of fault detection, fault continuity and linkage. The XL Efficient UNET is performing far worse than the two other Efficient UNET.

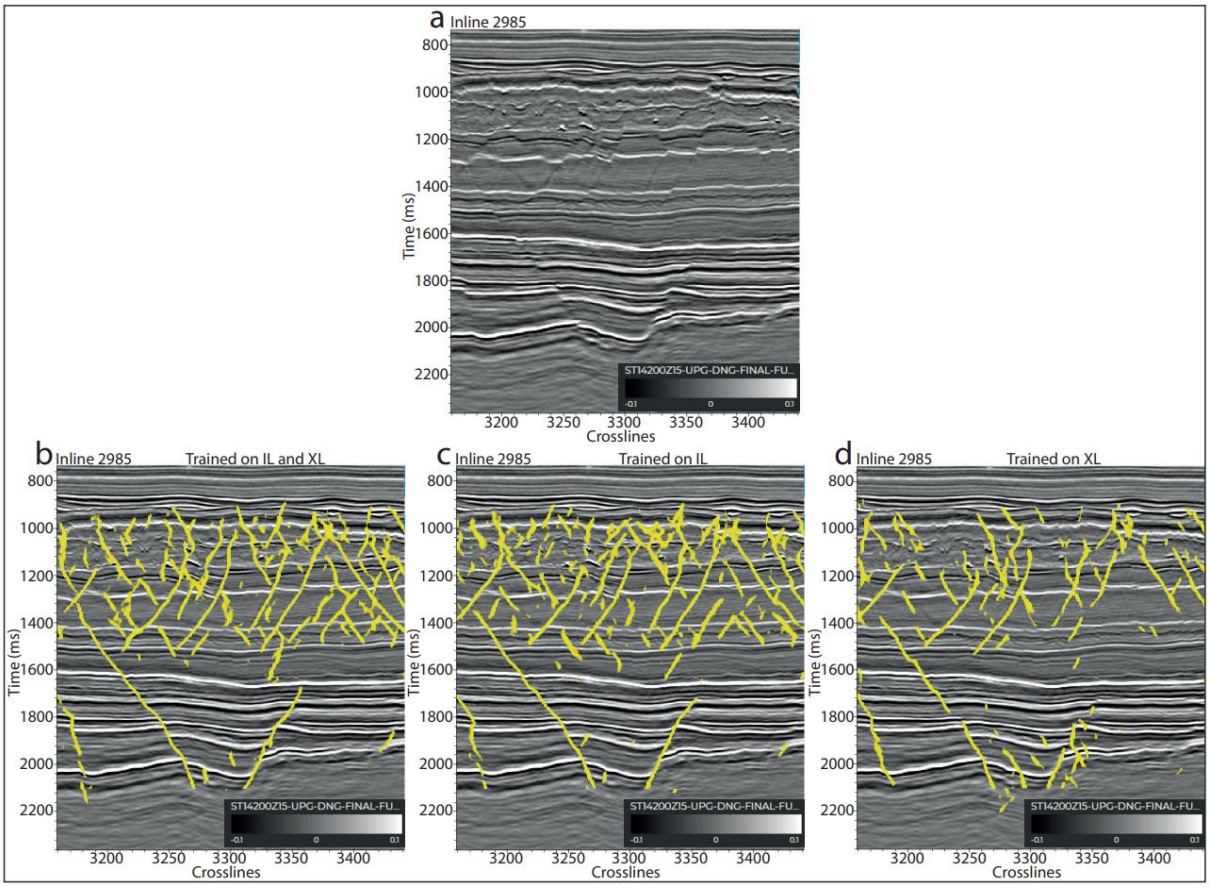

Figure 4-7: Images of Inline 2985 from volume ST14200Z15_OBN_Full_Stack in survey ST14200_OBN comparing the performance of Efficient UNET b) trained and tested on both Inlines (IL) and Crosslines (XL) (model ID: 4751), c) trained and tested only on IL (model ID: 4797) and d) trained and tested only on XL (model ID: 4798). Otherwise, the Efficient UNET have grid distortion 1D applied and the same hyperparameters are used for training and testing (Patch size: 192 x 192, Training Epochs: 50 and Dropout: 0.3).

Completing the same comparison on crosslines in seismic volume ST14200Z15-OBN, it is observed that the IL Efficient UNET (figure 4-8 c) is outperforming both the IL/XL Efficient UNET (figure 4-8 b) and the XL Efficient UNET (figure 4-8 d), in terms of fault detection, fault

continuity and linkage. The largest difference between figure 4-8 b and figure 4-8 c is seen in the less pronounced faults. Even tough fault predictions are performed on crosslines, the XL Efficient UNET is being outperformed.

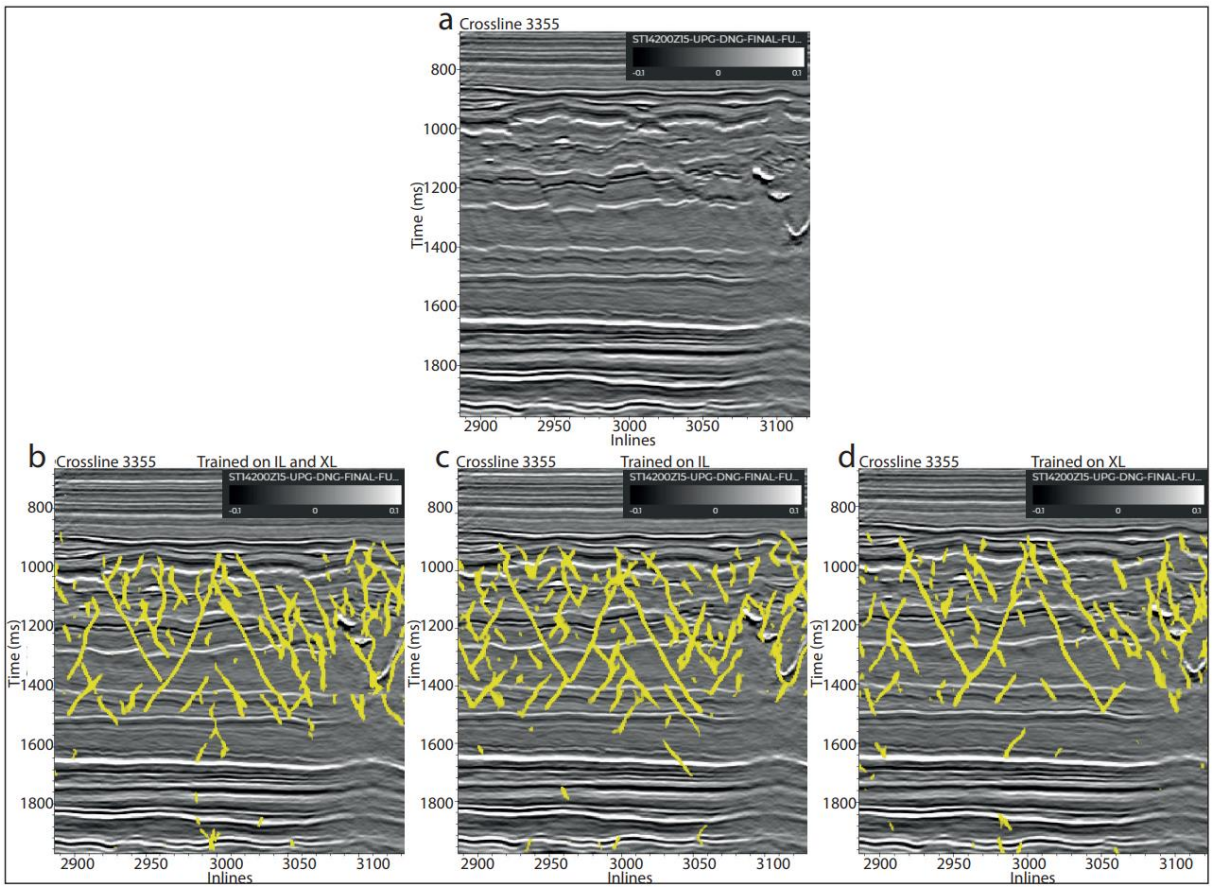

Figure 4-8: Images of Crossline 3355 from volume ST14200Z15_OBN_Full_Stack in survey ST14200_OBN comparing the performance of a Efficient UNET b) trained and tested on both Inlines (IL) and Crosslines (XL) (model ID: 4751), c) trained and tested only on IL (model ID: 4797) and d) trained and tested only on XL (model ID: 4798). Otherwise, the Efficient UNET have grid distortion 1D applied and the same hyperparameters are used for training and testing (Patch size: 192 x 192, Training Epochs: 50 and Dropout: 0.3).

The comparison of fault predictions on seismic inlines in seismic volume LN17001_Full_Stack (figure 4-9) reveals that the IL/XL Efficient UNET (figure 4-9 b) has the best performance. There is no signifficant difference between the IL/XL Efficient UNET and the IL Efficient UNET (figure 4-9 c) fault predictions within the main fault, but the IL/XL Efficient UNET has better detection and more continuous predictions of the smaller surrounding faults. The XL Efficient UNET (figure 4-9 d) in similarity to seismic volume ST14200Z15_OBN_Full_Stack has the worst performance, both in sense of prediction of the main and surrounding faults.

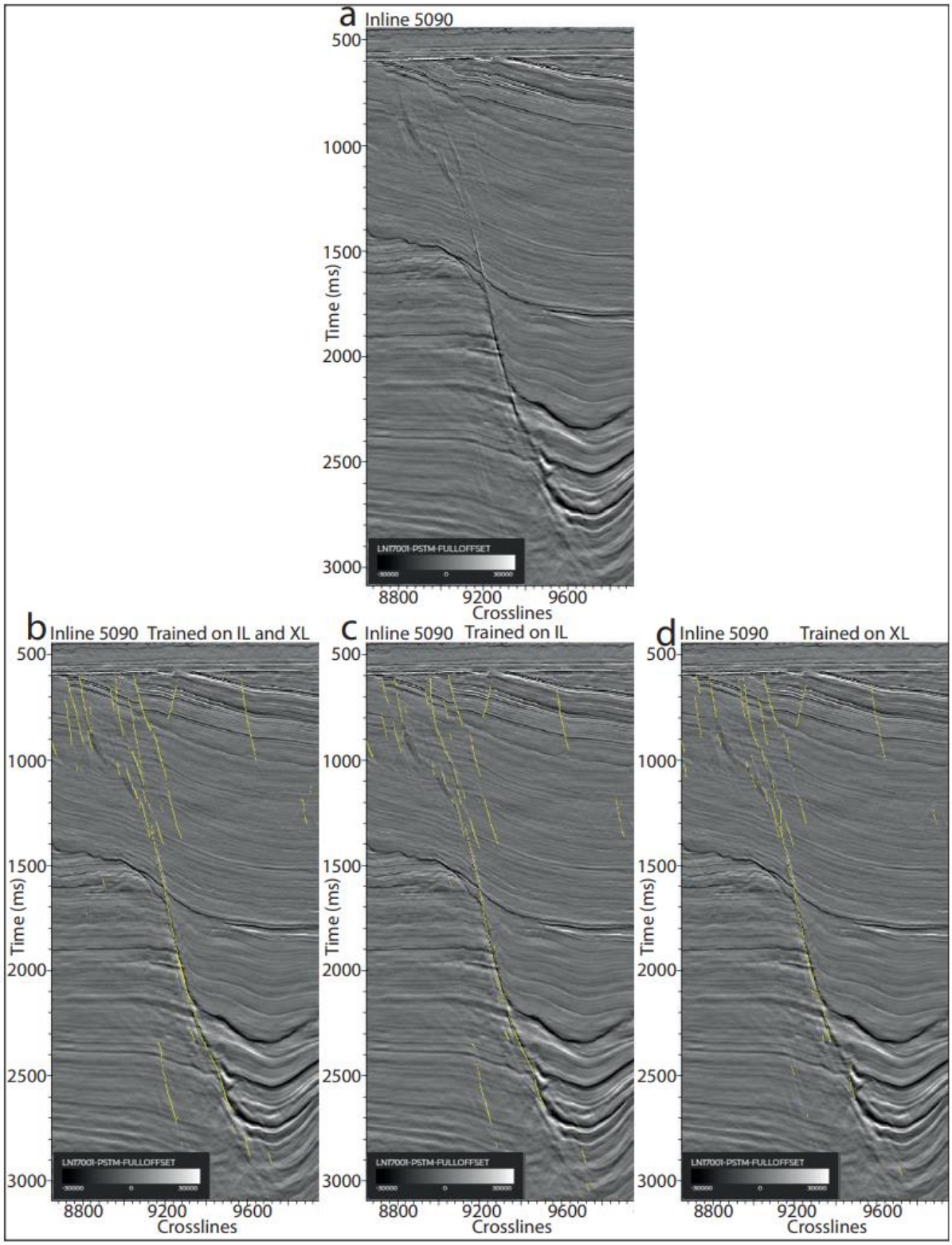

Figure 4-9: Images of Inline 5090 from volume LN17001_Full_Stack in survey LN17001 3D survey comparing the performance of a Efficient UNET b) trained and tested on both Inlines (IL) and Crosslines (XL) (model ID: 4852), c) trained and tested only on IL (model ID: 4877) and d) trained and tested only on XL (model ID: 4878). Otherwise, the Efficient UNET have grid distortion 1D applied and the same hyperparameters are used for training and testing (Patch size: 320 x 320, Training Epochs: 200 and Dropout: 0.3).

In figure 4-10 the same comparison as in figure 4-9 is illustrated, only for seismic crosslines in seismic volume LN17001_Full_Stack instead of inlines. Again, when comparing between

the IL/XL Efficient UNET (figure 4-10 b) and the IL Efficient UNET (figure 4-10 c), there are a lot of similarities in the fault predictions. But overall, the IL Efficient UNET detects greater portions of the larger faults while simultaneously having larger continuous fault segments. Otherwise, the two Efficient UNET have a similar coverage of smaller faults and fault segments. Similar to the other comparisons, the XL Efficient UNET (figure 4-10 d) has the worst performance.

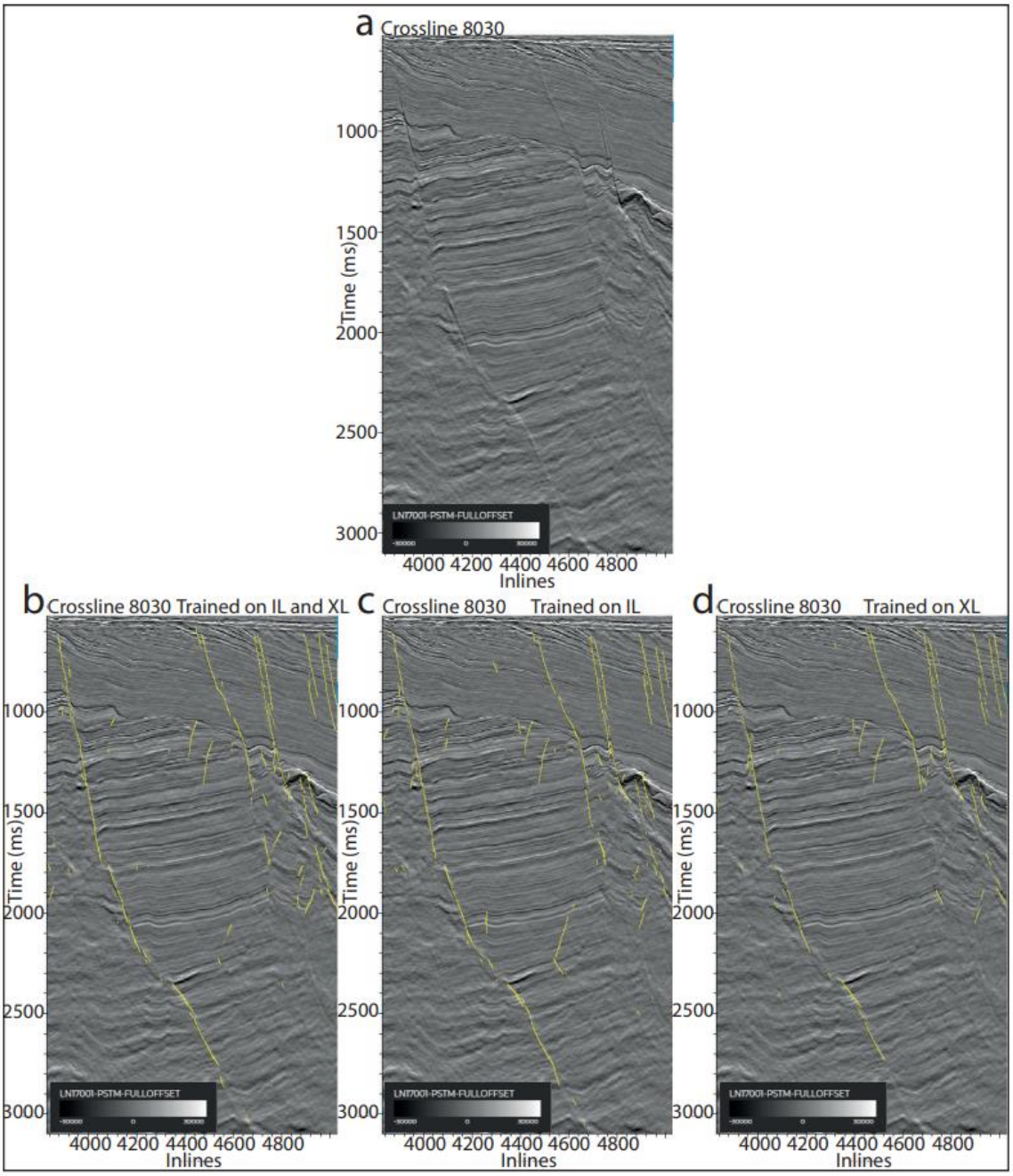

Figure 4-10: Images of Crossline 8030 from volume LN17001_Full_Stack in survey LN17001 3D survey comparing the performance of a Efficient UNET b) trained and tested on both Inlines (IL) and Crosslines (XL) (model ID: 4852), c) trained and tested only on IL (model ID: 4877) and d) trained and tested only on XL (model ID: 4878). Otherwise, the Efficient UNET have grid distortion 1D applied and the same hyperparameters are used for training and testing (Patch size: 320 x 320, Training Epochs: 200 and Dropout: 0.3).

At last, we compare IL/XL Efficient UNET to IL Efficient UNET and XL Efficient UNET fault predictions on 3D seismic volume SG9202_Full_Stack. The IL/XL Efficient UNET in figure 4-11 b is compared to IL Efficient UNET (figure 4-11 c) and XL Efficient UNET (figure 4-11 d). First, the comparison is performed on inlines in the seismic volume where increasingly worse fault predictions are observed figure 4-11 b-d.

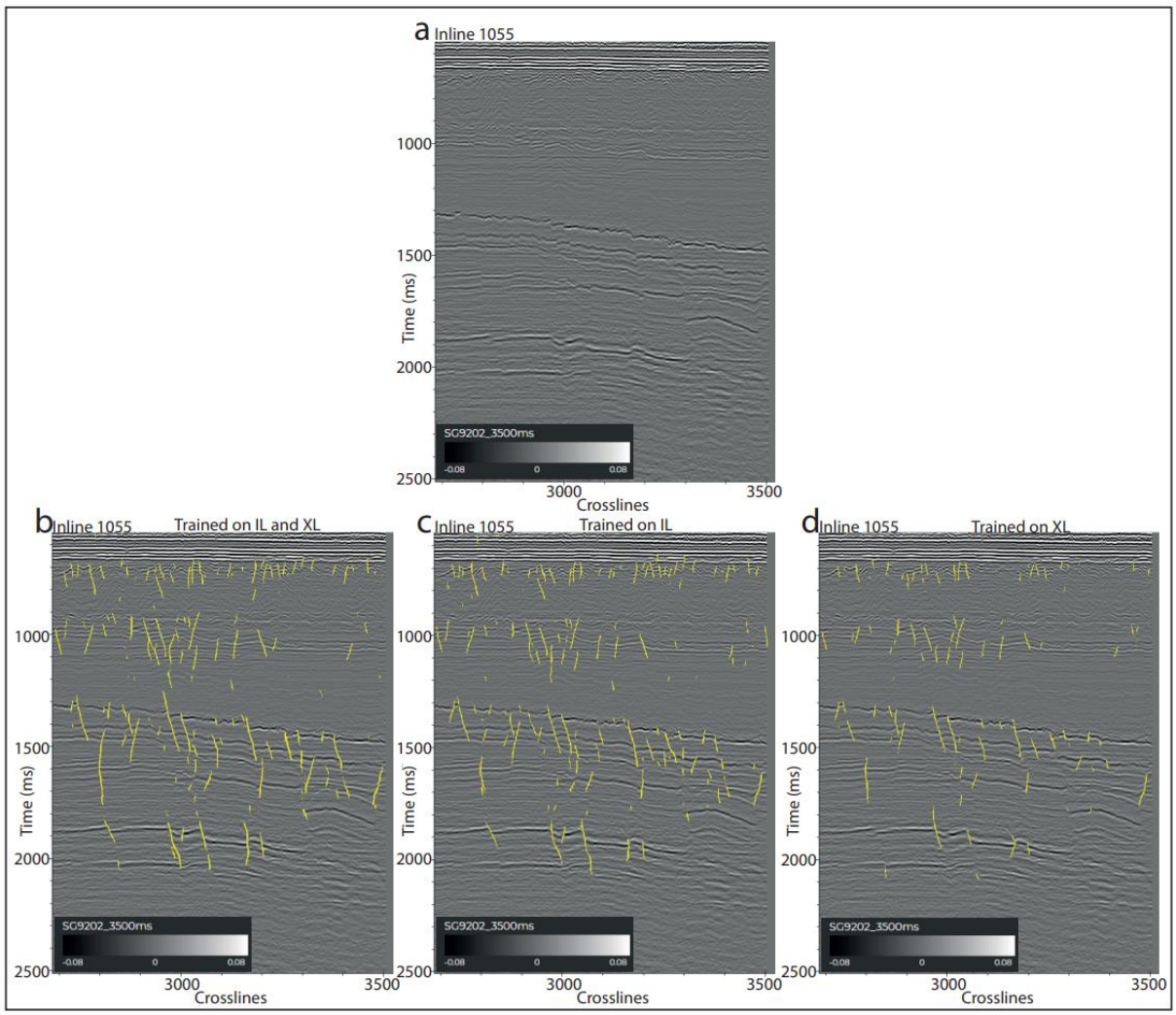

Figure 4-11: Images of Inline 1055 from volume SG9202_Full_Stack in survey SG9202 comparing the performance of a Efficient UNET b) trained and tested on both Inlines (IL) and Crosslines (XL) (model ID: 5115), c) trained and tested only on IL (model ID: 5121) and d) trained and tested only on XL (model ID: 5122). Otherwise, the Efficient UNET have grid distortion 1D applied and the same hyperparameters are used for training and testing (Patch size: 320 x 320, Training Epochs: 200 and Dropout: 0.3).

In figure 4-12 the exact same Efficient UNET are compared as in figure 4-11, only on crosslines instead. Similar, to figure 4-11 the IL/XL Efficinent UNET (figure 4-12 b) is outperforming the the two others (figure 4-12 c and figure 4-12 d). Additionally, it should be said that none of the models preform well on this seismic section, as very few of the faults are identified. Especially, the large fault pentrating almost the entire seismic section is poorly captured.

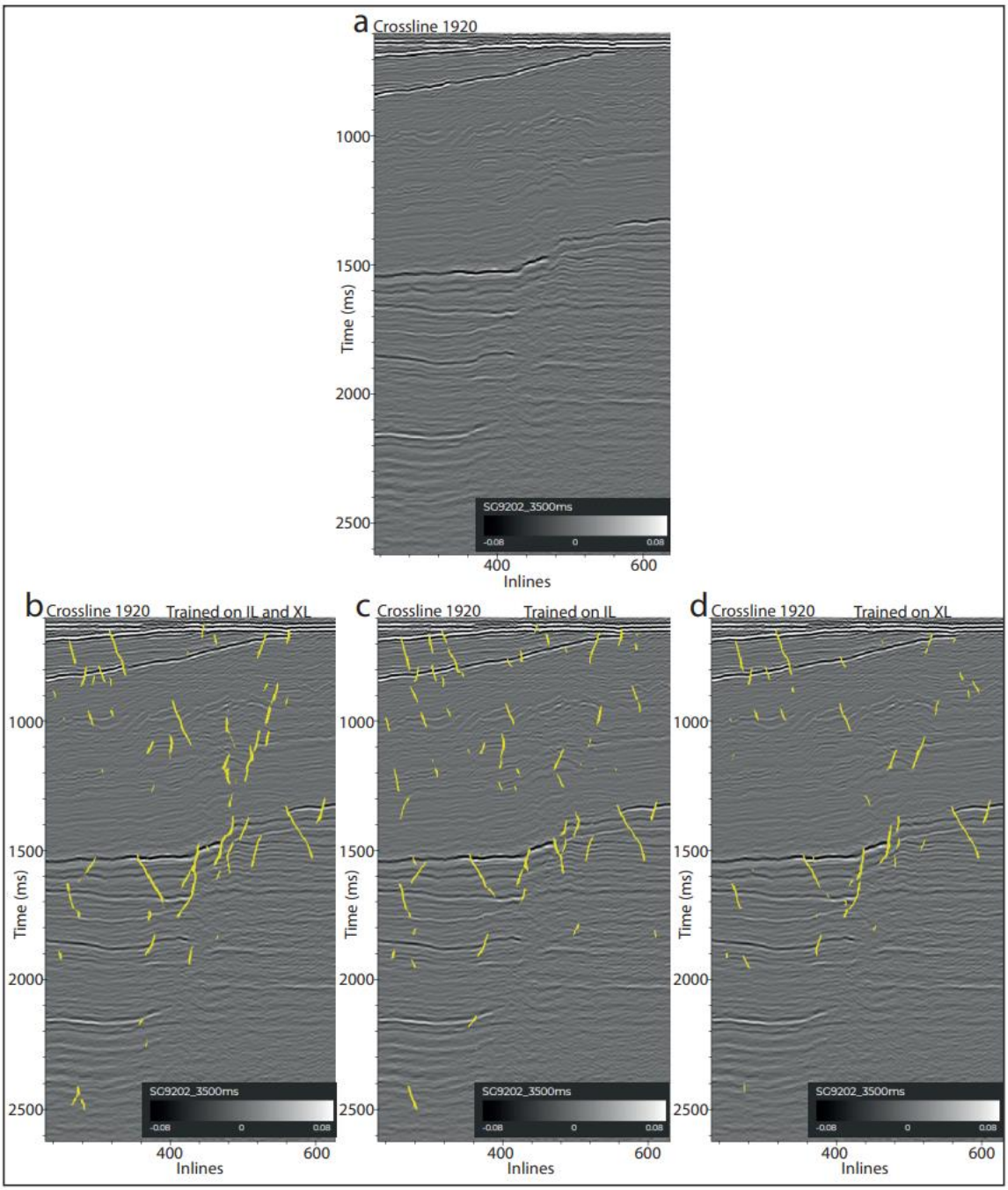

Figure 4-12: Images of Crossline 1920 from volume SG9202_Full_Stack in survey SG9202 comparing the performance of a Efficient UNET b) trained and tested on both Inlines (IL) and Crosslines (XL) (model ID: 5115), c) trained and tested only on IL (model ID: 5121) and d) trained and tested only on XL (model ID: 5122). Otherwise, the Efficient UNET have grid distortion 1D applied and the same hyperparameters are used for training and testing (Patch size: 320 x 320, Training Epochs: 200 and Dropout: 0.3).

4.1.6 Comparison between Efficient UNET and Light UNET

Previously, the effect of different data augmentations and change of hyperparameter values was explored for Efficient UNET, but what happens if the same modifications are applied to Light UNET. To compare the performance of the two CNN model architectures, best performing data augmentation paired with the best combination of hyperparameter values for the Efficient UNET was applied to Light UNET.

For volume ST14200Z15-OBN none of the hyperparameter adjustments improved the performance of the default hyperparameters, therefore the same setup was applied to the Light UNET. The comparison of the two CNN architectures is visualized in figure 4-13. Both CNN have overall managed to detect most faults in the seismic section. Although the Efficient UNET (figure 4-13 b) has a higher detection ratio and is able to detect less pronounced fault segments. The continuity of fault predictions and connectivity of fault predictions is also better with the Efficient UNET, resulting in longer, connected fault segments compared to the Light UNET (figure 4-13 c).

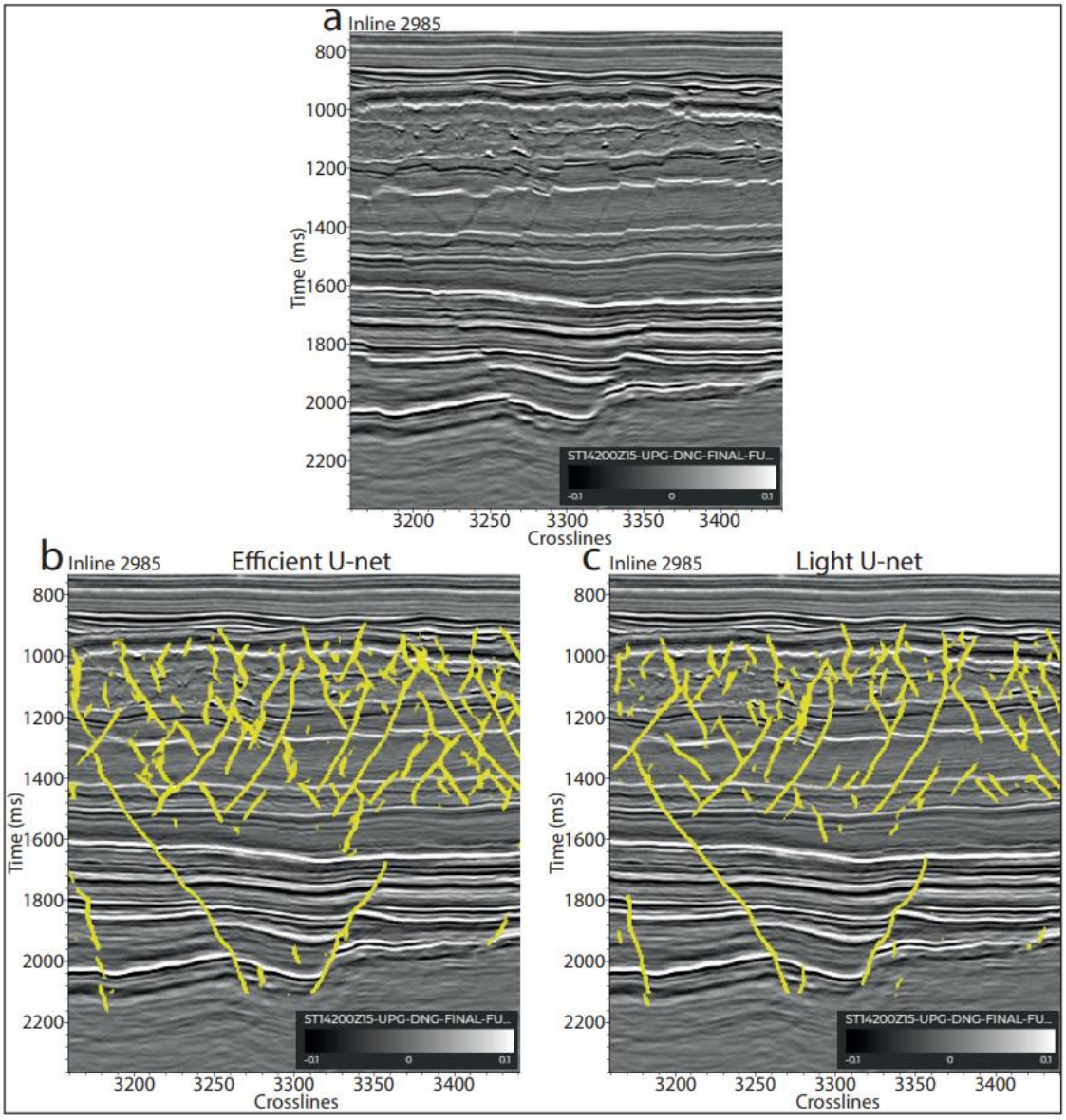

Figure 4-13: Images of Inline 2985 from volume ST14200Z15_OBN_Full_Stack in survey ST14200_OBN comparing the performance of a Efficient UNET with the performance of a Light UNET. Both models have grid distortion 1D applied and the same hyperparameters are used for training and testing (Patch size: 192 x 192, Training Epochs: 50 and Dropout: 0.3). a) Seismic without any interpretation, b) faults predicted by a Efficient UNET (model ID: 4751) and c) faults predicted by a Light UNET (model ID: 4829).

In the comparison of Efficient UNET and Light UNET on seismic volume LN17001_Full_Stack, grid distortion 1D in combination with patch size 320 x 320 pixels, 200 training epochs and dropout 0.3 was used. This combination of data augmentation and hyperparameter values resulted in the best fault predictions for the Efficient UNET. In figure 4-14, the comparison between the Efficient and Light UNET is shown for seismic volume LN17001_Full_Stack. The Light UNET in figure 4-14 c further exceeds the performance of the Efficient UNET in figure 4-14 b, which is identified by more coverage of the faults and larger interpreted and connected fault segments in general.

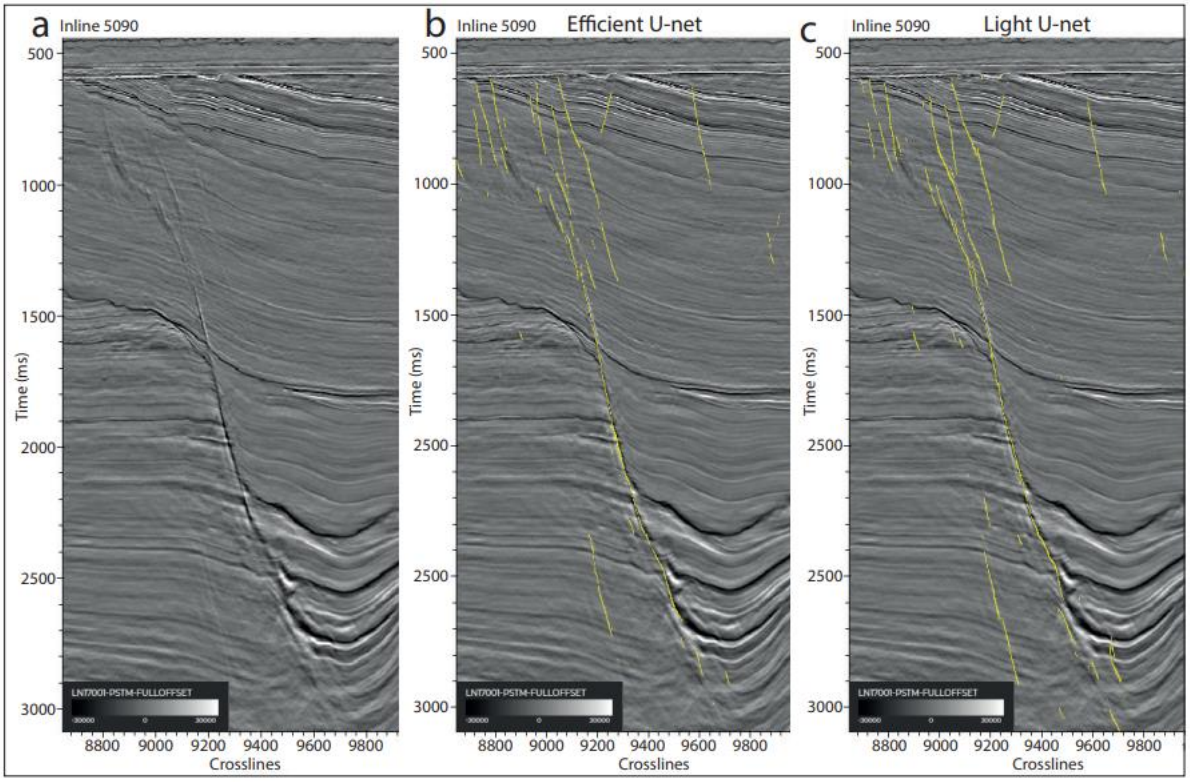

Figure 4-14: Images of Inline 5090 from volume LN17001_Full_Stack in survey LN17001 3D survey comparing the performance of a Efficient UNET with the performance of a Light UNET. Both models have grid distortion 1D applied and the same hyperparameters are used for training and testing (Patch size: 320 x 320, Training Epochs: 200 and Dropout: 0.3). a) Seismic without any interpretation, b) faults predicted by a Efficient UNET (model ID: 4839) and c) faults predicted by a Light UNET (model ID: 4852).

The performance of the best performing Efficient UNET (figure 4-15 b) on 3D seismic volume SG9202_Full_Stack (grid distortion 1D, 320 x 320 patch size, 200 epochs, 0.3 dropout) was compared to a Light UNET (figure 4-15 c) with identical parameters as the Efficient UNET. In contrast to volume LN17001_Full_Stack and in similarity to volume ST14200Z15_OBN, in this case the Efficient UNET is performing better than the Light UNET. The Efficient UNET in general predicts a significantly larger portion of the faults visible in seismic. It also manages to connect the predicted faults segments better, leading to more continuous predictions.

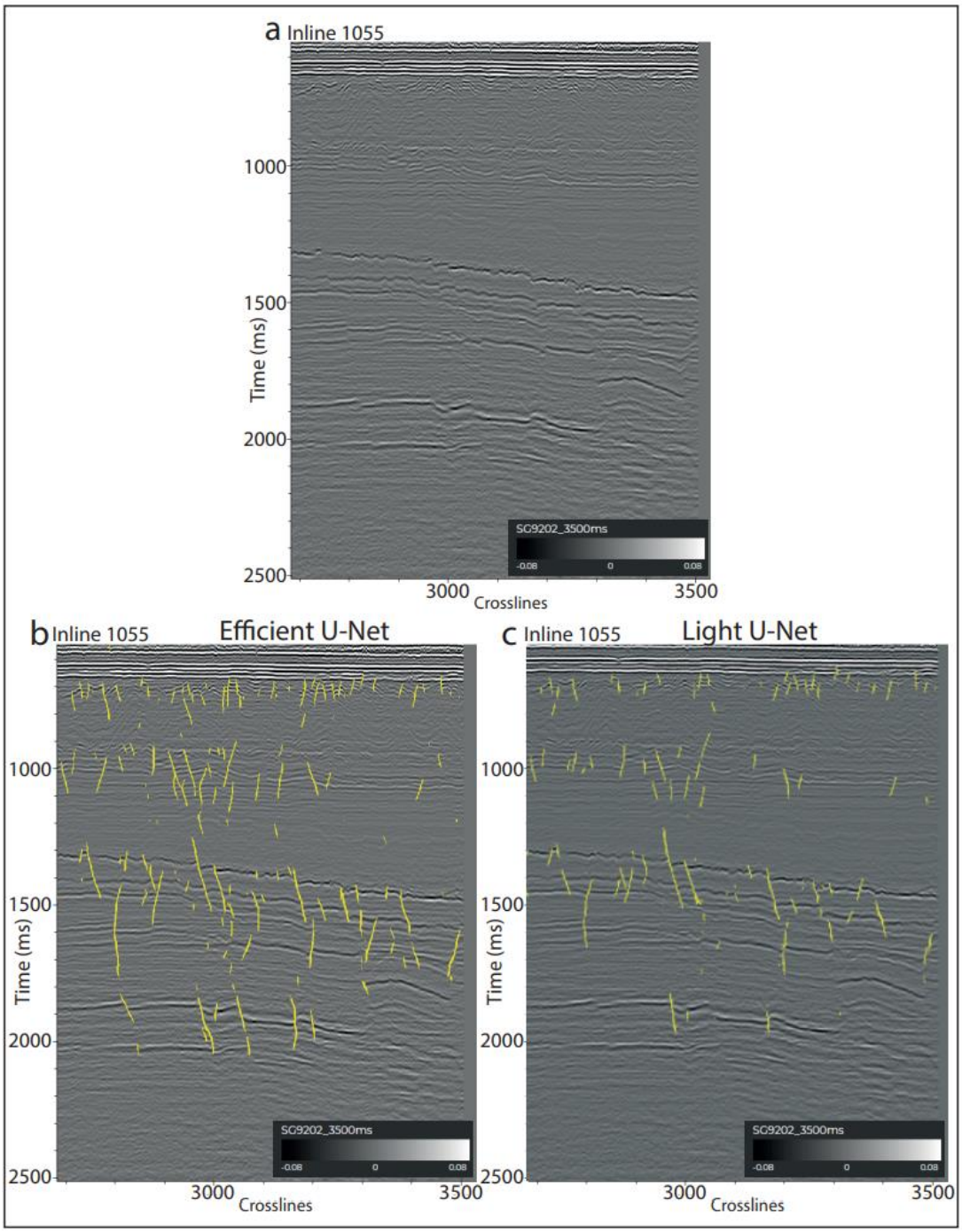

Figure 4-15: Images of Inline 1055 from volume SG9202_Full_Stack in survey SG9202 comparing the performance of a Efficient UNET with the performance of a Light UNET. Both models have grid distortion 1D applied and the same hyperparameters are used for training and testing (Patch size: 320 x 320, Training Epochs: 200 and Dropout: 0.3). a) Seismic without any interpretation, b) faults predicted by a Efficient UNET (model ID: 5115) and c) faults predicted by a Light UNET (model ID: 5120).

4.1.7 Model scores

An important part of evaluating the performance of the CNN presented in sections 4.1.1 – 4.1.6, besides visual evaluation and geological sense check of the predictions, is to monitor and observe the models statistical results or scores. The models are evaluated in form of

various metrics/validation metrics, confusion matrix/validation confusion metrics and overall train/test scores. In this section all scores of the several CNN are presented in table 4-1 and 4-2. Table 4-1 gives an overview of some technical information which for the most part already was presented in the result sections above, such as the model type, hyperparameters, training/testing on IL/XL, IL or XL and data augmentation technique applied. In addition, validation confusion matrix scores and overall model train/test scores are presented. Table 4-2 is a complimentary table to Table 4-1 where additional scores from training/testing are included.

The CNN with model ID 4751, 4852 and 5115 were by visual evaluation determined to the best performing models on 3D seismic volumes ST14200Z15-OBN, LN17001_Full_Stack and SG9202_Full_Stack, respectively. This decision was based on a combination of factors, such as the portion of detected faults, continuity of fault predictions and linkage between different faults. In contrast, the model scores do not consider the CNN performance with the same complexity, they purely consider with pixels were correctly or wrongly segmented as either faults or background. With that in mind, the statistical model scores are given below for each survey.

4.1.7.1 Model Scores: ST14200Z15-OBN

There is a general observation regarding CNN trained and tested on 3D seismic volume ST14200Z15-OBN: the one model where no data augmentation was applied (model ID 4749), received the best train and test scores (table 4-1 and 4-2), whilst models applying data augmentation received significantly lower scores. These results provide a contrast to the results from section 4.1.1 where all models with data augmentation applied, clearly outperform model 4749. Model 4751, which visually had the best fault prediction performance, received fairly good train/test scores, although model 4749 achieved significantly better scores.

4.1.7.2 Model Scores: LN17001_Full_Stack

The scores from table 4-1 and 4-2 regarding the CNN fault predictions on 3D seismic volume LN17001_Full_Stack, similar to the scores from volume ST14200Z15_OBN_Full_Stack do not always match the observations made in sections 4.1.1 – 4.1.6. One example is figure 4-2 where an Efficient UNET (ID 4750) without data augmentation applied, was compared to models with three different data augmentation techniques applied (models 4772, 4755 and 4773). From the visual comparison and geological sense check, the fault predictions performed by the Efficient UNET with data augmentation applied, generally outperformed the model which did not apply data augmentation. This observation is not confirmed by the scores in table 4-1 and 4-2, as the overall train/test scores are similar and the percentage of

correctly interpreted faults (TF) is significantly lower for the models utilizing data augmentation. When hyperparameters were changed, the CNN scores improved. Model 4839, which in addition to grid distortion 1D was trained and tested on 320 x 320 patch size and 200 epochs, achieved higher scores, which also is reflected by the seismic image in figure 4-5. Another observation is that models trained and tested on only inlines or crosslines (models 4877 and 4878) receive greater scores than for instance model 4839, despite similar or worse performance on seismic, as captured in figure 4-9 and 4-10. If model 4877 and 4878 are ignored, model 4852 receives the best score, which is slightly better than model 4839, which corresponds to the results from figure 4-14 in the geological sense check.

4.1.7.3 Model Scores: SG9202_Full_Stack

The model scores achieved by CNN trained and tested on 3D seismic volume SG9202_Full_Stack (figure 4-2 and 4-3), in contrast to the CNN trained and tested on the other 3D seismic volumes, correspond fairly well to visual observations made in seismic. Model 4986, where data augmentation was not utilized has a lower score than model 4987, 4988 and 4991 were different techniques of data augmentation was applied. The model scores overall (with one exception), increase and decrease according to how the CNN performance was evaluated in sections 4.1.1 – 4.1.6. One exception in the correlation between the statistical model scores and the visually observed fault prediction performance is found with models 5121 and 5122. These two models are trained and tested only on either inlines or crosslines, which in similarity to the models from volume LN17001_Full_Stack, led to similar or higher performance ratings than some other, better performing models such as model 5115.

Table 4-1: Overview of CNN presented in the results, including the model ID, model type (architecture), central parameters that were changed, validation scores and model scores. TF = True Fault, TB = True Background, FF = False Fault, FB = False Background, Val=Validation.

								Val. Confusion Matrix				Overall Scores	
Model ID	Volume	Model Type	Patch Size	Epochs	Dropout	Line Selection IL/XL	Augmentation	TF (%)	TB (%)	FF (%)	FB (%)	Train Score	Test Score
4749	ST14200	Efficient U-Net	192, 192	50	0,3	IL/XL	None	95,7	98,7	1,3	4,3	0,986	0,986
4757	ST14200	Efficient U-Net	192, 192	50	0,3	IL/XL	Flip	65,2	97,2	2,8	34,8	0,979	0,979
4751	ST14200	Efficient U-Net	192, 192	50	0,3	IL/XL	Grid Distortion 1D	74,9	96,4	3,6	25,1	0,980	0,980
4758	ST14200	Efficient U-Net	192, 192	50	0,3	IL/XL	Elastic Transform 1D	71,5	96,8	3,2	28,5	0,980	0,980
4754	ST14200	Efficient U-Net	320, 320	50	0,3	IL/XL	Grid Distortion 1D	69,9	98,0	2,0	30,1	0,975	0,974
4842	ST14200	Efficient U-Net	192, 192	200	0,3	IL/XL	Grid Distortion 1D	75,9	98,0	2,0	24,1	0,980	0,980
4843	ST14200	Efficient U-Net	192, 192	200	0,4	IL/XL	Grid Distortion 1D	78,2	97,8	2,2	21,8	0,981	0,981
4797	ST14200	Efficient U-Net	192, 192	50	0,3	IL	Grid Distortion 1D	56,3	95,9	4,1	43,7	0,967	0,967
4798	ST14200	Efficient U-Net	192, 192	50	0,3	XL	Grid Distortion 1D	58,6	96,2	3,8	41,4	0,976	0,976
4829	ST14200	Light U-Net	192, 192	50	0,3	IL/XL	Grid Distortion 1D	53,8	97,8	2,2	46,2	0,968	0,968
4750	LN17001	Efficient U-Net	192, 192	50	0,3	IL/XL	None	64,5	99,3	0,7	35,5	0,989	0,989
4772	LN17001	Efficient U-Net	192, 192	50	0,3	IL/XL	Flip	27,0	99,3	0,7	73,0	0,989	0,989
4755	LN17001	Efficient U-Net	192, 192	50	0,3	IL/XL	Grid Distortion 1D	28,4	99,3	0,7	71,6	0,989	0,989
4773	LN17001	Efficient U-Net	192, 192	50	0,3	IL/XL	Elastic Transform 1D	23,1	99,4	0,6	76,9	0,988	0,988
4756	LN17001	Efficient U-Net	320, 320	50	0,3	IL/XL	Grid Distortion 1D	31,9	99,5	0,5	68,1	0,992	0,992
4839	LN17001	Efficient U-Net	320, 320	200	0,3	IL/XL	Grid Distortion 1D	68,9	99,2	0,8	31,1	0,994	0,994
4840	LN17001	Efficient U-Net	320, 320	200	0,4	IL/XL	Grid Distortion 1D	57,9	99,2	0,8	42,1	0,993	0,993
4877	LN17001	Efficient U-Net	320, 320	200	0,3	IL	Grid Distortion 1D	67,9	99,4	0,6	32,1	0,997	0,997
4878	LN17001	Efficient U-Net	320, 320	200	0,3	XL	Grid Distortion 1D	77,7	99,5	0,5	22,3	0,996	0,996
4852	LN17001	Light U-Net	320, 320	200	0,3	IL/XL	Grid Distortion 1D	70,1	99,1	0,9	29,9	0,994	0,994
4986	SG9202	Efficient U-Net	192, 192	50	0,3	IL/XL	None	53,1	98,6	1,4	46,9	0,984	0,974
4987	SG9202	Efficient U-Net	192, 192	50	0,3	IL/XL	Flip	50,5	98,7	1,3	49,5	0,987	0,979
4988	SG9202	Efficient U-Net	192, 192	50	0,3	IL/XL	Grid Distortion 1D	48,2	98,7	1,3	51,8	0,986	0,979
4991	SG9202	Efficient U-Net	192, 192	50	0,3	IL/XL	Elastic Transform 1D	48,0	98,8	1,2	52,0	0,987	0,979
4992	SG9202	Efficient U-Net	320, 320	50	0,3	IL/XL	Grid Distortion 1D	56,9	98,8	1,2	43,1	0,991	0,983
5115	SG9202	Efficient U-Net	320, 320	200	0,3	IL/XL	Grid Distortion 1D	68,4	98,9	1,1	31,6	0,994	0,985
5118	SG9202	Efficient U-Net	320, 320	200	0,4	IL/XL	Grid Distortion 1D	60,3	98,9	1,1	39,7	0,993	0,984
5121	SG9202	Efficient U-Net	320, 320	200	0,3	IL	Grid Distortion 1D	62,6	99,2	0,8	37,4	0,996	0,985
5122	SG9202	Efficient U-Net	320, 320	200	0,3	XL	Grid Distortion 1D	70,5	99,5	0,5	29,5	0,997	0,991
5120	SG9202	Light U-Net	320, 320	200	0,3	IL/XL	Grid Distortion 1D	64,2	99,1	0,9	35,8	0,995	0,988

Table 4-2: Complimentary table to table 4-1. Presents all test/validation scores for the CNN included in the results. The scores include all metrics, train/test (validation) scores and final model train/test scores. TF = True Fault, TB = True Background, FF = False Fault, FB = False Background, Val = Validation.

	Matrix Scores										Confusion Matrix				Val. Confusion Matrix				Overall scores	
Model ID	Loss	Val. Loss	F1 Macro	Val. F1 Macro	Accuracy	Val. Accuracy	Crossentropy	Val. Crossentropy	Mean IOU	Val. Mean IOU	TF(%)	TB (%)	FF (%)	FB (%)	TF (%)	TB (%)	FF (%)	FB (%)	Train Score	Test Score
4749	0,00	0,01	0,99	0,99	0,99	0,99	0,06	0,06	0,88	0,82	97,1	99,4	0,6	2,9	95,7	98,7	1,3	4,3	0,986	0,986
4757	0,02	0,06	0,98	0,96	0,98	0,98	0,08	0,08	0,75	0,64	84,8	98,5	1,5	15,2	65,2	97,2	2,8	34,8	0,979	0,979
4751	0,01	0,06	0,99	0,96	0,98	0,98	0,08	0,08	0,78	0,65	89,5	98,8	1,2	10,5	74,9	96,4	3,6	25,1	0,980	0,980
4758	0,01	0,06	0,98	0,96	0,98	0,98	0,08	0,08	0,77	0,65	88,8	98,7	1,3	11,2	71,5	96,8	3,2	28,5	0,980	0,980
4754	0,01	0,04	0,99	0,97	0,98	0,98	0,09	0,09	0,76	0,67	89,1	98,8	1,2	10,9	69,9	98,0	2,0	30,1	0,975	0,974
4842	0,01	0,04	0,99	0,97	0,98	0,98	0,08	0,08	0,81	0,71	93,0	99,0	1,0	7,0	75,9	98,0	2,0	24,1	0,980	0,980
4843	0,01	0,04	0,99	0,97	0,98	0,98	0,07	0,07	0,82	0,71	93,4	99,1	0,9	6,6	78,2	97,8	2,2	21,8	0,981	0,981
4797	0,02	0,08	0,98	0,95	0,97	0,97	0,10	0,10	0,75	0,59	86,6	98,3	1,7	13,4	56,3	95,9	4,1	43,7	0,967	0,967
4798	0,01	0,08	0,99	0,95	0,98	0,98	0,08	0,08	0,75	0,60	86,0	98,8	1,2	14,0	58,6	96,2	3,8	41,4	0,976	0,976
4829	0,02	0,08	0,98	0,97	0,97	0,97	0,13	0,13	0,75	0,63	86,0	98,5	1,5	14,0	53,8	97,8	2,2	46,2	0,968	0,968
4750	0,01	0,08	0,99	0,95	0,98	0,98	0,08	0,08	0,75	0,60	86,0	98,8	1,2	14,0	64,5	99,3	0,7	35,5	0,989	0,989
4772	0,01	0,04	0,99	0,99	0,99	0,99	0,05	0,05	0,70	0,57	69,2	99,4	0,6	30,8	27,0	99,3	0,7	73,0	0,989	0,989
4755	0,01	0,04	0,99	0,99	0,99	0,99	0,05	0,05	0,70	0,58	73,7	99,3	0,7	26,3	28,4	99,3	0,7	71,6	0,989	0,989
4773	0,01	0,04	0,99	0,99	0,99	0,99	0,05	0,05	0,70	0,57	72,8	99,3	0,7	27,2	23,1	99,4	0,6	76,9	0,988	0,988
4756	0,01	0,03	0,99	0,99	0,99	0,99	0,04	0,04	0,71	0,59	75,4	99,5	0,5	24,6	31,9	99,5	0,5	68,1	0,992	0,992
4839	0,00	0,02	1,00	0,99	0,99	0,99	0,03	0,03	0,79	0,66	89,0	99,7	0,3	11,0	68,9	99,2	0,8	31,1	0,994	0,994
4840	0,00	0,02	1,00	0,99	0,99	0,99	0,03	0,03	0,78	0,62	87,6	99,6	0,4	12,4	57,9	99,2	0,8	42,1	0,993	0,993
4877	0,00	0,01	1,00	0,99	1,00	1,00	0,02	0,02	0,84	0,66	93,8	99,8	0,2	6,2	67,9	99,4	0,6	32,1	0,997	0,997
4878	0,00	0,01	1,00	0,99	1,00	1,00	0,02	0,02	0,86	0,73	94,9	99,8	0,2	5,1	77,7	99,5	0,5	22,3	0,996	0,996
4852	0,00	0,02	1,00	0,99	0,99	0,99	0,03	0,03	0,80	0,65	90,0	99,7	0,3	10,0	70,1	99,1	0,9	29,9	0,994	0,994
4986	0,01	0,05	0,98	0,98	0,98	0,98	0,07	0,09	0,70	0,63	75,8	98,7	1,3	24,2	53,1	98,6	1,4	46,9	0,984	0,974
4987	0,02	0,05	0,99	0,98	0,99	0,98	0,06	0,09	0,70	0,63	71,5	99,1	0,9	28,5	50,5	98,7	1,3	49,5	0,987	0,979
4988	0,02	0,05	0,99	0,98	0,99	0,98	0,06	0,09	0,68	0,62	69,1	99,0	1,0	30,9	48,2	98,7	1,3	51,8	0,986	0,979
4991	0,02	0,05	0,99	0,98	0,99	0,98	0,06	0,08	0,70	0,63	72,3	99,0	1,0	27,7	48,0	98,8	1,2	52,0	0,987	0,979
4992	0,01	0,04	0,99	0,98	0,99	0,98	0,04	0,07	0,72	0,64	78,9	99,3	0,7	21,1	56,9	98,8	1,2	43,1	0,991	0,983
5115	0,01	0,03	0,99	0,99	0,99	0,99	0,03	0,07	0,79	0,67	88,9	99,5	0,5	11,1	68,4	98,9	1,1	31,6	0,994	0,985
5118	0,01	0,03	0,99	0,98	0,99	0,98	0,03	0,07	0,77	0,65	85,6	99,4	0,6	14,4	60,3	98,9	1,1	39,7	0,993	0,984
5121	0,00	0,03	1,00	0,99	1,00	0,99	0,02	0,07	0,84	0,68	93,4	99,6	0,4	6,6	62,6	99,2	0,8	37,4	0,996	0,985
5122	0,00	0,02	1,00	0,99	1,00	0,99	0,02	0,04	0,86	0,73	95,0	99,7	0,3	5,0	70,5	99,5	0,5	29,5	0,997	0,991
5120	0,00	0,03	0,99	0,99	0,99	0,99	0,03	0,07	0,80	0,67	89,2	99,5	0,5	10,8	64,2	99,1	0,9	35,8	0,995	0,988

4.2 Fault Characterization using ML models

The CNN with the overall best performance on predicting faults on 3D seismic volume LN17001_Full_Stack in survey LN17001 was utilized to predict and characterize minor faults in the damage zone of major faults along predefined scanlines. The particular CNN chosen for this task was the Light UNET with model ID 4852.

4.2.1 Determination of Damage Zone Surrounding Major Faults

For characterizing the fault damage zone, one fault in particular was chosen to be the main fault of interest and an array of scanlines was placed along 7 different inlines (5000, 5180, 5360, 5540, 5720, 5900 and 6080) in the LN17001_Full_Stack seismic volume. The fault F3, in figure 4-16, is the major studied fault. This fault is also highlighted in figures 4-17 – 4-29. This fault is located within the Polhem Subplatform, west of the Jason FC and the Loppa High (Indrevær et al., 2016). Similar to most of the larger faults within the Polhem Subplatform, F3 is a N-S striking normal fault. The fact that other large faults exist within the chosen scanline locations cannot be ignored, as it naturally would affect the population of minor faults around them. These larger (major) faults are considered and highlighted wherever they are present in both the inlines and fault density plots in figures 4-17 – 4-29. For each inline, 6 additional scanlines were made at varying depths (800ms, 1300ms, 1800ms, 2300ms 2800ms and 3300ms TWT) to capture vertical variation in addition to lateral variation across the fault damage zone. Along each scanline, the frequency of faults was calculated per kilometer to roughly determine the extent of the faults damage zone.

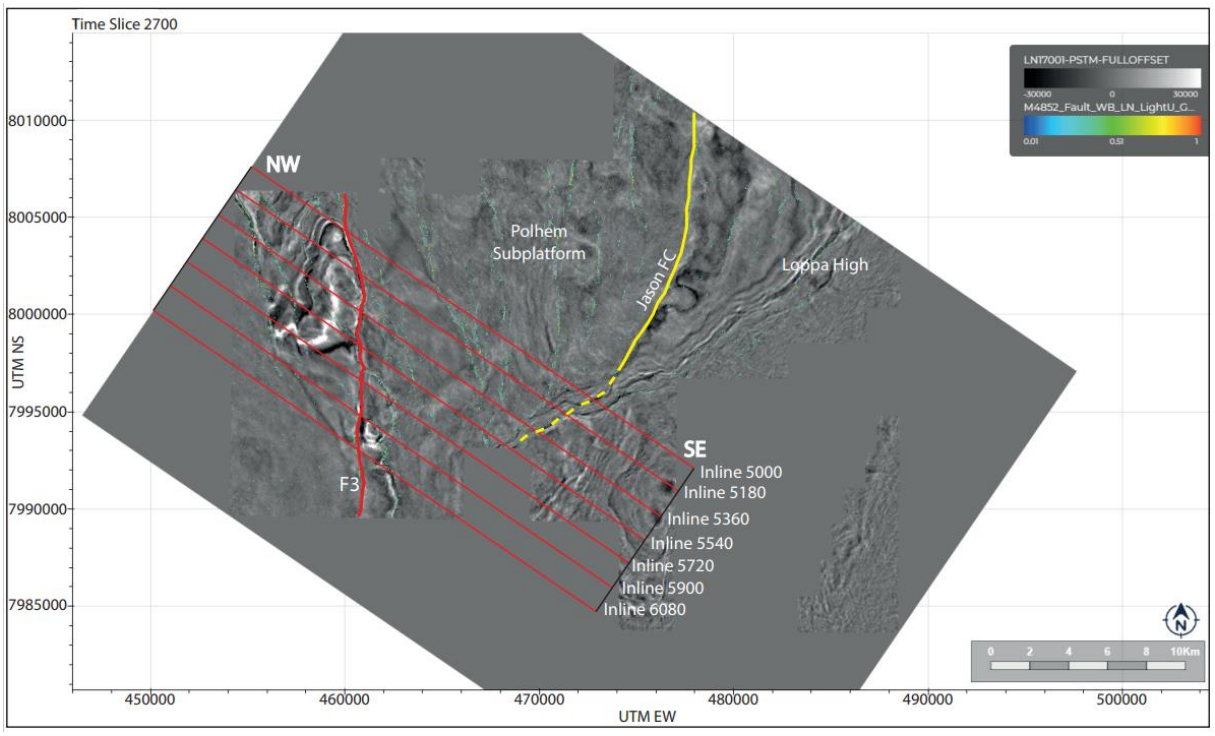

Figure 4-16: Time slice 2700ms (TWT) of 3D seismic volume LN17001_Full_Stack in survey LN17001_PSTM_FULLOFFSET with all 7 scanlines placed on Inline 5000, 5180, 5360, 5540, 5720, 5900 and 6080. Each scanline contains further 6 scanlines at different depths 800ms, 1300ms, 1800ms, 2300ms 2800 and 3300ms TWT. For reference, the Jason FC, and fault F3 (main fault of interest) are included.

Both Inline 5000 (figure 4-17) and the accompanying fault frequency plots (figure 4-18), indicate that the populations of minor faults are affected by several larger faults in addition to F3. At least three other large faults (Jason FC, F1 and F2) affect the occurrence of minor faults crossing the scanlines in Inline 5000. Considering F3, all fault frequency plots show an increased frequency within 1 to 2 km horizontal distance away from the fault, except from the scanline at 3300ms TWT where none of the larger faults are present. For scanlines at 800ms TWT and 1800ms TWT, a large fault frequency increase is noticed within 1 km horizontal distance to F3. In addition, the population of minor faults around F3 is generally high at shallower depths (600-1300ms TWT) and on the hanging wall (HW) side (Summarized in table 4-3 and fault frequency plot figure 4-18). These observations on the fault frequency plots could be related to splaying of faults towards the faults tip at shallow depths, where the numerous minor faults branch of the major fault (figure 4-17). The minor faults close to F3 are observed to link with it between 1300 and 1800ms TWT (figure 4-17). Generally, all minor faults are synthetic and form with a similar angle (dip orientation) to F3, except the two minor faults branching of the main fault on the footwall side, just below where the previously mentioned linkage occurs. These two faults appear subvertical to vertical (figure 4-17).

From the fault frequency plots and inline 5000 (figure 4-18), both faults F1 and F2 are surrounded by a relatively high frequency of minor faults compared to the rest of the area. This applies for F1 at 1300ms TWT, and for F2 at 800ms and 1800ms TWT.

Table 4-3: Summarizing the quantity of all faults surrounding fault F3. The number of fault surrounding F3 given for each inline (5000, 5180, 5360, 5540, 5720, 5900, 6080), depth (800, 1300, 1800, 2300, 2800, 3300ms TWT) and whether they are located on the footwall (FW) or hanging wall (HW). NV=Fault F3 is not visible.

Depth (TWT)	800ms	1300ms	1800ms	2300ms	2800ms	3300ms
Inline 5000 FW	1	0	2	2	3	NV
Inline 5000 HW	5	2	1	1	2	NV
Inline 5180 FW	2	1	NV	2	1	NV
Inline 5180 HW	4	4	NV	0	0	NV
Inline 5360 FW	NV	NV	NV	0	3	2
Inline 5360 HW	NV	NV	NV	1	2	0
Inline 5540 FW	NV	NV	NV	1	1	1
Inline 5540 HW	NV	NV	NV	0	1	0
Inline 5720 FW	NV	NV	NV	NV	0	NV
Inline 5720 HW	NV	NV	NV	NV	1	NV
Inline 5900 FW	NV	NV	NV	2	1	NV
Inline 5900 HW	NV	NV	NV	0	0	NV
Inline 6080 FW	NV	NV	NV	NV	1	NV
Inline 6080 HW	NV	NV	NV	NV	0	NV

At 800ms TWT a generally large number of minor faults is observed between the hanging wall of F2 and footwall of F3. From the plots (figure 4-18) and seismic image (figure 4-17) it is difficult to determine a boundary between the damage zones of the two faults as they seem to overlap, also there is about one kilometer where faults are absent, close to F3 on the footwall side. A cumulative fault frequency plot was created to determine the damage zone of fault F3. The cumulative fault frequency plot is presented in the discussion in Figure 5-2. This extent of the damage zone is measured where the height of fault F3 is approximately 11,5km.

Another observation from figure 4-17 and 4-18 is that the number of faults in general decreases with depth, and the decrease is drastic at depths beyond the extent of the major faults. Also, the depth at which faults exist increases away from the Selis Ridge.

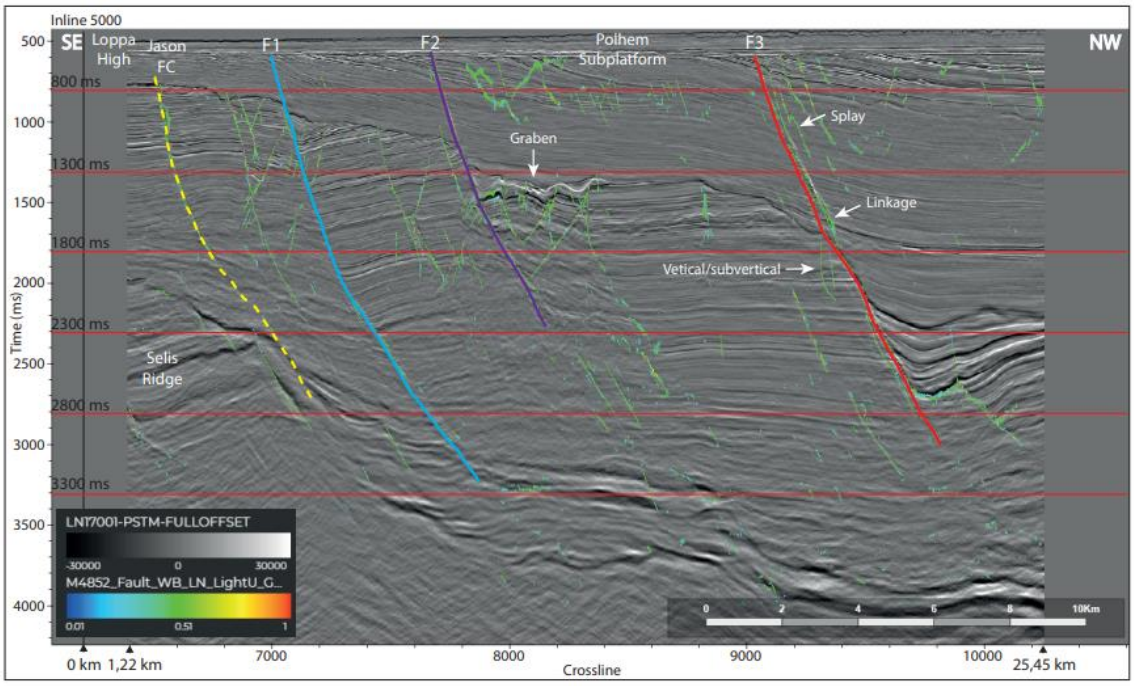

Figure 4-17: Inline 5000 in 3D seismic volume LN17001_Full_Stack in survey LN17001_PSTM_FULLOFFSET with fault predictions from a 3D fault volume created by applying the Light UNET with model ID 4852 (Patch size: 320 x 320, Training Epochs: 200 and Dropout: 0,3). Scanlines 800ms, 1300ms, 1800ms, 2300ms, 2800ms and 3300ms TWT are highlighted with red lines, including the main fault of interest (F3). Other large faults in the seismic section are the Jason FC (Yellow dotted line), F1 (Blue) and F2 (Purple).

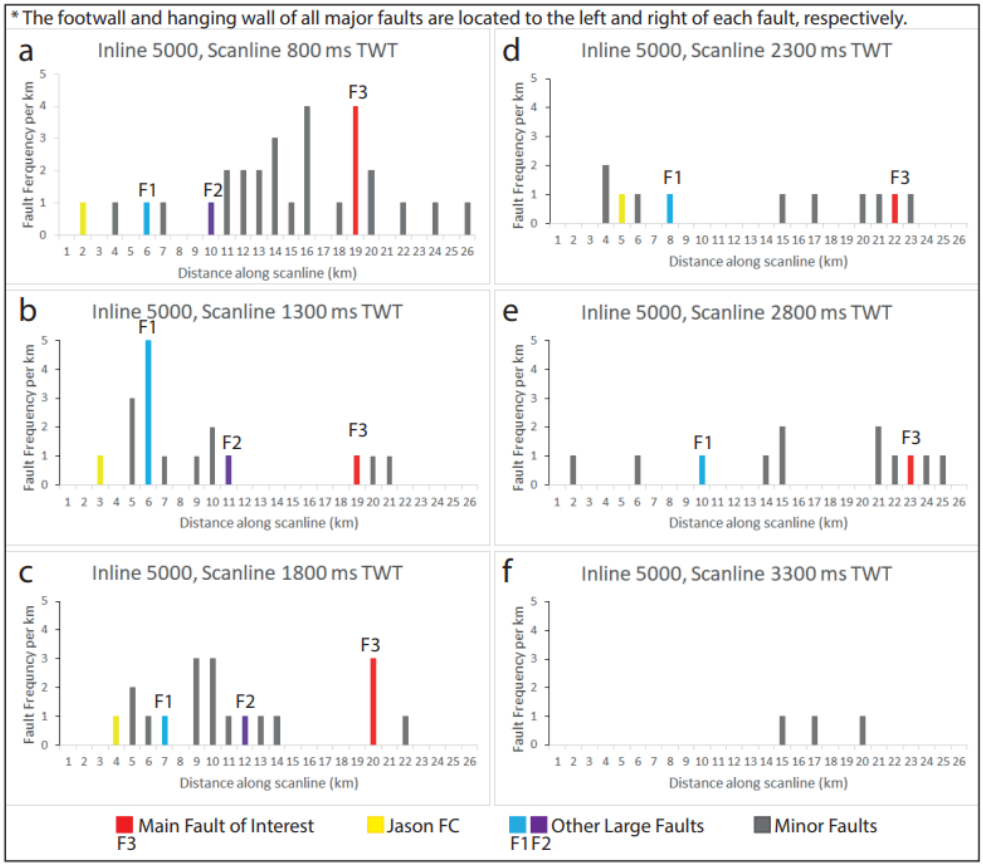

Figure 4-18: Fault Frequency plots for Inline 5000 in 3D seismic volume LN17001_Full_Stack in survey LN17001_PSTM_FULLOFFSET. Plots a-f represent the individual scanlines ranging from 800-3300ms TWT. The Jason FC and the other major faults (F1, F2 and F3) are marked whenever they cross the scanline. Minor faults are grey.

When observing Inline 5180 (figure 4-19) and the accompanying fault frequency plots (figure 4-20) some similarities to Inline 5000 are found. The surrounding area of F3 again shows an increased fault frequency at shallower depths, especially on the hanging wall side, representing splay towards the faults tip (figure 4-19). As in Inline 5000 linkage between the splaying faults and F3 may be expected, but it is not visible in the seismic image. F3 cannot be traced on the scanline at 1800ms TWT, but a increased population of minor faults exist around where the fault is expected to be located. The minor faults are antithetic, accommodating strain and linking the two larger fault segments located above and below the structure together (figure 4-19).

On Inline 5180 the other large faults again have an increased population of minor faults in their surrounding area, most pronounced around F2 (figure 4-19 and 4-20). Overall, most faults are found towards the shallower depths, nearby F2 and F3. A spike in fault occurrence is noticed at the scanline at 1800ms TWT. The spike is pronounced on the hanging wall side of F2, where part of the fault block between F2 and F3 has collapsed. This collapse is characterized by faults with opposite directions of dip on opposing sides of the structure, forming its own small graben structure. That collapse is also highly noticeable in seismic inline 5000, but faults within the structure are poorly captured by the scanlines. At depths exceeding the visible extent of F2, the frequency of minor faults is still quite high, perhaps indicating the faults existence at those depths. Additionally, an increased fault frequency is noticed on the north-western end of the scanlines, at a significant distance away from any of the larger faults, especially visible in the fault frequency plots at 800, 1300 and 1800ms TWT. In the location of that fault population (which also contains several antithetic faults), in Inline 5360 (figure 4-21) an additional larger fault (F5) will appear. At 3300ms TWT, the occurrence of faults is sparce.

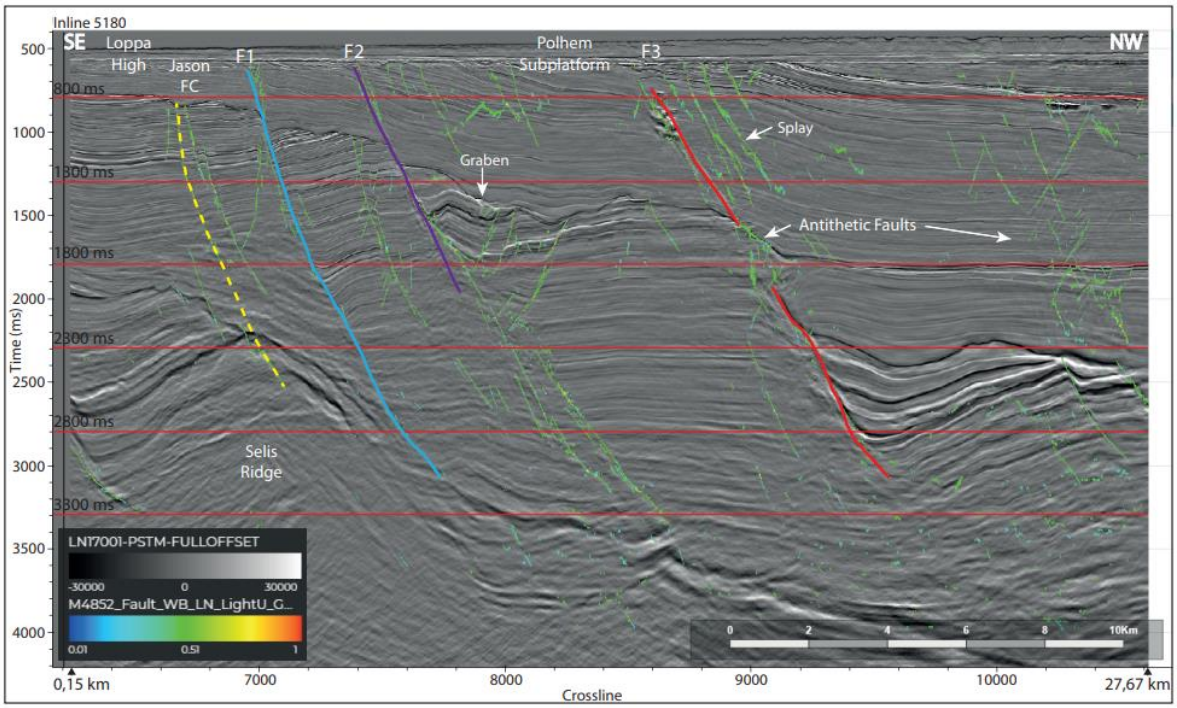

Figure 4-19: Inline 5180 in 3D seismic volume LN17001_Full_Stack in survey LN17001_PSTM_FULLOFFSET with fault predictions from a 3D fault volume created by applying the Light UNET with model ID 4852 (Patch size: 320 x 320, Training Epochs: 200 and Dropout: 0,3). Scanlines 800ms, 1300ms, 1800ms, 2300ms, 2800ms and 3300ms TWT are highlighted with red lines, including the main fault of interest(F3). Other large faults in the seismic section are the Jason FC (Yellow dotted line), F1 (Blue) and F2 (Purple).

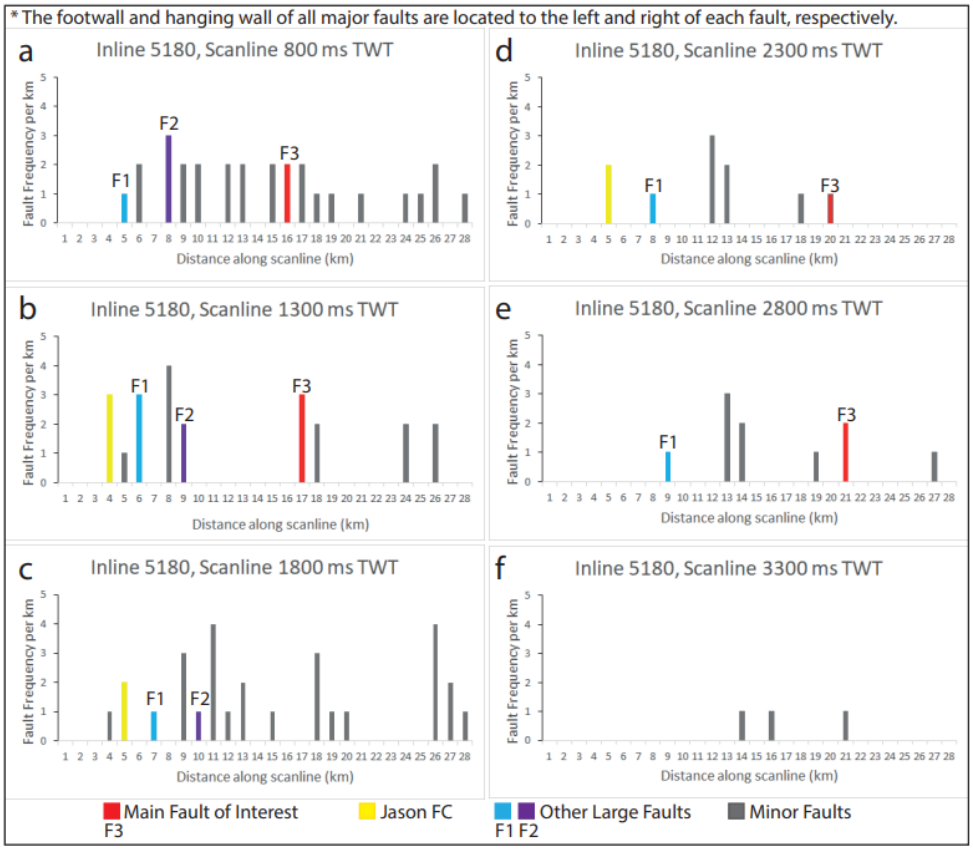

Figure 4-20: Fault Frequency plots for Inline 5180 in 3D seismic volume LN17001_Full_Stack in survey LN17001_PSTM_FULLOFFSET. Plots a-f represent the individual scanlines ranging from 800-3300ms TWT. The Jason FC and the other major faults (F1, F2 and F3) are marked whenever they cross the scanline. Minor faults are grey.

On Inline 5360 (figure 4-21) some significant changes can be observed. F3 has become less extensive (approx. height: 7km) and no longer penetrates through the scanlines at 800, 1300 and 1800ms TWT. F3 now penetrates deeper, past the scanline at 3300ms TWT. Generally, there are very few minor faults located around F3, also in the seismic above it there is an absence of faults, reaching all the way to the seabed. As the extent of F3 has decreased, especially towards shallower depths, a new larger fault is noticed (F4). A segment of F4 overlaps with F3. F4 seems to accommodate a significant part of the strain at shallower depths, which in the previous inlines was accommodated by F3. In the fault frequency plots in figure 4-22 the highest frequencies of minor faults are now located around F4 and F2. The fault pattern surrounding the F4 is at shallower depths (600-1300ms TWT) similar to the patterns previously observed around F3, with the largest amount of faults occurring on the hanging wall side of the fault. No linkage can be observed between minor faults and F3 in seismic. The scanline at 800ms TWT in fact registers the highest frequency of faults within close distance to the F4. The fault frequency between F2 and the F4 at 800ms TWT is not significantly higher than compared to the rest of the scanline, in difference to what was previously observed between the F2 and F3.

A large amount of minor faults still occurs due to the graben structure located at the hanging wall of F2 (figure 4-21), especially noticeable on the fault frequency plot from the scanline located at 1800ms TWT (figure 4-22). As mentioned in the paragraph about inline 5180, a second new larger fault is present on inline 5360 (F5). Towards the north-western end of the scanlines the increase in fault frequency occurs around that fault. The number of faults at large depths has to some degree increased compared to the pervious inlines, considering the fault frequency plot at 3300ms TWT.

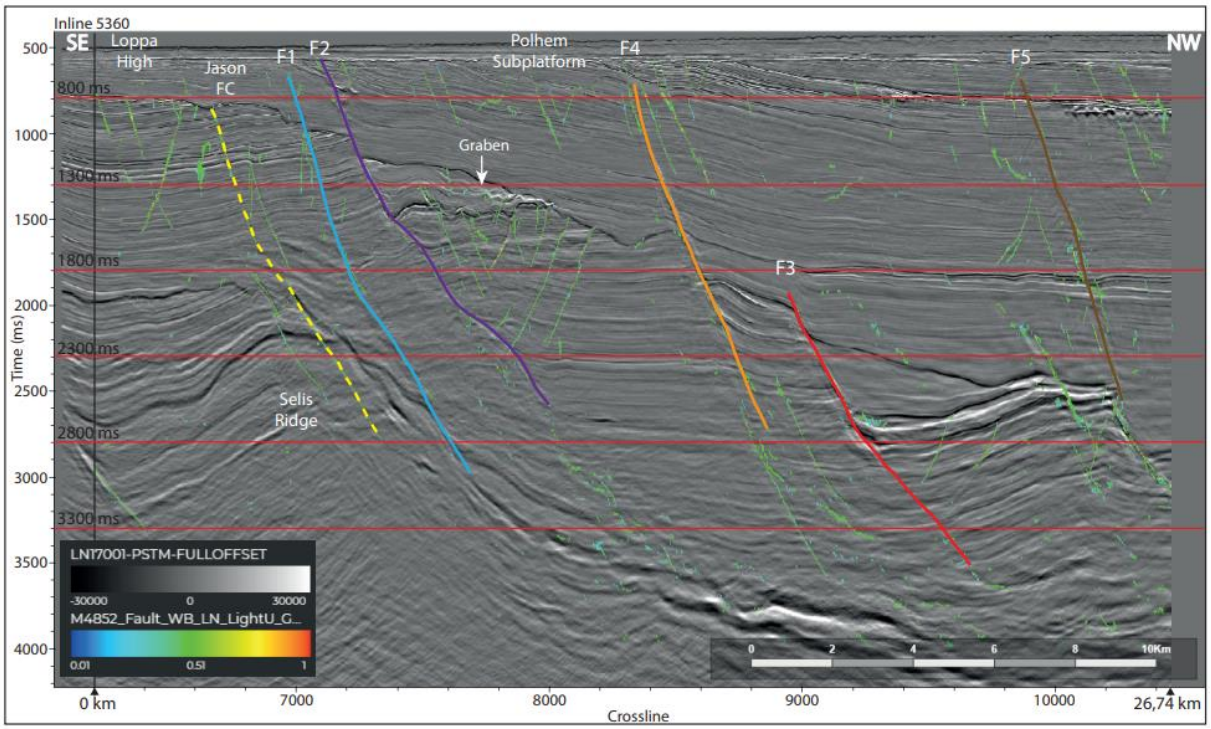

Figure 4-21: Inline 5360 in 3D seismic volume LN17001_Full_Stack in survey LN17001_PSTM_FULLOFFSET with fault predictions from a 3D fault volume created by applying the Light UNET with model ID 4852 (Patch size: 320 x 320, Training Epochs: 200 and Dropout: 0,3). Scanlines 800ms, 1300ms, 1800ms, 2300ms, 2800ms and 3300ms TWT are highlighted with red lines, including the main fault of interest(F3). Other large faults in the seismic section are the Jason FC (Yellow dotted line), F1 (Blue), F2 (Purple), F4 (Orange) and F5 (Brown).

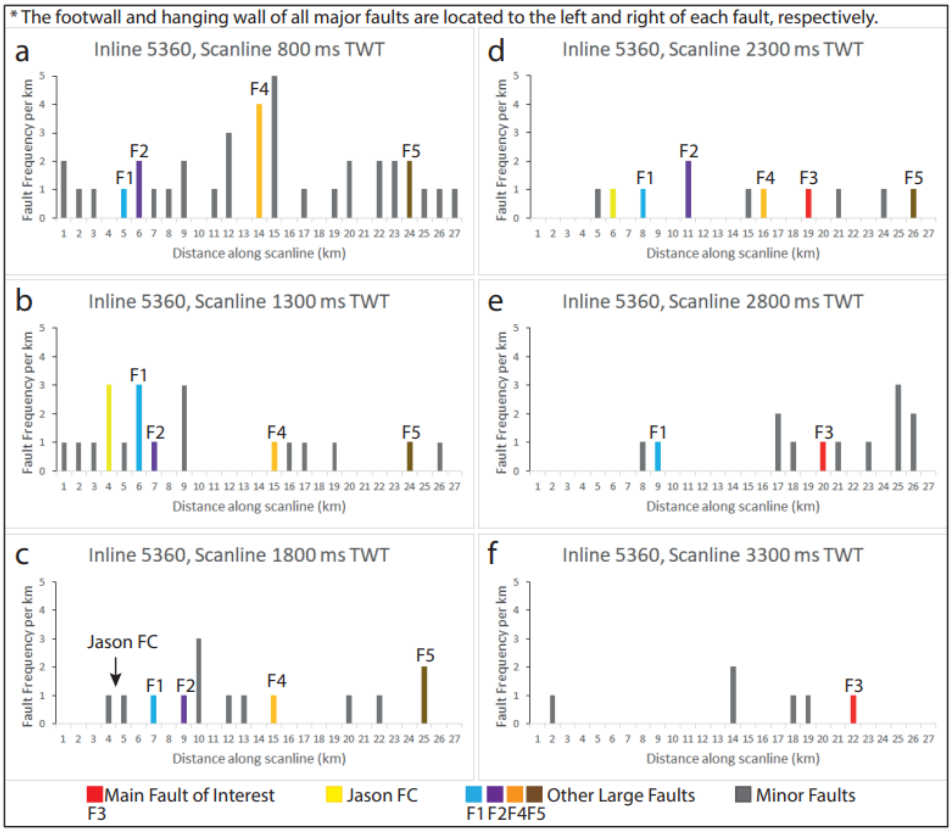

Figure 4-22: Fault Frequency plots for Inline 5360 in 3D seismic volume LN17001_Full_Stack in survey LN17001_PSTM_FULLOFFSET. Plots a-f represent the individual scanlines ranging from 800-3300ms TWT. The Jason FC and the other major faults (F1, F2, F3, F4 and F5) are marked whenever they cross the scanline. Minor faults are grey.

In Inline 5540 (figure 4-23), the absence of faults above F3 remains. F4, as previously, is accommodating strain towards the shallower depths in place of F3. Splay towards the tip of the orange fault is visible. In contrast to previous observations in the seismic inlines, the majority of minor faults in the splay is located on the footwall of F4. Some linkage between minor faults and the F4 is visible. Most clearly visible in seismic is the linkage at around 1200ms TWT between F4 and a minor fault on the hanging wall side (figure 4-23). Another example of linkage is observed between the scanlines at 1800ms and 2300ms TWT, where two antithetic faults on the footwall of F4 branch of it. Compared to Inline 5360 (figure 4-21), the angle of dip of F4 has increased in Inline 5540, also the dip is increasing slightly with depth generally forming a steeper angle to the horizontal compared to most of the surrounding minor faults. In comparison to F4, the angle of dip of F3 is decreasing with depth and forming a pronounced bend at 2500ms TWT.

In Inline 5540, some of the fault visible in the previous inlines are no longer occurring or are just partly visible. For example, F1 is not occurring in Inline 5540 and F2 is only partly visible, which to some degree is explained by the gap in seismic coverage. Both the seismic section and the fault frequency plots (figure 4-23 and 4-24) show that most faults and the highest frequency of faults occur in the range of 800-2300ms TWT and accumulate between F2 and F4 or on the hanging wall side of F5. Similar to all previous scanlines, the occurrence of faults at large depths (3300ms TWT) is sparce.

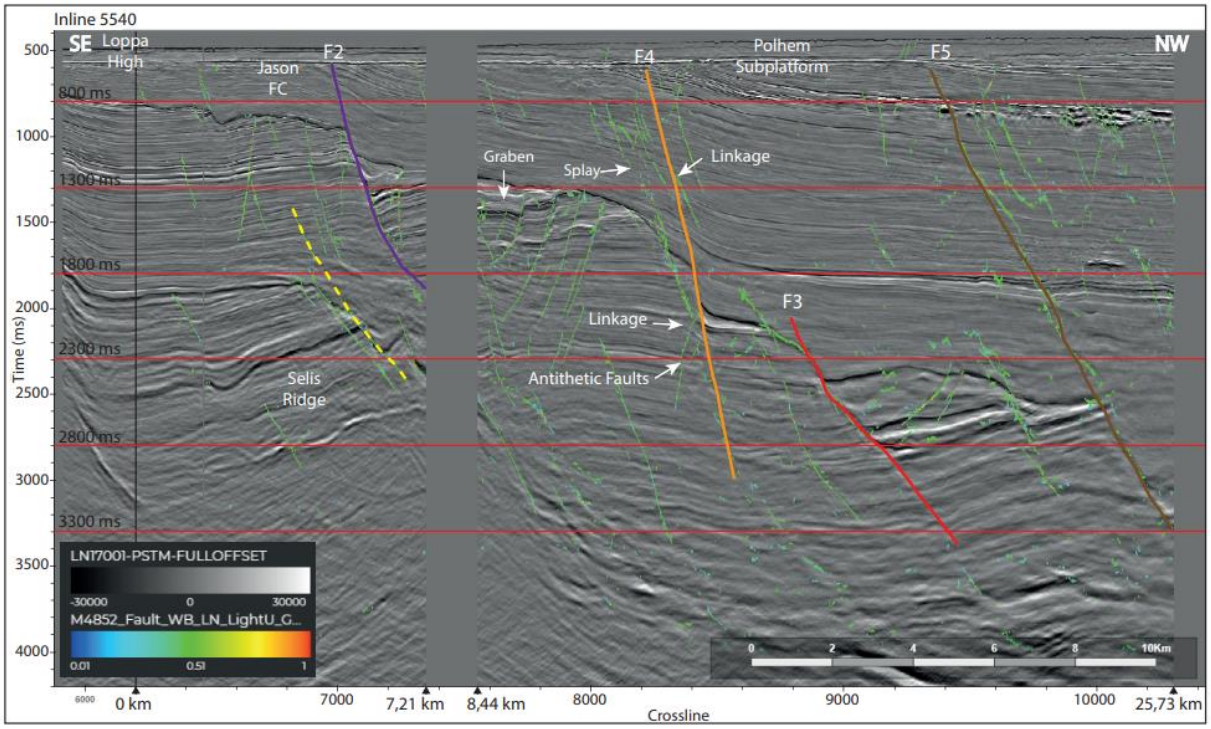

Figure 4-23: Inline 5540 in 3D seismic volume LN17001_Full_Stack in survey LN17001_PSTM_FULLOFFSET with fault predictions from a 3D fault volume created by applying the Light UNET with model ID 4852 (Patch size: 320 x 320, Training Epochs: 200 and Dropout: 0,3). Scanlines 800ms, 1300ms, 1800ms, 2300ms, 2800ms and 3300ms TWT are highlighted with red lines, including the main fault of interest (F3). Other large faults in the seismic section are the Jason FC (Yellow dotted line), F2 (Purple), F4 (Orange) and F5 (Brown).

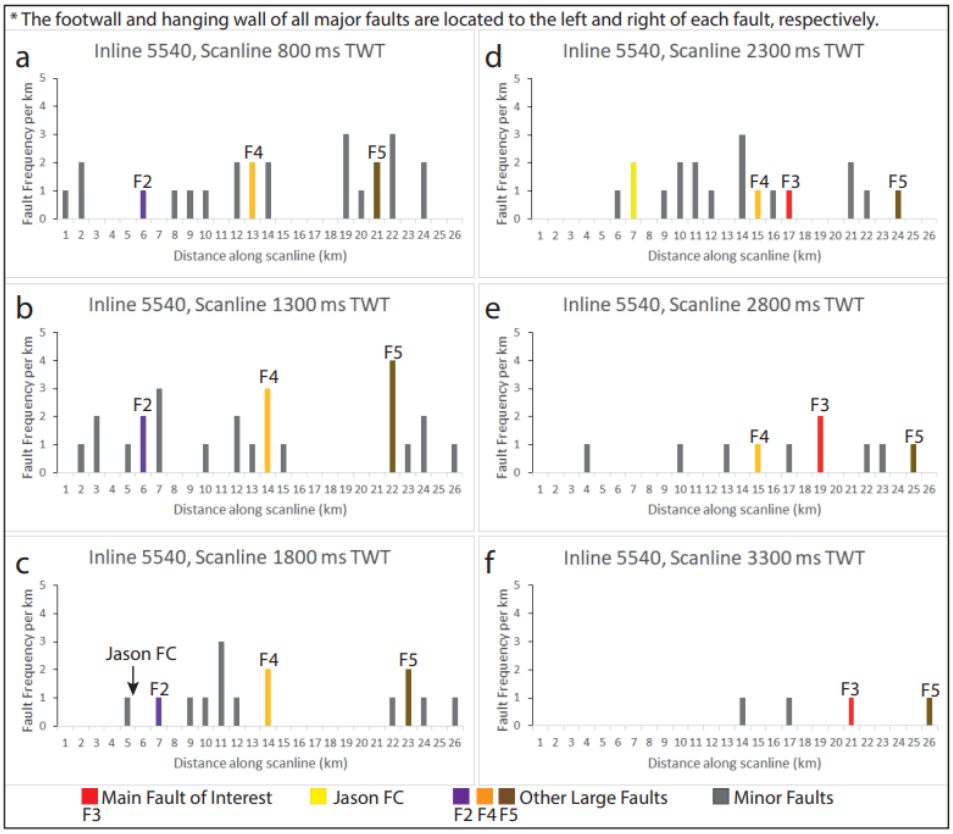

Figure 4-24: Fault Frequency plots for Inline 5540 in 3D seismic volume LN17001_Full_Stack in survey LN17001_PSTM_FULLOFFSET. Plots a-f represent the individual scanlines ranging from 800-3300ms TWT. The Jason FC and the other major faults (F2, F3, F4 and F5) are marked whenever they cross the scanline. Minor faults are grey.

Due to the sparce coverage of the seismic survey on Inline 5720, it is difficult to analyze proper results from the first 10km of the scanlines and seismic image (figure 4-25). The absence of seismic is also a continuing issue for Inlines 5900 (figure 4-27) and 6080 (figure 4-29). Considering F3, the height of the fault is reduced drastically (approx. height: 3,5km) to the point where it is only crossing the scanline at 2800ms TWT. The fault frequency around the F4 has decreased, especially at shallower depths (figure 4-25 and 4-26). Some minor faults are still forming a splay towards the tip of the orange fault in the hanging wall without any visible linkage (figure 4-25).

Generally, most minor faults are located on the hanging wall side of F5. Moving southeast an absence of faults is noticed, as in inlines 5360 and 5540. A high frequency of faults is also observed around what is interpreted to be F2, but due to poor seismic coverage it is difficult to exactly identify the fault or properly interpret the population of faults around it.

In Inline 5900 in figure 4-27, it is noticeable that F3 slightly has increased in height (approx. height: 5km) compared to Inline 5720. F4 is surrounded by significantly more minor faults than F3 which is visible on seismic and in the fault frequency plots in figure 4-28, 800-2300ms TWT. The number of minor faults surrounding the F4 is most significant towards the shallower depths, represented by the scanline at 800ms TWT. Also noticeable from the 800ms TWT scanline is that most fault are located close to F4, splaying towards it (figure 4-27). No minor faults are within immediate distance of F3. One major difference from Inline 5720 is that F5 has decreased in height, but still a lot of minor faults exist both above and NW of F5.

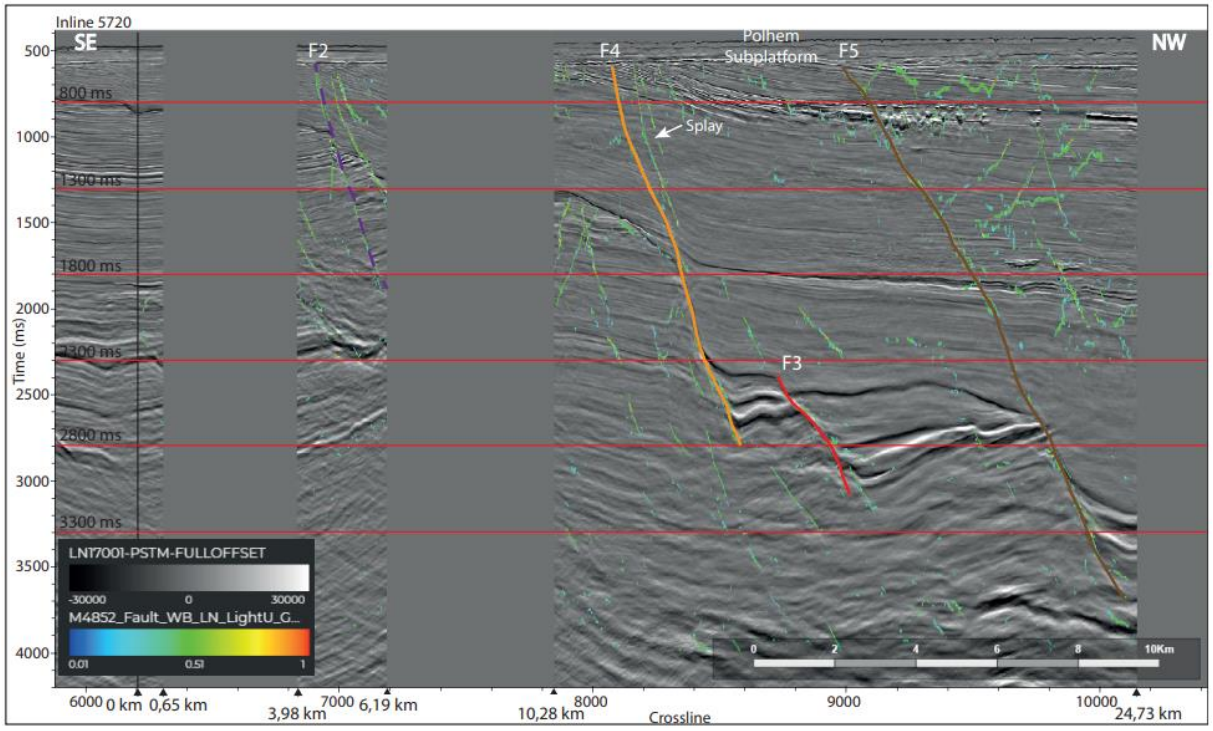

Figure 4-25: Inline 5720 in 3D seismic volume LN17001_Full_Stack in survey LN17001_PSTM_FULLOFFSET with fault predictions from a 3D fault volume created by applying the Light UNET with model ID 4852 (Patch size: 320 x 320, Training Epochs: 200 and Dropout: 0,3). Scanlines 800ms, 1300ms, 1800ms, 2300ms, 2800ms and 3300ms TWT are highlighted with red lines, including the main fault of interest(F3). Other large faults in the seismic section are F2 (Purple dotted line), F4 (Orange) and F5 (Brown).

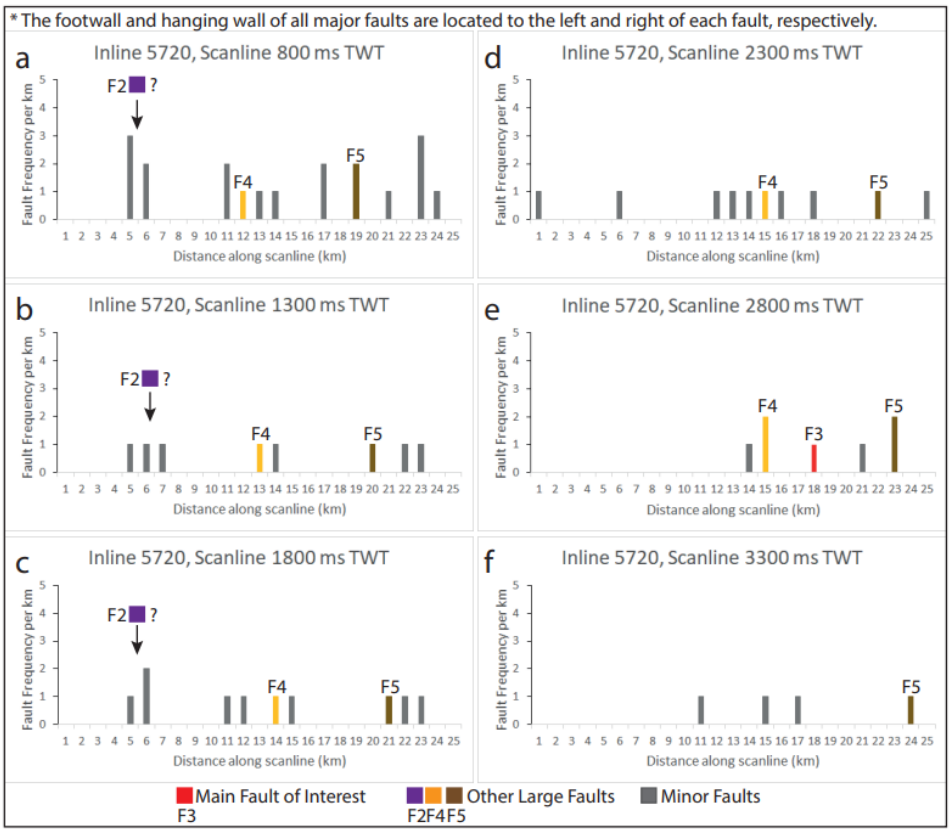

Figure 4-26: Fault Frequency plots for Inline 5720 in 3D seismic volume LN17001_Full_Stack in survey LN17001_PSTM_FULLOFFSET. Plots a-f represent the individual scanlines ranging from 800-3300ms TWT. The Jason FC and the other major faults (F2, F3, F4 and F5) are marked whenever they cross the scanline. Minor faults are grey.

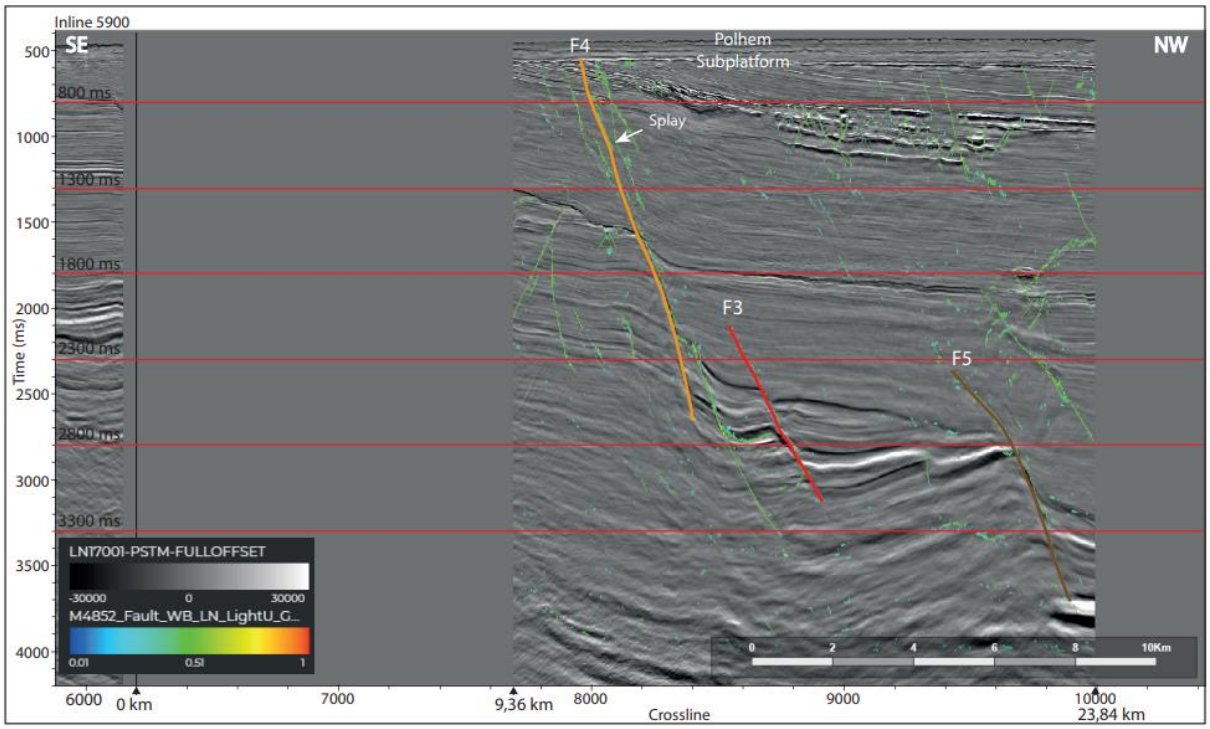

Figure 4-27: Inline 5900 in 3D seismic volume LN17001_Full_Stack in survey LN17001_PSTM_FULLOFFSET with fault predictions from a 3D fault volume created by applying the Light UNET with model ID 4852 (Patch size: 320 x 320, Training Epochs: 200 and Dropout: 0,3). Scanlines 800ms, 1300ms, 1800ms, 2300ms, 2800ms and 3300ms TWT are highlighted with red lines, including the main fault of interest(F3). Other large faults in the seismic section are F4 (Orange) and F5 (Brown).

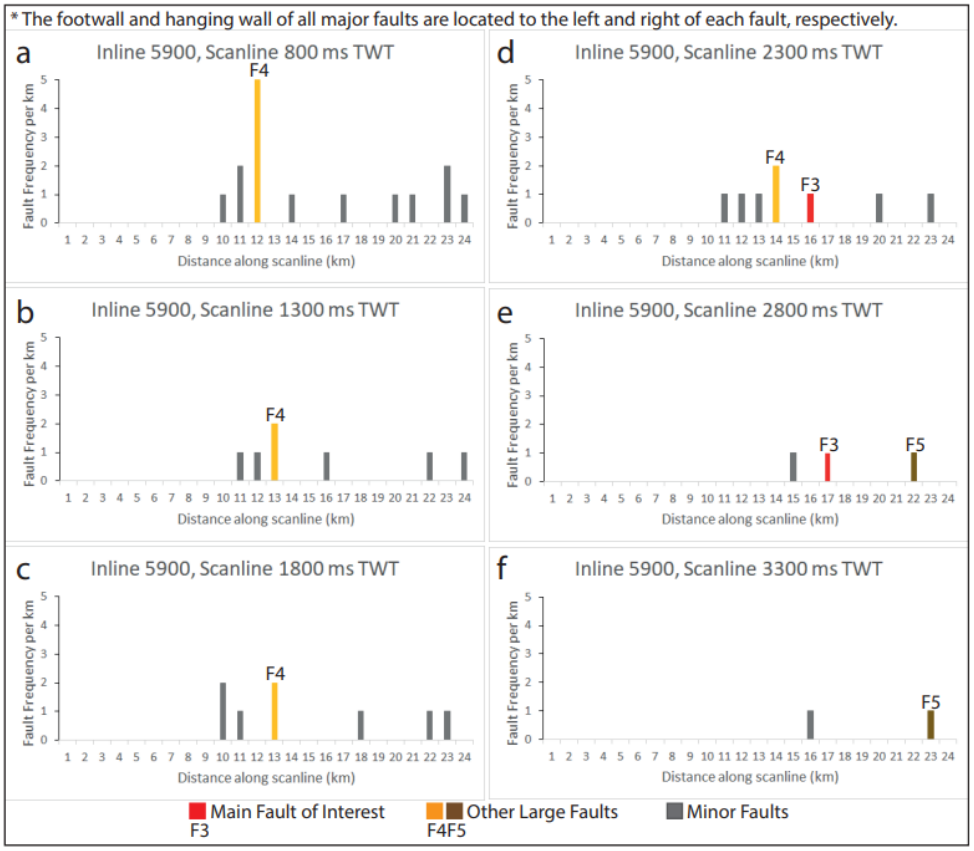

Figure 4-28: Fault Frequency plots for Inline 5900 in 3D seismic volume LN17001_Full_Stack in survey LN17001_PSTM_FULLOFFSET. Plots a-f represent the individual scanlines ranging from 800-3300ms TWT. The Jason FC and the other major faults (F3, F4 and F5) are marked whenever they cross the scanline. Minor faults are grey.

In scanline 6080 (figure 4-29), in general less faults are visible than in the previously observed scanlines. F3 (approx. height: 2,7km) and F5 are very short, and there are no minor faults surrounding them. F4 is the feature of most significance in these sections of scanlines. Both, in terms of height and minor surrounding faults, repeatedly observing that the majority of minor faults are found as a splay towards the upper tip of the fault (see scanline at 800ms TWT). In the seismic section at 1800ms TWT a population of minor faults can be observed without any immediate relation to a larger fault. As there are few faults visible in Inline 6080 the fault frequency plot is left out.

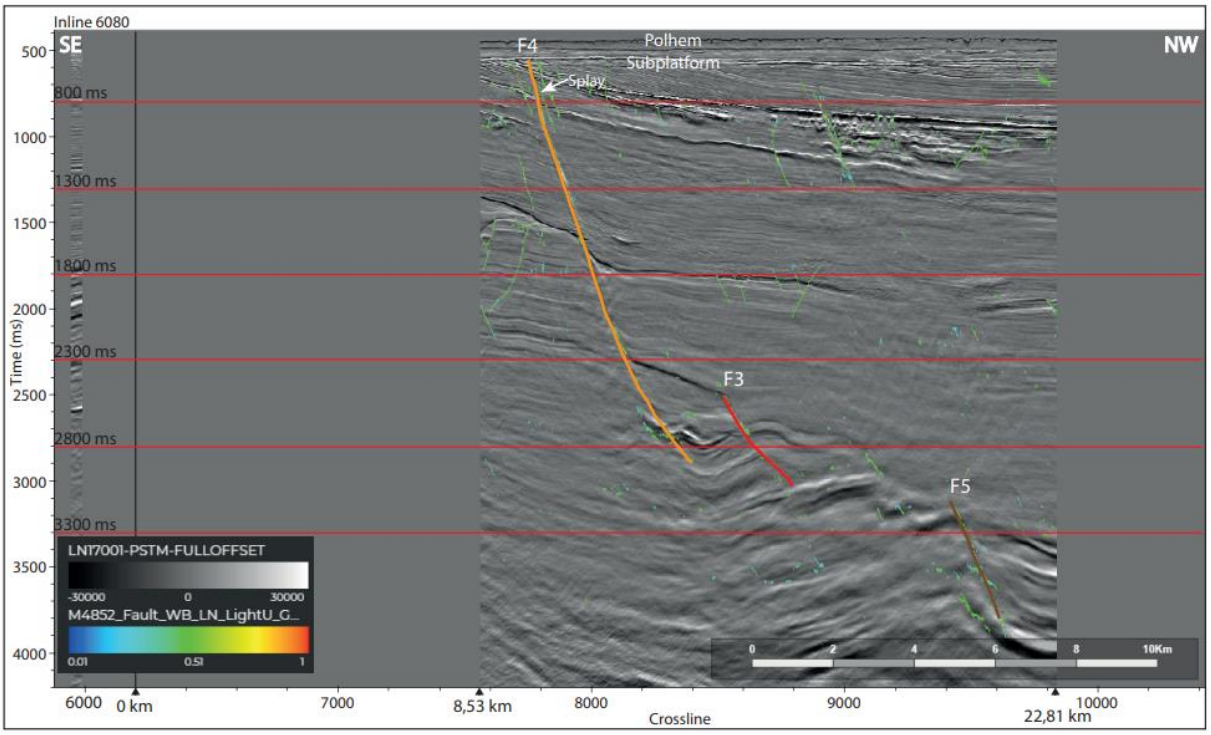

Figure 4-29: Inline 6080 in 3D seismic volume LN17001_Full_Stack in survey LN17001_PSTM_FULLOFFSET with fault predictions from a 3D fault volume created by applying the Light UNET with model ID 4852 (Patch size: 320 x 320, Training Epochs: 200 and Dropout: 0,3). Scanlines 800ms, 1300ms, 1800ms, 2300ms, 2800ms and 3300ms TWT are highlighted with red lines, including the main fault of interest(F3). Other large faults in the seismic section are F4 (Orange) and F5 (brown).

5 Discussion

5.1 Fault Interpretation with Deep Learning

In this part of the discussion, the role of data augmentation and different types of augmentation filters will be discussed. Then the affect of network and hyperparameters on the quality of the predicted faults will be discussed.

During the process of finding suiting parameters for grid distortion 1D and elastic transformation 1D presented in table 3-1 it became clear that the data augmentation parameters need to be chosen carefully to improve fault predictions. The results for the three surveys studied in this thesis indicate that small geometric transformations are preferred. The changes must be large enough to implement more diversity to the training data. Larger changes in the seismic data caused by grid distortion 1D or elastic transformation 1D can generate images that have significant differences from the geological setting of the survey study area. Heavily exaggerated parameters will cause highly unrealistic geological structures. The effect different data augmentation parameters have on the scores of on CNN during the process of finding optimal parameters is provided in table 8-1 and 8-2 in the Appendix. There is very little published literature about the application of data augmentation on seismic interpretation. Wu et al. (2019) applied flipped images to their seismic data when training their CNN, but until this point no work on the application of other geometric transformation techniques on seismic such as grid distortion or elastic transformation is published. Data augmentations that have been applied in other semantic segmentation tasks can be adopted for ML seismic interpretation. For example in the field of medical research several data augmentation techniques have been applied to semantic segmentation problem with success (e.g. Frid-Adar et al., 2018).

The application of data augmentation in terms of simple geometric transformations, like horizontal flip, grid distortion 1D and elastic transform 1D on Efficient UNET compared to the exact same networks without data augmentation provide a solid base for discussion. From the results, it appears that the model score cannot always be used as a criteria to verify the performance of the trained models. In several cases in this study some models achieve lower scores compared to certain other models, whilst the geological visual check of the models performance would expect the opposite to be true. This observation is linked to models trained and tested on non-augmented seismic vs. models trained and tested on data augmented cases. In general, models that were trained and tested without any data augmentation tend to achieve higher scores than models trained and tested on augmented seismic. Although, in visual comparison data augmented CNN usually have the better predictions. In seismic volume ST14200Z15_OBN_Full_Stack this observation is very

prominent: in figure 4-1, all augmentations (figure 4-1 c, d, e) improve the performance of the model significantly compared to figure 4-1 b where data augmentation is not applied, which is in clear contrast to what the scores of the respective models in tables 4-2 and 4-3 indicate. This observation is also made in the two other seismic volumes although the contrast is not that large as in volume ST14200Z15_OBN_Full_Stack, which is plausible as the effect of data augmentation on fault predictions on those two volumes initially is less significant. The effect of data augmentation is greater when the data quality is better. This observation is important and can be used in ML imaging of faults to enhance the trained model performance. The generally lower model scores related to data augmentation may be caused by the increase of training and testing data, increasing the room for error. The performance of data augmented models on seismic despite the lower scores is still better as they experienced more diversity during training. As discussed earlier the ML metric (F1 score or confusion matrix of test and train data) is not alone the best criteria for model performance quality check. In addition, geological sense check on unseen slices have to be used to evaluate the quality of trained models.

In addition to data augmentation the adjustment of hyperparameters in the train and test structure of the CNN is important. The results of this study show that changing the values of hyperparameters such as number of epochs, patch size and dropout has varying effects on CNN, depending on which seismic volume they were utilized on. The three different 3D seismic volumes of this study have different characteristics in terms of resolution, quality (noise), size, and fault geometries and dimensions. The differences in the 3D seismic volumes are reflected in the fault prediction performance of the CNN, revealing different limitations or problems for each seismic volume. Such limitations or problems are poor continuity or segmentation of fault predictions due to the large size of some faults, and sparce coverage of predicted faults caused by noise in the seismic.

As mentioned earlier in the discussion, data augmentation improved the CNN fault prediction more significantly on volume ST14200Z15_OBN_Full_Stack, than on volume LN17001_Full_Stack or SG9202_Full_Stack. This can be partly related to the quality of the data as the level of noise is quite low. In addition, seismic volume ST14200Z15_OBN_Full_Stack contains generally rather small faults (e.g. figure 4-4) compared to seismic volume LN17001_Full_Stack comprising larger faults (e.g. figure 4-5). It is in general harder to capture the full length of the very large similar to the example in the LN17001 survey. These larger faults in volume LN17001_Full_Stack probably cause issues to the deep learning architecture, resulting in a lower percentage of faults detected compared to volume ST14200Z15_OBN_Full_Stack. As default, the model uses patches of size 192 x 192 pixels that are fed to the network, which may cause the network to struggle with the

identification of larger faults as continuous. The implementation of a larger patch size (320 x 320 pixels) improved on the performance on the LN17001_Full_Stack, probably because larger portions of faults are fitted within the same patch.

In this comparison, in addition the sampling interval of the seismic volumes should be considered. The sampling interval corresponds to the vertical length of pixels in the seismic images. Volumes ST14200Z15_OBN_Full_Stack has a 4ms sampling interval (vertical), whilst volume LN17001_Full_Stack and SG9202_Full_Stack both have a 2ms sampling interval (vertical). Applying the patch size to our sampling intervals for seismic volume ST14200Z15_OBN_Full_Stack a 192 x192 pixel patch size and 320 x 320 patch size correspond to a 768ms x 192 patch size and 1280ms x 320 patch size, respectively. For the two other seismic volumes the same patch sizes correspond to a 384ms x 192 patch size and 640ms x 320 patch size, respectively. For better visualization figure 5-1 demonstrates the extent of each patch size on the three 3D seismic volumes.

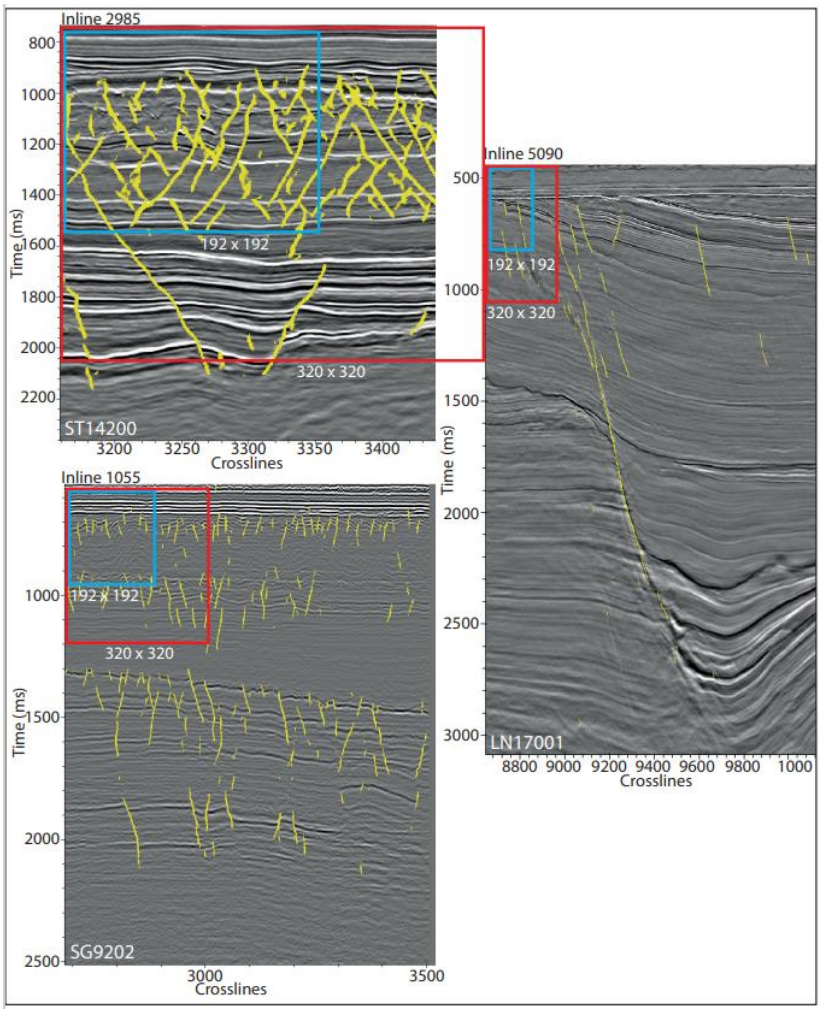

Figure 5-1: Visualization of the how the patch sizes 192 x 192 pixels (blue box) and 320 x 320 pixels (red box) relate to 3D seismic volumes ST14200Z15_OBN_Full_Stack, LN17001_Full_Stack and SG9202_Full_Stack, and the size of existing faults.

Increasing the training epochs from 50 to 200 in addition to the larger patch size (320 x 320 pixels, figure 4-5 c) increased the Efficient UNET fault prediction performance on 3D seismic volume LN17001_Full_Stack (figure 4-5 d). The Efficient UNET improvement in the increased training epoch case, may be a result of reduced overfitting. This is not indicated by the difference between loss and validation loss in table 4-3. In contrast increasing the number of training epochs had a negative effect on the Efficient UNET fault prediction performance on seismic volume ST14200Z15_OBN_Full_Stack (figure 4-4 d). Possibly, the Efficient UNET does not require the same duration of training to learn the seismic patterns in volume ST14200Z15_OBN_Full_Stack as in volume LN17001_Full_Stack and therefore learns irrelevant patterns and thus starts overfitting.

Generally, in all three models it is noticed that the increase of dropout from 0.3 to 0.4 if any, has a negative effect on the Efficient UNET fault prediction performance, indicating that randomly zeroing out additional neuron activation values during the training process is not beneficial.

Observations made on seismic volume SG9202_Full_Stack provide contrast to observations made in the two other seismic volumes of this study. Whilst data augmentation in some sort showed quite noticeable improvement on the fault predictions of CNN on seismic volume ST14200Z15_OBN_Full_Stack and LN17001_Full_Stack, data augmentation had only the slightest improvements on volume SG9202_Full_Stack. This is also the case for adjustment of hyperparameters. This is most likely caused by the poor quality of the seismic images of volume SG9202_Full_Stack compared to the two other volumes. The seismic data in volume SG9202_Full_Stack is generally noisy making it difficult to detect faults. This may further indicate that data augmentation is not suited for improving CNN fault predictions on noisy seismic data.

5.2 Fault Characterization using ML predicted faults

When detecting, analyzing and characterizing geological features in seismic such as faults, the resolution of the seismic data in many cases is a limiting factor. Seismic resolution generally limits the level of available details. In contrast, outcrop studies provide the possibility of more detailed small-scale analysis (Walsh and Watterson, 1988; Shipton et al., 2006; Wibberley et al., 2008; Bastesen et al., 2013; Childs et al., 2009). On the other hand, the advantage of using 3D seismic data to characterize faults is the ability to provide a better overview of the faults as part of a fault system as well as a 3D structure of individual faults at seismic scale. In addition, the seismic volume LN17001_Full_Stack in survey LN17001 3D survey is collected using TopSeis-technology. This results in higher seismic resolution (8.33 m inline spacing and 6.25 m crossline spacing) compared to traditional full stack seismic

technology such as the two other seismic surveys (12.50 m inline and crossline spacing) utilized in this study. TopSeis-technology improves the clarity of seismic images, improving the resolution for tasks such as characterizing faults and their damage zone compared to previous seismic methods.

Seismic resolution is not the only factor limiting detail. In addition, the length of the chosen scanlines for the task of fault characterization only allows to characterize to a certain amount of detail. Due to the extent of the seismic survey and the large dimensions (faults reach heights of at least 12 km) of the major faults present (referring to F1, F2, F3, F4 and F5), in this area of specific interest, is it making sense to choose scanlines and intervals that match these dimensions. For instance, the dimensions of the scanlines (>20 km length) and the intervals in the fault frequency plots have to be fitted to the seismic resolution. Meaning that the spacing of intervals needs to be appropriate with respect to the spacing between faults occurring in the seismic images, thus 1 kilometer fault frequency plot spacing was chosen. This spacing limits the level of precision of the fault frequency plots when it comes to determining the characteristics such as the extent of the fault damage zone. On the other hand, increasing the precision of the fault frequency plots by reducing the interval spacing, reduces the number of registered faults and therefore their frequency. The inaccuracy of the fault frequency plot is demonstrated in figure 5-2. The damage zone of F3 on Inline 5000 (800ms TWT) is determined by the use of a cumulative fault frequency plot, visualizing the damage zone of the fault with a grey background. The cumulative fault frequency plot is suggesting the total width of the damage zone to be 4 km. The damage zone is asymmetric and wider on the footwall (FW). We manage to determine the fault damage zone on a km-scale, but not more precise than that.

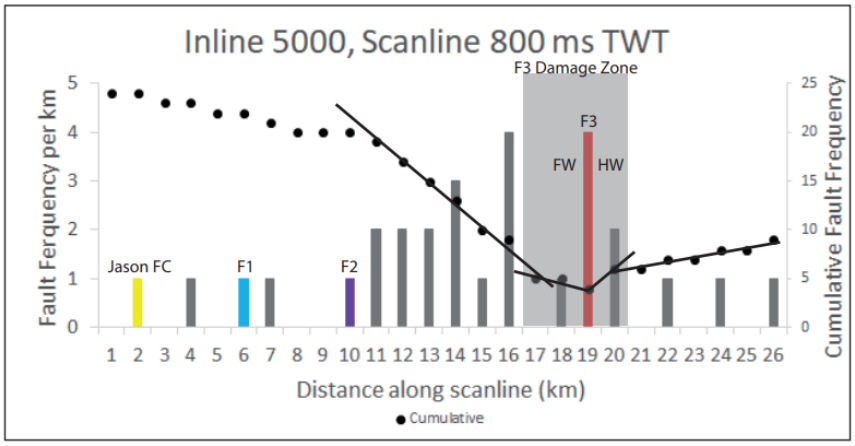

Figure 5-2: Diagram from Inline 5000 (800ms TWT) in 3D seismic volume LN17001_Full_Stack. The diagram is combining fault a frequency plot (in columns) with a cumulative fault frequency plot (dots). In the cumulative fault frequency plot the number of faults increases away from F3 on either side. The black lines indicate the change in slope for the cumulative plot. The estimated damage zone of F3 is marked in grey. FW = footwall. HW = hanging wall.

6 Conclusions

This study explores the use of deep learning for identification and characterization of faults as a supervised binary segmentation problem on three separate 3D seismic volumes from different seismic surveys located on the Norwegian Continental Shelf. The 3D seismic volumes cover different characteristics in terms of fault geometries, scales and seismic data quality. In this study I utilized Efficient UNET and Light UNET CNN, derived from the UNET CNN architecture originally developed for semantic segmentation tasks in the field of medical research. Mainly, this study was conducted for the purpose of two things 1) exploring how the application of data augmentation to training data and the adjustment of hyperparameter values during the learning process of CNN would affect the fault identification performance, and 2) Extracting fault statistics from ML predicted fault probability volumes to characterize some of the imaged faults and study the link between distribution of smaller faults around larger faults. We conclude this study with the following remarks:

- Appropriate adjustment of parameters controlling the degree of geometric transformation applied by the data augmentation techniques to the seismic training data, sets a solid base for the CNN fault prediction quality.
- Data augmentation in general improved the CNN capacity, thus improving fault predictions. Improvement was commonly noticed by performing visual checks of the fault predictions in seismic, while the model scores generally either indicated worse or hardly noticeable improvement when data augmentation was applied to CNN.
- The quality and characteristics of the seismic data plays a significant role, controlling the amount of improvement data augmentation can give the CNN fault predictions. The adjustment of hyperparameters can additionally improve the CNN fault prediction, although the improvement of fault predictions is significantly limited by poor seismic quality.
- Characterizing faults imaged through deep learning in seismic data provides a data driven source of fault distribution.
- In the specific LN17001_Full_Stack 3D seismic volume characterization of fault geometries and the width of fault damage zone was possible while utilizing CNN fault predictions. Although, precision was limited by the large scale of faults, scanlines and interval spacing of the fault frequency plots.

7 References

- Admasu, F., Back, S. and Toennies, K. (2006). Autotracking of faults on 3D seismic data, *Geophysics,* 71(6), pp. A49-A53. doi: 10.1190/1.2358399.
- Agarwal, R. (2019) *The 5 Classification Evaluation metrics every Data Scientist must know.* Available at https://towardsdatascience.com/the-5-classification-evaluation-metrics-you-must-know-aa97784ff226 (Accessed 12.01.2022).
- Agterberg, F. P. (1966). Markov schemes for multivariate well data, *Proceedings, symposium on applications of computers and operations research in the mineral industries*, 2, pp. X1–X18.
- Ahmed, S. (2020). Structural analysis of Horda Platform and Stord Basin in the Norwegian North Sea using Machine Learning methods. Master's Thesis. University of Oslo.
- Aseev, A., Deng, A. and Fan, D. (2019). Application of Deep Learning in Subsurface Faults Detection With Seismic Data, *CS230,* Stanford University.
- Aqrawi, A. A. and Boe T. H. (2011). Improved fault segmentation using a dip guided and modified 3D Sobel filter, *SEG Technical Program Expanded Abstracts,* pp. 999-1003. doi: 10.1190/1.3628241.
- Badrinarayanan, V., Kendall, A. and Cipolla, R. (2017). SegNet: A Deep Convolutional Encoder-Decoder Architecture for Image Segmentation, *IEEE Transactions on Pattern Analysis and Machine Intelligence,* 39(12), pp. 2481-2495. doi: 10.1109/TPAMI.2016.2644615.
- Bahorich, M. and Farmer, S. (1995). 3-D seismic discontinuity for faults and stratigraphic features; the coherence cube, *The Leading edge,* 14(10), pp. 1053-1058. doi: 10.1190/1.1437077.
- Bakker, P. (2002). Image structure analysis for seismic interpretation, Ph. D. thesis, Delft University of Technology.
- Barnett, J. A., Mortimer, J., Rippon, J. H., Walsh, J. J. and Watterson, J. (1987). Displacement geometry in the volume containing a single normal fault, *AAPG bulletin,* 71(8), pp. 925-937. doi:10.1306/948878ED-1704-11D7-8645000102C1865D.
- Bastesen, E., Braathen, A., Nøttveit, H., Gabrielsen, R. H. and Skar, T. (2009). Extensional fault cores in micritic carbonates – Case studies from the Gulf of Corinth, Greece, *Journal of Structural geology,* 31(4), pp. 403-420. doi: 10.1016/j.jsg.2009.01.005.
- Bastesen, E., Braathen, A. and Skar, T. (2013). Comparison of scaling relationships of extensional fault cores in tight carbonate and porous sandstone reservoirs, *Petroleum geoscience,* 19(4), pp 385-398. doi: 10.1144/petgeo2011-020.
- Baudon, C. and Cartwright, J. (2008). The kinematics of reactivation of normal faults using high resolution throw mapping, *Journal of Structural Geology,* 30(8), pp. 1072–1084. doi: 10.1016/j.jsg.2008.04.008.
- Bell, R. E., Jackson, C. A-L., Whipp, P. S. and Clements, B. (2014). Strain migration during multiphase extension: Observations from the northern North Sea, *Tectonics,* 33(10), pp. 1935-1963. doi: 10.1002/2014TC003551.
- Bense, V. F., Gleeson, T., Loveless, S. E., Bour, O. and Scibek, J. (2013). Fault zone hydrology, *Earth-science reviews,* 127, pp. 171-192. doi: 10.1016/j.earscirev.2013.09.008.
- Bergh, S.G. and Grogan, P. (2003). Tertiary structure of the Sørkapp-Hornsund Region, South Spitsbergen, and implications for the offshore southern extension of the fold-thrust belt, *Norsk Geologisk Tidsskrift*, 83(1), pp. 43–60.

- Berglund, L.T., Augustson, J., Færseth, R., Gjelberg, J. and Ramberg-Moe, H. (1986). The evolution of the Hammerfest Basin, in: Spencer, A. M., Campbell, C. J., Hanslien, S. H., Holter, E., Nelson, P. H. H., Nysæther, E. and Ormaasen, E. G. (eds) *Habitat of Hydrocarbons on the Norwegian Continental Shelf.* London: Graham & Trotman, pp. 319–338.
- Bergslien, D. (2002). Balder and Jotun – two sides of the same coin? A comparison of two Tertiary oil fields in the Norwegian North Sea, *Petroleum geoscience,* 8(4), pp. 349-363. doi: 10.1144/petgeo.8.4.349.
- Besly, B. M. (1998). Carboniferous, in Glennie K. W. (eds.) *Petroleum Geology of the North Sea: Basic Concepts and Recent Advances* (4th edn.), London: Blackwell Science, pp. 104-136. doi: 10.1002/9781444313413.
- Bhattacharyya, S., Jha, S., Tharakunnel, K. and Westland, J. C. (2011). Data mining for credit card fraud: A comparative study, *Decision Support Systems*, 50(3), pp. 602-613. doi: 10.1016/j.dss.2010.08.008.
- Boiy, E. and Moens, M-F. (2009). A machine learning approach to sentiment analysis in multilingual Web texts, *Information retrieval*, 12, pp. 526-558. doi: 10.1007/s10791-008-9070-z.
- Braathen, A., Tvervanger, J., Fossen, H., Skar, T., Cardozo, N., Semshaug, S. E., Bastesen, E. and Sverdrup, E. (2009). Fault facies and its application to sandstone reservoirs, *AAPG bulletin,* 93(7), pp. 891-917. doi: 10.1306/03230908116.
- Breiman, L. (2001). Random forests, *Machine learning,* 45(1), pp. 5-32. doi: 10.1023/A:1010933404324.
- Breivik, A.J., Faleide, J.I. and Gudlaugsson, S.T. (1998). Southwestern Barents Sea margin: late Mesozoic sedimentary basins and crustal extension, *Tectonophysics*, 293(1-2), pp. 21–44. doi: 10.1016/S0040-1951(98)00073-0.
- Brekke, H. (2000). The tectonic evolution of the Norwegian Sea Continental Margin with emphasis on the Vøring and Møre basins, *Geological Society, London, Special Publications*, 167(1), pp. 327-378. doi: 10.1144/GSL.SP.2000.167.01.13.
- Brekke, H., Sjulstad, H. I., Magnus, C. and Williams, R.W. (2001). Sedimentary environments offshore Norway – an overview, *Norwegian Petroleum Society Special Publications,* 10, pp. 7-37. doi: 10.1016/S0928-8937(01)80006-0.
- Bruce, D. R. S. and Stemmerik, L. (2003). Carboniferous, in: Evans, D., Graham, C., Armour, A. and Bathurst, P. (eds.) *The Millennium Atlas: Petroleum geology of the central and northern North Sea,* London: The Geological Society of London, pp. 83-89.
- Bryn, P., Berg, K., Forsberg, C.F., Solheim, A. and Kvalstad, T.J. (2005). Explaining the Storegga Slide, *Marine and Petroleum Geology*, 22(1-2), pp. 11-19. doi: 10.1016/j.marpetgeo.2004.12.003.
- Cao, J. and Roy, B. (2017). Time-lapse reservoir property change estimation from seismic using machine learning, *The Leading Edge*, 36(3), pp. 234–238. doi: 10.1190/tle36030234.1.
- Caumon, G., Collon-Drouaillet, P., Le Carlier de Veslud, C., Viseur, S. and J. Sausse. (2009). Surface-based 3D Modeling of Geological Structures, *Mathematical Geosciences*, 41(8), pp. 927–945. doi: 10.1007/s11004-009-9244-2.
- Chaki, S., Routray, A. and Mohanty, W. K. (2018). Well-Log and Seismic Data Integration for Reservoir Characterization: A Signal Processing and Machine-Learning Perspective, *IEEE Signal Processing Magazine,* 35(2), pp. 72-81. doi: 10.1109/MSP.2017.2776602.

- Chang, C-C. and Lin, C-J. (2011). LIBSWM: A library for support vector machines, *ACM transactions on intelligent systems and technology,* 2(3), pp. 1-27. doi: 10.1145/1961189.1961199.
- Charnock, M. A., Kristiansen, I. L., Ryseth, A. and Fenton, J. P. G. (2001). Sequence Stratigraphy of the Lower Jurassic Dunlin Group, Northern North Sea, *Norwegian Petroleum Society Special Publications,* 10, pp. 145-174. doi: 101016/S0928-8937(01)80012-6.
- Childs, C., Manzocchi, T., Walsh, J. J., Bonson, C. G., Nicol, A. and Schöpfer, M. P. J. (2009). A geometric model of fault zone and fault rock thickness variations, *Journal of structural geology,* 31(2), pp. 117-127. doi: 10.1016/j.jsg.2008.08.009.
- Christiansson, P., Faleide, J. I. and Berge, A. M. (2000). Crustal structure in the northern North Sea: an integrated geophysical study, *Geological Society, London, Special Publications,* 167(1), pp. 15-40. doi: 10.1144/GSL.SP.2000.167.01.02.
- Ching, T., Himmelstein, D. S., Beaulieu-Jones, B. K., Kalinin, A. A., Do, B. T., Way, G. P., Ferrero, E., Agapow, P-M., Zietz, M., Hoffman, M. M., Xie, W., Rosen, G. L., Lengerich, B. J., Israeli, J., Lanchantin, J., Woloszynek, S., Carpenter, A. E., Shrikumar, A., Xu, J., Cofer, E. M., Lavender, C. A., Turaga, S. C., Alexandari, A. M., Lu, Z., Harris, D. J., DeCaprio, D., Qi, Y., Kundaje, A., Peng, Y., Wiley, L. K., Segler, M. H. S., Boca, M. S., Swamidass, S. J., Huang, A., Gitter, A. and Greene, C. S. (2018). Opportunities and obstacles for deep learning in biology and medicine, *Journal of the Royal Society interface*, 15(141). doi: 10.1098/rsif.2017.0387.
- Choi, J-H., Edwards, P., Ko, K. and Kim, Y-S. (2016). Definition and classification of fault damage zones: A review and a new methodological approach, *Earth-science reviews,* 152, pp. 70-78. doi: 10.1016/j.earscirev.2015.11.006.
- Clark, S.A., Glørstad-Clark, E., Faleide, J.I., Schmid, D., Hartz, E.H. and Fjeldskaar, W. (2014). Southwest Barents Sea rift basin evolution: comparing results from backstripping and time-forward modelling, *Basin Research*, 26(4), pp. 550-566. doi: 10.1111/bre.12039.
- Clemmensen, L., Steel, R. and Jacobsen, V. (1980). Some aspects of Triassic sedimentation and basin development: east Greenland, north Scotland and North Sea, in: Norsk Petroleumsforening, *The Sedimentation of North Sea Reservoir Rocks, 11-14 May,* Geilo, Norway, pp. 1-21.
- Cortes, C. and Vapnik, V. (1995). Support-vector networks, *Machine learning*, 20(3), pp. 273–297. doi: 10.1007/BF00994018.
- Coward, M. P., Dewey, J. F., Hempton, M., Holroyd, L. and Mange, M. A. (2003). Tectonic evolution, in: Evans, D., Graham, C., Armour, A. and Bathurst, P. (eds.) *The Millennium Atlas: Petroleum geology of the central and northern North Sea*. London: The Geological Society of London, pp. 17-33.
- Cowie, P. A. and Scholz, C. H. (1992). Growth of faults by accumulation of seismic slip, *Journal of Geophysical Research,* 97(B7), pp. 11085-11095. doi: 10.1029/92JB00586.
- Cubuk, E. D., Zoph, B., Mane, D., Vasudevan, V. and Le, Q. V. (2018). AutoAugment: Learning Augmentation Policies from Data, *arXiv.* doi: 10.48550/arXiv.1805.09501.
- Dahlgren, K.I.T., Vorren, T.O., Stoker, M.S., Nielsen, T., Nygård, A. and Sejrup, H.P. (2005). Late Cenozoic prograding wedges on the NW European continental margin: their formation and relationship to tectonics and climate, *Marine and Petroleum Geology*, 22(9-10), pp. 1089-1110. doi: 10.1016/j.marpetgeo.2004.12.008.
- Datacamp. (2019) *Neural Network Models in R*. Available at: https://www.datacamp.com/community/tutorials/neural-network-models-r (Accessed 12.01.2022).

- Davies, R. J., O'Donnell, D., Bentham, P. N., Gibson, J. P. C., Curry, M. R., Dunay, E. and Maynard, J. R. (1999). The origin and genesis of major Jurassic unconformities within the triple junction area of the North Sea, UK, *Geological Society, London, Petroleum Geology Conference series, 5, pp. 117-131. doi: 10.1144/0050117.*
- Dawers, N. H., Anders, M. H. and Scholz, C. H. (1993). Growth of normal faults; displacement-length scaling, *Geology (Boulder),* 21(12), pp. 1107-1110. doi: 10.1130/0091-7613(1993)021<1107:GONFDL>2.3.CO;2.
- Deng, C., Fossen, H., Gawthorpe, R. L., Rotevatn, A., Jackson, C. A-L. and Fazlikhani, H. (2017). Influence of fault reactivation during multiphase rifting: The Oseberg area, northern North Sea rift, *Marine and petroleum geology,* 86, pp. 1252-1272. doi: 10.1016/j.marpetgeo.2017.07.025.
- Deza, M. M. and Deza, E. (2009). *Encyclopedia of distances.* Berlin: Springer.
- Di, H., Shafiq, M. and AlRegib, G. (2018). Patch-level MLP classification for improved fault detection, *SEG Technical Program Expanded Abstracts,* pp. 2211-2215. doi: 10.1190/segam2018-2996921.1.
- Dimakis, P., Braathen, B.I., Faleide, J.I., Elverhøi, A. and Gudlaugsson, S.T. (1998). Cenozoic erosion and the preglacial uplift of the Svalbard-Barents Sea region, *Tectonophysics*, 300(1-4), pp. 311-327. doi: 10.1016/S0040-1951(98)00245-5.
- Dodge, D. A. and Harris, D. B. (2016). Large-Scale Test of Dynamic Correlation Processors: Implications for Correlation-Based Seismic Pipelines, *Bulletin of the Seismological Society of America,* 106(2), pp. 435-452. doi: 10.1785/0120150254.
- Doré, A. G. (1991). The structural foundation and evolution of Mesozoic seaways between Europe and the Arctic, *Palaeogeography, Palaeoclimatology, Palaeoecology,* 87(1-4), pp. 441-492. doi: 10.1016/0031-0182(91)90144-G.
- Dorn, G., James, H., Dopkin, D. and Payne, B. (2005). Automatic Fault Extraction in 3D Seismic Interpretation, *Conference Proceedings, 67th EAGE Conference and Exhibition*. doi: 10.3997/2214-4609-pdb.1.F035.
- Dowla, F. U., Taylor, S. R. and Anderson, R. W. (1990). Seismic discrimination with artificial neural networks: Preliminary results with regional spectral data, *Bulletin of the Seismological Society of America,* 80(5), pp. 1346-1373.
- Downie, R. (1998). Devonian, in Glennie, K. W. (eds.) *Petroleum Geology of the North Sea: Basic Concepts and Recent Advances* (4th edn.), London: Blackwell Science, pp. 85-103. doi: 10.1002/9781444313413.
- Dozat, T (2016). Incorporating Nesterov Momentum into Adam, *Workshop track-ICLR 2016.*
- Dramsch, J. S. (2020). Chapter One – 70 years of machine learning in geoscience in review, *Advances in Geophysics,* 61, pp. 1-55. doi: 10.1016/bs.agph.2020.08.002.
- Dreyer, T., Whitaker, M., Dexter, J., Flesche, H. and Larsen, E. (2005). From spit system to tide-dominated delta: integrated reservoir model of the Upper Jurassic Sognefjord Formation on the Troll West Field, *Geological Society, London, Petroleum Geology Conference series,* 6(1), pp. 423-448. doi: 10.1144/0060423.
- Duchi, J., Hazan, E. and Singer, Y. (2011). Adaptive subgradient methods for online learning and stochastic optimization, *Journal of machine learning research,* 12, pp. 2121-2159.
- Duque-Arias, D., Velasco-Forero, S., Deschaud, J-E., Goulette, F., Serna, A., Decenière, E. and Marcotegui, B. (2021). On Power Jaccard Losses for Semantic Segmentation, *Proceedings of the 16th International Joint Conference on Computer Vision, Imaging and Computer Graphics Theory and Applications.* pp. 561-568. DOI: 10.5220/0010304005610568.

- Ellevset, S. O., Knipe, R. J., Olsen, T. S., Fisher, Q. J. and Jones, G. (1998). Fault controlled communication in the Sleipner Vest Field, Norwegian continental shelf; detailed, quantitative input for reservoir simulation and well planning, *Geological Society, London, Special Publications,* 147(1), pp. 283–297. doi: 10.1144/GSL.SP.1998.147.01.19.
- Evans, D., Harrison, Z., Shannon, P.M., Laberg, J.S., Nielsen, T., Ayers, S., Holmes, R., Hoult, R.J., Lindberg, B., Haflidason, H., Long, D., Kuijpers, A., Andersen, E.S. and Bryn, P. (2005). Palaeoslides and other mass failures of Pliocene to Pleistocene age along the Atlantic continental margin of NW Europe, *Marine and Petroleum Geology*, 22(9-10), pp. 1131-1148. doi: 10.1016/j.marpetgeo.2005.01.010.
- Faleide, J. I., Bjørlykke, K. and Gabrielsen, R. H. (2015). Geology of the Norwegian Continental Shelf, *Petroleum Geoscience,* pp. 603-637. doi: 10.1007/978-3-642-34132-8_25.
- Faleide, J. I., Gudlaugsson, S. T. and Jacquart, G. (1984). Evolution of the western Barents Sea, *Marine and petroleum geology,* 1(2), pp. 123-150. doi: 10.1016/0264-8172(84)90082-5.
- Faleide, J.I., Solheim, A., Fiedler, A., Hjelstuen, B.O., Andersen, E.S. and Vanneste, K. (1996), Late Cenozoic evolution of the western Barents Sea-Svalbard continental margin, *Global and Planetary Change*, 12(1-4), pp. 53-74. doi: 10.1016/0921-8181(95)00012-7.
- Faleide, J.I., Tsikalas, F., Breivik, A.J., Mjelde, R., Ritzmann, O., Engen, O. and Eldholm, O. (2008). Structure and evolution of the continental margin off Norway and the Barents Sea*. Episodes*, 31(1), pp. 82–91. doi: 10.18814/epiiugs/2008/v31i1/012.
- Faleide, J.I., Vågnes, E., and Gudlaugsson, S.T. (1993). Late Mesozoic-Cenozoic evolution of the southwestern Barents Sea, *Geological Society, London, Petroleum Geology Conference series,* 4(1), pp. 933-950. doi: 10.1144/0040933.
- Fisher, M. J. and Mudge, D. C. (1998). Triassic, in: Glennie, K. W. (eds.) *Petroleum Geology of the northern North Sea: Basic Concepts and Recent Advances* (4th edn.). London: Blackwell Science, pp. 212-244. doi: 10.1002/9781444313413.
- Fossen, H., Dallmann, W. and Andersen, T. B. (2008). The mountain chain rebounds and founders. The Caledonides are worn down: 405-359 million years, in: Ramberg, I. B., Bryhni, I., Nøttvedt, A. and Rangers, K. (eds.) *The making of a land. Geology of Norway,* Norsk Geologisk Forening, pp. 232-259.
- Fredman, N., Tveranger, J., Semshaug, S., Braathen, A. and Sverdrup, E. (2007). Sensitivity of fluid flow to fault core architecture and petrophysical properties of fault rock in siliciclastic reservoirs; a synthetic fault model study, *Petroleum geoscience,* 13(4), pp. 305-320. doi: 10.1144/1354-079306-721.
- Frid-Adar, M., Diamant, I., Klang, E., Amitai, M., Goldberger, J. and Greenspan, H. (2018). GAN-based synthetic medical image augmentation for increased CNN performance in liver lesion classification, *Neurocomputing,* 321, pp. 321-331. doi: 10.1016/j.neucom.2018.09.013.
- Færseth, R. B., Gabrielsen, R. H. and Hurich, C. A. (1995). Influence of basement in structuring of the North Sea Basin, offshore southwest Norway, *Norsk Geologisk Tidsskrift,* 75(2-3), pp. 105-119.
- Færseth, R. B. and Ranvås, R. (1998). Evolution of the Oseberg fault-block in context of the northern north sea structural framework, *Marine and Petroleum gGology,* 15(5), pp. 467-490. doi: 10.1016/S0264-8172(97)00046-9.
- Fulkerson, B. (1995). Machine Learning, Neural and Statistical Classification, *Technometrics,* 37(4), pp. 459. doi: 10.1080/00401706.1995.10484383.

- Gabrielsen, R.H. (1984). Long-lived fault zones and their influence on the tectonic development of the southwestern Barents Sea, *Journal of the Geological Society*, 141(4), pp. 651–662. doi: 10.1144/gsjgs.141.4.0651.
- Gabrielsen, R. H. and Færseth, R. B. (1988). Cretaceous and Tertiary reactivation of master fault zones of the Barents Sea, in: Dallmann, W. K., Ohta, Y. and Andresen, A. (eds.) *Tertiary Tectonics of Svalbard. Extended Abstracts from Symposium Held in Oslo*, Norwegian Polar Institute Report Series, 46, pp. 93–97.
- Gabrielsen, R.H., Færseth, R.B. and Jensen, L.N. (1990). *Structural Elements of the Norwegian Continental Shelf, Part 1: The Barents Sea Region*. Stavanger: Norwegian Petroleum Directorate.
- Gabrielsen, R.H., Grunnaleite, I. and Ottesen, S. (1993). Reactivation of fault complexes in the Loppa High area, southwestern Barents Sea, *Norwegian Petroleum Society Special Publications,* 2, pp. 631–641. doi: 10.1016/B978-0-444-88943-0.50041-1.
- Gabrielsen, R.H., Grunnaleite, I. and Rasmussen, E. (1997). Cretaceous and Tertiary inversion in the Bjørnøyrenna Fault Complex, south-western Barents Sea, *Marine and Petroleum Geology*, 14(2), pp. 165-178. doi: 10.1016/S0264-8172(96)00064-5.
- Gabrielsen, R. H., Faleide, J. I., Pascal, C., Braathen, A., Nystuen, J. P., Etzelmuller, B. and O'Donnell, S. (2010). Latest Caledonian to Present tectonomorphological development of southern Norway, *Marine and petroleum geology,* 27(3), pp. 709-723. doi: 10.1016/j.marpetgeo.2009.06.004.
- Gabrielsen, R. H., Faleide, J. I., Leever, K. A. and Grunnaleite, I. (2011). Strike-slip related inversion-tectonics of the southwestern Barents Sea (Norwegian Shelf) in a plate tectonic perspective, *Geophysical Research Abstracts,* 13, EGU2011-9229.
- Gatys, L. A., Ecker, A. S. and Bethge, M. (2015). A neural algorithm of artistic style, *ArXiv.* doi: 10.48550/arXiv.1508.06576.
- Gersztenkorn, A. and Marfurt, K. J. (1999). Eigenstructure-based coherence computations as an aid to 3-D structural and stratigraphic mapping, *Geophysics,* 64(5), pp. 1468-1479. doi: 10.1190/1.1444651.
- Girshick, R., Donahue, J., Darrell, T. and Malik, J. (2014). Rich feature hierarchies for accurate object detection and semantic segmentation, *2015 IEEE Conference on Computer Vision and Pattern Recognition,* pp. 580-587. Doi: 10.1109/CVPR.2014.81.
- Glennie, K. W. (1995). Permian and Triassic rifting in northwest Europe, *Geological Society, London, Special Publication,* 91(1), pp. 1-5. doi: 10.1144/GSl.SP.1995.091.01.01.
- Glennie, K. W. and Underhill, J. R. (1998). Origin, Development and Evolution of Structural Styles, in: Glennie, K.W. (eds.) *Petroleum Geology of the North Sea: Basic Concepts and Recent Advances* (4th edn.). London: Blackwell Science, pp. 42-84. doi: 10.1002/9781444313413.
- Glørstad-Clark, E. (2011). Basin analysis in western Barents Sea area: The interplay between accommodation space and depositional system, PhD thesis, University of Oslo.
- Glørstad-Clark, E., Faleide, J.I., Lundschien, B.A. and Nystuen, J.P. (2010). Triassic seismic sequence stratigraphy and paleogeography of the western Barents Sea area, *Marine and Petroleum Geology*, 27(7), pp. 1448–1475. doi: 10.1016/j.marpetgeo.2010.02.008.
- Gómez, R. (2018). *Understanding Categorical Cross-Entropy Loss, Binary Cross-Entropy Loss, Softmax Loss, Logistic Loss, Focal Loss and all those confusing names.* Available at https://gombru.github.io/2018/05/23/cross_entropy_loss/ (Accessed 12.01.2022).

- Goodfellow, I. J., Pouget-Abadie, J., Mirza, M., Xu, B., Warde-Farley, D., Ozair, S., Courville, A. and Bengio, Y. (2014). Generative Adversarial Networks, *NIPS.*
- Goodfellow, I., Bengio, Y. and Courville, A. (2016) *Deep Learning.* MIT Press. Available at: https://www.deeplearningbook.org/ (Accessed 07.04.2022).
- Gregersen, U., Michelsen, O. and Sørensen, J. C. (1997). Stratigraphy and facies distribution of the Utsira formation and the Pliocene sequences in the northern North Sea, *Marine and Petroleum Geology,* 14(7-8), pp. 893-914. doi: 10.1016/S0264-8172(97)00036-6.
- Grogan, P., Østvedt-Ghazi, A.M., Larssen, G.B., Fotland, B., Nyberg, K., Dahlgren, S. and Eidvin, T. (1999). Structural elements and petroleum geology of the Norwegian sector of the northern Barents Sea, *Geological Society, London, Petroleum Geology Conference series*, 5(1), pp. 247–259. doi: 10.1144/0050247.
- Groshong, R. H. (2006) *3-D Structural Geology: A Practical Guide to Quantitative Surface and Subsurface Map Interpretation.* 2nd edn. Berlin: Springer.
- Gudlaugsson, S.T., Faleide, J.I., Johansen, S.E. and Breivik, A.J. (1998). Late Paleozoic structural development of the South-western Barents Sea, *Marine and Petroleum Geology*, 15(1), pp. 73–102. doi: 10.1016/S0264-8172(97)00048-2.
- Guillen, P., Larrazabal, G., González, G., Boumber, D. and Vilalta, R. (2015). Supervised learning to detect salt body, *SEG Technical Program Expanded Abstracts,* pp. 1826-1829. doi: 10.1190/segam2015-5931401.1.
- Guo, B., Lu, L. and Luo, Y. (2018). A new method for automatic fault detection using convolutional neural network, *SEG Technical program expanded abstracts,* pp. 1951-1955. doi: 10.1190/segam2018-2995894.1.
- Hale, D. (2009). Structure-oriented smoothing and semblance, *CWP Report 635.*
- Hale, D. (2013). Methods to compute fault images, extract fault surfaces, and estimate fault throws from 3D seismic images, *Geophysics,* 78(2), pp. O33-O43. doi: 10.1190/geo2012-0331.1.
- Hall, M. and Hall, B. (2017). Distributed collaborative prediction: Results of the machine learning contest, *The Leading Edge,* 36 (3), pp. 267–269. doi: 10.1190/tle36030267.1.
- Hamann, N.E., Wittaker, R.C. and Stemmerik, L. (2005). Geological development of the Northeast Greenland Shelf, *Geological Society, London, Petroleum Geology Conference series,* 6, pp. 887–902. doi: 10.1144/0060887.
- Hamar, G., Jakobsson., Ormaasen, D. and Skarpnes, O. (1980). Tectonic development of the North Sea north of the Central Highs, in: Norsk Petroleumsforening, *The sedimentation of the North Sea Reservoir Rocks, 11-14 May,* Geilo, Norway, pp. 1-11.
- He, K., Gkioxari, G., Dollár, P. and Girshick, R. (2017). Mask R-CNN, *2017 IEEE International Conference on Computer Vision,* pp. 2980-2988. doi: 10.1109/ICCV.2017.322.
- Helland-Hansen, W., Ashton, M., Lømo, L. and Steel, R. (1992). Advance and retreat of the Brent delta: recent contributions to the depositional model, *Geological Society, London, Special Publications,* 61(1), pp. 109-127. doi: 10.1144/GSL.SP.1992.061.01.07.
- Hermes, L., Frieauff, D., Puzicha, J. and Buhmann, J. M. (1999). Support vector machines for land usage classification in Landsat TM imagery, 1, pp. 348–350. doi: 10.1109/IGARSS.1999.773494.
- Hjelstuen, B.O., Eldholm, O. and Faleide, J.I. (2007). Recurrent Pleistocene mega-failures on the SW Barents Sea margin, *Earth and Planetary Science Letters*, 258(3-4), pp. 605-618. doi: 10.1016/j.epsl.2007.04.025.

- Ho, T. K. (1995). Random decision forests, *Proceedings of 3rd international conference on document analysis and recognition*, 1, pp. 278–282. doi: 10.1109/ICDAR.1995.598994.
- Hochreiter, S. and Schmidhuber, J. (1997). Long short-term memory, *Neural computation,* 9(8), pp. 1735–1780.
- Huang, K-Y., Chang, W. R. I. and Yen, H. T. (1990). Self-organizing neural network for picking seismic horizons, *SEG Technical Program Expanded Abstracts,* pp. 313-316. doi: 10.1190/1.1890183.
- Huang, L., Dong, X. and Clee, T. E. (2017). A scalable deep learning platform for identifying geologic features from seismic attributes, *The Leading edge,* 36(3), pp. 249-256. doi: 10,1190/tle36030249.1.
- Hulbert, C., Rouet-Leduc, B., Ren, C. X., Riviere, J., Bolton, D. C., Marone, C. and Johnson, P. A. (2018). Estimating the Physical State of a Laboratory Slow Slipping Fault from Seismic Signals, *ArXiv.* doi: 10.48550/arXiv.1801.07806.
- Husmo, T., Hamar, G. P., Høiland, O., Johannessen, E. O., Rømuld, A., Spencer, D., Graham, C., Armour, A. and Bathurst, P. (eds.) *The Millennium Atlas: Petroleum geology of the central and northern North Sea.* London: The Geological Society of London, pp. 129-155.
- IBM Cloud Education (2020). *Recurrent Neural Networks.* Available at: https://www.ibm.com/cloud/learn/recurrent-neural-networks (Accessed 14.06.2022).
- Indrevær, K., Gabrielsen, R. H. and Faleide, J. I. (2016). Early Cretaceous synrift uplift and tectonic inversion in the Loppa High area, southwestern Barents Sea, Norwegien shelf, *Journal of the Geological Society,* 174(2), pp. 242-254. doi: 10.1144/jgs2016-066.
- Jaccard, J. (1901). Distribution de la flore alpine dans le bassin des dranses et dans quelques regions voisines. *Bulletin de la Societe Vaudoise des Sciences Naturelles,* 37(140), pp. 241-172. doi: 10.5169/seals-266440.
- Jamil, D. *Discussing Feed Forward & Back Propagation in Neural Networks.* Available at: https://d3nyal.medium.com/discussing-feed-forward-back-propagation-90032850782a (Accessed 14.06.2022).
- Jebsen, C. and Faleide, J.I. (1998). Tertiary rifting and magmatism at the western Barents Sea margin (Vestbakken volcanic province): III international conference on Arctic margins, ICAM III; abstracts; plenary lectures, talks and posters, pp. 92.
- Kadurin, A., Nikolenko, S., Khrabrov, K., Aliper, A. and Zhavoronkov, A. (2017). druGAN: An Advanced Generative Adversarial Autoencoder Model for de Novo Generation of New Molecules with Desired Molecular Properties in Silico, *molecular pharmaceutics,* 14(9), pp. 3098–3104. doi: 10.1021/acs.molpharmaceut.7b00346.
- Kim, Y-S. and Sanderson, D. J. (2005). The relationship between displacement and length of faults: a review, *Earth-science reviews,* 68(3-4), pp. 317-334. doi: 10.1016/j.earscirev.2004.06.003.
- Kingma, D. P. and Ba, J. (2014). Adam: A method for Stochastic Optimization, *arXiv.* doi: 10.48550/arXiv.1412.6980.
- Knipe, R. J., Jones, G. and Fisher, Q. J. (1998). Faulting, fault sealing and fluid flow in hydrocarbon reservoirs, *Geological Society, London, Special Publications,* 147(1), pp. vii-xxi. doi: 10.1144/GSL.SP.1998.147.01.01.
- Kohonen, T. (1982). Analysis of a simple self-organizing process, *Biological cybernetics*, 44(2), pp. 135-140. doi: 10.1007/BF00317973.
- Kolyukhin, D. and Torabi, A. (2012). Statistical analysis of the relationships between faults attributes, *Journal of Geophysical Research: Solid Earth,* 117(B5). doi: 10.1029/2011JB008880.

- Krizhevsky, A., Sutskever, I. and Hinton, G. E. (2012). Imagenet classification with deep convolutional neural networks, in: *Proceedings of the 25th International Conference on Neural Information Processing Systems*. Stand university, pp. 1097-1105.
- Krumbein, W. C. and Dacey, M. F. (1969). Markov chains and embedded markov chains in geology, *Journal of the International Association for Mathematical Geology*, 1(1), pp. 79–96.
- Kusznir, N. J. and Karner, G. D. (2007). Continental lithospheric thinning and breakup in response to upwelling divergent mantle flow: Application to the Woodlark, Newfoundland and Iberia margins, *Geological Society, London, Special Publications,* 282(1), pp. 389–419. doi: 10.1144/SP282.16.
- Kuzma, H. A. (2003). A support vector machine for AVO interpretation, *SEG Technical Program Expanded Abstracts*, 22(1), pp. 181–184. doi: 10.1190/1.1817668.
- Kyrkjebø, R., Gabrielsen, R. H. and Faleide, J. I. (2004). Unconformities related to the Jurassic-Cretaceous synrift-post-rift transition of the northern North Sea, *Journal of the Geological Society,* 161(1), pp. 1-17. doi: 10.1144/0016-764903-051.
- Laberg, J.S. and Vorren, T.O. (1996). The Middle and Late Pleistocene evolution of the Bear Island Trough Mouth Fan, *Global and Planetary Change*, 12(1-4), pp. 309-330. doi: 10.1016/0921-8181(95)00026-7.
- Laursen, I., Fugelli, E. and Lervik, K. S. (1995). Sequence stratigraphic framework of the Paleocene and Eocene successions, block 16/1,Norwegian North Sea, *Norwegian Petroleum Society Special Publication*, 5, pp. 471-481. doi: 10.1016/S0928-8937(06)80082-2.
- LeCun, Y. and Bengio, Y. (1998). Convolutional networks for images, speech, and time series, in: Arbib, M. A. (eds.) *The handbook of brain theory and neural networks*. MIT Press, pp. 255–258.
- LeCun, Y., Bengio, Y. and Hinton, G. (2015). Deep learning, *Nature,* 521, pp. 436-444. doi: 19.1038/nature14539.
- LeCun, Y., Bottou, L., Bengio, Y. and Hafner, P. (1998). Gradient-based learning applied to document recognition, *Proceedings of the IEEE*, 86(11), pp. 2278–2324. doi: 10.1109/5.726791.
- Lei, Y., Scheffer, N., Ferrer, L. and Mclaren, M. (2014). A novel scheme for speaker recognition using a phonetically-aware deep neural network, *2014 IEEE International 21 Conference on Acoustics, Speech and Signal Processing (ICASSP),* 04-09 May 2014.
- Lemley, j., Bazrafkan, S. and Corcoran, P. (2017). Smart Augment-Learning an Optimal Data Augmentation Strategy, *arXiv.* doi: 10.48550/arXiv.1703.08383.
- Lervik, K-S. (2006). Triassic lithostratigraphy of the Northern North Sea Basin, *Norsk Geologisk Tidsskrift,* 86(2), pp. 93-115.
- Liu, X., Liu, W., Mei, T. and Ma, H. (2016). A Deep Learning-Based Approach to Progressive Vehicle Re-Identification for Urban Surveillance, in: Leibe, B., Matas, J., Sebe, N. and Welling, M. (eds.) *Computer Vision – ECCV 2016. ECCV 2016. Lecture Notes in Computer Science, 9906*. Springer, Cham, pp. 869-884.
- Li, F. and Lu, W. (2014). Coherence attribute at different spectral scales, *Interpretation,* 2(1), pp. SA99-SA106. doi: 10.1190/INT-2013-0089.1.
- Lidmar-Bergström, K. (1982). *Pre-Quaternary geomorphological evolution in southern Fennoscandia.* Sveriges geologiska undersökning.

- Lidmar-Bergström, K. (1993). Denudation surfaces and tectonics in the southernmost part of the Baltic Shield, *Precambrian research,* 64(1-4), pp. 337-345. doi: 10.1016/0301-9268(93)90086-H.
- Long, J., Shelhamer, E. and Darrell, T. (2014). Fully Convolutional Networks for Semantic Segmentation, *arXiv.* doi: 10.48550/arXiv.1411.4038.
- Lundmark, A. M., Bue, E. P., Gabrielsen, R. H., Flaat, K., Strand, T. and Ohm S. E. (2013). Provenance of late Palaeozoic terrestrial sediments on the northern flank of the Mid North Sea High: detrital zircon geochronology and rutile geochemical constraints, *Geological Society special publication,* 386(1), pp. 243-259. doi: 10.1144/SP386.4.
- Luo, X., Jiang, C., Wang, W., Xu, Y., Wang, J-H. and Zhao, W. (2019). User behavior prediction in social networks using weighted extreme learning machine with distribution optimization, *Future Generation Computer Systems*, 93, pp. 1023-1035. doi: 10.1016/j.future.2018.04.085.
- Maggi, A., Ferrazzini, V., Hibert, C., Beauducel, F., Boissier, P. and Amemoutou, A. (2017). Implementation of a Multistation Approach for Automated Event Classification at Piton de la Fournaise Volcano, *Seismological Research Letters,* 88(3), pp. 878-891. doi: 10.1785/0220160189.
- Marfurt, K. J., Sudhaken, V., Gersztenkorn, A., Crawford, K. D. and Nissen, S. E. (1999). Coherency calculations in the presence of structural dip, *Geophysics,* 64(1), pp. 104-111. doi: 10.1190/1.1444508.
- Marjanovic, M., Kovacevic, M., Bajat, B. and Vozenilek, V. (2011). Landslide susceptibility assessment using SVM machine learning algorithm, *Engineering Geology,* 123(3), pp. 225-234. doi: 10.1016/j.enggeo.2011.09.006.
- Marsall, J. E. A. and Hewett, A. J. (2003). Devonian, in Evans, D., Graham, C., Armour, A. and Bathurst, P. (eds.) *The Millennium Atlas: Petroleum geology of the central and northern North Sea.* London: The Geological Society of London, pp. 65-81.
- Martire, I., da Silva, P., Plastino, A., Fabris, F. and Freitas, A. A. (2017). A novel probabilistic jaccard distance measure for classification of sparse and uncertain data, in: de Faria Paiva, E. R., Merschmann, L. and Cerri, R. (eds.) *5th Brazilian Symposium On Power Jaccard Losses for Semantic Segmentation 567 on Knowledge Discovery, Mining and Learning (KDMiLe),* pp. 81–88.
- Matalas, N. C. (1967). Mathematical assessment of synthetic hydrology, *Water Resources Research*, 3(4), pp. 937–945. doi: 10.1029/WR003i004p00937.
- Matcha, A. C. N. (2021) *A 2021 guide to Semantic Segmentation.* Available at https://nanonets.com/blog/semantic-image-segmentation-2020/ (Accessed 12.01.2022).
- Matlab one. (2022). *Recurrent neural networks (RNN).* Available at: https://matlab1.com/recurrent-neural-networks-rnn/ (Accessed 14.06.2022).
- McClay, K. R., Whitehouse, P. S., Dooley, T. and Richards, M. (2004). 3D evolution of fold and thrust belts formed by oblique convergence, *Marine and petroleum geology, 21(7), pp. 857-877. doi: 10.1016/j.marpetgeo.2004.03.009.*
- Mitchell, T. M. (1997). Machine learning. New York: McGraw-Hill.
- Mohri, M., Rostamizadeh, A. and Talwalker, A. (2012). *Foundations of machine learning*, The MIT Press.
- Mosser, L., Dubrule, O. and Blunt, M. J. (2018). Conditioning of three-dimensional generative adversarial networks for pore and reservoir-scale models, *arXiv.* doi: 10.48550/arXiv.1802.05622.

- Nesterov, Y. (1983). A method of solving a convex programming problem with convergence rate O ($1/k^2$), *Proceedings of the USSR Academy of Sciences,* 269, pp. 543-547.
- Newendorp, P. D. (1976). *Decision analysis for petroleum exploration*. United States.
- Nicol, A., Watterson, J., Walsh, J. J. and Childs, C. (1996). The shapes, major axis orientations and displacement patterns of fault surfaces, *Journal of structural geology,* 18(2-3), pp 235-248. doi: 10.1016/S0191-8141(96)80047-2.
- Nygård, A., Sejrup, H.P., Haflidason, H. and Bryn, P. (2005). The glacial North Sea Fan, southern Norwegian Margin: architecture and evolution from the upper continental slope to the deep-sea basin, *Marine and Petroleum Geology*, 22(1-2), pp. 71-84. doi: 10.1016/j.marpetgeo.2004.12.001.
- Nøttvedt, A., Gabrielsen, R. H. and Steel, R. J. (1995). Tectonostratigraphy and sedimentary architecture of rift basins, with reference to the northern North Sea, *Marine and Petroleum Geology,* 12(8), pp. 881-901. doi: 10.1016/0264-8172(95)98853-W.
- Nøttvedt, A., Johannessen, E. P. and Surlyk, F. (2008). The Mesozoic of Western Scandinavia and East Greenland, *Episodes,* 31(1), pp. 59-65. doi: 10.18814/epiiugs/2008/v31i1/009.
- Odinsen, T., Reemst, P., Van Der Beek, P., Faleide, J. I. and Gabrielsen, R. H. (2000). Permo-Triassic and Jurassic extension in the northern North Sea: results from tectonostratigraphic forward modelling, *Geological Society, London, Special Publications,* 167(1), pp. 83-103. doi: 10.1144/GSL.SP.2000.167.01.05.
- Paszke, A., Gross, S., Chintala, S., Chanan, G., Yang, E., DeVito, Z., Lin, Z., Desmaison, A., Antiga, L. and Lerer, A. (2017). Automatic differentiation in PyTorch, *31st Confence on,* Long Beach, CA, USA.
- Pedersen, S. I., Randen, T., Sønneland, L. and Steen, Ø. (2002). Automatic fault extraction using artificial ants, *SEG technical program expanded abstracts,* 21(1), pp. 512-515. doi: 10.1190/1.1817297.
- Pedersen, S. I., Skov, T., Hetlelid, A., Fayemendy, P., Randen, T. and Sønneland, L. (2003). New paradigm of fault interpretation, *SEG technical program expanded abstracts,* 22(1), pp. 350-353. doi: 10.1190/1.1817918.
- Pedregosa, F., Varoquaux, G., Gramfort, A., Michel, V., Thirion, B., Grisel, O., Blondel, M., Prettenhofer, P., Weiss, R., Dubourg, v., Vanderplas, J., Passos, A., Cournapeau, D., Brucher, M., Perrot, M. and Duchesnay, E. (2011). Scikit-learn: Machine learning in Python, *Journal of Machine Learning Research,* 12, pp. 2825–2830. doi: 10.5555/1953048.2078195.
- Perez, L. and Wang, J. (2017). The Effectiveness of Data Augmentation in Image Classification using Deep Learning, *arXiv.* doi: 10.48550/arXiv.1712.04621.
- Phillips, T. B., Fazlikhani, H., Gawthorpe, R. L., Fossen, H., Jackson, C. A-L., Bell, R. E., Faleide, J. I. and Rotevatn, A. (2019). The Influence of Structural Inheritance and Multiphase Extension on Rift Development, the Northern North Sea, *Tectonics,* 38(12), pp. 4099-4126. doi: 10.1029/2019TC005756.
- Preston, F. W. and Henderson, J. (1964). Fourier Series Characterization of Cyclic Sediments for Stratigraphic Correlation, in Merriam, D. F. (eds.) *Symposium on cyclic sedimentation*, Kansas Geological Survey, Bulletin 169, pp. 415-424.
- Preto, N., Kustatscher, E. and Wignall, P. B. (2010). Triassic climates – State of the art and perspectives, *Palaeogeography, Palaeoclimatology, Palaeoecology,* 290(1-4), pp. 1-10. doi: 10.1016/j.palaeo.2010.03.015.
- Rahman, M. A. and Wang, Y. (2016). Optimizing intersection-over-union in deep neural networks for image segmentation, in: *Advances in Visual Computing. ISVC*

2016. Lecture Notes in Computer Science, 10072, Springer: Cham, pp. 234–244. doi: 10.1007/978-3-319-50835-1_22.

- Rattey, R. P. and Hayward, A. B. (1993). Sequence stratigraphy of a failed rift system: the Middle Jurassic to Early Cretaceous basin evolution of the Central and Northern North Sea, *Geological Society, London, Petroleum Geology Conference series,* 4(1), pp. 215-249. doi: 10.1144/0040215.
- Ravnås, R. and Bondevik, K. (1997). Architecture and controls on Bathonian-Kimmeridgian shallow-marine synrift wedges of the Oseberg-Brage area, northern North Sea, *Basin research,* 9(3), pp. 197-226. doi: 10.1046/j.1365-2117.1997.00041.x.
- Ravnås, R., Nøttvedt, A., Steel, R. J. and Windelstad, J. (2000). Syn-rift sedimentary architectures in the Northern North Sea, *Geological Society, London, Special Publications,* 167(1), pp. 133-177. doi: 10.1144/GSL.SP.2000.167.01.07.
- Reddy, R. and Bonham-Carter, G. (1991). A decision-tree approach to mineral potential mapping in snow lake area, Manitoba, *Canadian Journal of Remote Sensing*, 17(2) pp. 191–200. doi: 10.1080/07038992.1991.10855292.
- Redmon, J., Divvala, S., Girshick, R. and Farhadi, A. (2016). You Only Look Once: Unified, Real-Time Object Detection, *ArXiv.* doi: 10.48550/arXiv.1506.02640.
- Ren, S., He, K., Girshick, R. and Sun, J. (2017). Faster R-CNN: Towards Real-Time Object Detection with Region Proposal Networks, *IEEE Transactions on Pattern Analysis and Machine Intelligence,* 39(6), pp. 1137-1149. doi: 10.1109/TPAMI.2016.2577031.
- Riber, L., Dypvik, H. and Sørlie, R. (2015). Altered basement rocks on the Utsira High and its surroundings, Norwegian North Sea, *Norwegian Journal of Geology,* 95(1), pp. 57-89. doi: 10.17850/njg95-1-04.
- Riis, F., Vollset, J. and Sand, M. (1986). Tectonic development of the western margin of the Barents Sea and adjacent areas, in: Halbouty, M.T. (eds.) *Future Petroleum Provinces of the world*, AAPG Special Volumes, 40, pp. 661–675. doi: 10.1306/M40454C31.
- Rise, L., Ottesen, D., Berg, K. and Lundin, E. (2005). Large-scale development of the mid-Norwegian margin during the last 3 million years, *Marine and Petroleum Geology*, 22(1-2), pp. 33-44. doi: 10.1016/j.marpetgeo.2004.10.010.
- Rivenæs, J. C., Otterlei, C., Zachariassen, E., Dart, C. and Sjøholm, J. (2005). A 3D stochastic model integrating depth, fault and property uncertainty for planning robust wells, Njord Field, offshore Norway, *Petroleum Geoscience*, 11(1), pp. 57–65. doi: 10.1144/1354-079303-612.
- Roberts, A. M., Yielding, G., Kusznir, N. J., Walker, I. and Dorn-Lopez, D. (1993). Mesozoic extension in the North Sea: constraints from flexural backstripping, forward modelling and fault populations, *Geological Society, London, Petroleum Geology Conference series,* 4(1), pp. 1123-1136. doi: 10.1144/0041123.
- Roberts, A. M., Yielding, G., Kusznir, N. J., Walker, I. and Dorn-Lopez, D. (1995). Quantitative analysis of Triassic extension in the northern Viking Graben, *Journal of the Geological Society,* 152(1), pp. 15-26. doi: 10.1144/gsjgs.152.1.0015.
- Roden, R. (2017). *Seismic Interpretation with Machine Learnign.* Available at: https://www.geoexpro.com/articles/2017/01/seismic-interpretation-with-machine-learning (Accessed 20.06.2022).
- Roden, R. and Santogrossi, P. (2017). Significant Advancements in Seismic Reservoir Characterization with Machine Learning, *The First – SPE Norway Magazine,* 3, pp. 14-19.

- Ronneberger, O., Fischer, P. and Brox, T. (2015). UNET: Convolutional Networks for Biomedical Image Segmentation, in: *International Conference on Medical image computing and computer-assisted intervention*. Berlin: Springer, pp. 234-241.
- Rosebrock, A. (2016). *Intersection over Union (IoU) for object detection.* Available at: https://pyimagesearch.com/2016/11/07/intersection-over-union-iou-for-object-detection/ (Accessed 14.06.2022).
- Rosenblatt, F. (1958). The perceptron: A probabilistic model for information storage and organization in the brain, *Psychological Review*, 65(6), pp. 386-408. doi: 10.1037/h0042519.
- Rouet-Leduc, B., Hulbert, C., Bolton, D.C., Ren, C. X., Riviere, J., Marone, C., Guyer, G. and Johnson, A. (2018). Estimating Fault Friction From Seismic Signals in the Laboratory, *Geophysical research letters,* 45(3), pp. 1321-1329. doi: 10.1002/2017GL076708.
- Rouet-Leduc, B., Hulbert, C., Lubbers, N., Barros, K., Humphreys, C. J. and Paul, A. (2017). Machine Learning Predicts Laboratory Earthquakes, *Geophysical research letters,* 44(18), pp. 9276-9282. doi: 10.1002/2017GL074677.
- Roy, R. (2019). *Generative Adversarial Networks (GAN).* Available at: Generative Adversarial Network (GAN) - GeeksforGeeks (Accessed 14.06.2022).
- Ryseth, A., Augustson, J.H., Charnock, M., Haugerud, O., Knutsen, S.-M., Midbøe, P.S., Opsal, J.G. and Sundsbø, G. (2003). Cenozoic stratigraphy and evolution of the Sørvestsnaget Basin, southwestern Barents Sea, *Norsk Geologisk Tidsskrift*, 83(2), pp. 107–130.
- Rønnevik, H., Beskow, B. and Jacobsen, H.P. (1982). Structural and Stratigraphic Evolution of the Barents Sea, *Canadian Society of Petroleum Geologists*, 8, pp. 431-440.
- Saha, S. (2018). *A comprehensive Guide to Convolutional Neural Networks – the ELI5 way.* Available at: https://towardsdatascience.com/a-comprehensive-guide-to-convolutional-neural-networks-the-eli5-way-3bd2b1164a53 (Accessed 14.06.2022).
- Samuel, A. L. (1959). Some Studies in Machine Learning Using the Game of Checkers, *IBM Journal of research and development*, 3(3), pp. 210–229. doi: 10.1147/rd.33.0210.
- Saunders, A.D., Fitton, J.G., Kerr, A.C., Norry, M.J. and Kent, R.W. (1997). The North Atlantic Igneous Province, Geophysical Monograph 100, *American Geophysical Union*, pp. 45–93. doi: 10.1029/GM100p0045.
- Schmidhuber, J. (2015). Deep learning in neural networks: An overview, *Neural Networks,* 61, pp. 85-117. doi: 10.1016/j.neunet.2014.09.003.
- Scholz, C. H., Dawers, N. H., Yu, J-Z., Anders, M. H. and Cowie, P. A. (1993). Fault growth and fault scaling laws: Preliminary results, *Journal of Geophysical Research,* 98(B12), pp. 21951-21961. doi: 10.1029/93JB01008.
- Schütt, K. T., Arbabzadah, F., Chmiela, S., Müller, K. R. and Tkatchenko, A. (2017). Quantum-chemical insights from deep tensor neural networks, *Nature,* 8. doi: 10.1038/ncomms13890.
- Schwarzacher, W. (1972). The Semi-Markov Process as a General Sedimentation Model, in: Merriam D. F. (eds.) *Mathematical Models of Sedimentary Processes. Computer Applications in the Earth Science*. Boston: Springer. doi: 10.1007/978-1-4684-1995-5_13.
- Seranne, M. and Seguret, M. (1987). The Devonian basins of western Norway: tectonics and kinematics of an extending crust, *Geological Society of London Special Publication,* 28, pp. 537-548. doi: 10.1144/gsl.sp.1987.028.01.35.

- Sezer, O. B. and Ozbayoglu, A. M. (2018). Algorithmic financial trading with deep convolutional neural networks: Time series to image conversion approach, *Applied Soft Computing*, 70, pp. 525-538. doi: 10.1016/j.asoc.2018.04.024.
- Shen, D., Wu, G. and Suk, H-I. (2017). Deep learning in Medical Image Analysis, *Annual Review of Biomedical Engineering*, 19, pp. 221-248. doi: 10.1146/annurev-bioeng-071516-044442.
- Shen, L., Zhang, Q., Cao, G. and Xu, H. (2019). Fall Detection Systems Based on Deep Learning and Image Processing for IoT Intrusion Detection, in: Barolli, L., Javaid, N., Ikeda, M. and Takizawa, M. *Complex, Intelligent, and Software Intensive Systems,* Proceedings of the 12th International Conference on Complex, Intelligent, and Software Intersive Systems. Berlin: Springer, pp. 590-598. doi: 10.1007/978-3-319-93659-8_53.
- Shickel, B., Tighe, P. J., Bihorac, A. and Rashidi, P. (2017). Deep EHR: a survey of recent advances in deep learning techniques for electronic health record (EHR) analysis, *IEEE Journal of Biomedical and Health Informatics*, 22, pp. 1589-1604. doi: 10.1109/JBHI.2017.2767063.
- Shipton, Z. K., Soden, A., Kirkpatrick, J. D. and Bright, A. M. (2006). How thick is a fault? Fault displacement-thickness scaling revised, in: Abercrombie, R., McGarr, A., Di Toro, G. and Kanamori, H. (eds.) *Earthquakes: Radiation Energy and the Physics of Faulting*, 170, pp. 193-198. doi: 10.1029/170GM19.
- Skogseid, J., Planke, S., Faleide, J.I., Pedersen, T., Eldholm, O. and Neverdal, F. (2000). NE Atlantic continental rifting and volcanic margin formation, *Geological Society, London, Special Publications,* 167(1), pp. 295-326. doi: 10.1144/GSL.SP.2000.167.01.12.
- Solheim, A., Berg, K., Forsberg, C.F. and Bryn, P. (2005). The Storegga Slide complex: repetitive large scale sliding with similar cause and development, *Marine and Petroleum Geology*, 22(1-2), pp. 97-107. doi: 10.1016/j.marpetgeo.2004.10.013.
- Smith, T. (2010). Unsupervised neural networks-disruptive technology for seismic interpretation, *Oil & gas journal,* 108, pp. 42-47.
- Steel, R. J. (1993). Triassic-Jurassic megasequence stratigraphy in the Northern North Sea: rift to post-rift evolution, *Geological Society, London, Petroleum Geology Conference series,* 4(1), pp. 299-315. doi: 10.1144/0040299.
- Steel, R. and Ryseth, A. (1990). The Triassic-early Jurassic succession in the northern North Sea: megasequence stratigraphy and intra-Triassic tectonics, *Geological Society, London, special publication,* 55(1), pp. 139-168. doi: 10.1144/GSL.SP.1990.055.01.07.
- Sund, T., Skarpnes, O., Jensen, L.N. and Larsen, R.M. (1986). Tectonic development and hydrocarbon potential offshore Troms, Northern Norway, in: Halbouty, N.T. (eds.) *Future Petroleum Provinces of the World*, AAPG Memoirs, 40, pp. 615–628.
- Sutskever, I., Martens, J., Dahl, G. and Hinton, G. (2013). On the importance of initialization and momentum in deep learning, *Proceedings of the 30th International Conference on Machine Learning (ICML-13),* pp. 1139-1147.
- Sørlie, R., Maast, T. E., Amundsen, H. E. F., Hammer, E., Charnock, M., Throndsen, I., Riber, L., Mearns, E. W., Dorn, A., Cummings, J. and Fredin, O. (2014). Petrographic and Samarium-Neodymium isotope signatures of the Johan Sverdrup discovery, Norwegian North Sea. *Presented at the "Brae Play" South Viking Graben, 22-27 April,* Aberdeen, Scotland, pp. 29-32.
- Tan, M. and Le, Q. V. (2019). EfficientNet: Rethinking Model Scaling for Convolutional Neural Networks, *arXiv.* doi: 10.48550/arXiv.1905.11946.

- Taylor, J. C. M. (1998). Upper Permian-Zechstein, in: Glennie, K. W. (eds.) *Petroleum Geology of the northern North Sea: Basic Concepts and Recent Advances* (4th edn.), London: Blackwell Science, pp. 174-211. doi: 10.1002/9781444313413.
- TensorFlow. (2021) *tf.keras.metrics.MeanIoU.* Available at https://www.tensorflow.org/api_docs/python/tf/keras/metrics/MeanIoU (Accessed 12.01.2022).
- Theano Development Team. (2016). Theano: A Python framework for fast computation of mathematical expressions, *ArXiv.* doi: 10.48550/arXiv.1605.02688.
- Tieleman, T. and Hinton, G. (2012). Lecture 6.5-rmsprop: Divide the Gradient by a Running Average of Its Recent Magnitude, *COURSERA: Neural Networks for Machine Learning,* 4, pp. 26-31.
- Torabi, A. and Berg, S. S. (2011). Scaling of fault attributes: A review, *Marine and petroleum geology,* 28(8), pp. 1444-1460. doi: 10.1016/j.marpetgeo.2011.04.003.
- Torabi, A., Ellingsen, T. S. S., Johannessen, M. U., Alaei, B., Rotevatn, A. and Chiarella, D. (2020). Fault zone architecture and its scaling laws: Where does the damage zone start and stop?, *Geological Society special publication,* 496(1), pp. 99-124. doi: 10.1144/SP496-2018-151.
- Tsikalas, F., Faleide, J. I., Eldholm, O. and Wilson, J. (2005). Late Mesozoic-Cenozoic structural and stratigraphic correlations between the conjugate mid-Norway and NE Greenland continental margins, *Geological Society, London, Petroleum Geology Conference series,* 6, pp. 785–801. doi: 10.1144/0060785.
- Turing, A. M. (1950). Computing Machinery and Intelligence. *Mind*, LIX(236), pp. 433– 460. Doi: 10.1093/mind/LIX.236.433.
- Vail, P. R., Mitchum Jr., R. M. and Thompsom III, S. (1977). Seismic Stratigraphy and Global Changes of Sea Level. Section 2. Application of Seismic Reflection Configuration to Stratigraphic Interpretation, in: Payton, C. E. (eds.) *Seismic Stratigraphy – Applications to Hydrocarbon Exploration.* American Association of Petroleum Geologists Special Publication M26, pp. 83-97.
- Valera, M., Guo, Z., Kelly, P., Matz, S., Cantu, V. A., Percus, A. G., Hyman, J. D., Srinivasan, G. and Viswanathan, H. S. (2017). Machine learning for graph-based representations of three-dimensional discrete fracture networks, *Computational geoscience,* 22(3), pp. 695-710. doi: 10.1007/s10596-018-9720-1.
- Vollset, J. and Doré, A. G. (1984). *A revised Triassic and Jurassic lithostratigraphic nomenclature for the Norwegian North Sea.* Stavanger: Norwegian Petroleum Directorate Bulletin 3.
- Walsh, J. J. and Watterson, J. (1988). Analysis of the relationship between displacement and dimensions of faults, *Journal of structural geology,* 10(3), pp. 239-247. doi: 10.1016/0191-8141(88)90057-0.
- Weaver, C. E. (1989). *Clays, muds, and shales.* 1st edn. Amsterdam: Elsevier.
- Whipp, P. S., Jackson, C. A-L., Gawthorpe, R. L., Dreyer, T. and Quinn, D. (2014). Normal fault array evolution above a reactivated rift fabric; a subsurface example from the northern Horda Platform, Norwegian North Sea, *Basin research,* 26(4), pp 523-549. doi: 10.1111/bre.12050.
- Wibberley, C. A. J., Yielding, G. and Di Toro, G. (2008). Recent advances in the understanding of fault zone internal structure: a review, *Geological Society Special Publication,* 299(1), pp. 5-33. doi: 10.1144/SP299.2.
- Wickman, F. (1968). Repose period patterns of volcanoes. v. general discussion and a tentative stochastic model, *Arkiv for Mineralogi och Geologi,* 4(5), pp. 351.
- Witten, I. H. and Frank, E. (2005). *Data Mining: Practical machine learning tools and techniques.* 2nd edn. San Francisco: Morgan Kaufmann Publishers.

- Wood, R.J., Edrich, S.P. and Hutchison, I. (1989). Influence of North Atlantic Tectonics on the Large-Scale Uplift of the Stappen High and Loppa High, Western Barents Shelf, in: Tankard, A.J. and Balkwill, H.R. (eds.) *Extensional Tectonics and Stratigraphy of the North Atlantic Margins*, AAPG Memoirs, 46, pp. 559–566. doi: 10.1306/M46497C36.
- Wu, X. (2017). Directional structure-tensor-based coherence to detect seismic faults and channels, *Geophysics,* 82(2), pp. A13-A17. doi: 10.1190/geo2016-0473.1.
- Wu, X. and Fomel, S. (2018). Automatic fault interpretation with optimal surface voting, *Geophysics,* 83(5), pp. O67-O82. doi: 10.1190/geo2018-0115.1.
- Wu, X., Geng, Z., Shi, Y., Pham, N., Fomel, S. and Caumon, G. (2020). Building realistic structure models to train convolutional neural networks for seismic structural interpretation, *Geophysics,* 85(4), pp. WA27-WA39. doi: 10.1190/geo2019-0375.1.
- Wu, X. and Hale, D. (2016). 3D seismic image processing for faults, *Geophysics,* 81(2), pp. IM1-IM11. doi: 10.1190/geo2015-0380.1.
- Wu, X., Liang, L., Shi, Y. and Fomel, S. (2019). FaultSeg3D: Using synthetic data sets to train an end-to-end convolutional neural network for 3D seismic fault segmentation, *Geophysics,* 84(3), pp. IM35-IM45. doi: 10.1190/geo2018-0646.1.
- Wu, X., Shi, Y., Fomel, S. and Liang, L. (2018). Convolutional neural networks for fault interpretation in seismic images, *SEG Technical program expanded abstracts,* pp. 1946-1950. doi: 10.1190/segam2018-2995341.1.
- Xie, S. and Tu, Z. (2015). Holistically-Nested Edge Detection, *2015 IEEE International Conference on Computer Vision,* pp. 1395-1403. doi: 10.1109/ICCV.2015.164.
- Xiong, W., Ji, X., Ma, Y., Wang, Y., AlBinHassan, N. M., Ali, M. N. and Luo, Y. (2018). Seismic fault detection with convolutional neural network, *Geophysics,* 83(5), pp. O97-O103. doi: 10.1190/geo2017-0666.1.
- Zhao, T. and Mukhopadhyay, P. (2018). A fault-detection workflow using deep learning and image processing, *SEG Technical program expanded abstracts,* pp. 1966-1970. doi: 10.1190/segam2018-2997005.1.
- Zhao, X. and Mendel, J. M. (1988). Minimum-variance deconvolution using artificial neural networks, *SEG Technical Program Expanded Abstracts*, pp. 738-741. doi: 10.1190/1.1892433.
- Zhao, Z and Gross, L. (2017). Using supervised machine learning to distinguish microseismic from noise events, *SEG Technical Program Expanded Abstracts,* pp. 2918-2923. doi: 10.1190/segam2017-17727697.1.
- Ziegler, P. A. (1978). North-western Europe: tectonics and basin development, *Geologie en Mijnbouw*, 57, pp. 589–626.
- Ziegler, P. A. (1992). North Sea rift system, *Tectonophysics,* 208(1-3), pp. 55-75. doi: 10.1016/0040-1951(92)90336-5.
- Zoph, B. and Le, Q. V. (2017). Neural architecture search with reinforcement learning, *International conference on learning representations.*

8 Appendix

Table 8-1: Overview of all CNN models made during this study, including the model ID, model type (architecture), central parameters that were changed, data augmentation parameters, validation scores and model scores. TF = True Fault, TB = True Background, FF = False Fault, FB = False Background.

								Grid Distortion 1D Parameters		Elastic Trans. 1D Params.			Validation Confusion Matrix				Overall Scores	
Model ID	Volume	Model type	Patch Size	Epochs	Dropout	Line selection IL/XL	Augmentation	Number of Steps	Distortion Limit	Alpha	Sigma	Alpha Affine	TF (%)	TB (%)	FF (%)	FB (%)	Train Score	Test Score
4663	ST14200	Efficient U-Net	192 192	50	0,3	IL/XL	None						86,0	98,8	1,2	14,0	0,980	0,980
4665	SG9202	Efficient U-Net	192 192	50	0,3	IL/XL	None						73,6	98,7	1,3	26,4	0,985	0,985
4679	ST14200	Efficient U-Net	192 192	50	0,3	IL/XL	Horizontal Flip						60,5	97,6	2,4	39,5	0,981	0,981
4680	SG9202	Efficient U-Net	192 192	50	0,3	IL/XL	Horizontal Flip						62,7	98,9	1,1	37,3	0,988	0,988
4682	ST14200	Efficient U-Net	192 192	50	0,3	IL/XL	Grid Distortion 1D	15	0,01				61,3	97,5	2,5	38,7	0,981	0,981
4683	ST14200	Efficient U-Net	192 192	50	0,3	IL/XL	Elastic Transform 1D			10	20	1	69,1	96,4	3,6	30,9	0,981	0,981
4684	ST14200	Efficient U-Net	192 192	50	0,3	IL/XL	All	15	0,01	10	20	1	57,6	97,9	2,1	42,4	0,981	0,981
4686	SG9202	Efficient U-Net	192 192	50	0,3	IL/XL	Grid Distortion 1D	15	0,03				69,9	98,7	1,3	30,1	0,989	0,989
4687	SG9202	Efficient U-Net	192 192	50	0,3	IL/XL	Elastic Transform 1D			10	20	1	71,3	98,6	1,4	28,7	0,989	0,989
4703	LN17001	Efficient U-Net	192 192	50	0,3	IL/XL	None						50,5	99,3	0,7	49,5	0,987	0,987
4704	LN17001	Efficient U-Net	192 192	50	0,3	IL/XL	Horizontal Flip						32,8	99,2	0,8	67,2	0,990	0,990
4705	LN17001	Efficient U-Net	192 192	50	0,3	IL/XL	Grid Distortion 1D	15	0,03				39,3	99,1	0,9	60,7	0,990	0,990
4706	LN17001	Efficient U-Net	192 192	50	0,3	IL/XL	Elastic Transform 1D			10	20	1	38,5	99,0	1,0	61,5	0,990	0,990
4707	ST14200	Efficient U-Net	192 192	50	0,3	IL/XL	Grid Distortion 1D	15	0,3				72,9	96,2	3,7	27,1	0,981	0,981
4708	ST14200	Efficient U-Net	192 192	50	0,3	IL/XL	Grid Distortion 1D	15	3				56,1	98,2	1,8	43,9	0,982	0,982
4709	ST14200	Efficient U-Net	192 192	50	0,3	IL/XL	Grid Distortion 1D	15	1				61,5	96,9	3,1	38,5	0,980	0,980
4710	ST14200	Efficient U-Net	192 192	50	0,3	IL/XL	Grid Distortion 1D	15	0,6				64,1	97,4	2,6	35,9	0,980	0,980
4711	ST14200	Efficient U-Net	192 192	50	0,3	IL/XL	Grid Distortion 1D	15	0,4				57,7	97,9	2,1	42,3	0,981	0,981
4712	ST14200	Efficient U-Net	192 192	50	0,3	IL/XL	Elastic Transform 1D			10	20	4	64,9	96,6	3,4	35,1	0,981	0,981
4713	ST14200	Efficient U-Net	192 192	50	0,3	IL/XL	Elastic Transform 1D			10	20	2	68,2	96,7	3,3	31,6	0,981	0,981
4714	ST14200	Efficient U-Net	192 192	50	0,3	IL/XL	Elastic Transform 1D			2	20	1	67,9	96,3	3,7	32,1	0,981	0,981
4715	ST14200	Efficient U-Net	192 192	50	0,3	IL/XL	Elastic Transform 1D			50	20	1	70,9	96,8	3,2	29,1	0,981	0,981
4716	ST14200	Efficient U-Net	192 192	50	0,3	IL/XL	Elastic Transform 1D			50	50	1	65,2	97,0	3,0	34,8	0,981	0,981
4717	ST14200	Efficient U-Net	192 192	50	0,3	IL/XL	Elastic Transform 1D			50	10	1	71,7	96,5	3,5	28,3	0,981	0,981
4747	ST14200	Efficient U-Net	192 192	50	0,3	IL/XL	Grid Distortion 1D	5	0,3				63,0	97,0	3,0	37,0	0,973	0,973
4748	ST14200	Efficient U-Net	192 192	50	0,3	IL/XL	Elastic Transform 1D			1	50	5	56,7	96,7	3,3	43,3	0,974	0,974
4749	ST14200	Efficient U-Net	192 192	50	0,3	IL/XL	None						95,7	98,7	1,3	4,3	0,986	0,986
4750	LN17001	Efficient U-Net	192 192	50	0,3	IL/XL	None						64,5	99,3	0,7	35,5	0,989	0,989
4751	ST14200	Efficient U-Net	192 192	50	0,3	IL/XL	Grid Distortion 1D	15	0,3				74,9	96,4	3,6	25,1	0,980	0,980
4754	ST14200	Efficient U-Net	320 320	50	0,3	IL/XL	Grid Distortion 1D	15	0,3				69,9	98,0	2,0	30,1	0,975	0,974
4755	LN17001	Efficient U-Net	192 192	50	0,3	IL/XL	Grid Distortion 1D	15	0,3				28,4	99,3	0,7	71,6	0,989	0,989
4756	LN17001	Efficient U-Net	320 320	50	0,3	IL/XL	Grid Distortion 1D	15	0,3				31,9	99,5	0,5	68,1	0,992	0,992
4757	ST14200	Efficient U-Net	192 192	50	0,3	IL/XL	Horizontal Flip						65,2	97,2	2,8	34,8	0,979	0,979
4758	ST14200	Efficient U-Net	192 192	50	0,3	IL/XL	Elastic Transform 1D			50	10	1	71,5	96,8	3,2	28,5	0,980	0,980
4761	LN17001	Efficient U-Net	320 320	50	0,3	IL/XL	Elastic Transform 1D			50	10	1	35,0	99,4	0,6	65,0	0,992	0,992
4762	LN17001	Efficient U-Net	320 320	50	0,3	IL/XL	Horizontal Flip						35,2	99,4	0,6	64,8	0,992	0,992
4772	LN17001	Efficient U-Net	192 192	50	0,3	IL/XL	Horizontal Flip						27,0	99,3	0,7	73,0	0,989	0,989
4773	LN17001	Efficient U-Net	192 192	50	0,3	IL/XL	Elastic Transform 1D			50	10	1	23,1	99,4	0,6	76,9	0,988	0,988
4781	LN17001	Efficient U-Net	192 192	50	0,3	IL	None						66,2	99,4	0,6	33,8	0,987	0,987
4782	LN17001	Efficient U-Net	192 192	50	0,3	XL	None						70,2	99,4	0,6	29,8	0,986	0,986

4783	LN17001	Efficient U-Net	320 320	50	0,3	IL	Horizontal Flip						51,6	99,3	0,7	48,4	0,995	0,995
4784	LN17001	Efficient U-Net	320 320	50	0,3	XL	Horizontal Flip						67,9	99,1	0,9	32,1	0,995	0,995
4785	LN17001	Efficient U-Net	320 320	50	0,3	IL	Grid Distortion 1D	15	0,3				58,0	99,2	0,8	42,0	0,995	0,995
4786	LN17001	Efficient U-Net	320 320	50	0,3	XL	Grid Distortion 1D	15	0,3				80,2	99,2	0,8	19,8	0,994	0,994
4787	LN17001	Efficient U-Net	320 320	50	0,3	IL	Elastic Transform 1D			50	10	1	54,6	99,3	0,7	45,4	0,995	0,995
4788	LN17001	Efficient U-Net	320 320	50	0,3	XL	Elastic Transform 1D			50	10	1	77,7	99,1	0,9	22,3	0,994	0,994
4791	LN17001	Efficient U-Net	320 320	50	0,3	IL/XL	None						28,3	99,7	0,3	71,7	0,991	0,991
4792	ST14200	Efficient U-Net	320 320	50	0,3	IL/XL	None						75,5	99,3	0,7	24,5	0,969	0,969
4793	ST14200	Efficient U-Net	192 192	50	0,3	IL	None						18,8	99,7	0,3	81,2	0,960	0,960
4794	ST14200	Efficient U-Net	192 192	50	0,3	XL	None						34,5	99,7	0,3	65,6	0,971	0,971
4795	ST14200	Efficient U-Net	192 192	50	0,3	IL	Horizontal Flip						45,0	97,4	2,6	55,0	0,966	0,966
4796	ST14200	Efficient U-Net	192 192	50	0,3	XL	Horizontal Flip						47,0	96,9	3,1	53,0	0,977	0,977
4797	ST14200	Efficient U-Net	192 192	50	0,3	IL	Grid Distortion 1D	15	0,3				56,3	95,9	4,1	43,7	0,967	0,967
4798	ST14200	Efficient U-Net	192 192	50	0,3	XL	Grid Distortion 1D	15	0,3				58,6	96,2	3,8	41,4	0,976	0,976
4799	ST14200	Efficient U-Net	192 192	50	0,3	IL	Elastic Transform 1D			50	10	1	53,9	96,2	3,8	46,1	0,967	0,967
4800	ST14200	Efficient U-Net	192 192	50	0,3	XL	Elastic Transform 1D			50	10	1	46,7	96,8	3,2	53,3	0,976	0,976
4837	LN17001	Efficient U-Net	192 192	200	0,3	IL/XL	None						93,7	99,6	0,4	6,3	0,995	0,995
4838	LN17001	Efficient U-Net	192 192	200	0,4	IL/XL	None						92,7	99,5	0,5	7,3	0,995	0,995
4839	LN17001	Efficient U-Net	320 320	200	0,3	IL/XL	Grid Distortion 1D	15	0,3				68,9	99,2	0,8	31,1	0,994	0,994
4840	LN17001	Efficient U-Net	320 320	200	0,4	IL/XL	Grid Distortion 1D	15	0,3				57,9	99,2	0,8	42,1	0,993	0,993
4835	ST14200	Efficient U-Net	192 192	200	0,3	IL/XL	None						98,2	99,5	0,5	1,8	0,993	0,993
4841	ST14200	Efficient U-Net	192 192	200	0,4	IL/XL	None						95,7	99,3	0,7	4,3	0,983	0,983
4842	ST14200	Efficient U-Net	192 192	200	0,3	IL/XL	Grid Distortion 1D	15	0,3				75,9	98,0	2,0	24,1	0,980	0,980
4843	ST14200	Efficient U-Net	192 192	200	0,4	IL/XL	Grid Distortion 1D	15	0,3				78,2	97,8	2,2	21,8	0,981	0,981
4811	LN17001	Light U-Net	192 192	50	0,3	IL/XL	None						31,2	99,4	0,6	68,8	0,985	0,985
4844	LN17001	Light U-Net	320 320	50	0,3	IL/XL	None						55,6	99,6	0,4	44,4	0,990	0,990
4845	LN17001	Light U-Net	192 192	200	0,3	IL/XL	None						70,3	99,5	0,5	29,7	0,990	0,990
4846	LN17001	Light U-Net	320 320	200	0,3	IL/XL	None						90,0	99,8	0,2	10,0	0,994	0,994
4847	LN17001	Light U-Net	192 192	200	0,4	IL/XL	None						58,3	99,3	0,7	41,7	0,989	0,989
4848	LN17001	Light U-Net	320 320	200	0,4	IL/XL	None						75,3	99,7	0,3	24,7	0,994	0,994
4849	LN17001	Light U-Net	192 192	50	0,3	IL/XL	Grid Distortion 1D	15	0,3				27,9	99,3	0,7	72,1	0,988	0,988
4850	LN17001	Light U-Net	320 320	50	0,3	IL/XL	Grid Distortion 1D	15	0,3				34,1	99,4	0,6	65,9	0,991	0,991
4851	LN17001	Light U-Net	192 192	200	0,3	IL/XL	Grid Distortion 1D	15	0,3				57,2	98,8	1,2	42,8	0,991	0,991
4852	LN17001	Light U-Net	320 320	200	0,3	IL/XL	Grid Distortion 1D	15	0,3				70,1	99,1	0,9	29,9	0,994	0,994
4853	LN17001	Light U-Net	192 192	200	0,4	IL/XL	Grid Distortion 1D	15	0,3				45,8	99,0	1,0	54,2	0,991	0,991
4854	LN17001	Light U-Net	320 320	200	0,4	IL/XL	Grid Distortion 1D	15	0,3				47,5	99,5	0,5	52,5	0,994	0,994
4823	ST14200	Light U-Net	192 192	50	0,3	IL/XL	None						58,4	97,7	2,3	41,6	0,959	0,959
4824	ST14200	Light U-Net	320 320	50	0,3	IL/XL	None						36,6	98,8	1,2	63,4	0,945	0,945
4855	ST14200	Light U-Net	192 192	200	0,3	IL/XL	None						89,6	99,0	1,0	10,4	0,975	0,975
4856	ST14200	Light U-Net	320 320	200	0,3	IL/XL	None						92,0	99,6	0,4	8,0	0,977	0,977
4857	ST14200	Light U-Net	192 192	200	0,4	IL/XL	None						89,2	99,0	1,0	10,8	0,976	0,976
4858	ST14200	Light U-Net	320 320	200	0,4	IL/XL	None						86,2	99,6	0,4	13,8	0,978	0,978

4829	ST14200	Light U-Net	192 192	50	0,3	IL/XL	Grid Distortion 1D	15	0,3				53,8	97,8	2,2	46,2	0,968	0,968
4830	ST14200	Light U-Net	320 320	50	0,3	IL/XL	Grid Distortion 1D	15	0,3				53,5	98,0	2,0	46,5	0,965	0,965
4859	ST14200	Light U-Net	192 192	200	0,3	IL/XL	Grid Distortion 1D	15	0,3				81,2	98,1	1,9	18,8	0,980	0,980
4860	ST14200	Light U-Net	320 320	200	0,3	IL/XL	Grid Distortion 1D	15	0,3				85,7	98,9	1,1	14,3	0,981	0,981
4861	ST14200	Light U-Net	192 192	200	0,4	IL/XL	Grid Distortion 1D	15	0,3				74,8	97,9	2,1	25,2	0,980	0,980
4862	ST14200	Light U-Net	320 320	200	0,4	IL/XL	Grid Distortion 1D	15	0,3				75,2	99,1	0,9	24,8	0,980	0,980
4877	LN17001	Efficient U-Net	320 320	200	0,3	IL	Grid Distortion 1D	15	0,3				67,9	99,4	0,6	32,1	0,997	0,997
4878	LN17001	Efficient U-Net	320 320	200	0,3	XL	Grid Distortion 1D	15	0,3				77,7	99,5	0,5	22,3	0,996	0,996
4879	LN17001	Efficient U-Net	320 320	200	0,4	IL	Grid Distortion 1D	15	0,3				58,7	99,3	0,7	41,3	0,996	0,996
4880	LN17001	Efficient U-Net	320 320	200	0,4	XL	Grid Distortion 1D	15	0,3				76,0	99,3	0,7	24,0	0,996	0,996
4881	LN17001	Light U-Net	192 192	50	0,3	IL	Grid Distortion 1D	15	0,3				45,3	99,0	1,0	54,7	0,993	0,993
4882	LN17001	Light U-Net	192 192	50	0,3	XL	Grid Distortion 1D	15	0,3				80,7	98,8	1,2	19,3	0,992	0,992
4883	LN17001	Light U-Net	320 320	50	0,3	IL	Grid Distortion 1D	15	0,3				58,5	99,3	0,7	41,5	0,995	0,995
4884	LN17001	Light U-Net	320 320	50	0,3	XL	Grid Distortion 1D	15	0,3				88,4	99,2	0,8	11,6	0,995	0,995
4885	LN17001	Light U-Net	192 192	200	0,3	IL	Grid Distortion 1D	15	0,3				69,5	99,2	0,8	39,5	0,995	0,995
4886	LN17001	Light U-Net	192 192	200	0,3	XL	Grid Distortion 1D	15	0,3				92,7	99,1	0,9	7,3	0,995	0,995
4887	LN17001	Light U-Net	320 320	200	0,3	IL	Grid Distortion 1D	15	0,3				73,2	99,5	0,5	26,8	0,997	0,997
4888	LN17001	Light U-Net	320 320	200	0,3	XL	Grid Distortion 1D	15	0,3				85,9	99,5	0,5	14,1	0,997	0,997
4889	LN17001	Light U-Net	192 192	200	0,4	IL	Grid Distortion 1D	15	0,3				62,4	99,1	0,9	37,6	0,994	0,994
4890	LN17001	Light U-Net	192 192	200	0,4	XL	Grid Distortion 1D	15	0,3				79,4	99,2	0,8	20,6	0,994	0,994
4891	LN17001	Light U-Net	320 320	200	0,4	IL	Grid Distortion 1D	15	0,3				52,2	99,6	0,4	47,8	0,997	0,997
4892	LN17001	Light U-Net	320 320	200	0,4	XL	Grid Distortion 1D	15	0,3				68,9	99,6	0,4	31,1	0,996	0,996
4911	LN17001	Light U-Net	256 400	200	0,3	IL/XL	Grid Distortion 1D	15	0,3				65,2	99,3	0,7	34,8	0,994	0,994
4912	LN17001	Light U-Net	256 400	200	0,3	IL	Grid Distortion 1D	15	0,3				72,8	99,4	0,6	27,2	0,994	0,994
4913	LN17001	Light U-Net	256 400	200	0,3	XL	Grid Distortion 1D	15	0,3				79,9	99,4	0,6	20,1	0,994	0,994
4916	ST14200	Light U-Net	192 192	50	0,3	IL	Grid Distortion 1D	15	0,3				44,3	97,0	3,0	55,7	0,959	0,959
4917	ST14200	Light U-Net	192 192	50	0,3	XL	Grid Distortion 1D	15	0,3				23,7	98,3	1,7	76,3	0,964	0,964
4918	ST14200	Light U-Net	144 256	50	0,3	IL/XL	Grid Distortion 1D	15	0,3				56,5	98,2	1,8	43,5	0,972	0,972
4919	ST14200	Light U-Net	144 256	50	0,3	IL	Grid Distortion 1D	15	0,3				50,7	98,1	1,9	49,3	0,961	0,961
4920	ST14200	Light U-Net	144 256	50	0,3	XL	Grid Distortion 1D	15	0,3				22,4	98,6	1,4	77,6	0,973	0,973
4951	ST14200	Efficient U-Net	192 192	50	0,4	IL/XL	Grid Distortion 1D	15	0,3				78,7	97,6	2,4	21,3	0,991	0,968
4986	SG9202	Efficient U-Net	192 192	50	0,3	IL/XL	None						53,1	98,6	1,4	46,9	0,984	0,974
4987	SG9202	Efficient U-Net	192 192	50	0,3	IL/XL	Horizontal Flip						50,5	98,7	1,3	49,5	0,987	0,979
4988	SG9202	Efficient U-Net	192 192	50	0,3	IL/XL	Grid Distortion 1D	15	0,3				48,2	98,7	1,3	51,8	0,986	0,979
4991	SG9202	Efficient U-Net	192 192	50	0,3	IL/XL	Elastic Transform 1D			50	10	1	48,0	98,8	1,2	52,0	0,987	0,979
4992	SG9202	Efficient U-Net	320 320	50	0,3	IL/XL	Grid Distortion 1D	15	0,3				56,9	98,8	1,2	43,1	0,991	0,983
5115	SG9202	Efficient U-Net	320 320	200	0,3	IL/XL	Grid Distortion 1D	15	0,3				68,4	98,9	1,1	31,6	0,994	0,985
5118	SG9202	Efficient U-Net	320 320	200	0,4	IL/XL	Grid Distortion 1D	15	0,3				60,3	98,9	1,1	39,7	0,993	0,984
5120	SG9202	Light U-Net	320 320	200	0,3	IL/XL	Grid Distortion 1D	15	0,3				64,2	99,1	0,9	35,8	0,995	0,988
5121	SG9202	Efficient U-Net	320 320	200	0,3	IL	Grid Distortion 1D	15	0,3				62,6	99,2	0,8	37,4	0,996	0,985
5122	SG9202	Efficient U-Net	320 320	200	0,3	XL	Grid Distortion 1D	15	0,3				70,5	99,5	0,5	29,5	0,997	0,991

Table 8-2: Complimentary table to table 8-1. Presents all test/validation scores for all CNN made during this study. The scores include all metrics, train/test (validation) scores and final model train/test scores. TF = True Fault, TB = True Background, FF = False Fault, FB = False Background, Val = Validation.

	Matrix Scores/Matrix Validation Scores										Confusion Matrix				Validation Confusion Matrix				Overall Scores	
Model ID	Loss	Val. Loss	F1 Macro	Val. F1 Macro	Accuracy	Val. Accuracy	Crossentropy	Val. Crossentropy	Mean IOU	Val. Mean IOU	TF (%)	TB (%)	FF (%)	FB (%)	TF (%)	TB (%)	FF (%)	FB (%)	Train Score	Test Score
4663	0,01	0,03	0,99	0,99	0,98	0,98	0,07	0,07	0,84	0,79	94,5	99,3	0,7	5,5	86,0	98,8	1,2	14,0	0,980	0,980
4665	0,01	0,03	0,99	0,98	0,99	0,99	0,06	0,06	0,74	0,67	83,4	99,2	0,8	16,6	73,6	98,7	1,3	26,4	0,985	0,985
4679	0,01	0,06	0,99	0,97	0,98	0,98	0,07	0,07	0,75	0,64	82,5	99,0	1,0	17,5	60,5	97,6	2,4	39,5	0,981	0,981
4680	0,01	0,03	0,99	0,98	0,99	0,99	0,05	0,05	0,70	0,65	75,1	99,2	0,8	24,9	62,7	98,9	1,1	37,3	0,988	0,988
4682	0,01	0,06	0,99	0,97	0,98	0,98	0,07	0,07	0,76	0,63	86,1	99,0	1,0	13,9	61,3	97,5	2,5	38,7	0,981	0,981
4683	0,01	0,06	0,99	0,96	0,98	0,98	0,07	0,07	0,76	0,62	85,8	99,1	0,9	14,2	69,1	96,4	3,6	30,9	0,981	0,981
4684	0,01	0,06	0,99	0,97	0,98	0,98	0,07	0,07	0,75	0,64	84,0	99,0	1,0	16,0	57,6	97,9	2,1	42,4	0,981	0,981
4686	0,01	0,03	0,99	0,98	0,99	0,99	0,05	0,05	0,73	0,66	80,2	99,3	0,7	19,8	69,9	98,7	1,3	30,1	0,989	0,989
4687	0,01	0,03	0,99	0,98	0,99	0,99	0,05	0,05	0,72	0,66	79,8	99,3	0,7	20,2	71,3	98,6	1,4	28,7	0,989	0,989
4703	0,01	0,03	0,99	0,99	0,99	0,99	0,06	0,06	0,73	0,64	85,0	99,2	0,8	15,0	50,5	99,3	0,7	49,5	0,987	0,987
4704	0,01	0,04	0,99	0,99	0,99	0,99	0,05	0,05	0,71	0,58	72,3	99,5	0,5	27,7	32,8	99,2	0,8	67,2	0,990	0,990
4705	0,01	0,03	0,99	0,99	0,99	0,99	0,05	0,05	0,72	0,59	79,1	99,4	0,6	20,9	39,3	99,1	0,9	60,7	0,990	0,990
4706	0,01	0,03	0,99	0,99	0,99	0,99	0,05	0,05	0,72	0,58	78,5	99,4	0,6	21,5	38,5	99,0	1,0	61,5	0,990	0,990
4707	0,01	0,06	0,99	0,96	0,98	0,98	0,07	0,07	0,76	0,62	86,2	98,9	1,1	13,8	72,9	96,2	3,7	27,1	0,981	0,981
4708	0,02	0,06	0,99	0,97	0,98	0,98	0,07	0,07	0,72	0,65	72,4	99,1	0,9	27,6	56,1	98,2	1,8	43,9	0,982	0,982
4709	0,02	0,07	0,99	0,96	0,98	0,98	0,07	0,07	0,73	0,61	80,8	98,9	1,1	19,2	61,5	96,9	3,1	38,5	0,980	0,980
4710	0,01	0,06	0,99	0,97	0,98	0,98	0,07	0,07	0,76	0,64	85,3	99,0	1,0	14,7	64,1	97,4	2,6	35,9	0,980	0,980
4711	0,01	0,07	0,99	0,97	0,98	0,98	0,07	0,07	0,75	0,64	84,4	98,9	1,1	15,6	57,7	97,9	2,1	42,3	0,981	0,981
4712	0,01	0,07	0,99	0,96	0,98	0,98	0,07	0,07	0,76	0,62	86,9	99,0	1,0	13,1	64,9	96,6	3,4	35,1	0,981	0,981
4713	0,01	0,06	0,99	0,96	0,98	0,98	0,07	0,07	0,76	0,62	86,6	99,0	1,0	13,4	68,2	96,7	3,3	31,6	0,981	0,981
4714	0,01	0,07	0,99	0,96	0,98	0,98	0,07	0,07	0,76	0,62	86,7	98,9	1,1	13,3	67,9	96,3	3,7	32,1	0,981	0,981
4715	0,01	0,06	0,99	0,96	0,98	0,98	0,07	0,07	0,76	0,63	86,8	99,0	1,0	13,2	70,9	96,8	3,2	29,1	0,981	0,981
4716	0,01	0,06	0,99	0,96	0,98	0,98	0,07	0,07	0,76	0,62	86,2	99,0	1,0	13,8	65,2	97,0	3,0	34,8	0,981	0,981
4717	0,01	0,06	0,99	0,96	0,98	0,98	0,07	0,07	0,76	0,63	86,8	98,9	1,1	13,2	71,7	96,5	3,5	28,3	0,981	0,981
4747	0,02	0,07	0,98	0,96	0,97	0,97	0,09	0,09	0,74	0,64	85,4	98,5	1,5	14,6	63,0	97,0	3,0	37,0	0,973	0,973
4748	0,03	0,08	0,98	0,96	0,98	0,98	0,09	0,09	0,70	0,61	72,9	98,5	1,5	27,1	56,7	96,7	3,3	43,3	0,974	0,974
4749	0,00	0,01	0,99	0,99	0,99	0,99	0,06	0,06	0,88	0,82	97,1	99,4	0,6	2,9	95,7	98,7	1,3	4,3	0,986	0,986
4750	0,01	0,08	0,99	0,95	0,98	0,98	0,08	0,08	0,75	0,60	86,0	98,8	1,2	14,0	64,5	99,3	0,7	35,5	0,989	0,989
4751	0,01	0,06	0,99	0,96	0,98	0,98	0,08	0,08	0,78	0,65	89,5	98,8	1,2	10,5	74,9	96,4	3,6	25,1	0,980	0,980
4754	0,01	0,04	0,99	0,97	0,98	0,98	0,09	0,09	0,76	0,67	89,1	98,8	1,2	10,9	69,9	98,0	2,0	30,1	0,975	0,974
4755	0,01	0,04	0,99	0,99	0,99	0,99	0,05	0,05	0,70	0,58	73,7	99,3	0,7	26,3	28,4	99,3	0,7	71,6	0,989	0,989
4756	0,01	0,03	0,99	0,99	0,99	0,99	0,04	0,04	0,71	0,59	75,4	99,5	0,5	24,6	31,9	99,5	0,5	68,1	0,992	0,992
4757	0,02	0,06	0,98	0,96	0,98	0,98	0,08	0,08	0,75	0,64	84,8	98,5	1,5	15,2	65,2	97,2	2,8	34,8	0,979	0,979
4758	0,01	0,06	0,98	0,96	0,98	0,98	0,08	0,08	0,77	0,65	88,8	98,7	1,3	11,2	71,5	96,8	3,2	28,5	0,980	0,980
4761	0,01	0,03	0,99	0,99	0,99	0,99	0,04	0,04	0,71	0,59	76,0	99,5	0,5	23,8	35,0	99,4	0,6	65,0	0,992	0,992
4762	0,01	0,01	0,99	0,99	0,99	0,99	0,04	0,04	0,72	0,59	71,3	99,6	0,4	28,7	35,2	99,4	0,6	64,8	0,992	0,992
4772	0,01	0,04	0,99	0,99	0,99	0,99	0,05	0,05	0,70	0,57	69,2	99,4	0,6	30,8	27,0	99,3	0,7	73,0	0,989	0,989
4773	0,01	0,04	0,99	0,99	0,99	0,99	0,05	0,05	0,70	0,57	72,8	99,3	0,7	27,2	23,1	99,4	0,6	76,9	0,988	0,988
4781	0,01	0,02	0,99	0,99	0,99	0,99	0,06	0,06	0,76	0,70	89,2	99,3	0,7	10,8	66,2	99,4	0,6	33,8	0,987	0,987
4782	0,01	0,03	0,99	0,99	0,99	0,99	0,06	0,06	0,77	0,73	90,0	99,3	0,7	10,0	70,2	99,4	0,6	29,8	0,986	0,986

4783	0,01	0,02	1,00	0,99	1,00	1,00	0,03	0,03	0,76	0,62	81,8	99,7	0,3	18,2	51,6	99,3	0,7	48,4	0,995	0,995
4784	0,01	0,02	1,00	0,99	0,99	0,99	0,03	0,03	0,79	0,66	85,7	99,7	0,3	14,3	67,9	99,1	0,9	32,1	0,995	0,995
4785	0,00	0,02	1,00	0,99	0,99	0,99	0,03	0,03	0,76	0,62	85,6	99,6	0,4	14,4	58,0	99,2	0,8	42,0	0,995	0,995
4786	0,00	0,01	0,99	0,99	0,99	0,99	0,03	0,03	0,78	0,70	88,7	99,6	0,4	11,3	80,2	99,2	0,8	19,8	0,994	0,994
4787	0,00	0,02	1,00	0,99	0,99	0,99	0,03	0,03	0,77	0,62	86,4	99,6	0,4	13,6	54,6	99,3	0,7	45,4	0,995	0,995
4788	0,00	0,01	1,00	0,99	0,99	0,99	0,03	0,03	0,78	0,69	89,3	99,6	0,4	10,7	77,7	99,1	0,9	22,3	0,994	0,994
4791	0,00	0,06	1,00	0,99	0,99	0,99	0,04	0,04	0,80	0,59	91,0	99,6	0,4	9,0	28,3	99,7	0,3	71,7	0,991	0,991
4792	0,01	0,03	0,99	0,99	0,98	0,98	0,12	0,12	0,84	0,78	95,7	99,3	0,7	4,3	75,5	99,3	0,7	24,5	0,969	0,969
4793	0,01	0,11	0,99	0,98	0,97	0,97	0,13	0,13	0,86	0,57	95,4	99,2	0,8	4,6	18,8	99,7	0,3	81,2	0,960	0,960
4794	0,01	0,10	0,99	0,98	0,98	0,98	0,11	0,11	0,87	0,64	95,5	99,4	0,6	4,5	34,5	99,7	0,3	65,6	0,971	0,971
4795	0,03	0,07	0,98	0,96	0,97	0,97	0,11	0,11	0,72	0,59	79,7	98,0	2,0	20,3	45,0	97,4	2,6	55,0	0,966	0,966
4796	0,02	0,09	0,98	0,96	0,98	0,98	0,08	0,08	0,74	0,59	80,6	98,8	1,2	19,4	47,0	96,9	3,1	53,0	0,977	0,977
4797	0,02	0,08	0,98	0,95	0,97	0,97	0,10	0,10	0,75	0,59	86,6	98,3	1,7	13,4	56,3	95,9	4,1	43,7	0,967	0,967
4798	0,01	0,08	0,99	0,95	0,98	0,98	0,08	0,08	0,75	0,60	86,0	98,8	1,2	14,0	58,6	96,2	3,8	41,4	0,976	0,976
4799	0,02	0,08	0,98	0,95	0,97	0,97	0,11	0,11	0,73	0,59	85,0	98,0	2,0	15,0	53,9	96,2	3,8	46,1	0,967	0,967
4800	0,02	0,10	0,98	0,95	0,98	0,98	0,08	0,08	0,74	0,59	83,7	98,7	1,3	16,3	46,7	96,8	3,2	53,3	0,976	0,976
4837	0,00	0,01	1,00	0,99	1,00	1,00	0,04	0,04	0,87	0,83	96,1	99,7	0,3	3,9	93,7	99,6	0,4	6,3	0,995	0,995
4838	0,00	0,01	1,00	0,99	1,00	1,00	0,04	0,04	0,86	0,82	95,8	99,7	0,3	4,2	92,7	99,5	0,5	7,3	0,995	0,995
4839	0,00	0,02	1,00	0,99	0,99	0,99	0,03	0,03	0,79	0,66	89,0	99,7	0,3	11,0	68,9	99,2	0,8	31,1	0,994	0,994
4840	0,00	0,02	1,00	0,99	0,99	0,99	0,03	0,03	0,78	0,62	87,6	99,6	0,4	12,4	57,9	99,2	0,8	42,1	0,993	0,993
4835	0,00	0,01	1,00	0,99	0,99	0,99	0,05	0,05	0,96	0,92	99,1	99,8	0,2	0,9	98,2	99,5	0,5	1,8	0,993	0,993
4841	0,00	0,01	1,00	0,99	0,99	0,99	0,07	0,07	0,92	0,89	98,5	99,6	0,4	1,5	95,7	99,3	0,7	4,3	0,983	0,983
4842	0,01	0,04	0,99	0,97	0,98	0,98	0,08	0,08	0,81	0,71	93,0	99,0	1,0	7,0	75,9	98,0	2,0	24,1	0,980	0,980
4843	0,01	0,04	0,99	0,97	0,98	0,98	0,07	0,07	0,82	0,71	93,4	99,1	0,9	6,6	78,2	97,8	2,2	21,8	0,981	0,981
4811	0,01	0,05	0,99	0,99	0,99	0,99	0,07	0,07	0,71	0,59	79,1	99,1	0,9	20,9	31,2	99,4	0,6	68,8	0,985	0,985
4844	0,00	0,02	0,99	0,99	0,99	0,99	0,04	0,04	0,76	0,68	87,5	99,5	0,5	12,5	55,6	99,6	0,4	44,4	0,990	0,990
4845	0,00	0,02	1,00	0,99	0,99	0,99	0,05	0,05	0,83	0,74	94,1	99,6	0,4	5,9	70,3	99,5	0,5	29,7	0,990	0,990
4846	0,00	0,00	1,00	1,00	1,00	1,00	0,03	0,03	0,89	0,83	96,8	99,8	0,2	3,2	90,0	99,8	0,2	10,0	0,994	0,994
4847	0,00	0,03	0,99	0,99	0,99	0,99	0,06	0,06	0,81	0,67	92,6	99,5	0,5	7,4	58,3	99,3	0,7	41,7	0,989	0,989
4848	0,00	0,01	1,00	1	0,99	0,99	0,03	0,03	0,86	0,76	95,7	99,8	0,2	4,3	75,3	99,7	0,3	24,7	0,994	0,994
4849	0,01	0,04	0,99	0,99	0,99	0,99	0,06	0,06	0,71	0,58	76,5	99,3	0,7	23,5	27,9	99,3	0,7	72,1	0,988	0,988
4850	0,01	0,03	0,99	0,99	0,99	0,99	0,05	0,05	0,72	0,59	80,0	99,5	0,5	20,0	34,1	99,4	0,6	65,9	0,991	0,991
4851	0,01	0,03	0,99	0,98	0,99	0,99	0,05	0,05	0,77	0,63	86,3	99,5	0,5	13,7	57,2	98,8	1,2	42,8	0,991	0,991
4852	0,00	0,02	1,00	0,99	0,99	0,99	0,03	0,03	0,80	0,65	90,0	99,7	0,3	10,0	70,1	99,1	0,9	29,9	0,994	0,994
4853	0,01	0,04	0,99	0,98	0,99	0,99	0,05	0,05	0,76	0,61	84,7	99,5	0,5	15,3	45,8	99,0	1,0	54,2	0,991	0,991
4854	0,00	0,02	1,00	0,99	0,99	0,99	0,03	0,03	0,79	0,63	88,6	99,7	0,3	11,4	47,5	99,5	0,5	52,5	0,994	0,994
4823	0,02	0,07	0,98	0,97	0,96	0,96	0,15	0,15	0,71	0,64	82,7	98,0	2,0	17,3	58,4	97,7	2,3	41,6	0,959	0,959
4824	0,03	0,07	0,98	0,97	0,96	0,96	0,23	0,23	0,65	0,61	66,9	98,1	1,9	33,1	36,6	98,8	1,2	63,4	0,945	0,945
4855	0,00	0,02	0,99	0,99	0,98	0,98	0,10	0,10	0,89	0,83	96,9	99,4	0,6	3,1	89,6	99,0	1,0	10,4	0,975	0,975
4856	0,00	0,01	1,00	0,99	0,98	0,98	0,09	0,09	0,91	0,88	97,9	99,6	0,4	2,1	92,0	99,6	0,4	8,0	0,977	0,977
4857	0,00	0,02	0,99	0,99	0,98	0,98	0,10	0,10	0,89	0,83	96,9	99,4	0,6	3,1	89,2	99,0	1,0	10,8	0,976	0,976
4858	0,00	0,02	1,00	0,99	0,98	0,98	0,08	0,08	0,91	0,86	97,6	99,7	0,3	2,4	86,2	99,6	0,4	13,8	0,978	0,978

4829	0,02	0,08	0,98	0,97	0,97	0,97	0,13	0,13	0,75	0,63	86,0	98,5	1,5	14,0	53,8	97,8	2,2	46,2	0,968	0,968
4830	0,01	0,07	0,99	0,97	0,97	0,97	0,15	0,15	0,75	0,63	86,0	98,7	1,3	14,0	53,5	98,0	2,0	46,5	0,965	0,965
4859	0,01	0,04	0,99	0,98	0,98	0,98	0,09	0,09	0,83	0,73	93,8	99,2	0,8	6,2	81,2	98,1	1,9	18,8	0,980	0,980
4860	0,01	0,02	0,99	0,99	0,98	0,98	0,08	0,08	0,86	0,78	95,4	99,4	0,6	4,6	85,7	98,9	1,1	14,3	0,981	0,981
4861	0,01	0,05	0,99	0,97	0,98	0,98	0,09	0,09	0,82	0,70	92,8	99,0	1,0	7,2	74,8	97,9	2,1	25,2	0,980	0,980
4862	0,01	0,03	0,99	0,99	0,98	0,98	0,08	0,08	0,84	0,75	94,8	99,3	0,7	5,2	75,2	99,1	0,9	24,8	0,980	0,980
4877	0,00	0,01	1,00	0,99	1,00	1,00	0,02	0,02	0,84	0,66	93,8	99,8	0,2	6,2	67,9	99,4	0,6	32,1	0,997	0,997
4878	0,00	0,01	1,00	0,99	1,00	1,00	0,02	0,02	0,86	0,73	94,9	99,8	0,2	5,1	77,7	99,5	0,5	22,3	0,996	0,996
4879	0,00	0,02	1,00	0,99	1,00	1,00	0,02	0,02	0,83	0,64	93,2	99,8	0,2	6,8	58,7	99,3	0,7	41,3	0,996	0,996
4880	0,00	0,01	1,00	0,99	1,00	1,00	0,02	0,02	0,85	0,71	94,3	99,8	0,2	5,7	76,0	99,3	0,7	24,0	0,996	0,996
4881	0,01	0,03	0,99	0,99	0,99	0,99	0,04	0,04	0,76	0,60	85,6	99,5	0,5	14,4	45,3	99,0	1,0	54,7	0,993	0,993
4882	0,01	0,02	0,99	0,99	0,99	0,99	0,04	0,04	0,78	0,69	88,9	99,4	0,6	11,1	80,7	98,8	1,2	19,3	0,992	0,992
4883	0,00	0,02	1,00	0,99	0,99	0,99	0,03	0,03	0,78	0,63	87,7	99,6	0,4	12,3	58,5	99,3	0,7	41,5	0,995	0,995
4884	0,00	0,01	1,00	0,99	0,99	0,99	0,03	0,03	0,79	0,71	91,0	99,6	0,4	9,0	88,4	99,2	0,8	11,6	0,995	0,995
4885	0,00	0,02	1,00	0,99	0,99	0,99	0,03	0,03	0,82	0,68	92,0	99,6	0,4	8,0	69,5	99,2	0,8	39,5	0,995	0,995
4886	0,00	0,01	1,00	0,99	0,99	0,99	0,03	0,03	0,83	0,77	94,1	99,6	0,4	5,9	92,7	99,1	0,9	7,3	0,995	0,995
4887	0,00	0,01	1,00	0,99	1,00	1,00	0,02	0,02	0,85	0,70	94,2	99,8	0,2	5,8	73,2	99,5	0,5	26,8	0,997	0,997
4888	0,00	0,01	1,00	0,99	1,00	1,00	0,02	0,02	0,87	0,77	95,6	99,8	0,2	4,4	85,9	99,5	0,5	14,1	0,997	0,997
4889	0,00	0,03	1,00	0,99	0,99	0,99	0,03	0,03	0,80	0,65	90,8	99,6	0,4	9,2	62,4	99,1	0,9	37,6	0,994	0,994
4890	0,00	0,02	1,00	0,99	0,99	0,99	0,03	0,03	0,82	0,73	93,3	99,6	0,4	6,7	79,4	99,2	0,8	20,6	0,994	0,994
4891	0,00	0,02	1,00	0,99	1,00	1,00	0,02	0,02	0,84	0,66	93,1	99,8	0,2	6,9	52,2	99,6	0,4	47,8	0,997	0,997
4892	0,00	0,02	1,00	0,99	1,00	1,00	0,02	0,02	0,86	0,73	95,2	99,8	0,2	4,8	68,9	99,6	0,4	31,1	0,996	0,996
4911	0,00	0,02	1,00	0,99	0,99	0,99	0,03	0,03	0,79	0,66	89,0	99,6	0,4	11,0	65,2	99,3	0,7	34,8	0,994	0,994
4912	0,00	0,01	1,00	0,99	0,99	0,99	0,03	0,03	0,80	0,68	91,1	99,7	0,3	8,9	72,8	99,4	0,6	27,2	0,994	0,994
4913	0,00	0,01	1,00	0,99	0,99	0,99	0,03	0,03	0,82	0,72	92,2	99,7	0,3	7,8	79,9	99,4	0,6	20,1	0,994	0,994
4916	0,02	0,09	0,98	0,96	0,96	0,96	0,18	0,18	0,73	0,58	85,6	98,0	2,0	14,4	44,3	97,0	3,0	55,7	0,959	0,959
4917	0,02	0,13	0,98	0,96	0,97	0,97	0,17	0,17	0,73	0,56	83,1	98,6	1,4	16,9	23,7	98,3	1,7	76,3	0,964	0,964
4918	0,01	0,06	0,98	0,97	0,98	0,98	0,11	0,11	0,75	0,64	86,7	98,6	1,4	13,3	56,5	98,2	1,8	43,5	0,972	0,972
4919	0,02	0,06	0,98	0,97	0,97	0,97	0,17	0,17	0,74	0,61	85,9	98,4	1,6	14,1	50,7	98,1	1,9	49,3	0,961	0,961
4920	0,02	0,13	0,98	0,97	0,98	0,98	0,12	0,12	0,74	0,56	84,2	98,7	1,3	15,8	22,4	98,6	1,4	77,6	0,973	0,973
4951	0,01	0,04	0,99	0,97	0,99	0,97	0,05	0,13	0,82	0,70	93,5	99,1	0,9	6,5	78,7	97,6	2,4	21,3	0,991	0,968
4986	0,01	0,05	0,98	0,98	0,98	0,98	0,07	0,09	0,70	0,63	75,8	98,7	1,3	24,2	53,1	98,6	1,4	46,9	0,984	0,974
4987	0,02	0,05	0,99	0,98	0,99	0,98	0,06	0,09	0,70	0,63	71,5	99,1	0,9	28,5	50,5	98,7	1,3	49,5	0,987	0,979
4988	0,02	0,05	0,99	0,98	0,99	0,98	0,06	0,09	0,68	0,62	69,1	99,0	1,0	30,9	48,2	98,7	1,3	51,8	0,986	0,979
4991	0,02	0,05	0,99	0,98	0,99	0,98	0,06	0,08	0,70	0,63	72,3	99,0	1,0	27,7	48,0	98,8	1,2	52,0	0,987	0,979
4992	0,01	0,04	0,99	0,98	0,99	0,98	0,04	0,07	0,72	0,64	78,9	99,3	0,7	21,1	56,9	98,8	1,2	43,1	0,991	0,983
5115	0,01	0,03	0,99	0,99	0,99	0,99	0,03	0,07	0,79	0,67	88,9	99,5	0,5	11,1	68,4	98,9	1,1	31,6	0,994	0,985
5118	0,01	0,03	0,99	0,98	0,99	0,98	0,03	0,07	0,77	0,65	85,6	99,4	0,6	14,4	60,3	98,9	1,1	39,7	0,993	0,984
5120	0,00	0,03	0,99	0,99	0,99	0,99	0,03	0,07	0,80	0,67	89,2	99,5	0,5	10,8	64,2	99,1	0,9	35,8	0,995	0,988
5121	0,00	0,03	1,00	0,99	1,00	0,99	0,02	0,07	0,84	0,68	93,4	99,6	0,4	6,6	62,6	99,2	0,8	37,4	0,996	0,985
5122	0,00	0,02	1,00	0,99	1,00	0,99	0,02	0,04	0,86	0,73	95,0	99,7	0,3	5,0	70,5	99,5	0,5	29,5	0,997	0,991